ORNL-5560

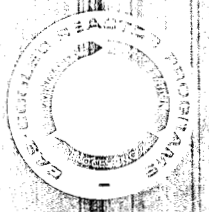

GAS-COOLED REACTOR PROGRAMS

GAS-COOLED FAST REACTOR PROGRAM ANNUAL PROGRESS REPORT FOR PERIOD ENDING DECEMBER 31, 1978

Uri Gat

P. R. Kasten

OAK RIDGE NATIONAL LABORATORY
OPERATED BY UNION CARBIDE CORPORATION - FOR THE DEPARTMENT OF ENERGY

Printed in the United States of America. Available from
National Technical Information Service
U.S. Department of Commerce
5285 Port Royal Road, Springfield, Virginia 22161
Price: Printed Copy $9.50; Microfiche $3.00

ORNL-5560
Dist. Category UC-77

Contract No. W-7405-eng-26

GAS-COOLED REACTOR PROGRAMS

GAS-COOLED FAST REACTOR PROGRAM ANNUAL PROGRESS REPORT FOR PERIOD ENDING DECEMBER 31, 1978

Uri Gat, Program Manager
Paul R. Kasten, Program Director

Date Published: August 1979

OAK RIDGE NATIONAL LABORATORY
Oak Ridge, Tennessee 37830
operated by
UNION CARBIDE CORPORATION
for the
U. S. Department of Energy

CONTENTS

	Page
SUMMARY	vii
1. GCFR CORE FLOW TEST LOOP	1
1.1 INTRODUCTION	1
1.1.1 Objectives	2
1.1.2 Test Capabilities	4
1.1.3 Capacity and Capabilities of Stage 1 CFTL	6
1.1.4 Documentation	8
1.2 ANALYTICAL ACTIVITIES	10
1.2.1 Application of $R(h^+)$ and $G(h^+)$ Functions	11
1.2.2 Flow Development in Entrance Region	16
1.2.3 Subchannel Analysis of the Test Section	16
1.2.4 Spacer Performance and Bundle Entrance Efforts	20
1.2.5 Structural Analysis of Test Bundle	20
1.2.6 Location of Thermocouples in the Test Section	26
1.2.7 Location of Pressure Taps in the Test Section	32
1.2.8 Thermal Analysis of Fuel Rod Simulator	33
1.3 DESIGN AND CONSTRUCTION OF THE LOOP	35
1.3.1 Stage 1 CFTL	36
1.3.2 Mechanical Equipment and Systems Design	37
1.3.2.1 Heat-Removal Systems	37
1.3.2.2 Piping and Equipment Layout	40
1.3.2.3 Building Facilities	42
1.3.2.4 Helium Circulator Development	45
1.3.2.5 Test Vessel Design	52
1.3.3 Electrical Equipment and Systems Design	54
1.3.3.1 Primary Power Distribution System	54
1.3.3.2 Test Bundle Power Supply and Control	56
1.3.3.3 Power Measurement for Fuel Rod Simulators	59
1.3.3.4 Electrical Protection for Fuel Rod Simulators	59
1.3.3.5 Auxiliary Power System	60
1.3.3.6 Development Support for Electrical Design	60
1.3.3.6.1 Test Bundle Power Supply and Control System	60
1.3.3.6.2 Power Measurement for Fuel Rod Simulators	62
1.3.3.6.3 Electrical Protection for Fuel Rod Simulators	63

Page

1.3.4 Instrumentation and Controls Design 63
1.3.4.1 Dynamic Simulation and Control Analysis 64
1.3.4.2 Helium Flow Control Analysis 65
1.3.4.3 Helium Flow Control Valves 70
1.3.4.4 Helium Flow Measurement 71
1.3.4.5 Helium Flowmeter Evaluation 75
1.3.4.6 Test Bundle Power Controllers 77
1.3.4.7 Integrated Control of Flow, Power, and Temperature 78
1.3.4.8 Helium Pressure and Temperature Measurements 79
1.3.4.9 Controls for Helium Supply and Helium Purification Systems 80
1.3.4.10 Control Interlocks 83
1.3.4.11 Data Acquistion System 84
1.3.4.12 Evaluation of X-Ray Imaging Equipment 85
1.3.5 Loop Schedules and Cost Estimating 86
1.3.6 Loop Procurement Activities 86
1.4 TEST BUNDLE DESIGN AND DEVELOPMENT 87
1.4.1 Test Bundle Design 87
1.4.1.1 Bundle Concept Design Study 87
1.4.1.2 Thermomechanical Design 91
1.4.1.3 Instrumentation 93
1.4.2 Development in Support of Test Bundle Design . . . 94
1.4.2.1 Fuel Rod Simulator Cladding-to-Tube-Sheet Joint 95
1.4.2.2 Connecting FRS Terminals to Power-Supply Leads 98
1.4.2.3 Fuel Rod Simulators for CFTL Test Bundles 100
1.4.2.4 Breakdown Voltage at the Electric Terminals of Fuel Rod Simulator 128
1.4.2.5 Permeation of Gases Through Boron Nitride Inside a Fuel Rod Simulator . . . 135
1.4.2.6 Small-Diameter Thermocouples for Fuel Rod Simulators 140
1.4.2.7 Structurally Related Measurements 162
1.4.3 Test Bundle Procurement 163
1.5 REFERENCES 166

2. GCFR SHIELDING AND PHYSICS STUDIES 169
2.1 INTRODUCTION 169
2.2 GRID-PLATE SHIELD-DESIGN CONFIRMATION EXPERIMENT 170
2.2.1 Experimental Results 170
2.2.2 Analysis of Results 171

Page

2.3 RADIAL BLANKET AND SHIELD EXPERIMENT 179
2.3.1 Preanalysis 179
2.3.1.1 Preanalysis of Blanket Configurations 181
2.3.1.2 Preanalysis for Shield Configurations 183
2.3.2 Experimental Configuration and Measurement Specifications 184
2.4 SHIELDING ANALYSIS IN SUPPORT OF GCFR DESIGN 185
2.4.1 Upper Axial Shield 185
2.4.2 Revised Radial and Lower Axial Shield Design . . . 190
2.5 GCFR REACTOR PHYSICS ANALYSIS 194
2.5.1 Analysis of Alternate Fuel Cycles 194
2.5.1.1 Heterogeneous GCFR Core Concepts 194
2.5.1.2 Fuel Cycle Sensitivity 196
2.5.2 Analysis of Swiss Critical Experiments for Prototypic GCFR Core Configurations Containing Thorium 200
2.6 REFERENCES 206

3. GCFR PRESSURE VESSEL AND CLOSURE STUDIES 209
3.1 INTRODUCTION 209
3.2 STEAM-GENERATOR CAVITY CLOSURE MODELS 209
3.3 REACTOR CORE CAVITY CLOSURE MODEL 211
3.3.1 Description of Closure 211
3.3.2 Parametric Study 212
3.3.2.1 Finite-Element Model 213
3.3.2.2 Analyses 214
3.3.2.3 Results 218
3.3.2.4 Conclusion and Recommendations 223
3.4 PCRV MODEL TEST FACILITY 224
3.5 REFERENCES 226

SUMMARY

INTRODUCTION

The ORNL Gas-Cooled Fast Reactor (GCFR) Program continued in 1978, the three major projects remaining the same as in calendar year 1977: Prestressed Concrete Reactor Vessel (PCRV) Closure Studies, Shielding and Physics Studies, and the Core Flow Test Loop (CFTL) Program. The main accomplishment in the PCRV program was completion of the steam generator closure experiment, which showed that the closure design is very conservative. The Shielding and Physics Studies concentrated on the axial shield experiment, which provided confidence in shielding calculation methods and confirmed streaming analysis methods. Shielding design support for the GCFR was also provided, and a radial shield and blanket experiment was designed and preanalyzed. Several alternate fuel cycles for the GCFR were analyzed and compared with similar Liquid-Metal Fast Breeder Reactor (LMFBR) cycles. In the CFTL program, most of the research and development related to the loop was completed, and construction of the loop commenced and progressed as scheduled. Thermohydraulic analysis methods were established. A staged approach to the CFTL, in which the Stage 1 loop will be constructed and operation will begin as scheduled but with a somewhat reduced capability commensurate with funding, was agreed to by all participants. Simulated fuel bundle design progressed satisfactorily but was not completed during the reporting period.

1. CORE FLOW TEST LOOP

The CFTL is a high-temperature, high-pressure, fast-transient, out-of-reactor helium circulation loop that is designed to supply helium at appropriate conditions to individual test bundles. A test bundle consists of electrically heated fuel or blanket rod simulators that are arranged to represent a segment of a fuel or control rod assembly or a full-size blanket assembly of the GCFR core. During 1978 the Title I design of the CFTL was substantially completed, a construction cost estimate was made, and the purchase of capital equipment was initiated. Near the end of the third quarter of 1978, a staged construction approach to achieve the 91-rod bundle capacity and full transient capability of the loop was adopted. Initially, a Stage 1 CFTL will be constructed to have a 37-rod bundle capacity and limited transient capability and is scheduled for completion near the end of FY 1981. Completion of the first test bundle, having 37 fuel rod simulators, is scheduled to complement completion of the Stage 1 CFTL. The conceptual test bundle design and an additional study utilizing an alternative "pressure-equalized" fuel rod simulator (FRS) were completed. The traditional "pressurized" concept was selected for the first bundle. The reference design of the FRS was changed to eliminate swaging of the rod cladding. The CFTL test objectives were redefined and formally adopted.

During 1978 the CFTL analysis tasks were subject to increasingly greater definition. The General Atomic Company (GA) codes COBRA*GCFR and TSPEC were made operational at ORNL. The SAGAPO computer program was

reviewed, which involved evaluation of the basic transform methods used to convert single-rod data to rods in bundles. The GA code FLAC was used to ensure that flow entering the test bundle would be fully developed before reaching the first grid spacer in the bundle. The original version of the ADINA code was enhanced to provide thermal loading capability in its beam element formulation and to give the user the option of tying structural degrees of freedom for efficient modeling of rigid spacer grids. Locations of TCs inside FRSs and on grid spacers and of pressure measurement taps were proposed for the first test bundle (AG1). A detailed thermal analysis was made of the nonswaged FRS.

The prinicpal ground rule for the design of Stage 1 CFTL is completion of all design work for the reference CFTL, which has a 91-rod bundle capacity and full transient test capability. The design of the mechanical components and systems was nearly completed for the heat-removal system, piping and equipment layout, building facilities and utilities, and test vessel. Development of the circulator prototype at Mechanical Technology, Inc., proceeded well, despite many vicissitudes; the rotary assembly was tested in atmospheric air and was ready to be installed in the pressure vessel at the end of the year.

Title II design of the primary power system was completed and Title II design of the test bundle power supply was started. Development work for the power measurement and electrical protection systems for individual FRSs was completed, and Title II design was started. Specification for the uninterruptible power system was completed.

Title I and Title II phases of the instrumentation and controls design progressed significantly during 1978. The dynamics simulator code ORCULT was modified and used to help resolve problems related to loop layout and component design. Commercially available valves appear to provide the range and response required for control of test bundle helium flow during steady-state and transient tests. A comprehensive evaluation of meters to measure the wide range of test bundle flow indicated that the venturi with multiple differential-pressure transmitters is the reference design and that the vortex shedding flowmeter should be examined. An evaluation of x-ray imaging indicated it should be used to estimate the bowing of test bundle rods and duct. An evaluation of systems utilizing both analog and digital techniques to provide coordinated control of helium flow, pressure, and temperature and of test bundle power was started. Loop temperature and pressure measurement requirements were defined, and commercially available components to meet those requirements were identified. The formal design review of the data acquisition system (DAS) was performed. All major DAS components have been delivered or are being purchased. A power controller for the FRSs was designed, and a bench model was built and tested successfully. Instrumentation for the helium supply, impurities injection, and purification systems was designed, and a specification was written for a gas chromatograph analyzer to measure trace-element impurities in the circulating helium. Design was started of control and safety interlock systems to protect the test bundle and loop components from damage caused by unsafe operating conditions and casualty events.

The E-Z PERT schedules and work breakdown structure were revised to reflect FY 1979 funding and FY 1978 progress in loop design and construction. A procurement schedule and status report was developed to coordinate procurement, storage, and retrieval of material for CFTL installation.

Design studies of the traditional, or pressurized, test bundle concept and a pressure-equalized bundle concept were completed, and the traditional design was selected for the first fuel test bundle. Thermal stress analysis of the tube sheet for the pressurized bundle concept indicated satisfactory temperature and stress distributions. An inlet plenum was devised that satisfactorily distributes helium into the bundle. The locations of internal TCs and x-ray imaging markers for the FRSs and of x-ray markers and pressure taps for the duct were chosen.

The evolutionary approach that was adopted for the Stage 1 CFTL was extended to the test bundles. Obtaining information on the thermal ratchetting of FRSs, the tube-sheet deflection at design conditions, and the cooling of tube-sheet and electrical leads, terminals, and connectors will be deferred until the operation of the first bundle. However, work that will be brought to fruition includes prooftesting the weld joining the cladding to the tube sheet, selecting the welding process [electron beam (EB) or the gas tungsten arc (GTA)], prooftesting the method for connecting FRS terminals to the power supply leads, completing the development of the FRS, and performing limited work on small-diameter TCs for the simulator.

Welds of the cladding to the tube sheet made by both the EB and GTA processes satisfactorily withstood the temperature and pressure cycling anticipated during CFTL operation. Tests indicated that the internal TCs for the FRSs could be stored satisfactorily by wrapping the electrical terminals to avoid damage during the welding operation; they could then be satisfactorily unwrapped. Designs of connectors for joining the electrical terminals to the power supply and brazing methods for making the joints were broached, which is probably the toughest problem in the assembly of CFTL test bundles.

The development program for CFTL FRSs included materials performance, fabrication, inspection, testing, and failure analysis tasks. Seven prototypes were fabricated, and five were subjected to operational testing. The first prototypes having variable-width heating elements were operated, and evaluation of Kanthal A1 alloy as a heating element material was initiated. The susceptibility of FRS TCs to early failure during thermal cycling and to shortened lifetimes at operating temperatures of 1000°C (1830°F) and above was noted. Intensive study indicated that TC lifetime could be increased by utilizing thermoelement material having small [0.025-mm (0.001-in.)] grain size and by minimizing the mechanical elongation of the TC during fabrication of the FRS fabrication. Testing indicated that, although the internal temperature of the nonswaged FRS was higher than that of a swaged one at the same operating conditions, the nonswaged prototypes were adequate for the CFTL test program, and the design was changed from swaged to nonswaged.

Tests to obtain information on the breakdown voltage in helium, nitrogen, and air between power terminals and internal TCs at the open end of an FRS indicated that the use of helium is marginal at the low pressures of some of the depressurization tests. Room-temperature tests

of the pressure difference across the cladding of a pressure-equalized FRS during both pressurization and depressurization transients indicate that the internal pressure lags the changing external pressure sufficiently to question seriously the adequacy of pressure-equalized rods in CFTL test bundles.

The high-temperature decalibration of small-diameter TCs made of both air- and argon-processed type K thermoelement materials revealed that TC stability was more affected by the choice of sheath materials than by the atmosphere used in processing the materials. Also, microprobe analysis indicated that changes in chemical composition of the thermoelements were greater for the stainless steel sheath than for the Inconel sheath and were greater for Alumel than for Chromel. Tests showed that the rate of formation of short-range order in Chromel and the rate of disordering in previously ordered Chromel are essentially the same. The insulated-junction TC was chosen as the reference for the CFTL FRSs because it has more reliability and less noise pickup than the intrinsic and grounded-junction thermocouples. The large failure rate of small-diameter TCs observed in previous FRS tests was found to be caused by a combination of the large grain size in some thermoelement material and the differential thermal expansion between the 316 stainless-steel rod cladding and the TC sheath and thermoelements, the latter two being considered as an entity. Manufacturers of high-temperature accelerometers and microphones have been found whose products meet or nearly meet the measurement and environmental requirements of the CFTL.

All materials needed to make the FRSs for the first bundle, including cladding, boron nitride preforms, power leads and terminals, and heating elements, should be delivered during 1979.

2. GCFR SHIELDING AND PHYSICS STUDIES

The experiment to confirm the design of the grid-plate shield was completed during this reporting period. Measurements for various configuratons consisted primarily of neutron spectrum determinations and their comparisons, with analytical predictions. In general, DOT calculations agreed well with measurements of relative intensity. However, Hornyak-button measurements that are indicative of the high-energy spectrum were usually higher than were DOT calculations. Calculations performed with other codes generally overpredicted the experimental results by factors of 1.5 to 2. Centerline predictions were usually closer to experimental results than were those off the centerline. When concentrating on neutron streaming paths between assemblies, agreements of measurements and calculations were reasonable for "close-in" measurements. At greater distances, the larger differences were attributed to scattering that was unaccounted for in the calculations. A smearing effect of the larger Bonner-ball sensors was visible in the results. Neutron streaming was determined to be sensitive to the void fraction and insensitive to variations in interassembly gaps. The DOT calculations were confirmed to predict reasonably well the grid-plate exposure.

The preanalysis for a planned radial blanket and shield experiment was performed. The experiment will be used for verification of radiation transport methods and of nuclear data that are useful in radial shield calculations. Part of the experiment will include a thorium oxide blanket; the results will be used to determine thorium nuclear data that have large uncertainties resulting from a lack of previous experimental data. One-dimensional (1D) calculations for the various configurations were completed as a part of the preanalysis. A spectrum modifier for the Tower Shielding Facility (TSF) was calculated so that the resulting spectrum resembles the GCFR spectrum. The modifier is a filter composed of 100-mm carbon steel, 90-mm aluminum, and 25-mm boron. Uranium blanket mockup configurations had to be adjusted to the availability of suitable uranium material for this experiment. Configurations of simulated boronated graphite shields were calculated, and material was ordered for the experiment.

Several GCFR shield design modifications were analyzed. Streaming paths and associated exposure of the PCRV and its liner were emphasized. The associated fluxes were calculated for the upper and lower axial shield and for the radial shield. The 2D modeling of the GCFR shielding configuration resulted in a rather large and involved problem, whose solution required special modifications of the DOT-IV code.

Several alternative fuel cycles for the GCFR were calculated, and some comparative analyses with LMFBRs were performed. Some of the fuel cycles are related to proliferation resistance. Comparative 2D and 3D calculations were completed to determine the adequacy of 2D simulations for fuel cycle studies. Beginning-of-life (BOL) and equilibrium cycles were calculated by using various fueling schemes of uranium-thorium and uranium-plutonium cycles. In some of these studies, perturbation theory methods were used in the calculations.

As part of the international program under the GCFR umbrella agreement, analysis support was provided for experiments performed at the Swiss Federal Institute for Reactor Development (EIR) in its Proteus Reactor. Configurations of plutonium-uranium and thorium oxide were calculated; particular emphasis was placed on calculations pertinent to the thorium oxide blanket. Preanalysis of the experiment involved sensitivities of calculated results to thorium cross-secton data and comparisons with EIR-calculated results. Preexperiment and postexperiment analyses revealed a low sensitivity of results to thorium cross-section values. In general, agreement between calculations and experimental results was satisfactory.

3. GCFR PRESSURE VESSEL AND CLOSURE STUDIES

The PCRV design verification and support activities involved closures for the steam-generator and reactor core cavities, and final reports for the tests of two 1/15-scale models of the steam-generator cavity closure plugs were published. An analytical parameter study was conducted to provide information required by the designer for selecting the thickness for the first model of the reactor core cavity closure plug. The study indicated that the working stress requirements were more restrictive than ultimate capacity and recommended a plug thickness of 2.29 m (7.51 ft)

to be modeled by the initial small-scale reactor cavity closure plug. Construction of the large-scale PCRV and closure model test facility was completed during 1978. The facility provides the capability for conducting ultimate strength tests of models up to about 3 m (9.81 ft) in diameter and 6 m (19.7 ft) high. The pressurization system is capable of providing pressures up to 207 MPa (30,000 psig).

1. GCFR CORE FLOW TEST LOOP

A. G. Grindell, R. E. MacPherson, and Uri Gat

1.1 INTRODUCTION — A. G. Grindell and W. R. Huntley

The ORNL Core Flow Test Loop (CFTL) Program for the Gas-Cooled Fast Reactor (GCFR) includes (1) construction of the CFTL; (2) construction of test bundles that simulate GCFR core assemblies and their operation in the CFTL under steady-state and normal, upset, emergency, and faulted conditions anticipated for the GCFR; (3) development tasks supporting the designs of the CFTL and the test bundles; (4) analyses supporting the construction and operation of the CFTL and the test bundles; and (5) acquisition and analysis of programmatic test data during test bundle operation.

For the CFTL loop, the Title I design for the mechanical and electrical disciplines, a substantial amount of instrumentation and controls design, and the Title II design for site modification (except for some electrical engineering) were completed in 1978. An updated cost estimate was made, and plans, schedules, and work breakdown structures (WBSs) were prepared for the design and construction of the loop and the first test bundle (AG1). The procurement of a modicum of loop equipment was initiated.

Near the end of the third quarter of 1978, a staged approach to achieve the 91-rod bundle capacity and full transient capability of the loop was adopted formally by the GCFR participants: Department of Energy (DOE), General Atomic Company (GA), Helium Breeder Associates (HBA), and ORNL. The design of the CFTL to the full 91-rod bundle capacity and full transient capability will be completed, including the installation layout of equipment and all associated interconnections. Initially, however, a Stage 1 CFTL will be constructed, which will have a 37-rod bundle capacity and a limited transient capability; completion will be scheduled for near the end of FY 1981. The assembly and initial operation of the first test bundle, AG1 having 37 fuel rod simulators (FRSs), is scheduled for the middle of FY 1982.

The conceptual test bundle design was completed. It utilizes the traditional pressurized rod simulator and tube sheet, both of which act as vessel pressure boundaries. An additional study was made of a "pressure-equalized" concept, in which both the rod cladding and the tube sheet sustain high gas pressure but are not vessel pressure boundaries. The traditional pressurized concept was adopted for bundle AG1.

Work on the swaged FRS was discontinued when the nonswaged FRS development progressed sufficiently to lead ORNL to propose it for the reference design.

1.1.1 Objectives

The viability of the GCFR depends strongly on the steady-state characteristics and the transient responses of the core assemblies according to the program plan[1] prepared for the CFTL by GA. Data on heat-transfer and pressure-drop characteristics of the core during steady-state operation are important in the design and costs of the GCFR. Data on the responses of the core assemblies to the transients anticipated for the GCFR are important in determining the design and safety margins of the core.

The principal objectives of the CFTL are the acquisition and analysis of test data on (1) thermal and pressure-drop characteristics, (2) design and safety margins, and (3) tribological structural behavior of test bundles that simulate portions of GCFR fuel and control assemblies and full-size blanket assemblies. Data will be taken under CFTL operating conditions that simulate GCFR steady-state, normal, upset, emergency, and faulted accident conditions. Depressurization and flow blockage conditions will also be simulated. The data will be used in the design confirmation of the GCFR core assemblies.

The CFTL is being designed to provide the needed information and test data. It will be a high-pressure, high-temperature, out-of-reactor helium circulation system that will supply the test requirements of the program plan and GA's CFTL test specifications[2] for individual CFTL test bundles that model GCFR core assemblies. The requirements include test

bundle power and heat removal; control of helium coolant flow rate, pressure, and temperature; and control of helium purity and injected gaseous impurities. The CFTL will simulate the test conditions specified for GCFR steady-state operation; normal, upset, and emergency transients; and rapid depressurization of helium inventory associated with the GCFR design-basis accident. It is being designed to impose on each installed test bundle either uniform or skewed power distributions as required.

A test bundle will consist of electrically heated FRSs or blanket rod simulators (BRSs) having appropriate spacer grids, hanger rods, and an enclosing duct arranged to represent a segment of a fuel or control rod assembly or to represent a full-size blanket assembly in the GCFR core. Temperatures and pressure-drop characteristics will be measured. The effects of thermal and mechanical interactions between the rods and the grid spacers and hexagonal duct, caused principally by transient operations and core undercooling, will be determined both by viewing and by measuring during out-of-loop examination. X-ray imaging equipment will be installed in the CFTL program as early as practicable to observe test bundle movement or deformation during operation.

CFTL test bundles simulating GCFR fuel, control, and blanket assemblies will be operated at flat or skewed power distributions at prescribed power levels and slopes and at steady-state or transient conditions. Transient operation will include prescribed variations, with time, of test bundle power, helium pressure, and coolant flow rate to simulate normal, upset, emergency, and faulted accident transients, which include depressurization accidents. These test bundle operations should provide data, observations, and experience to (1) validate analytical methods employed to predict steady-state and transient performance of full-size GCFR core assemblies, (2) demonstrate the cyclic behavior of the core assemblies, (3) determine unknown core assembly performance and endurance deficiencies, (4) evaluate thermally induced bowing of individual rod simulators and test bundles, (5) examine (within limits of the simulators) the test bundle behavior in marginal undercooling tests beyond the faulted fuel temperature limit and thermal gradients, and (6) perform exploratory tests of local flow blockage.

1.1.2 Test Capabilities

The CFTL test capabilities were discussed in the previous annual report.[3] Briefly, the CFTL provides up to 4100 kW of electrical power to test bundles, simulates flat or skewed power distributions, and can simulate accident transients involving tenfold and larger changes in bundle power and in helium coolant flow rate and pressure in times as short as 1 s. The steady-state operating requirements of the CFTL shown in Table 1.1 were modified only slightly during the past year. Some test capabilities that we have defined better in the past year are described below.

The stored thermal energy in an FRS differs from that in a GCFR fuel rod at a given power and cladding temperature. To provide comparable thermal behavior of an FRS during a power transient, it will be necessary to vary CFTL power slightly from the GCFR power prescribed with test specifications. For example, during a simulated GCFR scram from a power level of 28 kW per rod, the CFTL power will have to be increased slightly because the FRS has less stored thermal energy than does a GCFR fuel rod under these conditions. Therefore, a code was devised for computer control of the bundle power system to permit FRS simulation of the thermal behavior of GCFR fuel and blanket rod cladding.

General Atomic has requested that the CFTL be capable of simulating depressurization accidents wherein the final back pressure is 0.1 MPa (14.5 psia) instead of the previous value of 0.15 MPa (22 psia). To obtain rapid helium loop depressurization to the new slightly subatmospheric pressure, it may be necessary to use auxiliary vacuum pumping at the low end of depressurization.

The CFTL will be capable of observing and measuring deflections of an individual FRS and the hexagonal shroud (duct) surrounding the test bundle during steady-state and transient operation. X-ray imaging will be used to provide records of the observations, from which we plan to make deflection measurements. Dense-metal reference markers will be strategically placed in the FRS, on the test vessel structure, and on the duct to allow measurement of test bundle deflections. X-ray film

Table 1.1. Steady-State Operating Requirements of the CFTL

Coolant	Helium
Design pressure, MPa (psia)	11.8 (1715)
Maximum operating pressure, MPa (psia)	10.3 (1500)
Normal operating pressure, MPa (psia)	9 (1300)
Minimum operating pressure, MPa (psia)	0.1 (14.5)
Test bundle data	
Test bundle ΔP,[a] kPa (psi)	278 (40.4)
Inlet temperature, °C (°F)	
Nominal	320 (610)
Minimum	260 (500)
Maximum	350 (660)
Outlet temperature, °C (°F)	
Nominal	550 (1020)
Minimum	260 (500)
Maximum	593 (1100)
Maximum total helium flow, kg/s (lb/s)	3.2 (7)
Helium flow per rod	
Core maximum, g/s (lb/hr)	30.5 (242)
Blanket maximum, g/s (lb/hr)	27 (215)
Core maximum linear power rating, kW/m (kW/ft)	33.6 (10.2)
Axial maximum-to-average power ratio	1.21
Maximum transverse fuel power gradient, %/cm (%/in.)	4 (10)
Minimum transverse power gradient, %/cm (%/in.)	0 (0)
Total simulated fuel rod length, mm (in.)	2220 (87.4)
Simulated core length, mm (in.)	1130 (44.5)
Axial blanket length (each end), mm (in.)	450 (17.7)
Maximum power per fuel rod, kW	38
Nominal power per rod, kW	28
Simulated radial blanket rod length, mm (in.)	2220 (87.4)
Power per blanket rod, kW	45

[a]Does not include losses at inlet and outlet of test vessel.

radiography will be used initially for steady-state observations. Real-time imaging will be obtained for transient testing, and x-ray fluoroscopic imaging will be aided by computer enhancing as required.

1.1.3 Capacity and Capabilities of Stage 1 CFTL

A staged construction approach to achieve the 91-rod bundle capacity and full transient capability for the CFTL was adopted formally by the GCFR participants: DOE, GA, HBA, and ORNL. In this approach the design of the full 91-rod capacity and full transient capability CFTL will be completed as soon as practicable. However, we will initially construct only a Stage 1 CFTL that has a 37-rod bundle capacity and a limited transient capability; this bundle is scheduled for completion near the end of FY 1981. The deferred equipment required to achieve full capacity and full transient capability for the CFTL will be designed before the Stage 1 CFTL is built and will be installed as needs and funds permit. Although the Stage 1 CFTL will not be equipped for GCFR depressurization accident simulation or for on-line helium purification control, it will be able to accomplish the majority of the tests specified in ref. 2 for AG1, which will have 37 FRSs. Table 1.2 summarizes the specified tests that can be carried out in the Stage 1 CFTL with a 37-rod bundle.

Only limited control of helium purity will be provided in the Stage 1 CFTL. Helium will be vented from the loop in batch mode operation and replaced with as-received helium from the Bureau of Mines to approach specified purity. Power skews can be simulated for a 37-rod bundle having the installed seven power zones, but larger bundles cannot be operated until additional power zones are installed. Test section flows will be fully controllable for all steady-state and constant-pressure transient conditions, as outlined in the system design description[4] and in the test specifications.[2] Major components that are being deferred to Stage 2 include the bypass heat exchanger (HX-2) and the associated bypass line around the circulators, six zones of electrical power, a spare circulator, the helium purification system, the depressurization system, the impurity addition system, the gas chromatograph, and the x-ray imaging system.

Table 1.2. Tests of a 37-Rod Bundle Which Can Be Accomplished in the Stage 1 CFTL

Test	Number of tests	
	Stage 1	Stage 2
Steady-state flow, unheated	11	
Normal transients, unheated	36	
Upset transients, unheated	5	
Emergency transients, unheated	∿3	
Depressurization transients, unheated		5
Steady state, uniform power	31	
Steady state, skewed power	33	
Steady state, single heated rod	82	
Normal transients, uniform power	13	
Normal transients, skewed power	25[a]	
Upset transients, uniform power	5	
Upset transients, skewed power	3	
Emergency transients, uniform power	2	
Depressurization transients		All
Margin tests	36	4[b]
Total	285	

[a] One test includes 1200 cycles at 145 s per cycle.

[b] May test to failure in this series.

We believed initially that the elimination of HX-2 from the Stage 1 CFTL would restrict the capability to perform rapid transients that simulate GCFR scrams. This belief was based on the purpose of the bypass line and HX-2: to divert the excess flow of relatively cool gas leaving the circulator discharge, which becomes available during simulated scrams, away from HX-1 and thus alleviate what might otherwise be a thermal shock to HX-1. However, after more careful consideration, we determined that, because of the low total power input associated with the 37-rod bundle, HX-2 is not essential to the simulation of GCFR scrams with the 37-rod bundle. During 37-rod-bundle operation, judicious choices of circulator operating point and attemperator flow will permit operation

of HX-1 at a temperature sufficiently low to avoid thermal quenching of HX-1 in a scram. Thus the Stage 1 CFTL will have the capability to simulate GCFR power scrams with a 37-rod bundle. However, scrams with a 91-rod bundle will cause excessive thermal shock at HX-1 unless HX-2 is available. (Computer simulations of a 61-rod bundle scram have not been completed.)

Simulations of a design-basis depressurization accident (DBDA) must await installation of the deferred depressurization system during Stage 2. On-line measurement and control of helium purity and adjustment of H_2:H_2O ratios in the circulating helium cannot be performed in Stage 1 because these functions require installation of the gas chromatograph, moisture monitor, helium purification, and impurity addition systems, which are also deferred.

The Stage 1 CFTL will have limited capability to measure structural deflections in the test bundle during loop operation. Only steady-state deflections will be observed by the ad hoc use of conventional x-ray source and film in conjunction with dense reference markers in the bundle FRS and on the duct and test-vessel structure. X-ray tests made with a mockup of the test vessel and bundle have shown that steady-state deflection information can be obtained with exposure times of about 1 min by using 420 kV and AA industrial x-ray film. Real-time deflection measurements during transient testing must await Stage 2, when x-ray fluoroscopy equipment will be provided.

The capabilities of the Stage 1 CFTL are summarized in Table 1.3.

1.1.4 Documentation

The first complete issue of the system design description (SDD) was approved by DOE and issued in June 1978.[4] The SDD is subject to change as the design progresses, as the development work comes to fruition, and as the criteria change to meet programmatic needs. Therefore, the SDD will be revised and issued again in the near future.

A Quality Assurance Program Plan (QAPP) for the CFTL construction was prepared and issued.[5] The QAPP covers the design, procurement, fabrication, assembly, and acceptance testing of the loop. It supersedes the CFTL Quality Assurance Program Index that was prepared earlier

Table 1.3. Capabilities of the Stage 1 CFTL

Coolant	Helium
Design pressure, MPa (psia)	11.8 (1715)
Maximum operating pressure, MPa (psia)	10.3 (1500)
Normal operating pressure, MPa (psia)	9 (1300)
Minimum operating pressure	Near ambient
Test bundle data	
Test bundle ΔP,[a] kPa (psi)	278 (40.4)
Inlet temperature, °C (°F)	
Nominal	320 (610)
Minimum	260 (500)
Maximum	350 (660)
Outlet temperature, °C (°F)	
Nominal	550 (1020)
Minimum	260 (500)
Maximum	593 (1100)
Maximum total helium flow, kg/s (lb/s)	3.2 (7)
Helium flow per rod, g/s (lb/hr)	30.5 (242)
Maximum core flow for 37 FRSs, kg/s (lb/s)	1.13 (2.5)
Core maximum linear power rating, kW/m (kW/ft)	33.6 (10.2)
Axial maximum-to-average power ratio	1.21
Maximum transverse fuel power gradient, %/cm (%/in.)	4 (10)
Minimum transverse power gradient, %/cm (%/in.)	0 (0)
Total simulated fuel rod length, mm (in.)	2220 (87.4)
Simulated core length, mm (in.)	1130 (44.5)
Axial blanket length (each end), mm (in.)	450 (17.7)
Maximum power per fuel rod, kW	38
Nominal power per fuel rod, kW	28
Simulated radial blanket rod length, mm (in.)	2220 (87.4)
Power per blanket rod, kW	45
Depressurization test capability	None
Helium purification	None
Spare circulators	None
X-ray deflection measurements	Film only, steady state

[a]Does not include losses at inlet and outlet of test vessel.

in the project. Individual QAPPs covering test bundle construction and loop operation will be issued later.

1.2 ANALYTICAL ACTIVITIES — J. P. Sanders, K. W. Childs,* J. C. Conklin, W. R. Nelson, and S. A. Hodge†

At a meeting of specialists on CFTL analysis held at GA in January 1978, the overall objectives and division of responsibilities for the associated task were reviewed. At the meeting, a modification of the COBRA*HE computer program[6] was provided to ORNL by GA; this modification, which had features to represent the flow through the edge channels of the bundle, was designated as COBRA*SIDE by GA.

All necessary adaptations of the COBRA*SIDE computer program were completed by April 1978. Using identical input, the calculated results from the UNIVAC-1110 computer at GA and those from the IBM 360 system at ORNL agreed to the fourth significant digit.

In June 1978 at a second meeting at GA, an updated version of the COBRA series of computer programs was provided by GA. The updated version, a modification of the COBRA-IV computer program,[7] was designated as COBRA*GCFR by GA. COBRA-IV for two-phase coolants was also in use at ORNL. This version of the COBRA series has improved numerical procedures plus other desirable input options. Because of the prior experience in adapting COBRA*SIDE for the IBM 360 system, the modification of COBRA*GCFR was completed in about two months and is now the primary computer program for CFTL bundle thermal-flow analysis.

A second computational code, TSPEC,[8] that GA had originated was provided to ORNL during the year. This code analyzes conditions in a typical flow channel and in the adjacent rod in the test bundle. The procedure was first written to evaluate the range of conditions that would be anticipated in the tests of the CFTL bundles. It was made operational at ORNL to provide a short computational procedure for evaluating the anticipated conditions along the FRSs during testing. This information is necessary for estimating the range of errors in the TC measurements that might result from thermal gradients along the TC

---

*Computer Sciences Division, UCND.

†ORAU Graduate Fellow, University of Texas, Austin.

leads or from variations caused by time-at-elevated-temperature history of the TC junction.

In July S. A. Hodge joined the analysis effort for the CFTL. Hodge is a graduate student of the University of Texas at Austin and is supported for a one-year term by a graduate fellowship of the Oak Ridge Associated Universities (ORAU). The addition of Hodge expanded the analysis effort at ORNL significantly without additional cost. (His efforts will also be the basis for a doctoral thesis at the University of Texas.) He began by evaluating the SAGAPO computer program[9] for the application of data obtained for single roughened rods in an annular geometry to bundles of roughened rods. This review involved an evaluation of the basic transform methods for converting single-rod data to correlations for multiple rods in bundles. SAGAPO was originally written for an IBM 360 computer, and a tailored version of the code for application to the CFTL has been made operational on the ORNL system. The SAGAPO formulation assumes that all rods in the bundle are the same diameter and are roughened over the same axial segment. However, the CFTL bundle has smooth larger-diameter hanger rods mixed with the roughened FRS, and additional modifications must be made in the coding.

Structural analytical procedures were developed throughout the year. After preliminary evaluation of calculational requirements and existing general computational proceudres, ORNL and GA agreed in June that we would evaluate the FRS structural performance and that GA would develop procedures for determining the grid spacer structural performance. These efforts were subsequently combined. Toward the end of the year, ORNL efforts were directed to the requirements for CFTL bundle structural instrumentation.

A summary of the overall goals for the analysis tasks at ORNL was prepared for a review meeting in Oak Ridge on November 8 and 9, 1978. An outline of this summary is included in Table 1.4.

1.2.1 Application of $R(h^+)$ and $G(h^+)$ Functions — S. A. Hodge

An adaptation of the computer code SAGAPO,[9] developed by A. Martelli at Karlsruhe in 1977 for steady-state thermal and fluid dynamic analysis

Table 1.4. Outline of Goals for the CFTL Analysis Task at ORNL

Prevention of unanticipated bundle failures
Prior to testing:
Obtain and implement thermal-flow computational methods
Obtain or develop structural analysis methods for bundle
Determine locations for critical thermal measurements
Estimate magnitude of significant structural measurements
Evaluate anticipated error measurements and establish confidence limits
Evaluate sources of error caused by sensor location
Determine error limits in signal generation
Determine error limits in data recording and reduction
Determine pretest values for critical measurements
During testing:
Make on-line comparisons of calculated and measured values
Extrapolate comparison prior to each level of testing
Compare measured values plus their error bands with computed values
Adjust input values, analytical models, or computational techniques to achieve statistical agreement with the trend of the experimental data
Compare structural performance predictions with posttest examinations
Preparation of experimental results for use by General Atomic Company in code verification
Reduce all data to appropriate physical measurements
Report error bands and their respective confidence limits for all measurements
Transcribe all measurements onto magnetic tape with appropriate identification of measurements and test conditions
Produce appropriate reports, as required, which present the experimental measurements and the related error bands and confidence limits

of gas-cooled bundles, was made fully operational on the ORNL IBM 360 computer. The program, originally written for an IBM system, was formulated from the listing in the user's guide and was tested against the sample input and corresponding output data provided in the manual.

In general, SAGAPO applies the $R(h^+)$ and $G(h^+)$ functions in a highly detailed analysis, which includes allowances for such phenomena as the thermal expansion of the bundle and the fin efficiency effects of the roughness ribs. Bundle flow channels are divided into subchannels and further into a user-designated number of sub-subchannels for the definition of equivalent annuli and for application of the method of Dalle Donne[10] for determination of the friction factor and the Stanton number.

SAGAPO is written for application to reactor bundles composed of rods of uniform diameter and surface characteristics. Therefore, the code must be modified for application to the proposed CFTL bundles, which have larger-diameter, smooth-surfaced hanger rods. The interspersion of smooth surfaces among the roughened surfaces of the fuel rods results in asymmetric velocity profiles between nonsimilar surfaces. The velocity profile width, between the roughened surface of a fuel rod and the surface of zero shear in the flow, will therefore vary with the Reynolds number.

The friction factors and heat-transfer coefficients computed by SAGAPO for the flow past a roughened rod depend on empirical correlations developed by Dalle Donne[10] at Karlsruhe. The correlation for the rough-wall friction factor f_1 is based on the equation

$$(2/f_1)^{1/2} = A[\ln(Y_L/h) - 1/2 - 1/(2 + Y_L/r_1)] + R \ , \qquad (1)$$

where Y_L is the width of the velocity profile, h is the roughness height, and r_1 is the volumetric radius of the roughened rod. The equation is derived by integration of the dimensionless velocity U^+, given by

$$U^+ = A \ln Y/h + R \ , \qquad (2)$$

from the rod surface to the surface of zero shear in annular geometry. Here Y is the perpendicular distance from the roughened surface, and the roughness parameter R is the boundary condition for the dimensionless velocity profile, that is, the value of U^+ at the tip of the roughness. Dalle Donne calculated the roughness parameter R using Eq. (1) by assuming that the slope A of this linear relation was equal to 2.5, the value determined in 1933 by Nikuradse for flow in sand-grain-roughened tubes. Using this procedure, Dalle Donne and others before him found that the calculated value of R was not constant for a given roughened surface but, rather, varied as a function of the ratio Y_L/h.

As part of the required modification to SAGAPO, a method has been developed for determination of the actual slope A from the experimental data of Dalle Donne.[10] This modification can be made by plotting the transformed data as illustrated in Fig. 1.1 for the first five rods tested. The slopes so determined are all significantly less than the generally accepted value of 2.5 and are given in the following table:

Rod No.	Slope A
1	2.00
2	2.20
3	2.05
4	2.00
5	2.10

This table shows that the slope A of the dimensionless velocity profile is determined by the characteristics of the roughened surface. Furthermore, when the correct slope A is used in Eq. (1), the roughness parameter R is not a function of the ratio Y_L/h but, rather, is a constant for a given roughened rod. For example, its value is equal to the ordinate intercept for the lines representing the rods of Fig. 1.1.

The assumption has long been generally held that fully roughened flow, which implies that the friction factor is independent of the Reynolds number, exists for values of the roughness Reynolds number

$$h^+ = h/D \ \mathrm{Re}(f/2)^{1/2} \tag{3}$$

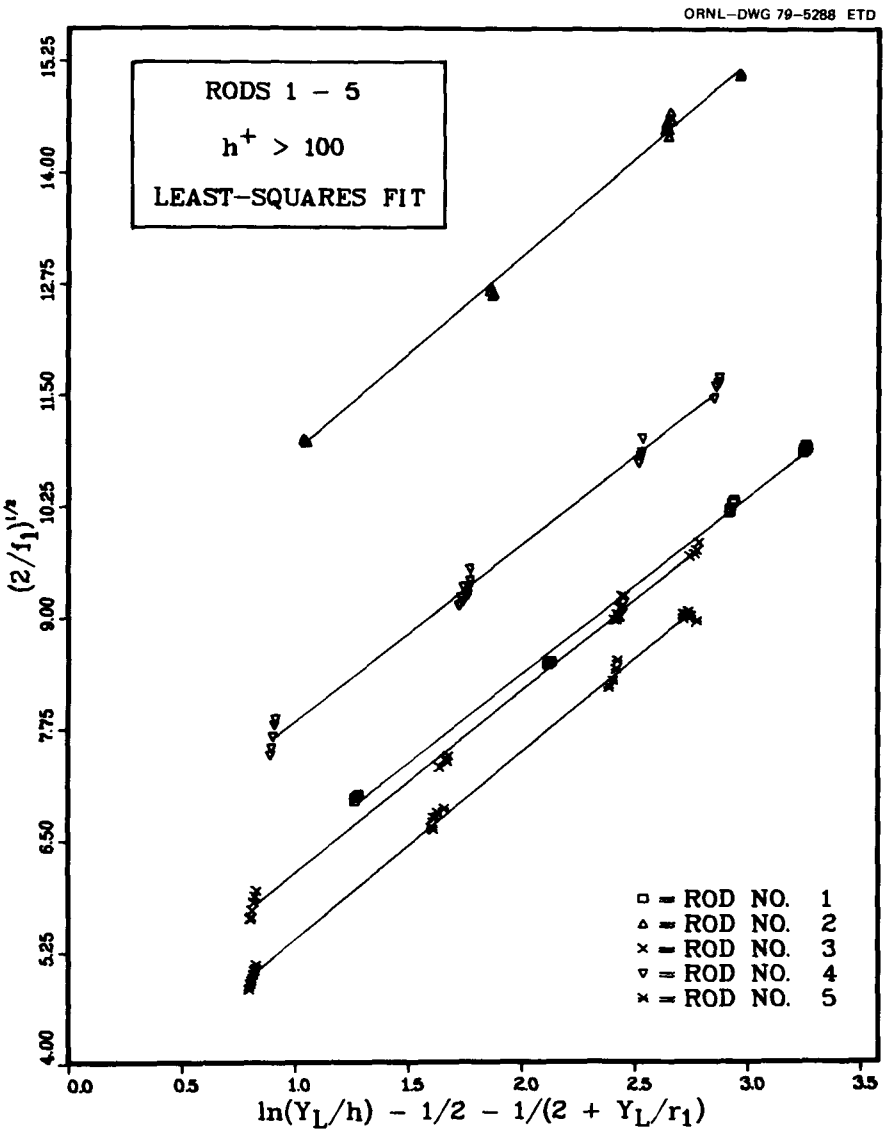

Fig. 1.1. Universal Law of Friction for Five Rods Tested by Dalle Donne.

greater than 70 in accordance with the results of Nikuradse. However, plots similar to those of Fig. 1.1 show that the lower h^+ limit for the fully rough flow regime is a function of the roughness height. The plotted points for rods 1 and 2, which have a relatively low roughness height, are coincident at each of the four general abscissa values within the spread of experimental error. On the other hand, the marked vertical point spread for rods 3, 4, and 5 results from a dependence of

the friction factor on the roughness Reynolds number, which indicates that fully roughened flow exists only at higher values of h^+.

The preceding results are to be used in the development of the required modification to the empirical correlations used in SAGAPO.

1.2.2 Flow Development in Entrance Region — J. C. Conklin

In the GCFR, helium will flow axially into the bundle of fuel rods that comprise the heart of the GCFR fuel assembly. For the CFTL, the flow is first introduced radially into the bundle of FRSs and then induced to turn 90° to flow axially in the bundle. The objective of this portion of the analysis is to ensure that the flow will be fully developed and therefore representative of the GCFR before it reaches the first grid spacer of the CFTL test bundle. A flow analysis code (FLAC) has been transmitted by GA to ORNL and is currently operational.[11]

The flow distribution for a 60° symmetrical segment of the entrance region for the 91-rod bundle at full flow and system pressure is presented in Figs. 1.2 to 1.4. This flow is fully developed at a point 200 mm (8 in.) downstream from the tube sheet, which is about 90 mm (3.6 in.) upstream from the first spacer.

The current design for the hanger rods and duct spacing restricts flow significantly in the edge channels and in the channels adjacent to the hanger rods. This effect may induce significant temperature gradients across the FRSs that are cooled by these low-flow channels.

The inlet to the entrance region was considered as a gap that had a flow area equal to the cross-section flow area of the bundle; it was assumed to extend across the top of the duct. The shape of this inlet does not affect the axial flow development, but it significantly affects the pressure loss across the inlet and the cross flow at the tube sheet. Different designs of this inlet will be evaluated as the designs for the test bundle and loop mature.

1.2.3 Subchannel Analysis of the Test Section — J. C. Conklin

The main analytical tool used to predict the flows and temperatures in the test section of the test bundle that simulates the GCFR core is

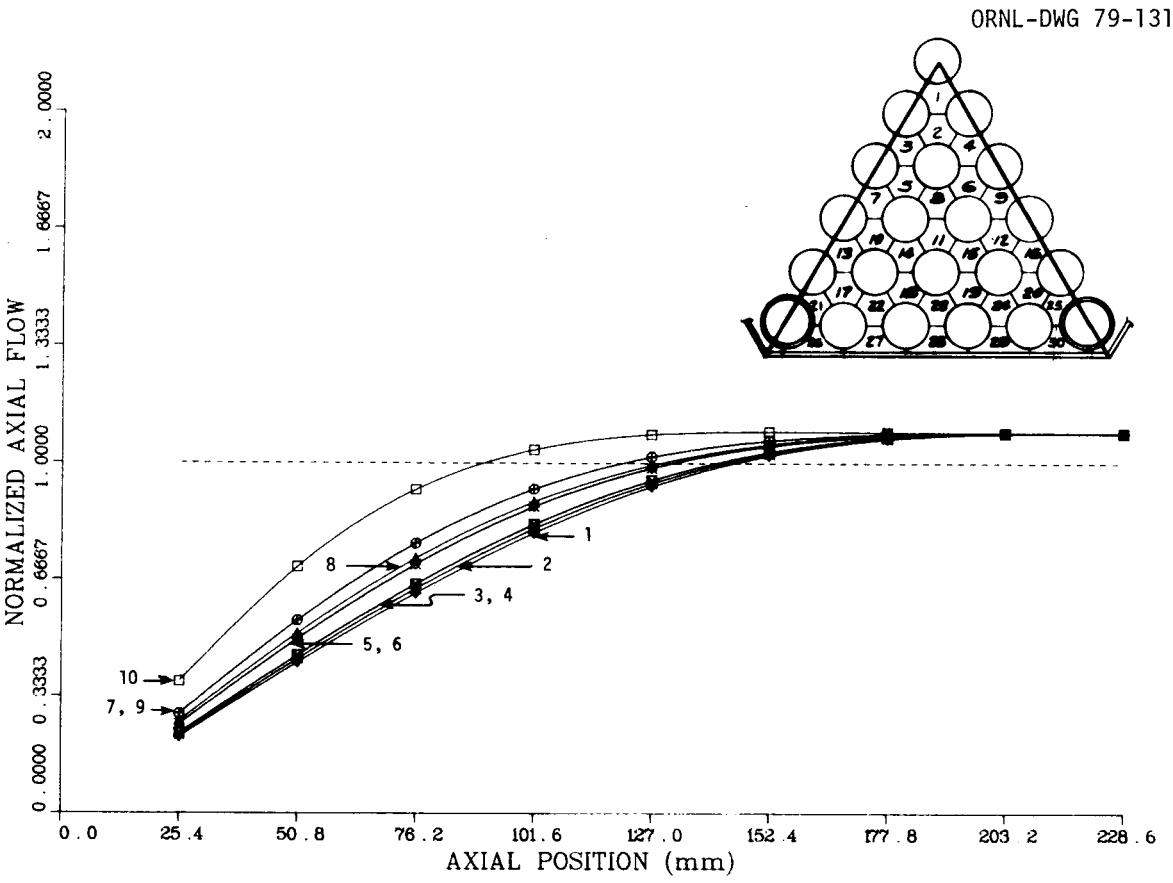

Fig. 1.2. Flow Distribution in the Inlet Section of the 91-Rod Core Flow Test Loop Bundle for the Interior Channels.

an appropriate version of COBRA. Three versions modified by GA are currently operational at ORNL: COBRA*HE, COBRA*SIDE, and COBRA*GCFR. The COBRA*HE and COBRA*SIDE codes are helium versions of COBRA-IIIC,[12] and COBRA*GCFR is a helium version of COBRA-IV;[7] COBRA*GCFR is the version in use.

The COBRA*HE code was implemented in 1977 and described in the annual report[13] for that year. COBRA*SIDE, implemented by April 1978, was an attempt to improve the prediction of temperatures and flows for the channels bound by a rough rod and a smooth wall. This version still did not perform adequately because of the inherent inaccuracy of attempting to represent the friction factor as a function of the bulk Reynolds number for the roughened rod-smooth wall channel and the relative roughness over a wide range of flow.

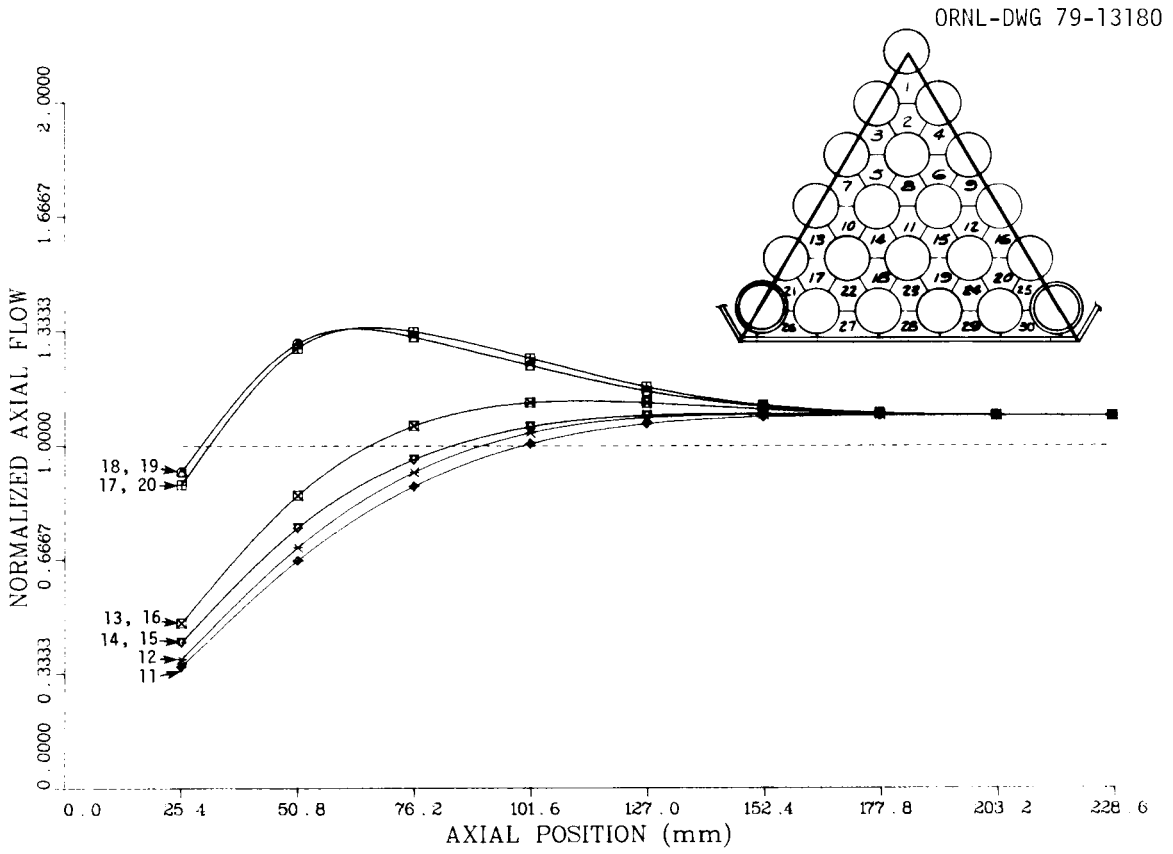

Fig. 1.3. Flow Distribution in the Inlet Section of the 91-Rod Core Flow Test Loop Bundle for Channels near the Middle of a 60° Radial Segment.

The COBRA*GCFR code was obtained from GA in June 1978 and was made operational on the ORNL IBM computer system in August for steady state only. The results of three input samples, representing three different geometries and flow conditions, agreed with those obtained from the UNIVAC-1110 computer to the fifth significant digit. Three other options of COBRA*GCFR, the restart, roll, and transient solution methods, need to be implemented.

The implementation of COBRA*GCFR and its ancillary programs was considerably faster than was the implementation of the earlier versions. The computer software and job-control language, developed for the implementation of COBRA*HE to allow for variable array dimensions, did not require substantial modifications for COBRA*GCFR, and COBRA-IV had been previously implemented by others at ORNL. That implementation of COBRA-IV required about one full man-year to complete.

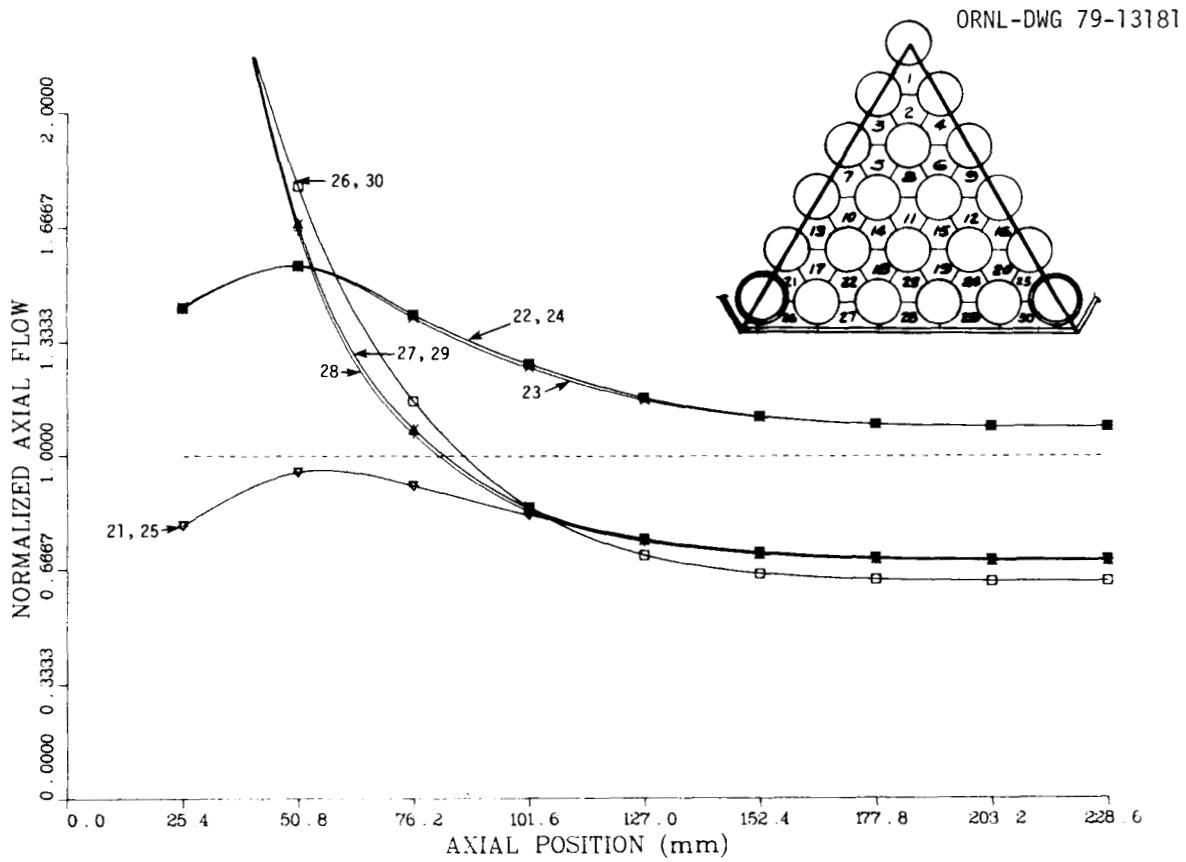

Fig. 1.4. Flow Distribution in the Inlet Section of the 91-Rod Core Flow Test Loop Bundle for Channels near the Edge of a 60° Radial Segment.

The COBRA*GCFR code uses methods to calculate friction factors and Stanton numbers for all channels that are developed from universal velocity profile theory and augmented with empirical results from experiments in Europe. These methods were separated from COBRA*GCFR and were appropriately modified for use in the CFTL loop simulation code ORCULT.

Input for the CFTL 37-rod bundle was prepared and executed for the current reference geometry (rod pitch = 11.2 mm, duct edge spacing = 30%) for the test requirements of 0.86-kg/s bundle flow at a pressure of 9.0 MPa and a power input of 28.0 kW per rod. The most significant result is the 150 K temperature gradient that exists across the rod adjacent to the duct at the position where the cladding changes from smooth to rough and the hot channel is the wall channel. Circumferential or axial cladding thermal conduction was not considered because suitable

methods for representing these effects are not yet available in COBRA*GCFR. This result indicates a possible deficiency in the current reference design.

1.2.4 Spacer Performance and Bundle Entrance Efforts — J. C. Conklin

Spacer effects and entrance region effects were discussed at a meeting with Paul Barroyer of the Swiss Federal Institute for Reactor Development (EIR) during his visit to the 1978 American Nuclear Society Winter Meeting in Washington, D.C., on November 15, 1978. In addition, general information about the experimental loops at EIR and the CFTL at ORNL was exchanged. The deformed grid spacer of the EIR AGATHE-HEX bundle 1 test was discussed, and Barroyer was informed of our urgent need for information to be used for modeling the grid spacer for the structural analysis of the CFTL bundle. He indicated that he would attempt to provide us with the appropriate information as soon as practicable.

1.2.5 Structural Analysis of Test Bundle — W. G. Dodge

In the initial phases of the development of structural analysis methods for the CFTL test bundles, it was agreed that both GA and ORNL will use computer codes that are currently operational on their local facilities. ORNL will use ADINA[14] and GA will use its version of the MARC code or a GA code called THREED. This decision was made to avoid the dilution of effort in making new codes operational and to allow each organization to concentrate immediately on various aspects of modeling the bundles. To ensure compatible results from the codes of each organization, "benchmark" problems will be identified and solved at each installation. The first such problem identified is that of an idealized model of a 37-rod CFTL assembly in which the spacer grids are assumed to be rigid and frictional interaction between the FRSs and spacer grids is neglected.

Two problems arose in use of the ADINA code for analysis of this model: (1) the original version of the code does not have thermal loading capability in its beam element formulation and (2) it does not

provide the user the option of tying structural degrees of freedom, a feature that is necessary for efficient modeling of the rigid spacer grids. The former problem was eliminated by development of a thermal load preprocessor called BLOAD, and the latter problem was corrected by a modification of the ADINA code.

The computer program BLOAD was written in FORTRAN IV and can be executed on the ORNL-PDP-10 computer system. The program can read the ADINA nodal and element definition cards and a data set that contains the temperature and temperature gradients at each node and can output a data set of ADINA load data-card images containing the corresponding pseudonodal forces and moments. The thermal gradients are defined in a rectangular global coordinate system and are transformed to the local coordinate system of each beam element. The pseudonodal loads are determined by calculating, in the local coordinate system, the nodal loads that produce an equivalent deformation and then transferring these loads back into the global system, where they are combined with the other nodal loads to establish the total load vector for the structure. The total load vector is stored in a data set in a format that is compatible with the input requirements of the ADINA code.

The capability for tying structural degrees of freedom was provided by modifying the algorithm in the ADINA code that assigns the equation numbers to the structural degrees of freedom. The ADINA code originally allowed the user to specify a free or fixed degree of freedom by specifying either a zero or a one, respectively, in the appropriate field of the nodal definition card. This capability was modified to allow the user to specify that the current node's degree of freedom is that of a previously defined node by specifying a value (the negative node number of the corresponding degree of freedom) in the appropriate field of the nodal definition card. These nodal degrees of freedom are assigned the same internal equation numbers and thus will be effectively tied together during subsequent assemblage and solution computation.

A specialized mesh generator program was written to assist in preparing the input data that are required for defining the finite-element model of the 37-rod assembly for the ADINA code. This program

runs off line on a Tektronix 4051 terminal and can generate an appropriate mesh for CFTL fuel assemblies. The program also has the capability for handling various rod pitches, duct thicknesses, number of rows of rods, and corner-rod offsets. By using the mesh generator, a complete set of input data required to perform an analysis of the 37-rod CFTL test assembly was prepared. The model is defined by using 55 nodes located on each of the 11 transverse planes that correspond to the position of the spacer grids in the assembly. The relative position of the nodes and the numbering system used for designating them is shown in Fig. 1.5. The FRSs are modeled by using three-dimensional (3D) elastic beam elements, whereas the duct is modeled by using two-dimensional (2D) elastic plane stress elements.

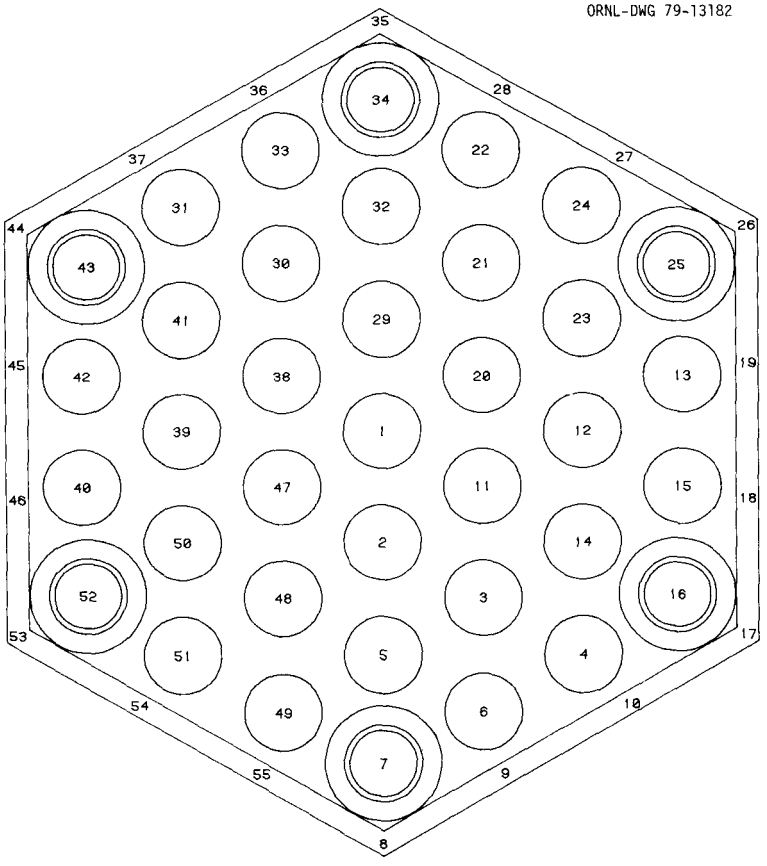

Fig. 1.5. Nodal Positions in the Finite-Element Structural Model of the 37-Rod Core Flow Test Loop Test Bundle.

In performing a finite-element structural analysis of a CFTL test bundle, each FRS must be modeled as a beam that has homogeneous material properties. An FRS is fabricated from a number of materials that have different physical properties. A typical cross section for the heated section of a rod is shown in Fig. 1.6; the portion fabricated from

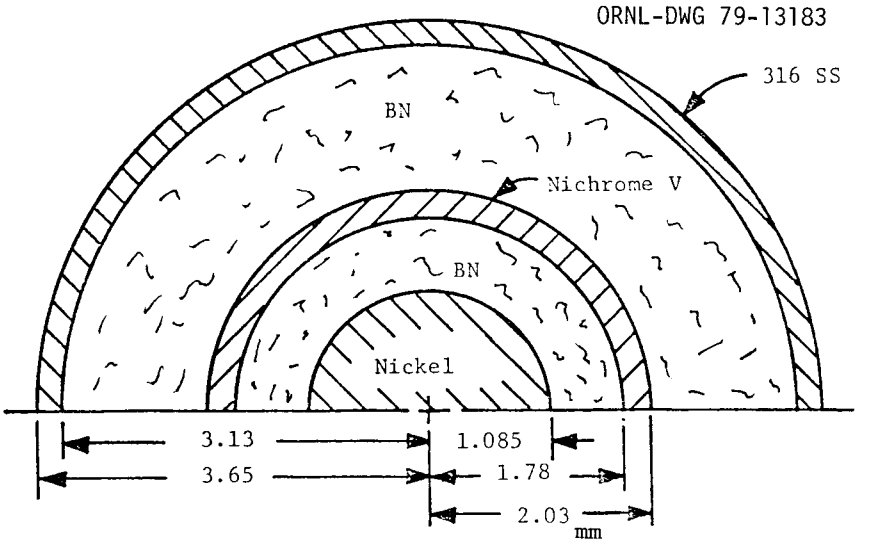

Fig. 1.6. Axial Cross Section of a Core Flow Test Loop Fuel Rod Simulator.

Nichrome V contains a helical slot along its axis. The deformation mechanisms to be modeled in the analysis are those of bending and axial extension. The pertinent material parameters are EI, αEI, AE, and αAE, where E is the modulus of elasticity, α is the coefficient of thermal expansion of the material, A is the cross-sectional area, and I is the second moment of the area of the section. In the theory of beam deformation, plane sections that are transverse to the beam axis remain plane and transverse to the deformed axis of the beam during deformation. Therefore, for a given deformation, the strain distribution in the composite beam will be the same as that in the actual FRS, and the properties of the composite beam may be determined by summing the contributions of each constituent.

The computed values of A and I are given in Table 1.5. The values for the material properties E and α in the table were obtained from several sources. The values for 316 stainless steel were obtained from the *Aerospace Structural Metals Handbook*[15] and correspond to a cladding temperature of 600°C (1110°F). The values for nickel and Nichrome V are representative room-temperature values, and the values for the boron nitride (BN) were taken from the Union Carbide Technical Information Bulletin No. 442-217[16] and, at best, represent nominal values. The physical properties of components manufactured from BN are strongly dependent on the manufacturing and fabrication process and are quite variable.

The computed composite values for EI and αEI are 12.86 N/m^2 and 224.6 $\times$ 10^{-6} N m^{-2} $°C^{-1}$, respectively. Almost 80% of the strength of the composite beam results from the stainless steel cladding, whereas almost 90% of the thermal bending is caused by thermal expansion in the cladding. The BN contributes about 10% of the bending strength but almost none of the thermal bending. The computed composite values for AE and αAE are 3.63 $\times$ 10^6 N and 57.8 N/°C, respectively. The stainless steel cladding contributes about one-half the total strength, whereas the Nichrome V and nickel contribute the greater portion of the remaining strength. Again, the BN contributes only about 10% of the strength and almost none of the thermal deformation.

Thus, obtaining a more accurate characterization of the BN is not necessary, and sufficiently accurate composite properties can be obtained by using a tabular value for the material constituents. More accurate values for the nickel and Nichrone V as a function of temperature are probably desirable if accurate modeling of the axial deformations of the FRSs is significant.

The analysis model for the 37-rod CFTL test bundle is assumed to be fixed rigidly at the cold end of the assembly, where all nodal degrees of freedom are identically zero. Also, the spacer grids are assumed to be rigid in the model, and the in-plane displacements of all nodes at each axial station are constrained to be equal. With these constraints on deformation, the basic model contains 1210 nodal degrees of freedom.

Table 1.5. Fuel Rod Simulator Composite Beam Properties

Material	E (GPa)	α (10^{-6} m m^{-1} °C^{-1})	A (mm^2)	I (mm^4)	EI (N/m^2)	αEI (10^{-6} N m^{-2} °C^{-1})	AE (10^6 N)	αAE (N/°C)
316 stainless steel	157	20.0	11.08	64.0	10.05	200.9	1.740	34.0
Boron nitride	21	0.5	17.83	62.0	1.30	0.6	0.374	0.2
Nichrome V	207	17.0	2.99	5.5	1.14	19.4	0.619	10.5
Boron nitride	21	0.5	6.26	6.8	0.14	0.1	0.131	0.1
Nickel	207	16.0	3.70	1.1	0.23	3.6	0.766	12.2
Total			41.86	139.4	12.86	224.6	3.630	57.8

The thermal loading condition for the analysis was constructed to approximate the temperatures and thermal gradients for anticipated conditions in the CFTL test bundle that correspond to a maximum power skew. To simplify the preparation of input data for this preliminary analysis, the rod temperatures were assumed to vary quadratically in the direction perpendicular to the flats of the bundle and to be constant in the orthogonal direction. The temperature of the duct was assumed to vary linearly. The mean rod temperatures and the temperature changes across the rods of the outer row on the hot and cold sides and the central rod are given in Table 1.6. The temperature changes for the other rods were determined by differentiation of the quadratic function obtained by fitting the rod temperatures shown in Table 1.6.

The model described above was analyzed by the ADINA finite-element code, and reasonable results were obtained. The magnitude of the computed deformations agreed closely with those obtained by simplified calculations. This result is to be expected for the 37-rod bundle because the stiffness of the assembly is dominated by that of the outer duct. The heater and hanger rods do not contribute appreciably to the overall assembly stiffness.

1.2.6 Location of Thermocouples in the Test Section — J. P. Sanders

A proposal that showed the location of thermocouples (TCs) in the FRSs for the first 37-rod test bundle was prepared in December 1977 and distributed in January 1978. Based on comments received from personnel at both ORNL and GA, the arrangement of the TCs was revised and presented, together with suggested locations for TCs in the gas stream and the location of pressure taps on the hexagonal duct, in a letter distributed in August 1978. The locations for the FRS TCs were based on the assumption that four TCs would be attached to the interior surface of the cladding at 90° circumferential intervals. We assumed that the FRS could be installed with this distribution of TCs in any azimuthal position.

The major objectives in selecting the location of these TCs were (1) to provide the information necessary to compare the performance of the bundles with the predictive procedures of the design computations

Table 1.6. Specified Temperatures for Preliminary Structural Analysis of a 37-Rod CFTL Test Assembly

Axial location (mm)	Rod temperature (°C)			ΔT across rods (°C)			Duct temperature (°C)	
	Hot	Center	Cold	Hot	Center	Cold	Hot	Cold
0	315	315	315	0	0	0	315	315
290	315	315	315	0	0	0	315	315
580	315	315	315	0	0	0	315	315
870	491	486	481	8.4	-1.5	-8.4	358	348
1020	602	592	582	9.9	-2.0	-9.9	404	384
1170	633	618	603	11.3	-2.1	-11.3	448	418
1320	666	646	626	12.3	-2.1	-12.3	477	437
1470	679	654	629	13.2	-2.0	-13.2	518	468
1620	689	666	629	15.4	-1.6	-15.4	553	493
1910	616	600	556	13.2	0	-13.2	577	517
2200	616	600	556	9.4	0	-9.4	579	517

and (2) to prevent the unanticipated failure of the bundle through overheating of one or more FRSs. To meet the first objective, TCs have been located at axial positions at which thermal measurements will be most sensitive to the flow and heat-transfer conditions. This location of TCs includes the positions of maximum thermal flux, points of significant flux at maximum gas temperatures, and regions at the start of the heated and roughened zones and near the spacer grids.

Thermocouples have been located in axial positions that represent the axial blanket segment of the fuel rods. In the upper (inlet) segment, some heat generation occurs in the electrical leads to the FRS heating element. This heat produces a sufficient temperature rise in the inlet gas so that maldistribution of coolant flow in this section can be detected. Because a uniform flow of coolant is desired, this measurement will be helpful in evaluating the condition. Thermocouples located in the lower blanket segment (where there is no internal heating) should approach the gas temperature in the adjacent subchannel. The exit subchannel gas temperature can be determined if the TC is located far enough from the heated section so that axial conduction in the rod does not affect its reading significantly and yet not so far that intersubchannel mixing of the gas has altered the gas temperature. Thermocouples located in the gas stream at the bundle exit will be of little value because intersubchannel mixing in the lower blanket segment will tend to equilibrate temperatures at the bundle exit away from the values that exist in the gas stream at the end of the heated section.

Thermocouples in the gas stream within the heated section will be quite helpful in evaluating the performance of the FRS. Because the TCs in the FRS are located on the inner surface of the cladding, a gas temperature measurement can be used to determine whether a high internal TC reading results from a local dearth of coolant (which might result from rod bowing and a distortion of bundle geometry) or from a higher thermal resistance between the TC and the cladding. In the absence of TCs in the gas stream, TCs in an adjacent FRS on the same subchannel at the same axial location can be used to isolate the cause of unanticipated high TC readings.

We proposed that gas stream TCs in the heated section be mounted on the upstream edge of the grid spacers in the same manner as that used by the EIR in its AGATHE-HEX bundles. Leads for these TCs might penetrate the pressure vessel through the hanger rods that support the grid spacers.

In response to suggestions by personnel at both GA and ORNL, two pairs of TCs in the FRS were located diametrically opposite each other at the same axial location. These pairs measure directly the thermal gradient that might induce thermal bowing of the FRS. The two axial locations chosen were those at which the largest diametrical gradient might be anticipated.

To limit the number of classes of FRS and thus minimize the quantity of replacement rods for bundle assembly, the number of different FRS TC configurations was limited to five. Concurrently, it was assumed that configurations could be substituted at the time of assembly if only one spare of a certain class were provided.

Figure 1.7 identifies the axial positions of interest over the length of the FRS by distance from the upper tube sheet and by reference numbers 1 to 8. Figure 1.8 shows the distribution of the TCs in each of the fine classes of FRS configurations that are designated A, B, C, D, and E. The cross sections for the arrangements are shown as they appear looking along the FRS from the inlet end. Configurations A and D have diametrically opposed TCs at the same axial locations.

Figure 1.9 identifies the rod and subchannel numbers for a 37-rod test bundle. The numbering sequence for the rod positions, made in accordance with a drawing supplied by GA, will be continued outward in a similar manner for the larger bundles. Subchannels have been defined as the symmetrical flow area bounded by three rods or by two rods and the hexagonal duct wall. Number designations given to these subchannels are arbitrary. The entire numbering sequence is referenced to the centerline of the inlet pipe of the test section.

Figure 1.10 shows the proposed TC configurations and orientations of the various FRSs in the 37-rod bundle. This figure indicates the location of TCs in the gas stream, for which it is assumed that the TC leads are enclosed in the bundle hanger rods and penetrate the hanger

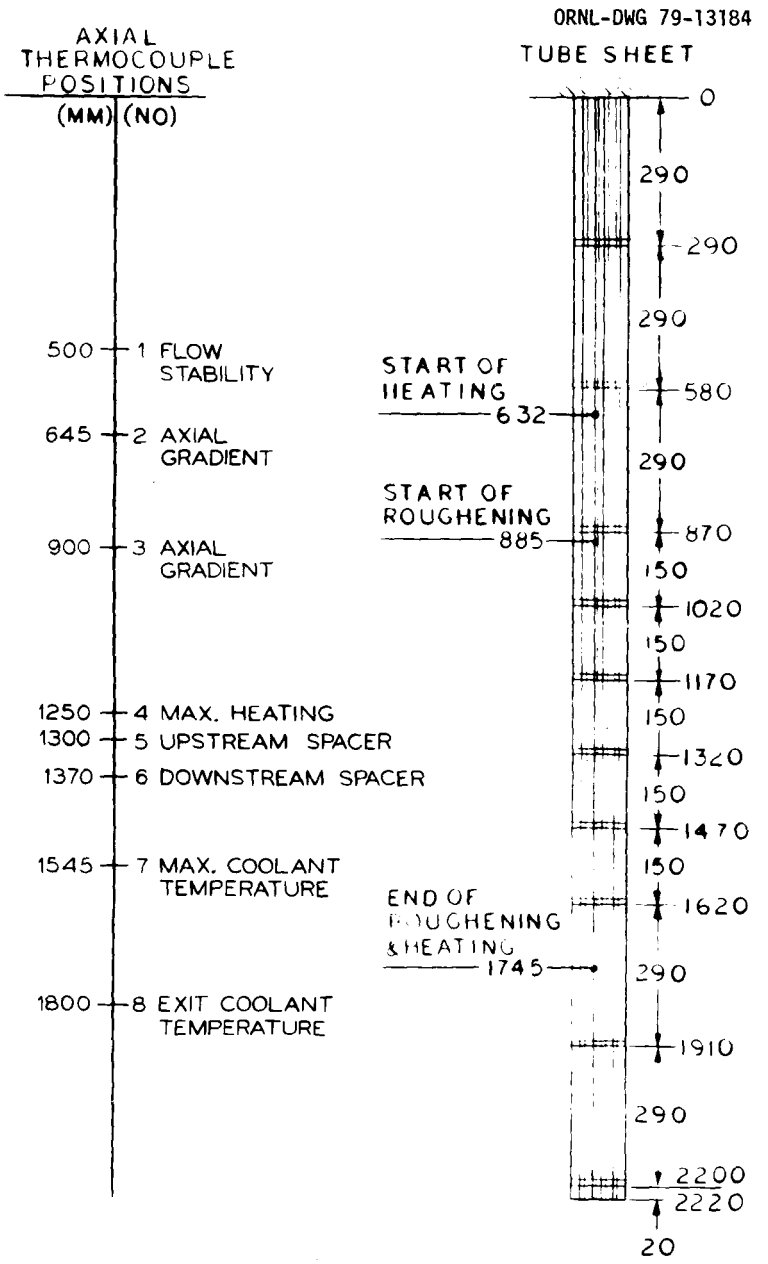

Fig. 1.7. Axial Location of Thermocouples in Core Flow Test Loop Fuel Rod Simulators.

rod configuration at the respective spacer grid locations. Each hanger rod will have only three TC leads, and each will exit at a different axial location.

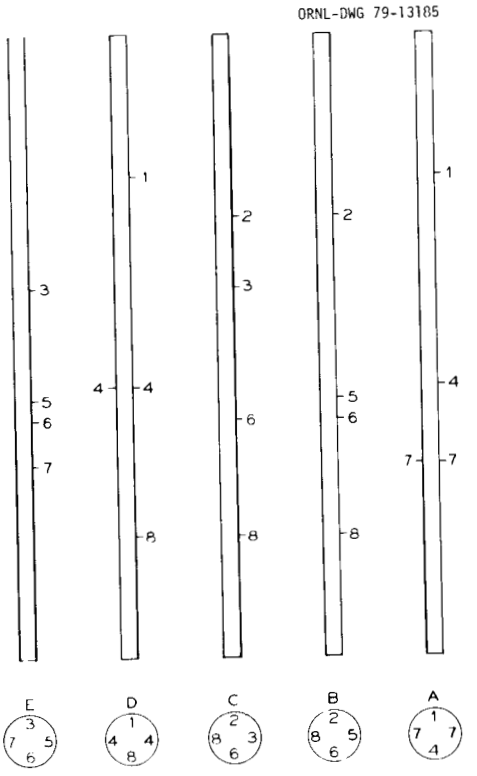

Fig. 1.8. Thermocouple Configurations for the Core Flow Test Loop Fuel Rod Simulators.

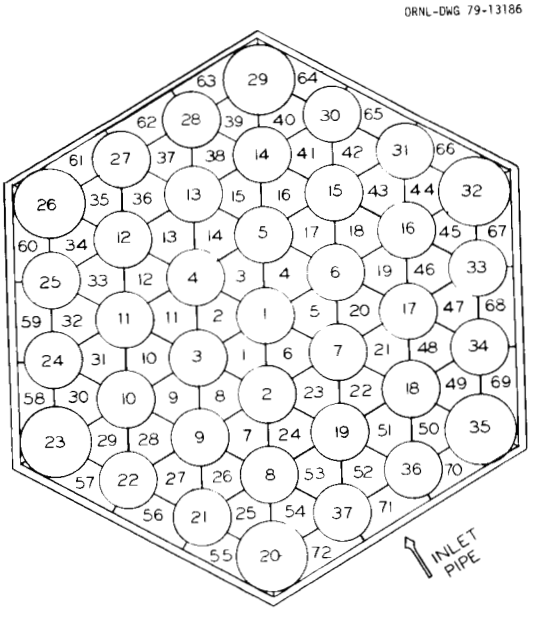

Fig. 1.9. Numbering System for Fuel Rod Simulators and Coolant Subchannels in 37-Rod Core Flow Test Loop Test Bundle.

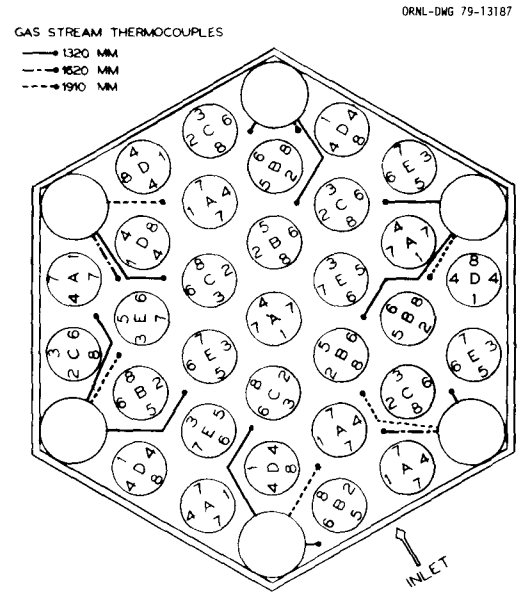

Fig. 1.10. Diagram of Types of Thermocouple Arrangements and Orientations and Location of Gas Stream Thermocouples in 37-Rod Core Flow Test Loop Test Bundle.

1.2.7 Location of Pressure Taps in the Test Section — J. P. Sanders

We assumed that pressure measurements in the test section would be limited to pressure taps placed through the face of the hexagonal duct. The most meaningful measurements, at least for the 37-rod bundle, apparently would be obtained along the axial midline of these hexagonal faces. These positions were identified relative to the centerline of the inlet pipe to the test section, and the positions were designated A, B, C, D, E, and F (Fig. 1.11).

The important axial positions at which pressure measurements would be significant are identified in Fig. 1.12. The axial positions were associated with one of the six radial locations that had been identified. In general, an attempt was made to locate on the same hexagonal duct face pressure taps that would be significant in indicating pressure differences, such as across a spacer grid. Allowance was made for the leads to the pressure taps; that is, taps close to the same axial location would not be placed on the same hexagonal duct face. The pressure tap locations are identified by number and letter.

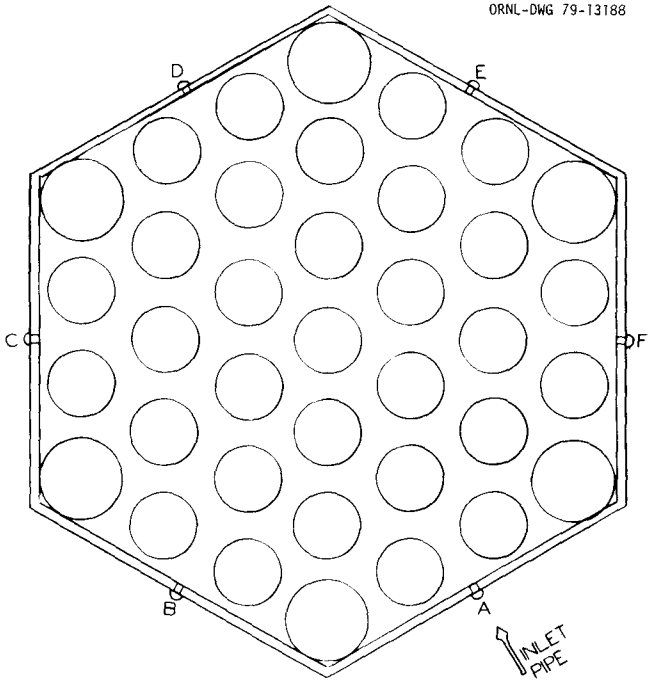

Fig. 1.11. Pressure Tap Locations on Hexagonal Duct Wall in 37-Rod Core Flow Test Loop Test Bundle.

1.2.8 Thermal Analysis of Fuel Rod Simulator — J. P. Sanders

A detailed thermal analysis of the nonswaged fuel rod simulator was made by using an R-θ nodal representation of the cross section at the point of maximum power generation. Calculated temperatures were compared with measured values in electrically heated FRSs that had a uniform linear heat generation and that were tested by using both water and sodium coolants to obtain representative heating rates and temperatures.

For the nonswaged rod, a contact coefficient between the BN filler and the outer sheath of 4.45×10^4 W/m^2 was used to match the calculated with the experimentally measured internal temperatures. This value is considerably larger than was expected.

The presence of the TC was found to act effectively as a "heat dam" that presented a significant obstacle to the uniform radial flow of heat. For postulated uniform internal circumferential heat generation and a postulated uniform external heat transfer coefficient and uniform sink temperature, significant circumferential gradients were indicated

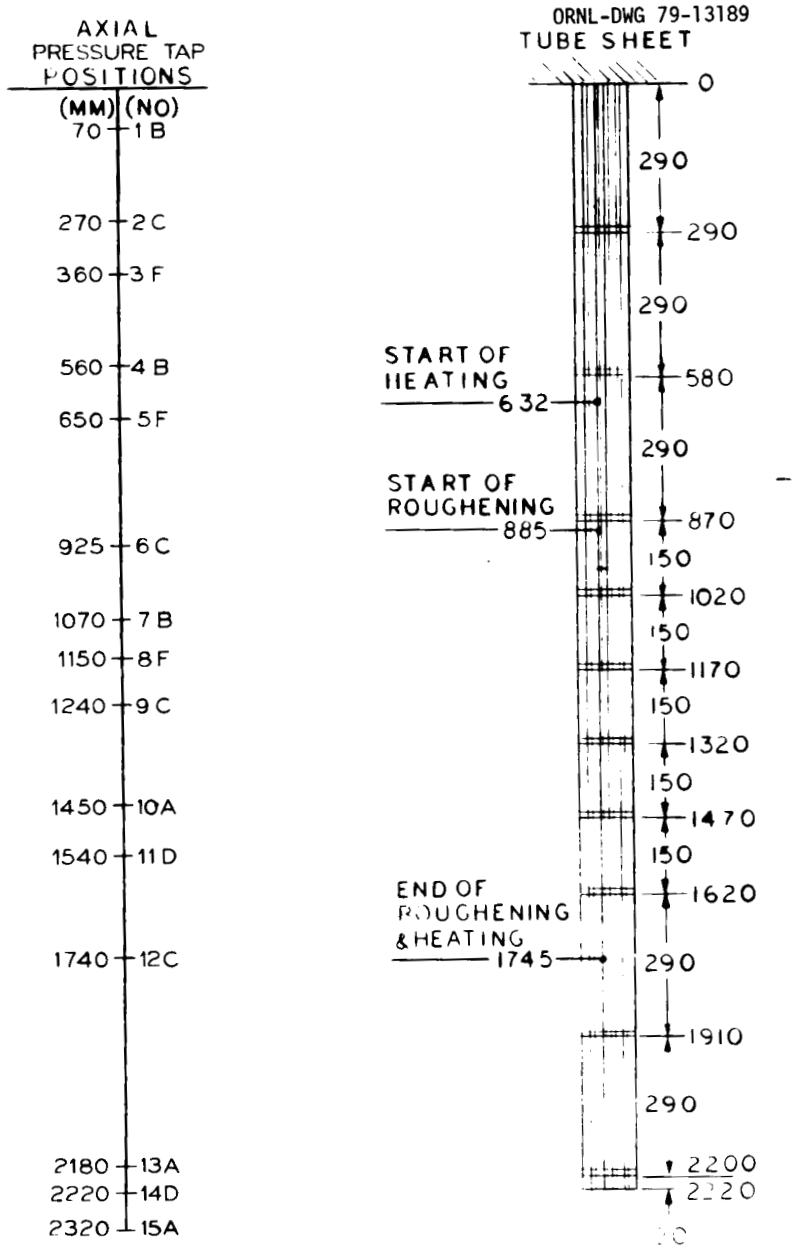

Fig. 1.12. Axial Location of Pressure Taps on Hexagonal Duct Wall in 37-Rod Core Flow Test Loop Test Bundle.

for a symmetrical segment of 0.785 radian. This gradient was about 16 K in the BN behind the TC and about 12 K on the outer cladding surface.

The calculation described above assumed that the TC was filled with MgO and that there was a significant gradient across the TC sheath. For the analytical model, which did not represent the details of the TC

internals, the radial gradient over the TC sheath was 88 K, and the gradient across the TC junction was estimated to be about 19 K. These thermal gradients occur at the maximum nominal heating rates proposed for the CFTL. The gradients at other points in the FRS, where the heating rate is lower, will be less.

Two points that became evident from the calculation were (1) the uniformity of the thermal flux at the sheath would be improved and (2) the uncertainty in the TC reading could be reduced if the TC insulating material had a better thermal conductivity. These results emphasize the value of TCs that either are insulated with BN or are back-filled with BN in the vicinity of the TC junction.

Comparisons were made between these calculated values and values obtained both from experiment and calculation for other ORNL programs that use electrically heated rods to simulate fuel rods. To the extent that comparison could be made for different geometries, the results of these calculations agreed both qualitatively and quantitatively.

1.3 DESIGN AND CONSTRUCTION OF THE LOOP — W. R. Huntley and C. W. Collins

The decision to construct the CFTL in stages was made to achieve programmatic operation of the first test bundle early in FY 1982 and to hold costs within anticipated funding. The principal impacts of the Stage 1 CFTL are (1) a reduction in test bundle capacity from 91 to 37 rods, (2) in-loop test capabilities, and (3) elimination of much of the development support for the loop design. Work was eliminated on error determination and transient response tests of stacked differential pressure transmitters for venturi flowmeters, on Grayloc flanges and test bundle and tube-sheet deflection, and on temperature control of the tube sheet. The principal ground rule for the Stage 1 CFTL is to complete all the design work on components or systems and their associated installations, which is necessary to produce the reference CFTL that has full 91-rod test bundle capacity and full transient test capabilities. From the completed design, only that equipment that is necessary for the Stage 1 CFTL will be purchased and installed; all other equipment will be deferred. As programmatic requirements and funding availability dictate, deferred items will be obtained and installed to achieve full CFTL

capacity and capability so that little or no additional design effort will be needed.

All the loop design activities reported in Sect. 1.3 with the exception of Sect. 1.3.1 are concerned with full capacity (91-rod test bundle) and full transient test capability of the CFTL.

1.3.1 Stage 1 CFTL — W. R. Huntley

The Stage 1 CFTL will have 37-rod test bundle capacity, limited transient test capability, and limited control of helium impurities but will have no rapid depressurization system to simulate GCFR depressurization accidents. Table 1.7 lists deferred equipment items for the Stage 1 CFTL. Costs of procurement and installation of the deferred equipment are estimated to be about $3 million when escalated to FY 1982 according to the present inflation guideline of 7%/year.

The power supply and control system for the CFTL test bundle will provide electricity to individual rows of rods to simulate the radial

Table 1.7. Deferred Equipment Items for the Stage 1 CFTL

Heat exchanger HX-2
Bypass line [10.16 cm (4-in.)] around circulators
Flowmeter FM-4
Flow control valve FCV-3
Helium purification system
Impurity addition system
Moisture monitor
Gas chromatograph
Depressurization line and vent valve FADV-1
Six zones of electrical power (500 kVA each)
One spare gas-bearing circulator
X-ray fluoroscopy system for deflection measurements
Remote positioning equipment for x-ray system
Shielding for x-ray fluoroscopy system
Instruments and controls for above items

flux gradient of a reactor. Each zone is parallel to one selected face of the hexagonal test bundle duct. Therefore, 7 zones of power are required to simulate power skew for a 37-rod bundle, and 13 zones are required for a 90-rod control rod bundle.

The Stage 1 CFTL will have only seven power zones and will therefore be limited to the testing of 37-rod bundles. Limiting the power supply to seven zones will allow deferral of six 500-kVA zone transformers and their related power-measurement and crowbar protective equipment, balance resistors, and test cabinets. The effects on loop test capability of both electrical and mechanical equipment deferrals are discussed in Sect. 1.1.3.

1.3.2 Mechanical Equipment and Systems Design — C. W. Collins

1.3.2.1 Heat-Removal Systems — W. A. Hartman and C. W. Collins

Engineering design of the main heat-removal system was completed. The drawings and a specification have been partially reviewed by the CFTL Design Reivew Team, and the system is nearly ready for construction. The main heat-removal system consists of (1) a large helium-to-air heat exchanger (HX-1) sized to remove 4.4 MW of test bundle and loop power and (2) a suitably large (35.4 m^3/s) air-cooling system comprised of a centrifugal fan, drive, dampers, and ductwork. The HX-1 configuration is presented in Fig. 1.13. A small heat-removal system, which is located in the circulator bypass line, is similar except for its smaller capacity [0.4 MW (5.66 m^3/s)]; it is intended to remove only the heat input to the loop by the helium circulators during rapid-transient conditions.

Detailed design of HX-1 and HX-2 (the bypass heat exchanger) resulted in minor changes to the configurations of the preliminary designs. Dimensions of the cooling air enclosures were decreased to minimize air-cooling bypass flow around the tube banks but allowing sufficient clearance between the tubes and enclosure for thermal expansion. Also, the structural support for the headers on both heat exchangers was changed to provide increased strength and lifting lugs were added to the heat exchangers. Loop performance analysis indicated a need for adding electrical heaters to HX-1 to compensate for heat losses in the piping system during extremely low-power test runs.

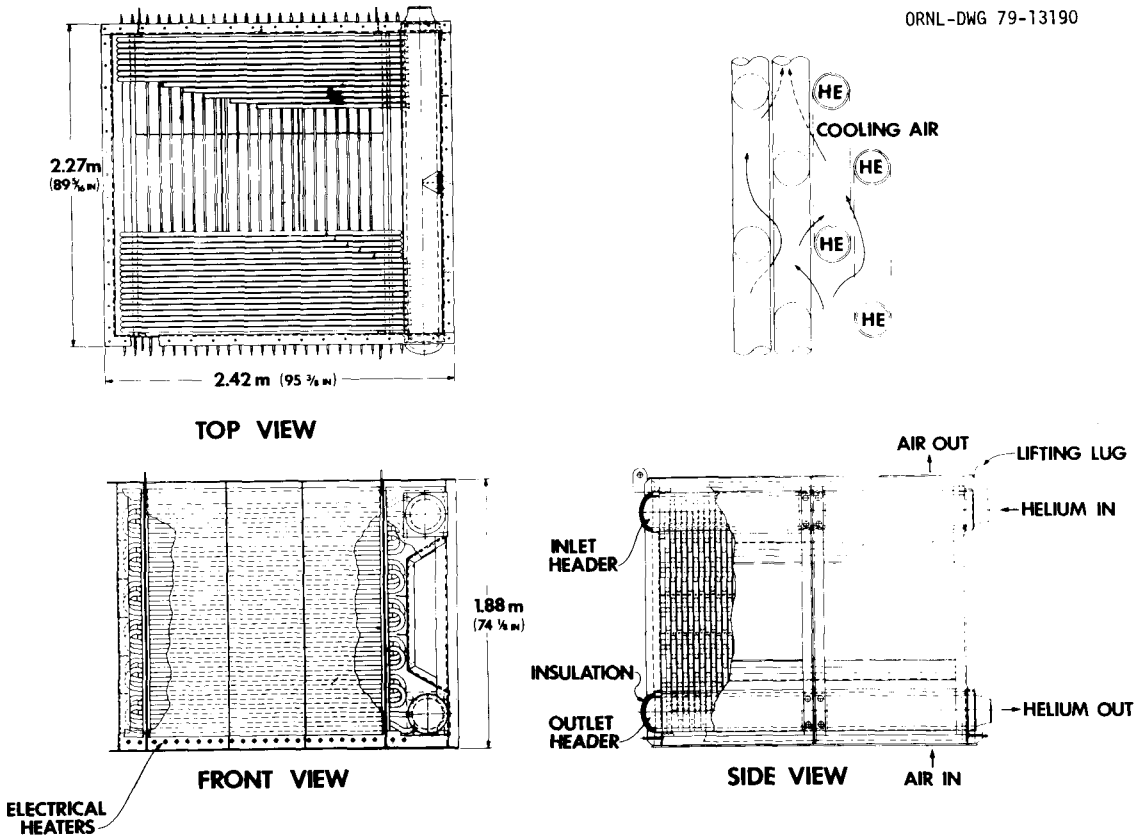

Fig. 1.13. Helium-to-Air Heat Exchanger HX-1 for Core Flow Test Loop.

Dynamic thermal-hydraulic analysis of the entire loop was used to predict thermal transients for HX-1. Stress analyses were performed for steady-state, transient, and cyclic loadings of the HX-1 pressure boundary. As a result it was found necessary to provide the headers with insulation to mitigate the effects of severe transients.

Following these changes to HX-1, heat-transfer performance and pressure loss (air and helium sides) calculations were repeated, drawings were revised, and the engineering specification was updated. A formal design review of HX-1 was performed by a team of peer engineers not assigned to the CFTL project. They examined the performance analysis, stress calculations, drawings, and the specification. Questions were satisfactorily resolved about welding methods, ducting design temperature, helium-side and air-side pressure losses, and heat exchanger vibrations. Two questions indicated the need for further work before the

design is complete: (1) tests must be performed on the curved segments of heat-transfer tubes to determine minimum thickness and ovality after bending to ensure that the requirements of *ASME Boiler and Pressure Vessel Code*, Section III, are satisfied; (2) startup of a similar heat exchanger in another experiment confirmed the concern of a review team member about possible acoustic resonance of a transverse acoustic standing wave in the rectangular cooling air enclosure. It is thought that air baffling will solve a similar acoustic problem in a heat exchanger currently being tested. If successful, the design of HX-1 will be changed to incorporate baffling. This change should reduce the possibility of acoustic resonance that is predicted to be highly probable in the current design of HX-1. The present design of the pressure boundary is acceptable; therefore, advance procurement of material has been initiated for the headers and tubes.

System assembly drawings for both large and small air-cooling systems were circulated for project review. Data sheets were also prepared for fans, drives, and dampers for both systems. Performance requirements of these systems were reviewed with personnel from the Instrumentation and Controls Division and the CFTL project, and drawings and data sheets were updated as a result of the review. Detailed design of these systems includes means to measure air-cooling temperature and flow. The pneumatic operators that have been specified for dampers and for variable inlet vanes on the fans are compatible with control signals and working air pressure, and they meet performance requirements such as response time and ease of positioning. The approved equipment data sheets have been used to solicit bids and to award procurement contracts. The fans, drives, and dampers have been ordered. The system assembly drawings have not been submitted for project approval because certified fan drawings, not yet received from the vendor, may require dimensional changes.

Other air-cooling system components, such as air filters and structural supports for ductwork and equipment, are similar to those normally found in standard industrial applications. These standard items were designed by UCC-ND Engineering and coordinated by Experimental Design Engineering as described later in this report.

1.3.2.2 Piping and Equipment Layout — W. A. Hartman

The helium systems include the primary helium circulation system and five ancillary systems. Engineering design activities on the primary helium circulation system include analysis of the preliminary designs of the piping and helium filter, development of greater detail, and incorporation of changes required to meet project objectives. The primary helium system also includes circulators, valves, flowmeters, and the test vessel, which are discussed later in this report.

Experimental Design Engineering personnel assisted the performance analysis group by developing analytical expressions for pressure losses in the heat exchangers, pipes, filter, and test vessel. Equations are based on preliminary design configurations and permit estimates of pressure losses for helium flowing at various pressures, temperatures, and flow rates. Results of the analysis were used (1) to confirm compatibility of the system pressure losses with the head versus capacity characteristics of three helium circulators working in series, (2) to select flow control valves, and (3) to identify potential problem areas. We determined that the pressure drop for the preliminary design of the helium filter was unacceptably large. The helium filter was redesigned to provide a larger filter area and a lower pressure drop. Drawings prepared for the revised design of the helium filter have been discussed with a filter vendor, who has suggested that a standard design filter be used to take advantage of existing expertise in meeting performance requirements.

A prototypic helium circulator has been built and is being tested. The mounting base for the prototype incorporates a maintenance and alignment tract that has been included in the experimental equipment arrangement. This inclusion made it necessary to relocate the circulators closer to the test vessel than was previously done. The drawings were revised to include necessary helium rerouting.

The Instrumentation and Controls group delineated requirements for controlling and monitoring helium flow. As a result, the pipe sizes for attemperation and bypass lines were revised to reduce pipe diameters. However, the test vessel and heat exchangers were not relocated from positions shown in the preliminary design.

The configurations of the helium circulation system components and interconnecting piping that reflect the design maturation are shown in Fig. 1.14.

The piping described above, with appropriate anchor points, was analyzed for stresses caused by thermal expansion and dead weight. We found it necessary to extend expansion loops to reduce thermal stresses; the number and types of pipe hangers were determined. The loop piping layout and equipment arrangment drawings have been updated to reflect the results of these detailed design activities.

The five ancillary helium systems include the (1) Loop Evacuation System (LES), (2) Helium Supply System (HSS), (3) Helium Venting System (HVS), (4) Helium Purification System (HPS), and (5) Gaseous Impurities Injection System (GIIS). The LES is required to remove atmospheric air from the loop piping and components prior to filling the loop with fresh helium. Design calculations were performed to select the type and size of vacuum pump and connecting pipe isolation valve. A mechanical rotary-type vacuum pump having an ultimate pressure capability of 0.133 Pa and a pumping speed of 8.33×10^{-3} m^3/s was found to be suitable. The

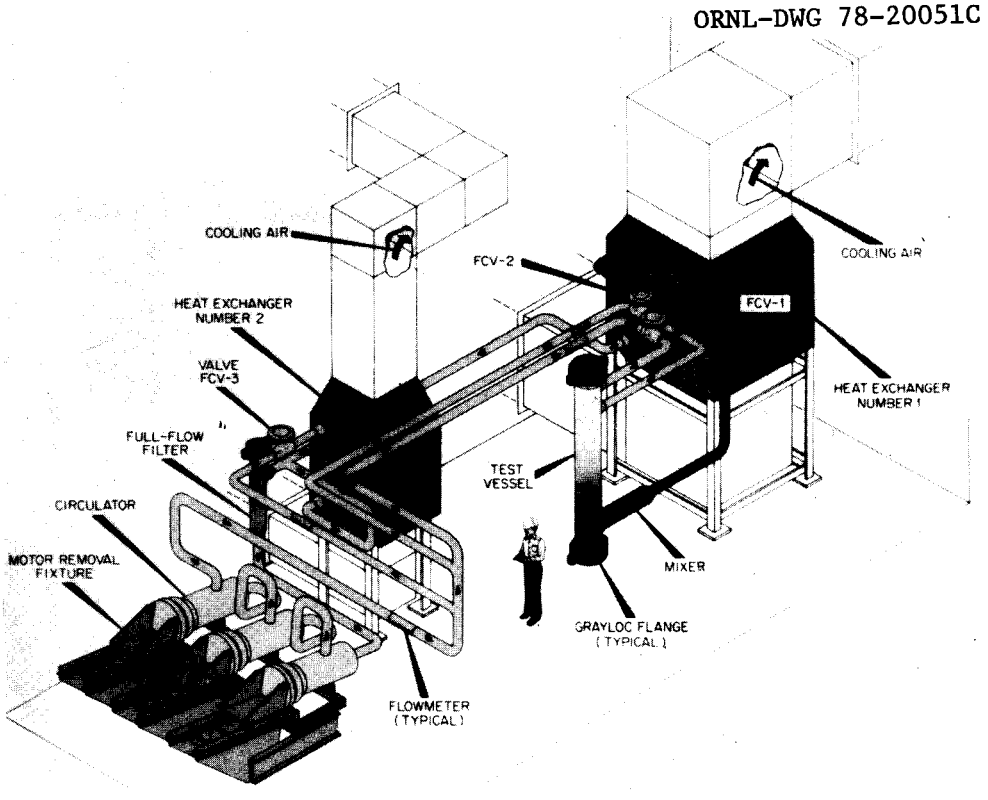

Fig. 1.14. Primary Helium System for Core Flow Test Loop.

connecting pipe must be as short as possible; a 0.1-m-diam (4-in.) pipe about 2 m (80 in.) long should permit such a small pump to evacuate the loop volume to the desired 20 Pa in less than 1 h. A ball valve will isolate the vacuum pump once the loop is pressurized with helium.

The preliminary design of the HVS has been expanded to include a needle valve for bleeding small amounts of helium to the atmosphere to control pressure during high-power operation. The increased temperature of helium volumes in the test-vessel outlet plenum, hot-leg pipe, and hot end of HX-1 may increase the loop pressure during tests at higher power unless means are provided to decrease the loop helium inventory. The HVS includes three parallel flow paths for helium to exit the system: (1) a safety valve ensures overpressure protection, (2) an orifice, in series with a rupture disk and a fast-acting valve, provides control of pressure during depressurization tests, and (3) the needle valve controls pressure for reasons just described. A detailed design drawing has been started to incorporate these features and to route piping so that rupture disks and orifice plates are accessible for changeout.

Design activities for the HSS have resulted in drawings that are certified for construction to provide a helium fill capability separate from the helium makeup system. The helium fill subsystem consists of a large supply trailer to be parked outdoors to supply helium to the pressure-control station. The final design of the makeup subsystem requires two banks of standard-size helium cylinders located near the experimental loop. Either bank can be connected to the loop through the pressure-control station. Except for the pressure-control station, the HSS is similar to compressed gas systems normally used in standard industrial practice.

Detailed design work on the HPS and the GIIS will be deferred until the next calendar year without affecting the construction schedule of the loop.

1.3.2.3 Building Facilities — W. A. Hartman

The design of standard structures and services normally provided to support a process such as this high-temperature–high-pressure helium

loop was completed. Most of the drawings, bills of material, data sheets, and specifications needed to provide site modifications and utilities for CFTL have been issued and certified for construction. Figure 1.15 presents an isometric drawing of the CFTL and its support systems.

Site modifications include the removal of inactive and unusable equipment, changes to existing structures, and the addition of new structures and systems. The modifications also provide for lighting, electrical power to nonexperimental equipment, heating, ventilation, air conditioning, fire protection, structural supports, and weather enclosures in Building 9201-3, where the CFTL is to be located.

A penthouse will be added to the roof of Building 9201-3, which will include an opening in the existing roof, a monorail, an electric hoist,

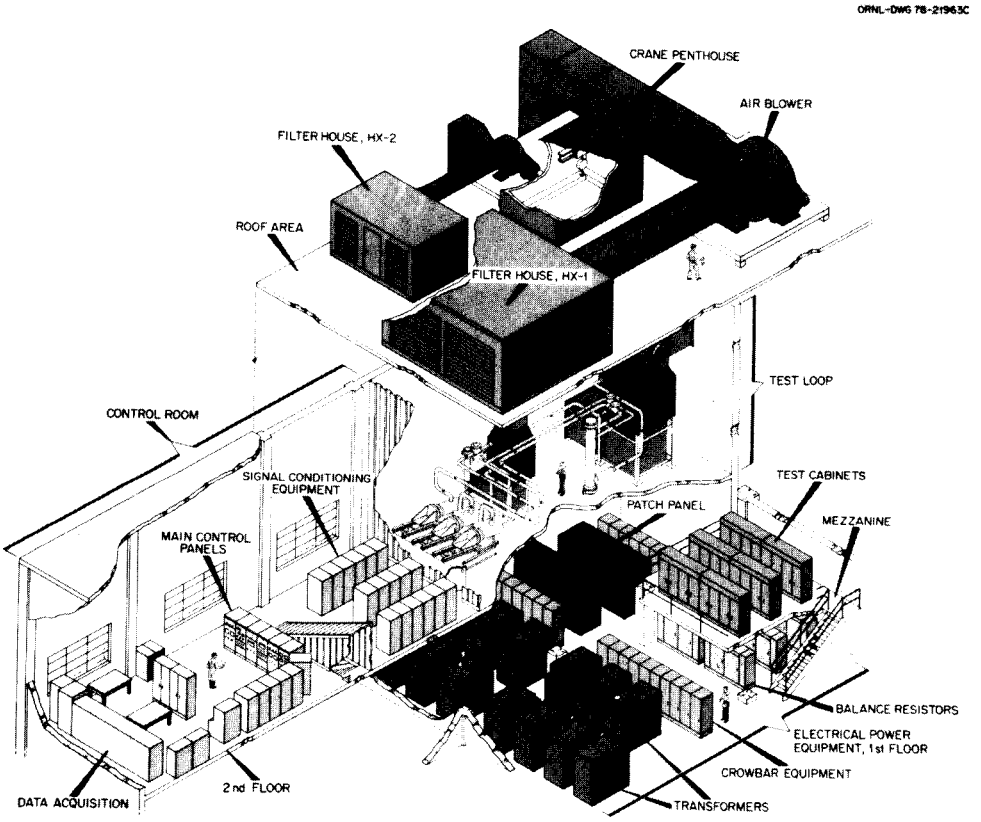

Fig. 1.15. Core Flow Test Loop and Support Systems.

and a weather enclosure. The penthouse and accessories will provide the capability and necessary vertical clearance for lifting test bundles during installation and removal from the test vessel.

Cooling air will be drawn into the heat-removal systems through air-cooling filter enclosures on the roof. As part of this work, the design of these two filter houses and of new structural supports for ductwork fans and drives that are part of the heat-removal system are complete.

The control room will be an enclosed space on the second floor of Building 9201-3 so that the environment can be controlled separately from the general building. A new enclosure will provide thermal insulation, fire resistance, and noise attenuation. A small heating, venting, and air-conditioning (HVAC) system will be added to control temperature; electrical service will be revised to provide adequate lighting and wall receptacles; and additions to the sprinkler system will provide fire protection.

The loop enclosure will involve erection of a new steel wall on the second floor of Building 9201-3. The enclosure will isolate the high-temperature-high-pressure helium system from the general building, protect personnel and operations in the building from heat and noise generated by the CFTL, and limit access to authorized personnel only.

Overpressure protection for the loop enclosure will be provided by a blowout hatch to be added to the east exterior wall. Ventilation will be provided by new exhaust fans, comfort heat will be supplied by steam unit heaters relocated from another area of the building, and inadequate lighting will be replaced with new fixtures.

Preparations on the second floor of Building 9201-3 will involve removal of inactive ventilation systems, lighting, monorails and hoists, walls, and miscellaneous structures. Minor structural modifications to the second floor will include new openings in the exterior walls of the loop enclosure area for penetration by air-cooling ducts and openings in the second floor for supplying electrical power to the test bundle.

First-floor preparations, including removal of unsuitable lights, monorails, and miscellaneous structures, will involve modifications to the existing building heating and ventilating system, walls, and

electrical service. Also, new enclosure walls, lights, and a ventilation system will have to be added. The enclosures will isolate electrical equipment from the general building, and new lighting will facilitate routine maintenance and inspection of electrical equipment. The ventilation system will remove heat losses from electrical equipment by forcing outside air through the rooms that contain this equipment.

A new, small concrete parking pad will be constructed just east of Building 9201-3 to accommodate the helium supply trailer described in Sect. 1.3.2.2.

Utilities work will include deletions, changes, and additions to piping systems in Building 9201-3 to provide instrument air, process water, steam, condensate drains, and water drains. A new system, dedicated to CFTL, will be installed at the site to supply helium (Sect. 1.3.2.2).

Existing instrument air service will be modified to provide air to the actuators in the air-cooling systems and to instrumentation and controls in general. This service will be distributed as required to the second-floor areas and to the roof of Building 9201-3.

The existing building process water system will be modified to provide cooling water to electrical equipment on the first floor and to helium circulators on the second floor. Drainage service will be provided accordingly.

The building steam and condensate system will be expanded to supply heat to environmental control equipment in the control room and in the loop enclosure. The capacity of existing air, water, steam, and drainage systems meets the requirements of CFTL.

1.3.2.4 Helium Circulator Development — H. C. Young

In the previous annual report on circulator development,[17] we estimated that reduced funding for FY 1978 and other problems would delay completion of the construction and performance testing of the circulator prototype at Mechanical Technology, Inc. (MTI). This work is covered by Phase II of our contract with MTI.

At year's end, despite vicissitudes in cost estimates and funding, delays in delivery of key components, and field problems with the power supply, the rotary assembly was tested in atmospheric air and was ready to be installed in the pressure vessel.

We believe a Phase II completion date of April 1979 can still be achieved if no additional serious problems arise.

Late in 1977, MTI advised us that they had reestimated the labor hours to complete Phase II, thus increasing the Phase II costs by $99 thousand. Representatives from the UCC-ND Purchasing and Auditing divisions visited MTI to review the reasons for the increase, and MTI was requested to provide additional information on the contributing factors. Mechanical Technology's reasons were evaluated by CFTL project personnel. Much of the increase resulted from MTI's incorrect original concept of the depth of technical information, analytical work, and quality assurance that we would require during Phase I and Phase II. We do, and will continue to, require detailed technical information from MTI to ensure, as far as practicable, that the circulators will meet our CFTL requirements and will have a minimum of modifications after installation in the CFTL. The revised cost estimate was eventually justified, and DOE provided additional funding to continue the circulator activities at MTI.

Although information from the UCC-ND Auditing Department indicated that MTI would soon be authorized by the cognizant defense contract audit agency to increase its labor overhead rate and general and administrative (G&A) rates retroactively to FY 1976, we expected that the costs would be added in FY 1979. However, in June 1978, MTI advised us that yet another increase in contract costs, this one of $83 thousand, was needed to cover the authorized increase in overhead and G&A to that date. At our request, MTI cooperated in holding the FY 1978 spending within available funding.

Although the order for the pressure vessel and motor cooling vessel was placed in January 1977 and delivery was promised by the manufacturer (Buehler Nuclear Products, Indianapolis) for October 1977, the schedule continued to slip despite strenuous efforts made by all parties to maintain it. Delivery was finally made in August 1978. The pressure vessel is shown in Fig. 1.16.

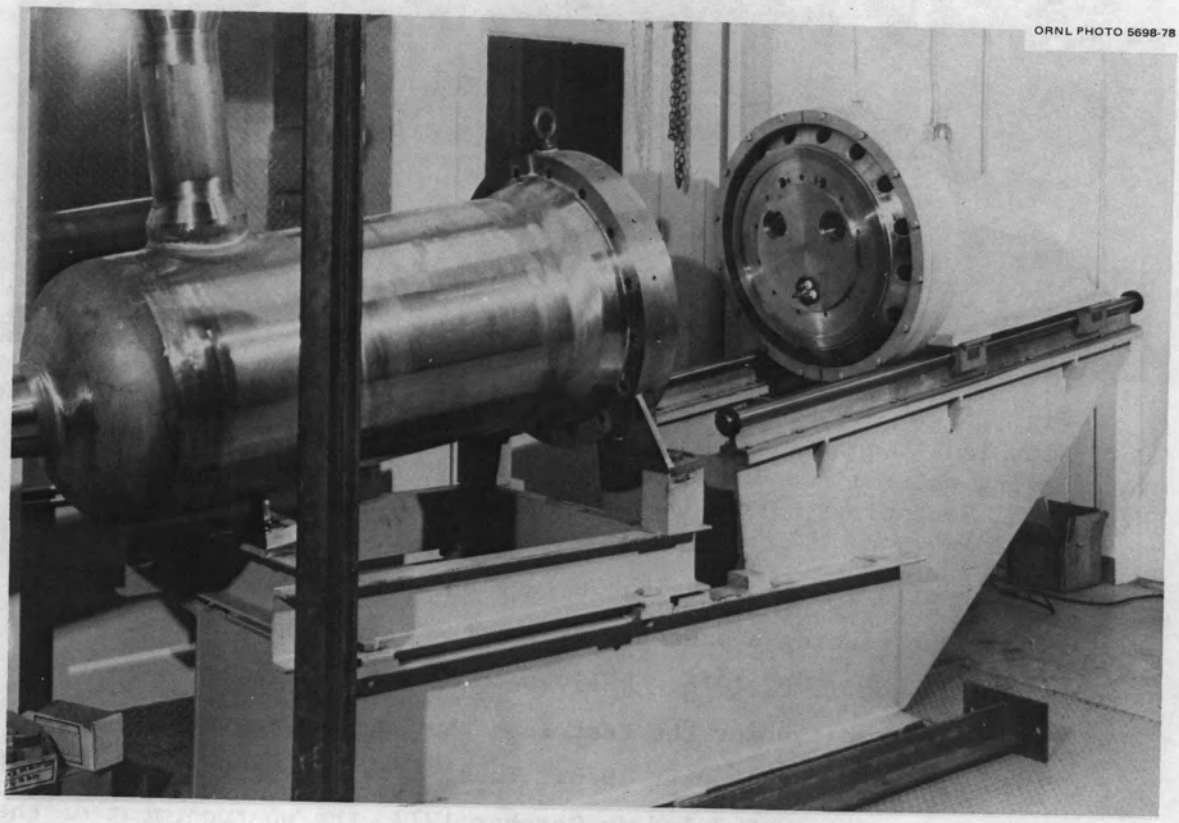

Fig. 1.16. Pressure Vessel and Base and Assembly Fixture for Core Flow Test Loop Helium Circulator. Circulator internals will be bolted to the retracted end flange. Courtesy Mechanical Technology, Inc.

The motor for the circulator prototype had been delivered to MTI in August 1977. Because the motor stator must be pressed into the motor cooling vessel assembly (Fig. 1.17) before an air test of the rotary assembly can be made, the late delivery of the cooling vessel brought efforts to run bench tests in air essentially to a standstill.

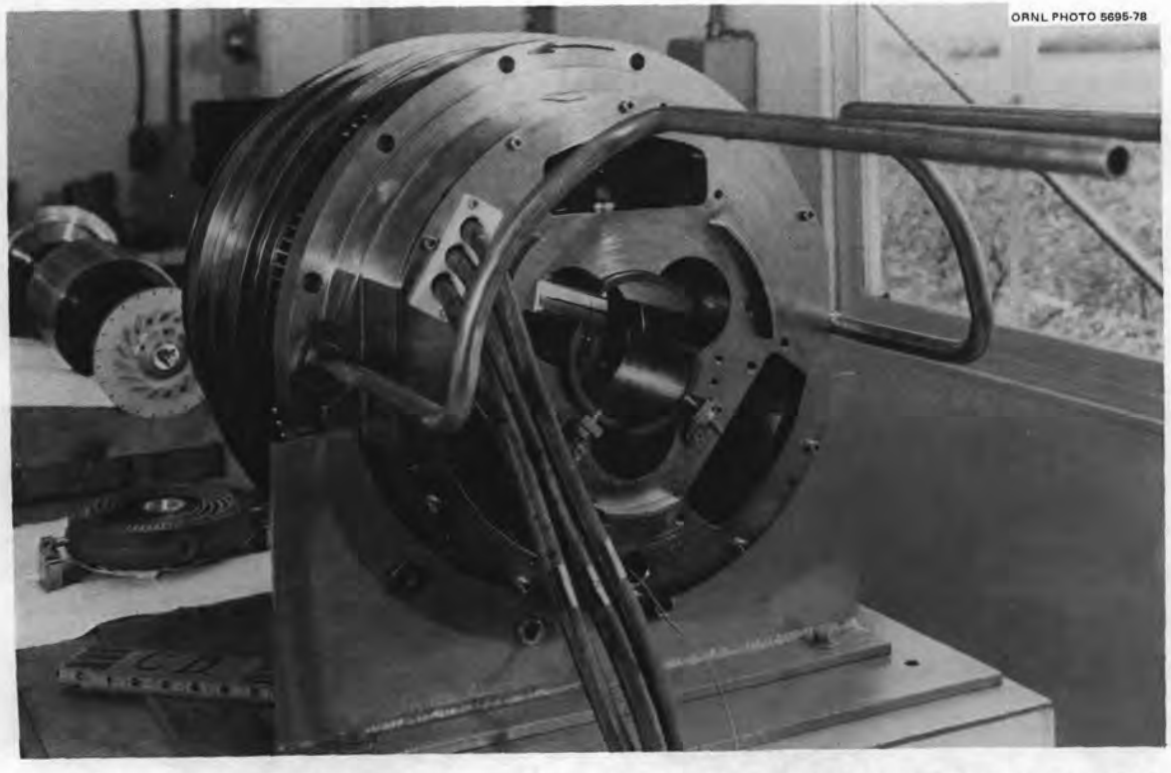

Fig. 1.17. Motor Cooling Vessel Assembly with Motor Stator Installed, Core Flow Test Loop Helium Circulator. Foreground shows Inconel piping for cooling water lines and the three motor power leads. Courtesy Mechanical Technology, Inc.

Because of a limit on available funding in FY 1977, ORNL required MTI to postpone placing a subcontract for the test loop and test loop instrumentation until FY 1978. Delivery of a 0.1-m-bellows (4-in.) sealed throttling valve for the test loop that had been promised for March 1978 was made in December 1978. Thus, even if the pressure vessels had been delivered as scheduled in October 1977, the postponement of the procurement of the test loop (because of lack of funding and aggravated by the late valve delivery) would have delayed completion of Phase II by about one year.

A solid-state variable-frequency power supply was purchased by UCC-ND from Servo-Optics, Inc., Dallas, Texas, and loaned to MTI for use in supplying the circulator motor during performance testing of the prototypic circulator. It will be used later to supply the production circulators during testing at MTI. This power supply was factory tested and delivered to MTI in January 1978. During shipment, damage to the silicon controlled rectifier (SCR) inverter module was incurred. A field engineer from Servo-Optics replaced the damaged parts and repeated

the specified tests. The supply operated satisfactorily, except that no provision was made for loading it to the design point.

We fabricated and shipped to MTI a 250-kVA water-cooled resistive dummy load for performing the design load tests. During testing with the dummy load in June 1978, several SCRs failed at full load. Replacement SCRs that had a higher voltage rating but less heat generation were furnished and installed by Servo-Optics; also, the top of the power supply cabinet was modified to provide better cooling. The power supply then satisfactorily passed an 8-h full-load test.

The power supply accelerated the ball-bearing-supported motor prototype of the circulator motor to 50 Hz (3000 rpm) in 0.7 s. Mechanical Technology, Inc., had specified an acceleration to 50 Hz (3000 rpm) in 1 s to protect the gas-film-lubricated bearings from wear damage during startup.

Stable operation of the power supply was demonstrated by using the ball-bearing-supported motor over the speed range from 60 to 400 Hz (3600 to 24,000 rpm). The protection system for reverse rotation was also demonstrated, and it will satisfactorily protect the unit. The power supply is shown in Fig. 1.18.

Mechanical Technology, Inc., completed fabrication of the internal parts for the circulator (Figs. 1.19 and 1.20) and ran the first bench tests in air in November 1978. To correct a minor rubbing problem at the thrust bearing during initial operation, portions of the thrust bearing adjacent to the chrome-oxidized rubbing surfaces were relieved 0.075 mm (0.003 in.) to achieve rubbing contact only on the mating chrome-oxidized surfaces. The rotary assembly then operated satisfactorily to 400 Hz (24,000 rpm). Mechanical Technology, Inc., reported that initial dynamic balancing was satisfactory so that planned precise balancing during the bench testing was not necessary.

During further bench testing, an optical isolator (a component in a printed control circuit in the power supply) failed, shutting off one phase of the power supply output so that the circulator motor would not start. The optical isolator was replaced by MTI, and bench testing was continued. Filters on the output signals from the capacitance-type bearing displacement sensors and ferrite rings on the power supply were installed by MTI to reduce electrical noise generated by the SCRs in the power supply.

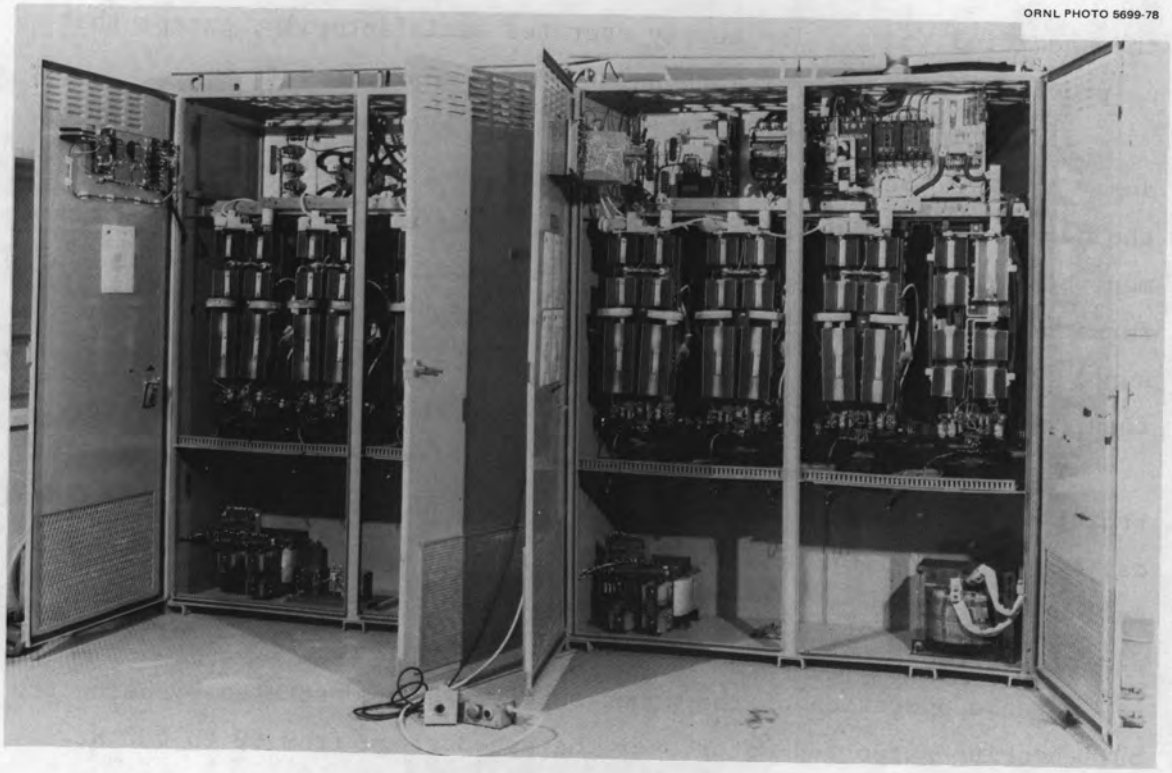

Fig. 1.18. Solid-State Variable-Frequency Power Supply for Core Flow Test Loop Helium Circulator, Showing Silicon Controlled Rectifiers and Control Circuitry.

Fig. 1.19. Internal Parts for Core Flow Test Loop Helium Circulator. Visible are rotating assembly consisting of impeller, solid motor rotor, journal bearings, and thrust disk (right); motor cooling vessel with stator installed (background); stationary thrust disk with spiral grooves (front of cooling vessel); and an assembled pivoted pad journal bearing (foreground). Courtesy Mechanical Technology, Inc.

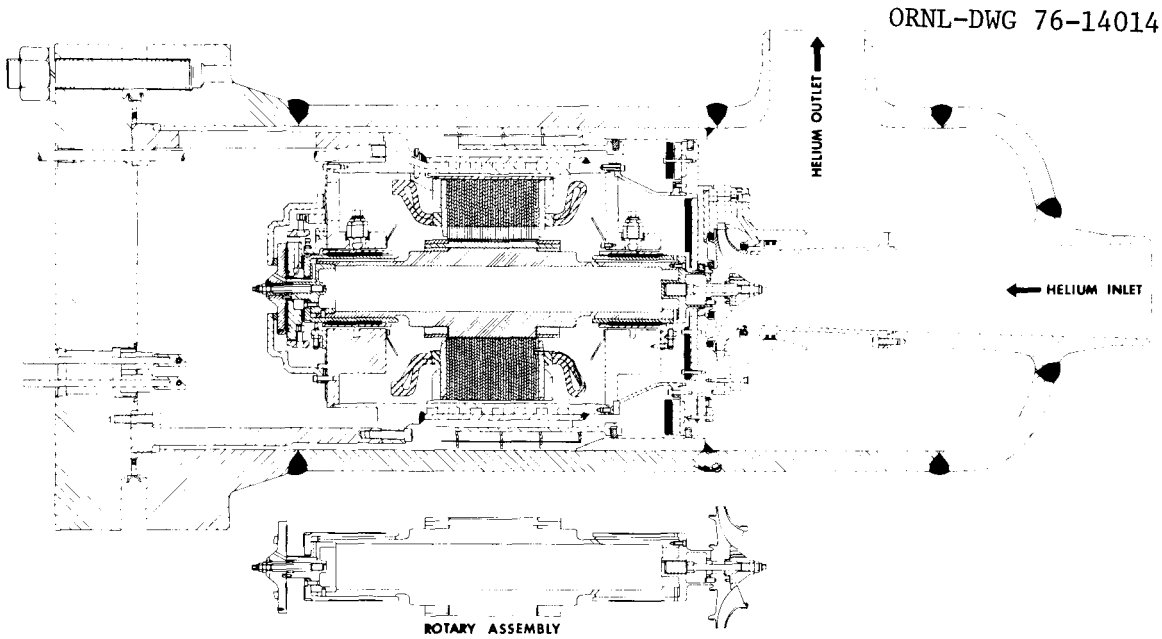

Fig. 1.20. Cross Section of Core Flow Test Loop Helium Circulator. Courtesy Mechanical Technology, Inc.

Mechanical Technology, Inc., has completed the bench tests in air and is ready to install the circulator internals into the pressure vessel that was earlier installed in the test loop. We expect that the test loop instrumentation will be calibrated and that the circulator and test loop shakedown operation will be started in February 1979.

Negotiation of the Phase III fixed-price contract with MTI for fabrication and testing of the CFTL production circulators is to be started by late February 1979. Procurement of the long-delivery items for Phase III, the motors and pressure vessels, was initiated in 1978. New cost estimates for these items were provided by MTI, and it was initially planned that MTI would handle these subcontracts. However, MTI agreed to permit UCC-ND to handle the contracts directly, and bid packages were prepared by ORNL for both the motors and pressure vessels.

The vessel manufacturer is to furnish all materials and to fabricate the vessels but is to provide only the ASME code (nuclear parts) stamp. We will be responsible for the stress analysis and the N-stamp. Transparencies of MTI's motor drawings and specifications were used for the motor bid package. The bid closing date was October 30, 1978, for both

the motors and pressure vessels. Bids were obtained for quantities of two and three motors and vessels; however, because of anticipated funding availability only two motors and two vessels will be ordered.

The low bidder for the vessels took several exceptions to the contract. These exceptions have been resolved, and the vessel contract will be placed in January 1979 to have a 15-month delivery date.

Only one motor bid was received; the original manufacturer of the motor for the circulator prototype declined to bid. The single bidder was evaluated and was judged to have greater capabilities to produce the motor stator than to produce the motor rotor, which requires precision machining and brazing operations. This bidder is to be awarded a contract for two stators. Additional bids will be solicited for fabrication of the two rotors.

1.3.2.5 Test Vessel Design — W. R. Clark

Work continued throughout the year on the conceptual design of the test vessel (Fig. 1.21), and a number of analytical tasks were undertaken to confirm the adequacy of various features of the design. Because one proposed structural measurement involves x-raying the test bundle during operation, the test vessel wall must be kept as thin as practicable in order to ensure an acceptable image. Therefore, low-alloy high-strength (LAHS) steel (SA-533) was chosen as the shell material, and an attemperation helium flow concept was developed to keep the vessel wall cool. The relatively cool [350°C (660°F)] flow of attemperation helium direct from the circulators is kept in contact with the inside wall of the test vessel by the use of a thermal barrier that separates the wall from the test bundle duct. At this temperature, the vessel wall material has good mechanical strength, and the wall thickness is minimized accordingly. However, the LAHS steel required closer examination of the joint where the shell is welded to the 316 stainless steel Grayloc hub because the LAHS steel needs a postweld heat treatment at conditions that sensitize the stainless steel. To avoid the sensitization, an Inconel 600 transition section will be welded to each end of the shell, and this unit will be heat-treated. Subsequently, the Inconel-stainless steel weld will be made; the Inconel transition section is, of course, long

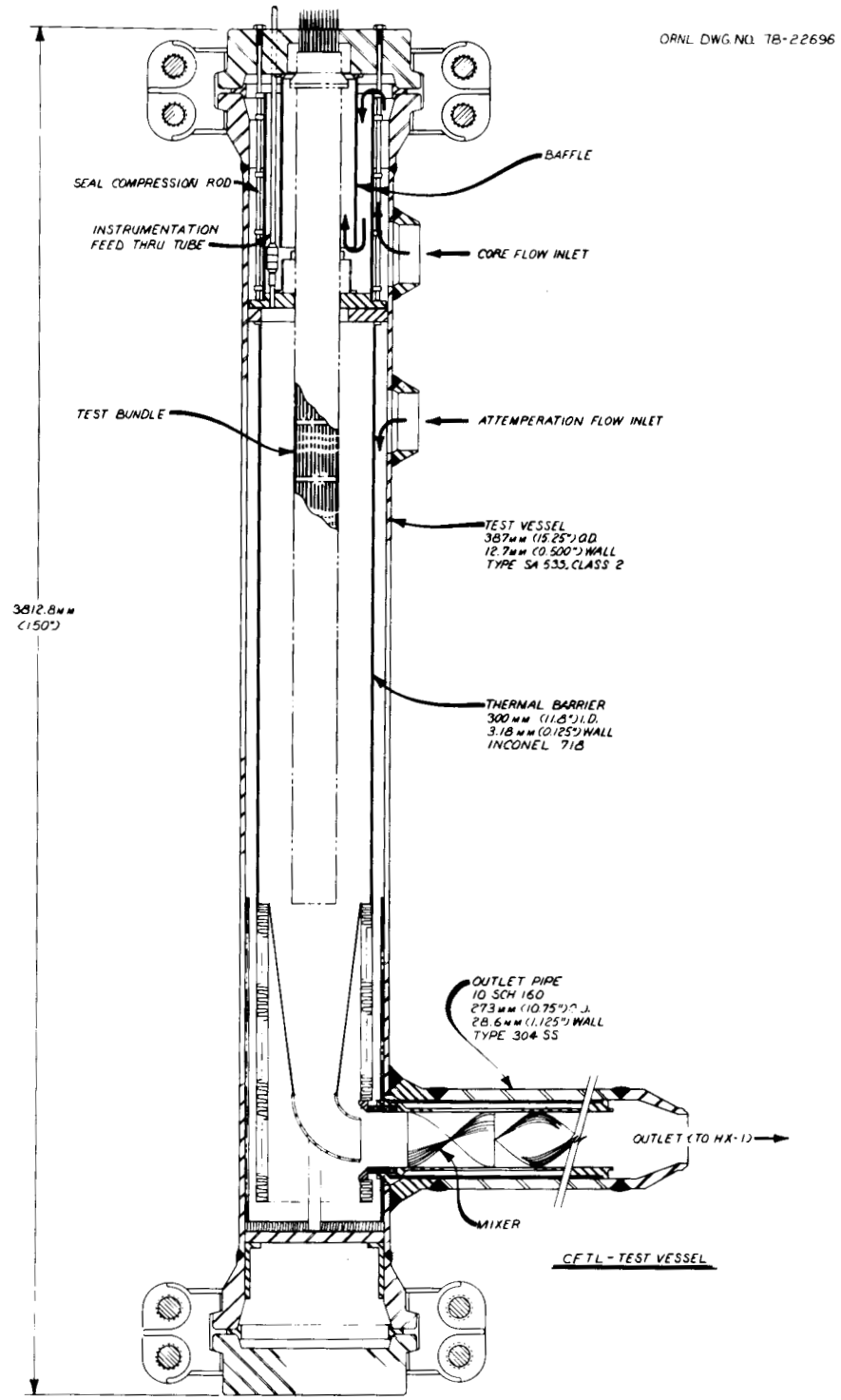

Fig. 1.21. Core Flow Test Loop Test Vessel with a 37-Rod Test Bundle Installed.

enough to keep the LAHS material out of the heat-affected zone during this process. This construction created concern about stresses caused by differential thermal expansion of the materials during service. Therefore, a stress analysis of the region was conducted by use of a finite-element computer code; results showed that stresses are within acceptable limits for the predicted conditions.

Thermal protection of the vessel wall in the outlet plenum region from the hot helium leaving the test bundle exit was also investigated. An arrangement using a tapered containment to funnel the hot bundle flow toward the outlet pipe to prevent it from directly contacting the vessel wall was chosen. Additional thermal protection of the wall is provided by a corrugated metal liner that surrounds the central containment. A thermal analysis of the region, made with a standard computer code for both steady-state and transient conditions, indicates that the proposed design maintains acceptable vessel wall temperatures. The outlet pipe, which contains a static mixer to ensure uniform blending of the bundle and attemperation flows, has corrugated metal liners similar to those in the outlet plenum to protect the pipe wall thermally. Thermal analysis of this region is currently under way. On completion of this analysis, a stress analysis of the outlet nozzle region by use of the metal temperatures predicted by the thermal analysis will be performed to complete verification of the adequacy of the design in this region.

Much of the recent effort has been directed toward analytically confirming the appropriateness of certain design features. This effort will be continued and will cover such critical regions as the flow inlet nozzles and the inner flange seal. Any necessary revisions to the conceptual design can then be incorporated into the detailed design drawings.

1.3.3 Electrical Equipment and Systems Design — R. B. Biggs

1.3.3.1 Primary Power Distribution System — R. B. Biggs and J. L. Miller

The Title II design for the primary power distribution system was completed. Subsequently, the equipment specifications and purchase

requisitions were written and submitted for bids, and an equipment contract was awarded to the RTE-Delta Corporation through its area representative, Torres Electrical Supply Company, Inc.

The primary power system consists of a 13.8-kV circuit breaker; two 2500-kVA, one 1000-kVA, and one 750-kVA transformers; and four units of 480-V switchgear as shown in Fig. 1.22. These dry-type transformers, along with the switchgear, will be installed indoors.

Short-circuit and circuit-breaker coordination studies were completed to ensure system safety. Proven standards of design were incorporated to provide a reliable system, and a quality assurance assessment plan was prepared to help ensure that the design met acceptable quality and reliability standards.

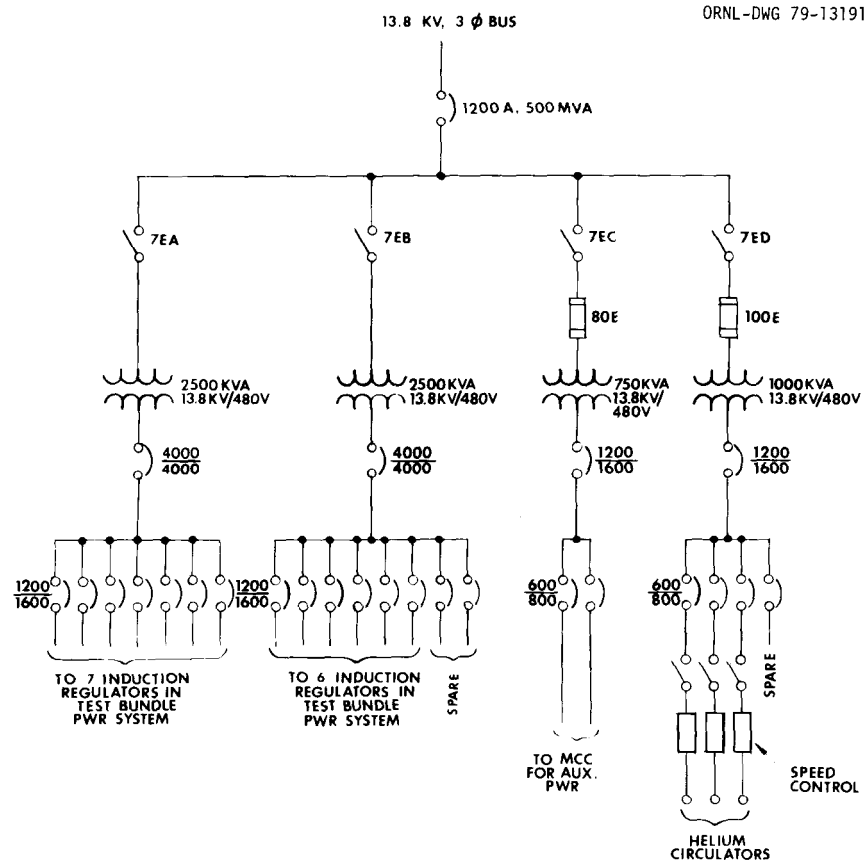

Fig. 1.22. One-Line Diagram of Core Flow Test Loop Primary Power Distribution.

1.3.3.2 Test Bundle Power Supply and Control — R. B. Biggs and C. F. Holloway

The Title II design of the test bundle power supply was started. The design consists of 13 zones of 500-kVA capacity each, one for each row of fuel rod simulators in the 90-rod control bundle, the currently largest CFTL test bundle. An individual zone (Fig. 1.23) is a linear multipower level (LMPL) ac power supply that consists of an induction voltage regulator and a transformer that has 15 selectable taps in the secondary winding to provide 15 equal increments of power. The taps are SCR controlled via a solid-state automatic or manual control system, whereas the induction voltage regulator is automatically or manually positioned with a dc motor. Other equipment in the circuit from the SCRs to an individual FRS (Fig. 1.23) includes a protective fuse, automatic "crowbar" protection components, patch panel, power measurement devices, power trim resistor, and test jacks. A block diagram of this equipment, which is mounted in control cabinets, is shown in Fig. 1.24.

A study was made for a suitable method to protect the zone power supply in the event of false firing of an SCR or failure of an SCR caused by shorting. As a result, the combination of a current-limiting fuse and an adjustable overcurrent detector will be provided for each pair of SCRs in the zone supply to protect against overload and short-circuit faults. The current-limiting fuses will provide protection for large short-circuit currents, and the overcurrent detector will be set to detect overcurrents that may not be sufficiently large to blow the current-limiting fuses. If overcurrent is detected, the zone supply controller will remove the signals from all SCR gates, and the main breaker of the supply will be tripped. Other contacts will be available to initiate additional protective action if experience proves necessary.

A study was conducted to determine whether or not alternating magnetic fields associated with the operation of the LMPL system would induce deleterious mechanical vibrations in the test bundle. The study was performed by an outside consultant and concluded that no deleterious vibrations would occur from the operation of the LMPL system.

The test bundle power and control system is designed to supply all the FRSs in a 91-rod test bundle. The system also is capable of being

ORNL-DWG 79-13192

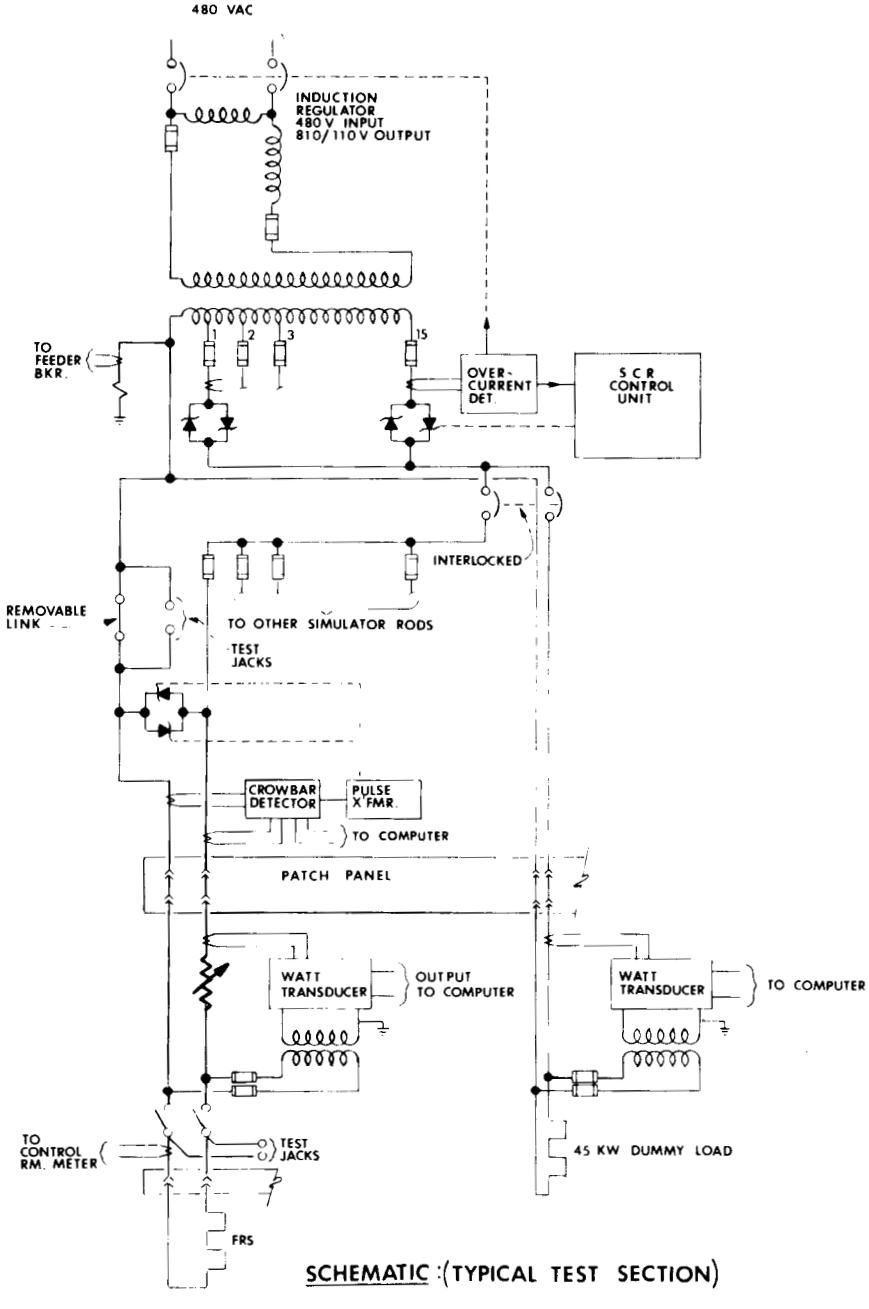

Fig. 1.23. Core Flow Test Loop Test Bundle Power Supply, Showing One Zone Feeding One Fuel Rod Simulator. Power control equipment and associated protective devices and power measurement, crowbar protection, and patch panel for fuel rod simulators are evident.

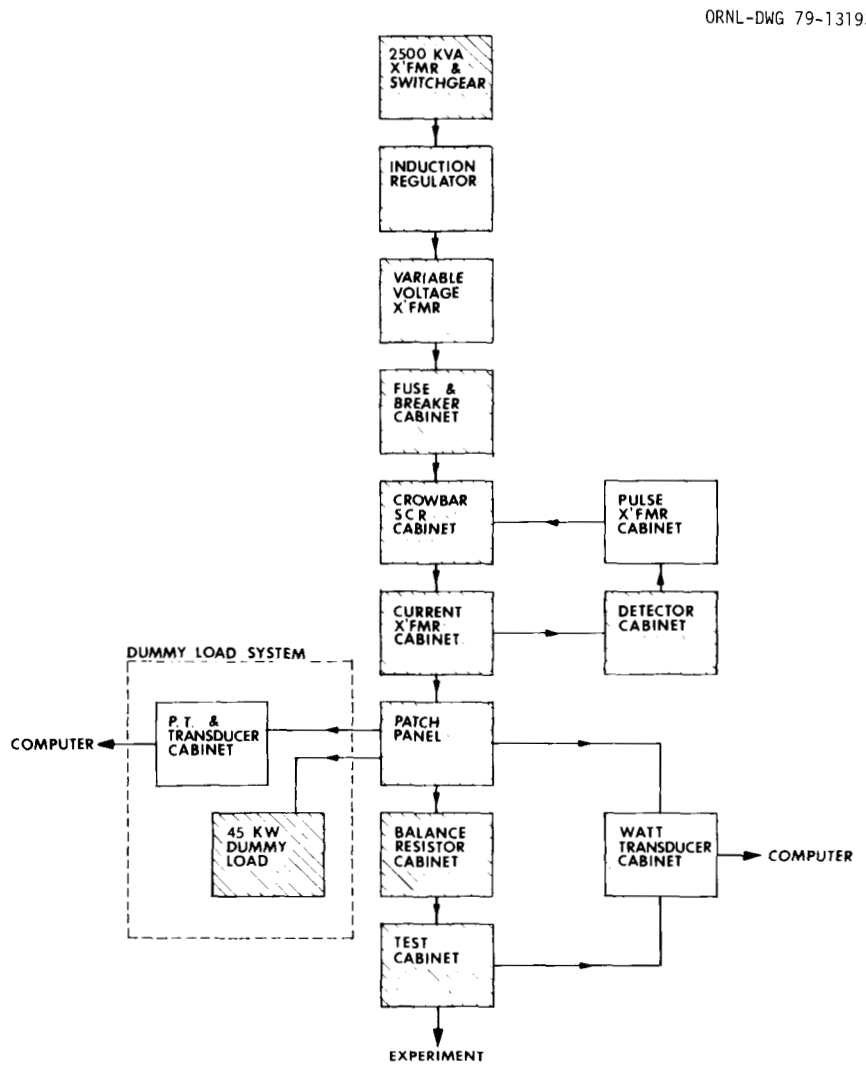

Fig. 1.24. Core Flow Test Loop Test Bundle Power Supply. Block diagram for one zone shows power equipment, control and protective equipment cabinets, and auxiliary equipment.

expanded conveniently to supply as much as 122 FRSs. Test features to facilitate system maintenance and troubleshooting were incorporated into the design, and operational interlocks were provided for system and personnel safety.

Most of the Title II design for the control cabinets was completed, as indicated by the cross-hatching in Fig. 1.24. Internal design review was initiated, and quality assurance assessments were performed. The layout for the control cabinets was completed, which permitted the design of conduit and cable trays to be started.

Some of the components for overcurrent protection were purchased in 1978. Prototypes of the components were tested satisfactorily prior to purchase.

The specification for the zone power transformers was written, and a purchase requisition was released for one unit with two options for a total of 12 additional units. After the transformers have been tested and evaluated satisfactorily, the options for the other 12 units will be exercised as required.

Preparation of the induction voltage regulator specification was started and is scheduled for completion in January of 1979. The specification and its purchase requisition will be released for bids under options similar to those for the transformers. The induction voltage regulator and the transformer will be tested as a system.

1.3.3.3 Power Measurement for Fuel Rod Simulators — R. B. Biggs and C. F. Holloway

The Title II design of the power measurement system for individual FRSs in a test bundle was started. The system consists of a current and potential transformer to feed a solid-state watt transducer. The design for mounting the current and potential transformer was completed. The remaining design for mounting the watt transducers and routing the output signal leads to the control room is scheduled to be completed in 1979.

1.3.3.4 Electrical Protection for Fuel Rod Simulators — R. B. Biggs, C. F. Holloway, and T. L. Hudson

The Title II design of the electrical protection for an individual FRS in a CFTL test bundle was started. The design will provide current-limiting fuses, overcurrent and leakage protection, and ground current protection. The design was completed for the current-limiting fuses, crowbar SCRs with snubbers, and overcurrent and leakage sensors that supply input to the overcurrent and leakage detectors. The remaining design for mounting the overcurrent and leakage modules and the crowbar SCR driver boards in control cabinets is scheduled to be completed in 1979.

1.3.3.5 Auxiliary Power System — R. B. Biggs and M. D. Trundle

The specification for the uninterruptible power supply was completed. This supply ensures that the DAS and a small number of required instruments have an uninterruptible source of power in case of loss of normal power. Also, the auxiliary power requirements for the CFTL were determined, and the design to provide this power was begun in 1978. Design completion is scheduled for 1979.

1.3.3.6 Development Support for Electrical Design — T. L. Hudson

1.3.3.6.1 Test Bundle Power Supply and Control System. The test bundle power is supplied from 13 individual zones in the LMPL ac power supply and control system. Each zone (Fig. 1.25) consists of an induction voltage regulator (IVR), whose output voltage is connected to the primary of a transformer having 15 secondary taps to provide equal power increments. The secondary taps are connected to the test bundle through the operation of 15 pairs of SCRs.

For steady-state operation at 100 to 2% power levels, the SCR control will be fixed constant at the highest voltage output from the transformer secondary, and the appropriate level of bundle power will be achieved by the manual operation of the IVR. For power levels lower than 2%, the SCR control will be fixed constant for an appropriately lower voltage output from the secondary, and the required power will again be achieved by the manual operation of the IVR. Skewed power operation of the test bundle will be attained by supplying each individual row of rods in the bundle with the voltage appropriate to its required power level from its individual zone supply.

Slow power transients starting from steady-state operation are achieved by the programmed operation of the IVR with an electric drive motor. A schematic diagram of the electric drive motor system is shown in Fig. 1.26. All fast power transients will be started from steady-state operation with the IVR set to give 100% nominal power when the SCRs are set to give maximum practical voltage output from the transformer secondary. The transient will be provided by the programmed operation of the 15 pairs of SCRs in the transformer secondary. A

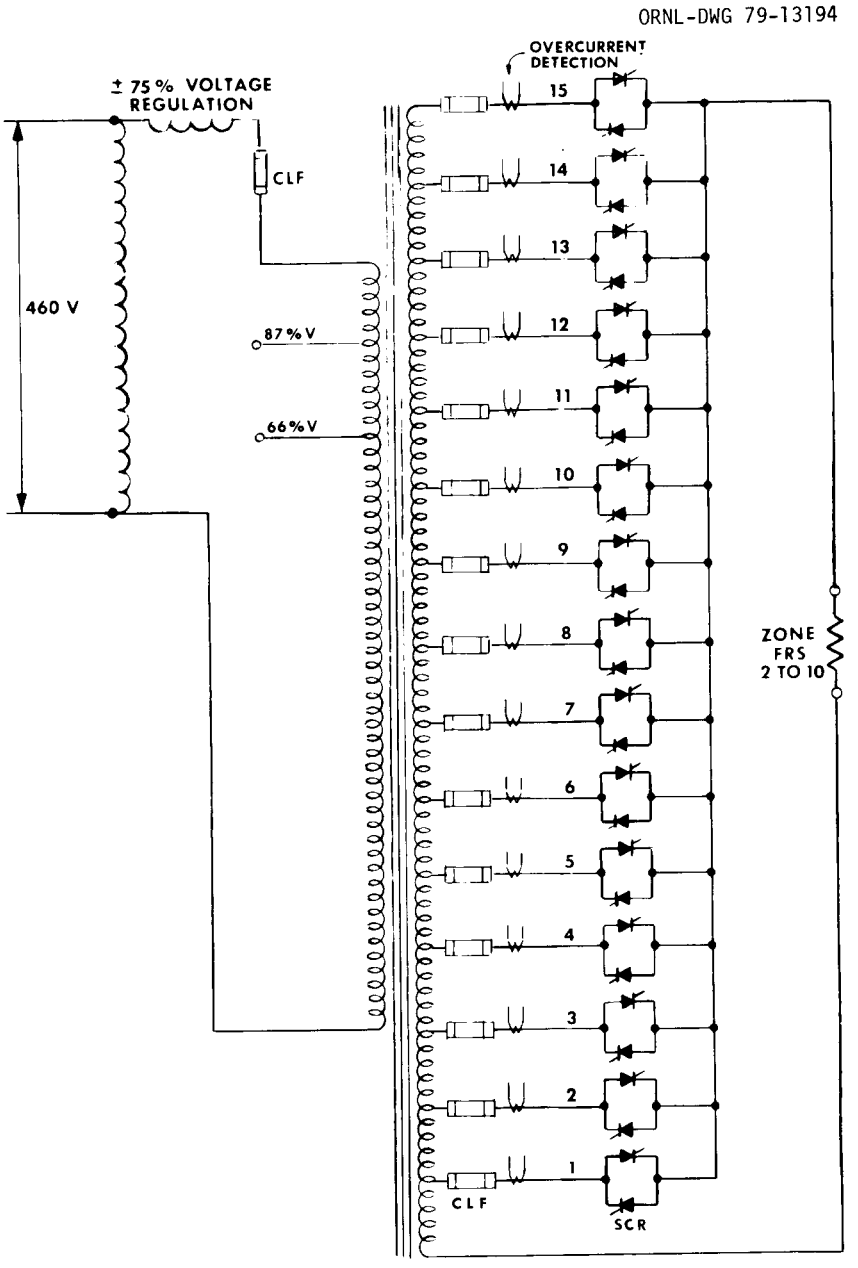

Fig. 1.25. Core Flow Test Loop Test Bundle Power Supply, Showing Induction Voltage Regulator and Power Supply Transformer for One Zone. Transformer has 15 secondary taps that provide equal increments of power to test bundle, and silicon controlled rectifier gates control the secondary tap to be used.

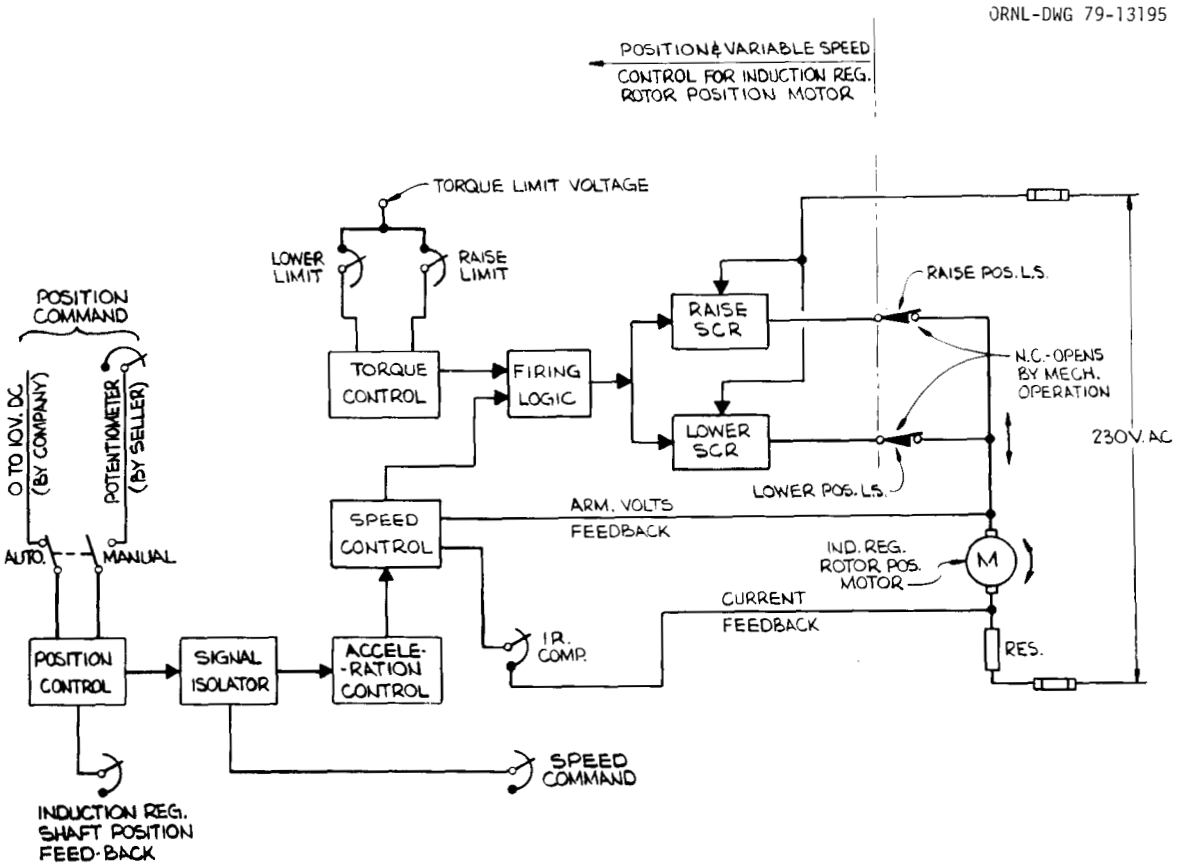

Fig. 1.26. Core Flow Test Loop Test Bundle Power Supply, Showing Electrical Drive System to Control Zone Induction Regulator.

transient programmer or a closed-loop control system will be used to direct the SCRs to produce the required power transient from 100% to zero within a time period as short as 0.25 s.

A 50-kW prototype of the LMPL system installed in the Single-Rod Sodium Loop (SRSL) was operated satisfactorily both in the steady-state mode and in timed cycle transients between two power levels. The prototype system is being used in testing prototypes of the CFTL FRSs.

1.3.3.6.2 Power Measurement for Fuel Rod Simulators. The steady-state and transient capabilities of the power measurement system for the FRSs have been established. The accuracy of the selected power measurement system in the 200-W to 45-kW power range with the Scientific Columbus model XL31K5A2 solid-state watt transducer and Westinghouse current and potential transformers was ±1% or less. The time constant for 63% response was 0.2 s. The power measurement system has been installed for testing with the FRS in the SRSL.

1.3.3.6.3 Electrical Protection for Fuel Rod Simulators. The overcurrent and leakage-current ranges have been selected, the prototype modules have been calibrated, and the module is now ready for testing with the FRS in the SRSL. Circuit changes made during the testing of the prototype modules have been included in the CFTL design. The schematic diagram, printed circuit board, and a five-module assembly design have been completed.

1.3.4 Instrumentation and Controls Design — P. G. Herndon

Both the Title I and Title II phases of instrumentation and controls design progressed significantly during 1978.

The CFTL test specifications[2] were analyzed to determine the operating conditions actually imposed on the CFTL. Difficulties created by certain tests were identified and, in most cases, eliminated by amendment of the test specifications. The CFTL dynamics simulator code ORCULT was modified for analysis of the evolving loop design and was used to help resolve loop layout and component design problems.

Analysis proved that adequate rangeability and response for helium flow control valves can be achieved by use of commercially available components and that closed-loop control of the test section flow is feasible. An in-depth evaluation of flowmeters that have application potential for helium flow measurement led to the decision (1) that a venturi meter with multiple differential pressure (ΔP) transmitters is the reference design for the CFTL and (2) that further evaluation of the vortex shedding flowmeter should be made.

An evaluation of x-ray imaging techniques led to the recommendation that it be used to make test bundle structural measurements.

An evaluation was started of systems using both analog and digital techniques to provide coordinated control of helium flow, pressure, temperature, and test bundle power.

Loop-temperature and pressure-measurement requirements were defined, and commercially available components to meet the requirements were identified.

The formal design review of the data acquisition system (DAS) was completed, and all major components are either ordered or have been delivered.

An FRS power controller was designed, and a bench model was built and tested successfully. The instrumentation for the helium supply, impurities injection, and purification systems was designed, and a specification was written for a gas chromatograph analyzer to measure trace-element impurities in the circulating helium. Design of the control and safety interlock systems to protect the test bundle and loop components from damage caused by unsafe operating conditions was started.

1.3.4.1 Dynamic Simulation and Control Analysis — S. J. Ball

Development work on the CFTL dynamics simulator code ORCULT was continued, and the detailed component models were modified to follow the evolving loop design. The ORCULT code is written in the IBM Continuous System Modeling Program (CSMP) language.

Follow-up studies were conducted on optimizing the design of the control schemes for the main 4-MW heat exchanger (HX-1) to cover the operating range from full-power cooling to a heating mode in which auxiliary heat could be used during low-power operation.

A number of studies were completed by use of the steady-state version of ORCULT to determine control valve rangeability requirements and the sensitivity of required valve C_v values to uncertainties in loop flow resistances and alternate loop design features. The studies confirmed the adequacy of proposed valve designs.

Follow-up studies were also conducted to find the maximum thermal gradients experienced by various parts of the loop during severe loop traumas such as simulations of the GCFR DBDA and inadvertent losses of test bundle power. The results were used to compute component stresses and to guide redesign efforts.

We used ORCULT further to study the DBDA that had a final loop pressure of 1.0 atm as opposed to the previously specified minima of 1.6 to 2.0 atm. Simulations were performed for the most conservative GCFR cases, which assume that two of three core auxiliary cooling system (CACS) loops are operational and contain 20% more afterheat than expected. Initial 91-rod bundle powers of 28, 30.8, and 38 kW per rod were assumed, and the

cases of higher power and lower final pressure led to predicted conditions that clearly exceed both bundle and loop design limits. These results are being used to help establish a reasonable set of limiting test conditions.

A circulator coastdown model was developed and incorporated into ORCULT for use in simulating loop failures and studying proposed loop emergency corrective actions.

During the year the staged construction and operation of CFTL was adopted, and ORCULT was used to help confirm the proposed idea of running the first-stage, 37-rod bundle tests without the bypass heat exchanger (HX-2).

A CSMP program was written to simulate the behavior of the proposed SCR controller for the FRS power when coupled to a detailed thermal model of an FRS. This program will be used to investigate the spurious clad motion that results from low-frequency power and temperature oscillations.

Frequency-response tests were run on two candidate watt transducers for measuring FRS power.

1.3.4.2 Helium Flow Control Analysis — A. D. McNutt

The CFTL test specifications[2] were analyzed to determine the operating conditions actually imposed on the CFTL. Considerable effort was expended in comparing the operating conditions with the physical capabilities of the CFTL and the limitations of available measuring instruments.

To explore the requirements for valves and flowmeters, we found it desirable to reduce the rather large ORCULT simulation code (Sect. 1.3.4.1) to a simple modeling program that could be economically and conveniently executed on a microprocessor-based computer system. Although the simplified model used essentially the same pressure drop versus flow relationships as ORCULT, it differed from the parent program in the following respects:

1. A somewhat different model of loop configuration was used that employed three mass storage nodes rather than the two used by ORCULT.
2. The circulator head and flow characteristics were represented by a different polynomial expression.

3. The division of loop variables into specified and dependent variables was changed; that is, some variables that were specified in ORCULT were found as computed results in the simplified model and vice versa.

4. Thermal effects were largely ignored.

The results calculated by the simplified model were in good agreement with those produced by ORCULT. Although not a validation of the assumed pressure-drop relationships, this agreement confirmed that the solutions produced were not artifacts of the integration methods, configurational assumptions, etc. Whenever the simplified model produced results that differed noticeably from those of ORCULT, the differences were directly traceable to the gross simplification of thermal effects noted above.

In several cases we found that the specified operating conditions were not within the capabilities of the CFTL or that they would require extreme efforts to implement the implied measurement and control system. In some test specifications the representation of pressure and flow changes by straight-line approximations resulted in unrealistic helium velocities and valve stem accelerations. In others, the ranges of mass flows specified were too large to be accommodated by available measurement and control components.

General Atomic was informed of the difficulties created by certain classes of tests, and in most cases the difficulties were eliminated by amendment of the test specifications. A major area that is still unresolved is the nature of the pressure, flow, and power variations that are to be produced in the simulation of depressurization transients. The measurement and control system is being designed on the basis of currently available information.

The analytical results obtained and the amendments to the test specifications have affected the CFTL design as follows:

1. Range requirements for the test bundle flow control valve are significantly less severe than previously thought. The flow rates for all bundles may be accommodated in a single valve body, and valve trim will need to be changed only when bundle sizes are changed.

2. Valve actuator speeds actually required are slower than previously thought. Adequate valve response may be achieved with commercially available packaged hydraulic actuator systems.

3. Valves, flowmeters, and piping for the attemperator and bypass lines have been reduced 15.24 to 10.16 cm (6- to 4-in.).

A major achievement of the flow analysis was the demonstration by simulation that closed-loop control of the test bundle flow is feasible for transient operations. Because of the large flow range, the inherent nonlinearities of the system, and the required rates of change, closed-loop control had been considered infeasible, and earlier simulations had confirmed that conventional control techniques would not produce satisfactory results.

However, there was considerable incentive to develop a satisfactory closed-loop control technique for CFTL helium flows. In general, closed-loop control offers the possibility of greater precision and reproducibility than can usually be achieved with open-loop control. In the case of the CFTL, additional considerations made closed-loop control particularly desirable. With open-loop control, preprogramming of the transient tests would be extremely laborious. The specified flow versus time data for each test would have to be converted into a specification of valve-stem-positioning signal versus time. Repeated computer simulations and some in-loop trial and error would probably be required to achieve the desired flow transients. In contrast, the flow versus time data may be preprogrammed directly when closed-loop control is used. Finally, protective control functions designed to limit circulator flow to a safe operating region would be more difficult to implement if the flow-control valves were operating in the open-loop mode to follow a specified motion.

The reason that conventional closed-loop control techniques were not successful in controlling the test section flow is that the open-loop gain of the system (i.e., the ratio of measured flow to valve-positioning signal) is not constant but is an approximate function of the square of the mass flow and the square root of pressure and temperature. The gain is, of course, also influenced by the circulator

operating point and the relative positions of the bypass and attemperator valves. Some degree of coupling with the power-to-flow ratio in the test section and heat exchanger HX-1 also occurs.

The variation in gain from mass flow can be partially compensated for by using an appropriately contoured valve plug and seat ring. However, the other factors influencing the gain cannot be satisfactorily accounted for by means of a simple process characterization curve, which rules out the use of the more common "adoptive gain" control techniques.

Although the maximum rates of change in the CFTL are somewhat fast for a large mechanical system, events in the loop occur rather slowly when considered from the viewpoint of an electronic digital controller. It was therefore considered possible to design an "intelligent" controller that would, while controlling the flow, estimate the system gain based on the immediate past history of flow response to valve position. A modified version of the ORCULT code that accounted for valve trim characterization, valve actuator dynamics, and flow measurement noise was used to test several prototype control algorithms. One algorithm was found that yielded quite good flow control for flow transients at both constant pressure and depressurization conditions.

Figure 1.27 shows simulation results for a constant-pressure flow transient, and Fig. 1.28 shows the results for a depressurization transient. In these simulations the difficulty of the control problem was aggravated by assuming an extremely slow, leaky valve as the primary control element and by conservatively estimating the effects of measurement noise. Considering these added problems, the ability of the controller to follow the flow demand signal is entirely satisfactory. In earlier simulations in which a more realistic valve model was used, the deviation between flow and flow demand was virtually indiscernible.

Since this work was done, similar control techniques that are reported to be functioning successfully in industrial environments have been found in the literature. As time permits, some of these techniques will be tested to determine if they offer advantages over the algorithm now being considered for use on the CFTL.

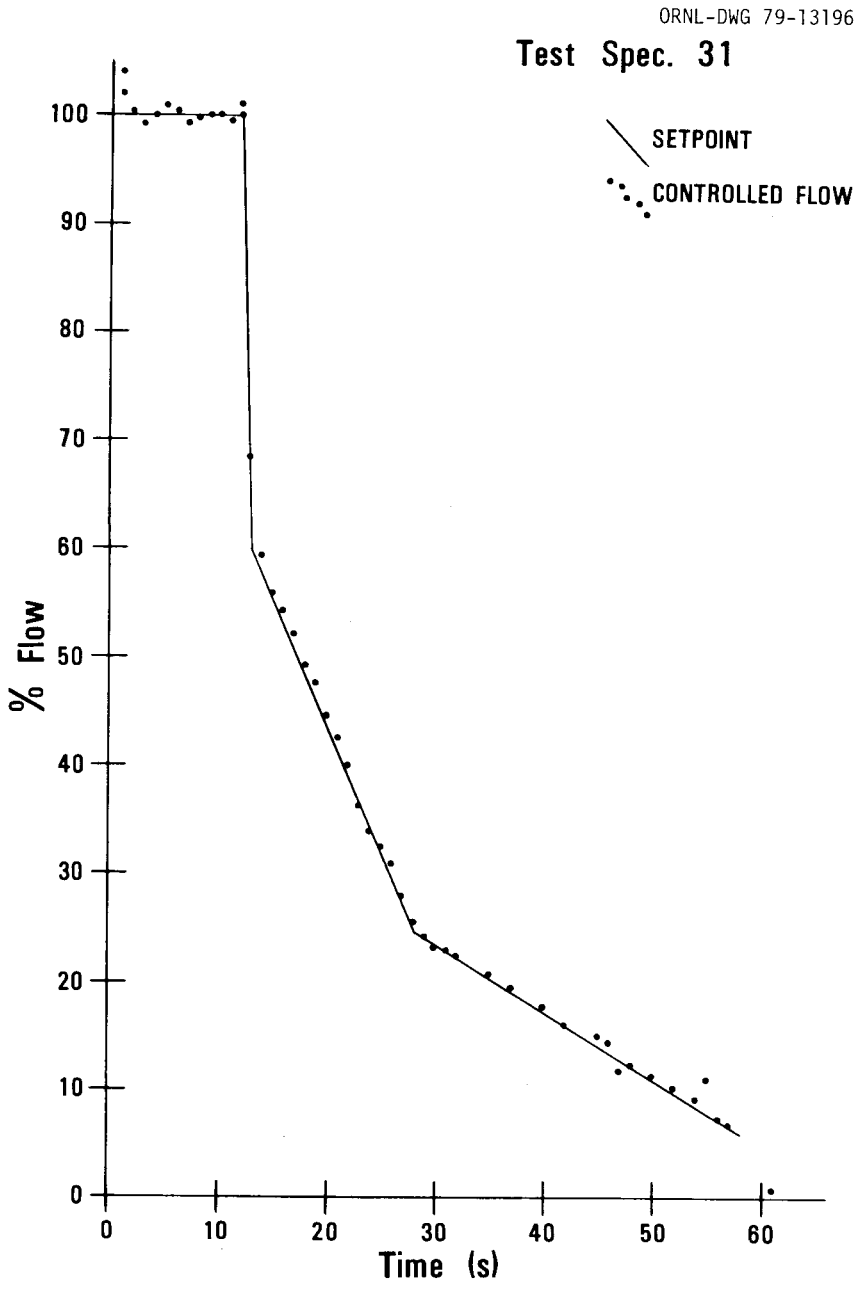

Fig. 1.27. ORCULT Simulation of Closed-Loop Control of Core Flow Test Loop Bundle Flow During a Fast Scram Transient at Constant Helium Pressure.

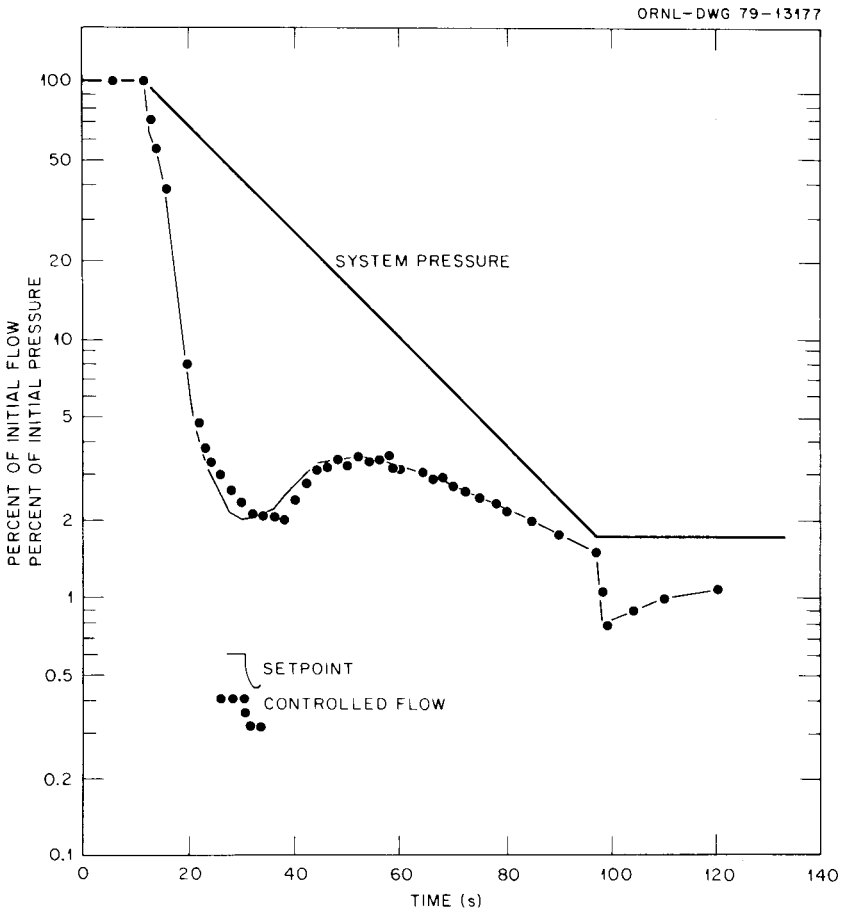

Fig. 1.28. ORCULT Simulation of Closed-Loop Control of Core Flow Test Loop Bundle Flow During a Depressurization Transient.

1.3.4.3 Helium Flow Control Valves P. G. Herndon and A. D. McNutt

A preliminary specification for the flow control valves was written in 1977. As a result of the flow analyses and investigation of commercially available valve systems, this specification was extensively revised during 1978.

As noted in Sect. 1.3.4.2, the flow analyses and subsequent test specification amendments resulted in a significant decrease in valve range requirements. This decrease reduced the total number of valve trims required and reduced the required valve body and trim combinations to those that are ordinarily manufactured.

Valve actuator speed and frequency-response specifications were also revised to reflect our more accurate knowledge of requirements.

In general, one would expect that increasing the speed of a control system component would enhance the overall system performance. However, a critical examination of that manufacturer's data for valve actuator systems indicates that higher speeds are often obtained at the expense of reductions in damping and in the margin of stability. Because simulation results indicated that an actuator with a slower operating speed than originally specified would perform reasonably well in our application, we considered it prudent to specify an actuator speed that could be obtained in a well-damped, high-stability hydraulic system.

The valve actuator specification was also modified to require that the hydraulic supply pump and high-pressure accumulator be made an integral part of the actuator assembly. Such designs are commercially available, and the associated reduction in hydraulic system piping will enhance reliability and reduce installation and maintenance costs.

C. W. Collins, the principal engineer responsible for the integrity of the CFTL pressure boundary, made extensive revisions to the specifications for the design and quality assurance of the valve pressure-retaining parts, which must be in accordance with the requirements for class 2 valves in Section III of the *ASME Boiler and Pressure Vessel Code*.

A draft of our valve specification was submitted to two valve manufacturers for comment. Both vendors indicated that our requirements were not extraordinary and that they would have no undue difficulty in producing our valves.

1.3.4.4 Helium Flow Measurement — P. G. Herndon and R. E. Toucey

The design of flowmeter systems for the CFTL centered on the application of venturi tubes, orifice plates, and vortex shedding meters because these are the only commercially available devices that meet the CFTL requirements identified in an in-depth evaluation[18] of flowmeters. The CFTL flow requirements are defined in refs. 2 and 19.

A venturi meter that has multiple (three) ΔP transmitters (Fig. 1.29) is the design basis for the measurement of helium coolant flow rates (flow measurement system) in each of the three different sizes of CFTL fuel test bundles. The flow rate is proportional to the square root of the ΔP produced across the venturi restriction. Each transmitter

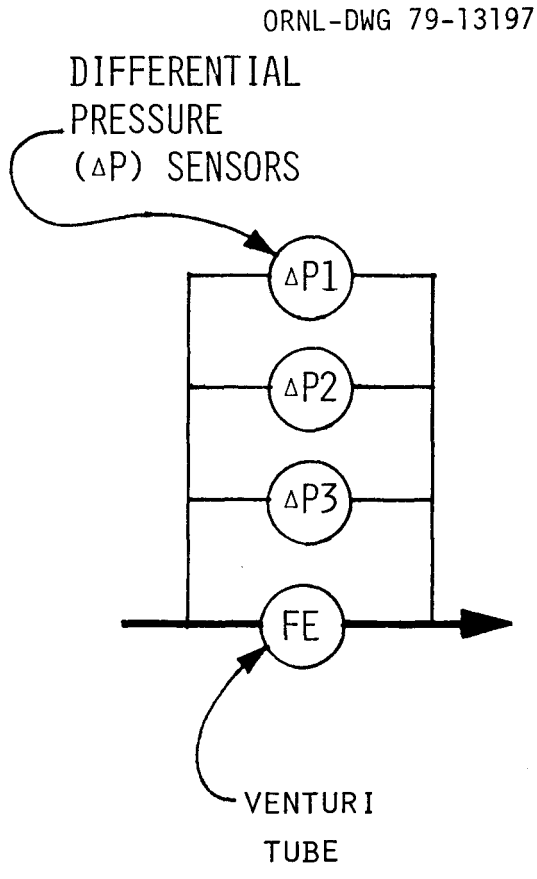

Fig. 1.29. Core Flow Test Loop Venturi Flow Element with Multiple Differential Pressure Transmitters.

measures an appropriate portion of the range of ΔP that is produced by the wide range of flows through the test bundle. The venturi measurement ranges are shown in Table 1.8. The venturi meter can measure all the individual bundle flow rates that are required by ref. 2, except for the extremely low flow tests conducted at low pressures (0.2 MPa) (which include a portion of the depressurization accident test) and the laminar flow tests conducted at 9-MPa pressure. All these flows produce differential pressures of less than 0.25 kPa (1 in. H_2O), which we considered beyond the ΔP transmitter capability. For the laminar flow tests to be conducted at 9-MPa pressure, we plan to replace the venturi with a sharp-edged orifice but to continue use of the multiple ΔP transmitter design.

Table 1.8. Measurement Range of CFTL Test Bundle Venturi Flow Elements

Venturi ΔP		Test bundle flow (g/s)			Loop operating pressure (MPa)
kPa	In. H_2O	37-rod	61-rod	91-rod	
112	450	980	1562	2310	9
1.3	5	100	164	243	
0.25	1	45	84	108	
23	94	240			
1.3	5	57			3
0.25	1	25			
2.3	9	20	33	50	
1.3	5	15	25	38	0.2
0.25	1	7	11	17	
92	370	860	1420	2100	
1.3	5	100	165	244	DBA[a]
0.75	3	10	15	22	9–0.15

[a]DBA = design basis accident.

However, the design-basis scheme presents some difficulty. The capability to measure the extremely low ΔPs between 0.25 and 1.3 kPa (1 and 5 in. H_2O) is uncertain. One reason for this uncertainty is that the lowest-range transmitter must withstand the largest differential that is produced at maximum flow rates but must not shift its calibration. Also, the general noise level of ΔP flow signals is relatively large compared with the small signal of 0.25 kPa (1 in. H_2O). In summary, because the flow measurement accuracy depends directly on the accuracy of the ΔP transmitters, we cannot predict the accuracy of the flow rates that are determined by measurements of ΔPs between 0.25 and 1.3 kPa (1 and 5 in. H_2O) until calibration tests are performed under these

conditions. We feel confident that ΔPs as low as 1.3 kPa (5 in. H_2O) can be measured by use of the lowest-range transmitter with accuracy acceptable to the required CFTL flow measurements. This low ΔP corresponds to 100, 164, and 243 g/s helium flow at 9 MPa (1305 psi) for the 27-, 61-, and 91-rod bundles, respectively, by using the bundle-associated venturi, and to 11, 16, and 21 g/s, respectively, by using the bundle-associated, sharp-edged orifice.

Most tests that require difficult-to-measure flow rates were eliminated by amendment of the test specifications[20] for the 37-rod bundle. The steady-state tests that require low flows at low pressures (0.2 MPa) and laminar flow tests conducted at 9 MPa were eliminated. The minimum flow rate specified for the steady-state tests conducted at 9 MPa was increased to 100 g/s to avoid the low ΔP measurement problem. The low-flow–low-ΔP measurement requirements for the 37-rod bundle transient tests are now being reevaluated by GA to determine the feasibility of increasing the minimum flow rates. All test specifications for the larger-size bundles are also being reevaluated to determine what relief is available for flow measurement with venturi and with orifice plate flowmeters.

An error analysis was performed to determine the accuracy of flow measurement to be expected from the venturi tube assembly of Fig. 1.29. The results of the analysis for a 21:1 flow range in a 37-rod test bundle are shown in Table 1.9. The accuracy of measurements below 1.3 kPa (5 in. H_2O) ΔP cannot be predicted until calibration tests are performed.

Because the performance of the venturi flowmeter scheme depends to a large extent on our ability to measure a wide range of ΔPs, a study of commercially available ΔP transducers was undertaken. The transducers used on the CFTL must have fast dynamic response (>10 Hz) for the measurement of flow transients and extreme ΔP overpressure tolerance so that the low-flow-range transmitter will maintain calibration when subjected to ΔP produced at high flow rates. The transmitters must also withstand severe shock and vibration. Results of the study indicate that a standard commercially available device having a movable diaphragm and a variable magnetic-reluctance position-sensing and signal-transducing system will meet CFTL requirements.

Table 1.9. Measurement Error at Various Flow Rates for Venturi with Multiple ΔP Transmitters CFTL Venturi Calibration — 37-Rod Bundle

Transmitter	Flow		ΔP			Uncertainty — 2σ			
	%	g/s	kPa	In. H_2O	%	±%[a]	±g/s	±%[b]	±g/s
$\Delta P1$	100	950	112	450	100	1.6	15	3.4	32
	75	715	63	253	56	1.83	13	3.52	25
	50	475	28	113	25	2.5	12	3.92	19
	38	359	16	64	14	4.3	16	5.22	19
$\Delta P2$	38	359	16	64	100	1.6	5.7	3.4	12
	28	270	9	36	56	1.83	5	3.52	9.5
	19	180	4	16	25	2.5	4.5	3.92	7
	14	134	2	9	14	4.3	5.8	5.22	7
$\Delta P3$	14	134	2	9	100	1.83	1.8	3.52	3.5
	10.5	100	1.3	5[c]	56	2.5	1.4	3.92	2.2
	7	67	0.6	2.5	25				
	4.7	45	0.25	1.0	11				

[a] Gas density deviation = ±1%.

[b] Gas density deviation = ±3%.

[c] Indeterminate below 1.5 kPa ΔP.

A loop piping configuration that uses flanged sections to accommodate either the venturi or the vortex shedding type flowmeter was designed. This configuration will permit the loop piping design to proceed before the final selection of a flowmeter is made.

1.3.4.5 Helium Flowmeter Evaluation — S. P. Baker, T. C. Morelock, and H. J. Metz

An evaluation[18] of potential flowmeters for CFTL was completed in June 1978 by a team of Instrumentation and Controls Division engineers and consultants consisting of S. P. Baker, P. G. Herndon, D. W. McDonald, H. J. Metz (Science Applications, Inc.), and F. M. Shofner

(Shofner Engineering Associates). The purpose of the evaluation was to perform an in-depth technical review of those flowmeters potentially applicable for use in the CFTL and to recommend a course of action to ensure that the optimum flowmeter is available for integration into the loop.

The important recommendations from the evaluation were:

1. A venturi tube with stacked ΔP transmitters should be the reference design flowmeter for bundle flow.
2. The development, test, and evaluation of the ion deflection flowmeter should be pursued.
3. The test and evaluation of the vortex shedding flowmeter should be pursued.

A low-pressure prototype of an ion deflection flowmeter made of polyvinyl chloride was designed, fabricated, and initially tested with air. The test results seemed promising, but unfortunately, the uncertainties associated with the use of this flowmeter in the high-pressure, relatively high-temperature helium environment indicated the need for an extensive development effort. Therefore, work with the ion deflection flowmeter was stopped to pursue the usefulness of the commercially available vortex shedding flowmeter.

Applicability of the vortex shedding flowmeter to the CFTL was investigated extensively. This flowmeter is available commercially from the Neptune Eastech Company and is being used by private industry. Initial studies showed that a single meter installed at each appropriate station will measure all flow ranges required in the circulator discharge line FM-3, in the attemperator supply line FM-2, and in the circulator bypass line FM-4.

A further in-depth review of Eastech's product line revealed that a modification of one of their vortex shedding flowmeter designs using thermistor sensors in a region of relatively cool temperature away from the flowing gas may be very usable at all CFTL flowmeter stations, including that for the test bundle flow. The design promises to cover the entire pressure and flow range given in the GA CFTL test specifications.[2]

A purchase order was written for the components needed to make a 100-mm (4-in.) meter that will be modified at ORNL to relocate the thermistor-sensing assembly in a lower-temperature environment outside the meter body. Engineering tests with the modified meter are planned during the first half of 1979 to prove that it will give satisfactory and reliable performance under CFTL conditions.

The vortex shedding flowmeter not only has a much wider range of measurement but is also more economical, more accurate, and easier to operate and maintain than the venturi meter.

1.3.4.6 Test Bundle Power Controllers — D. W. McDonald

The power for the test bundle FRSs will be distributed via 13 zone power supplies. Each zone supply will consist of a motor-driven induction regulator and a tapped transformer-thyristor switching configuration referred to as the LMPL system.[21] Each zone will supply power to a row of FRSs in a test bundle. Each row will consist of up to 11 FRSs, depending on row location and bundle size. Figure 1.30 demonstrates the partitioning of zones in a 37-rod bundle.

Each zone will be controlled by a power controller designed especially for use with the CFTL zone power supplies. The controller offers three modes of control: a manual mode, an automatic closed-loop

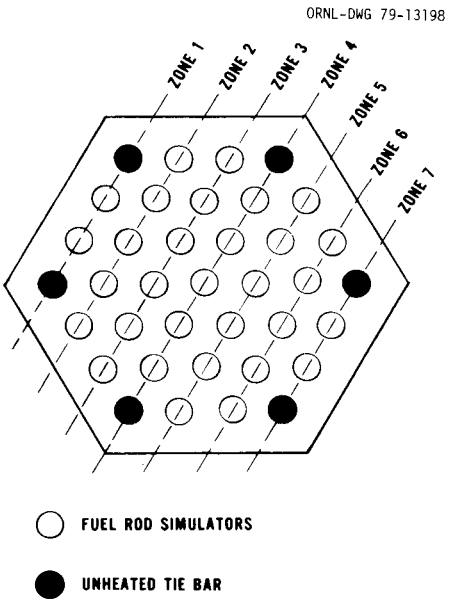

Fig. 1.30. Power Zones for a 37-Rod Test Bundle in the Core Flow Test Loop.

control mode, and an external control mode. In the manual mode any one of the 15 SCR pairs can be turned on to select the appropriate ac voltage level needed to supply the desired steady-state power to each FRS. In the closed-loop mode the controller compares the actual voltage level applied to a zone having the desired level and calculates which SRC pairs to turn on to adjust the ac voltage to keep the average power in a zone at the level demanded by the power set-point signal. This calculation is done 60 times per second. The automatic closed-loop mode will be used primarily during a fast bundle power transient. In the external control mode, control of the bundle power is relinquished to some external device such as the loop process control computer.

The controller has been tested on a four-tap transformer prototype with good results. However, certain nonlinearities in the CFTL power supply design prevent extrapolation of the prototypic performance to the larger CFTL system. Therefore, computer simulations of the system have been written and are being analyzed for insight into improving the automatic closed-loop control mode. The current controller design will also be used with the 50-kW prototype ac power supply[22] in FRS tests.

1.3.4.7 Integrated Control of Flow, Power, and Temperature — A. D. McNutt

The CFTL control requirements were more clearly defined during this reporting period and were compared with the capabilities and limitations of commercially available control systems. Systems using both analog and digital techniques are being evaluated. Transient operation of the CFTL will require coordinated control of the flow control valves, test bundle power supplies, and heat exchangers. Although test bundle flow and power are varied in accordance with the test specifications, the attemperator and circulator bypass flows must be manipulated to protect heat exchanger HX-1 from thermal shock and to maintain circulator flow in a safe operating region. Heat removal in the heat exchangers must be controlled to protect the circulators from high temperatures and to maintain test bundle inlet temperature at the specified value. In the event of an emergency, the control system must be capable of switching smoothly from a test transient to a shutdown transient that will shut the entire system down safely.

The wide operating range of all test conditions and the necessity for coordinated action indicate that the CFTL can best be controlled with a central device that has reasonably sophisticated computational and decision-making capability. Alternatives examined include general-purpose computers, packaged industrial digital control systems, and modular digital systems designed primarily for large-scale laboratory installations. Because of the uncertainties inherent in the design and operation of an experimental installation, the third alternative is the most attractive. Employing a modular approach to system design, a hardware system may be readily configured to meet our requirements, both present and evolving, thus minimizing initial costs while providing for convenient and readily made expansion or reconfiguration.

The modular system under consideration is based on Computer Automated Measurement and Control (CAMAC), an internationally recognized standard for modular digital equipment. Use of this standard ensures that compatible, high-quality components can be obtained from a number of sources. System intelligence is supplied by a 16-bit microprocessor equipped with advanced arithmetic capability. Sufficient memory and mass storage to allow programming in a high-level computer language are available. General-purpose software, including program development and input/output utilities, may be purchased as a part of the basic system. The system can be configured such that additional processing capability may be added as required.

1.3.4.8 Helium Pressure and Temperature Measurements — R. E. Toucey and K. R. Carr

A continuous measurement of helium pressure over a range extending from 0.15 to 9 MPa (20 to 1300 psia) is required during simulation of a GCFR depressurization accident, which represents the largest range of pressure change in CFTL operation and a turndown ratio of 60:1. Measurement uncertainty specified for the CFTL is ±1% at full scale and ±3.5 kPa (± 0.5 psia) at the 0.15-MPa level. The measurement systems must withstand depressurization in as little as 60 s, with much of the change occurring in the first 20 to 30 s.

A commercially available device that uses a force-balanced, quartz Bourdon-tube measuring element apparently meets our requirements. The device has quite fast response, and the quoted accuracy is ±0.04% of full-scale reading. For a full-scale reading of 10 MPa, the measurement uncertainty is ±4 kPa.

Initial studies of the temperature measurement of flowing helium in the CFTL piping over a wide range of velocity and density conditions were completed. Because of the wide range of helium mass flow rates, it may be necessary to install a faster-responding, and necessarily fragile, sensor for low mass-flow rates and a slower-responding, more rugged sensor for high mass-flow rates. The wide range of flow rates may be illustrated by considering that the lowest and highest rates required in the test section inlet line are equivalent, respectively, to ambient air (1 atm pressure at 25°C) flowing at 0.05 m/s and at 106 m/s.

Sensors capable of making the required measurements are commercially available, but no single element has been sufficiently tested to show that it will be satisfactory under all CFTL conditions. One ORNL-designed and two commercially designed sensors that may be suitable will be investigated further. It may be prudent to test the candidate sensors. The tests would not have to be elaborate and would require three or four man-weeks of effort. The tests would include a determination of the survivability at the high flow rates, time response at the low flow rates, and the need for a thermal radiation shield.

1.3.4.9 Controls for Helium Supply and Helium Purification Systems — P. G. Herndon

Development of the instrument application diagram shown in Fig. 1.31 for the helium supply, impurities injection, and purification systems was completed.

The investigation of gas analyzers that are suitable for the measurement of trace quantities of H_2, N_2, CH_4, CO, and CO_2 in the CFTL circulating helium gas was completed. The low levels of the impurities (a few parts per million as shown in Table 1.10) dictated the selection

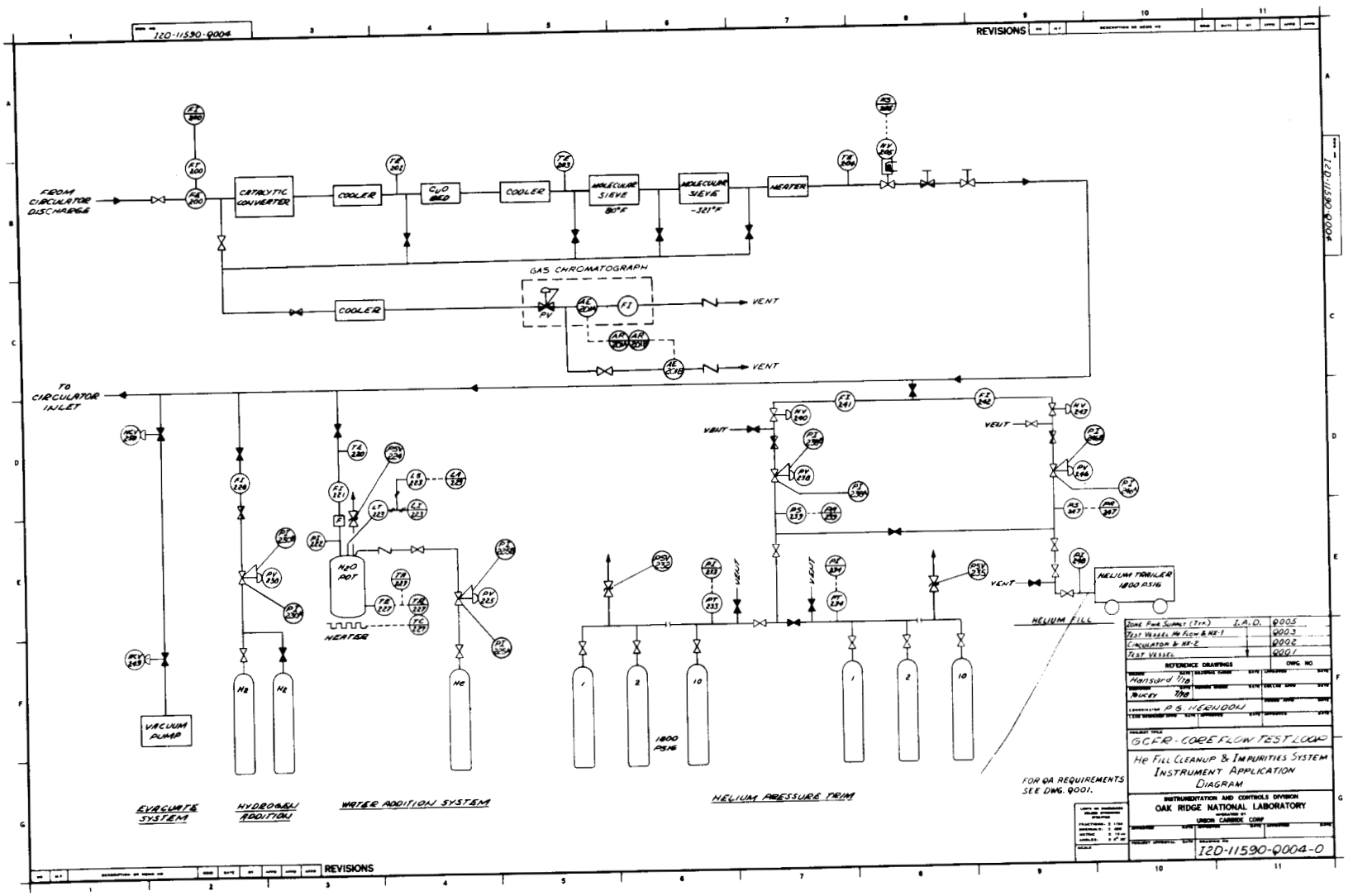

Fig. 1.31. Instrumentation Diagram for Core Flow Test Loop Helium Supply and Purification Systems.

Table 1.10. CFTL Helium Analysis

Component	Purified levels (ppm)	Maximum loop operating levels (ppm)	Instrument range (ppm)
H_2	3	960	0-10, 0-100, 0-1000
O_2	<1	2.3	0-5
N_2	<1	12	0-10, 0-20
CH_4	<1	2.3	0-5
CO	3	12	0-20
CO_2	<1	1.2	0-5
H_2O	<1	96	0-10, 0-100, 0-1000
Ne	23	23	No measurement
Ar	10 (assumed)		No measurement
Miscellaneous hydrocarbons	<1 (assumed)		No measurement

of a chromatograph utilizing a helium ionization detector with specially jacketed components to prevent atmospheric contamination. A specification incorporating these features was completed. The specified chromatograph requires manual selection of the sample point but will give three to four complete analyses per hour of the selected point, will present integrated values in bar graph form, and will have a data acquisition system interface capability.

Water vapor is also an important contaminant component, and measuring it on a chromatograph dedicated to permanent gas analysis is usually impractical. Therefore, a separate Keidel electrolytic hygrometer will be used in parallel with the gas chromatograph to provide a continuous analysis of moisture level. A specification for this instrument was also completed.

1.3.4.10 Control Interlocks — S. J. Ball, P. G. Herndon, A. D. McNutt, and C. I. Rose

During 1978 the requirements for detecting potentially unsafe operating conditions were more fully identified, and safe shutdown procedures to protect the test bundle and the loop from damage were outlined. We emphasize that the precise definition of what constitutes an unsafe operating condition and the precise actions to be taken when such conditions are detected will be further studied and refined as the system design proceeds. However, an automatic system capable of protecting the test bundle and loop from damage by anticipated casualty events will be installed prior to CFTL operation. We will provide sufficient measurement hardware to detect problems and sufficiently sophisticated control hardware to provide operating sequences that will bring the test bundle and loop to a safe shutdown to protect them from undesirable operating conditions.

The conditions requiring safety shutdowns may be broadly classified into three categories: (1) operating conditions that may lead directly to equipment damage, such as high-pressure boundary temperature or high or low values of helium flow; (2) equipment malfunctions that may cause the equipment to damage itself and/or indirectly damage other equipment by causing system conditions to exceed limits (examples of events in this category are control valve failure and failure of the FRS power supplies); and (3) measurement and control system malfunctions that may result in a failure to detect events in the first or second category or that, through misoperation, actually cause these events.

Two basic shutdown procedures have been outlined to deal with the events in the above three categories. The goal of both procedures is to bring operation to an expeditious halt without imposing transients on the test bundle more severe than those encountered under the specified test conditions. The first procedure, designated scram A, consists of a controlled reduction in bundle power and flow that is similar to a fast test transient. This procedure would be invoked on detection of events in the first category and for selected events in the second and third categories. Scram A is based on the assumption that, although some test conditions may be out of limits or certain equipment may be

operating abnormally, all key system conditions are still controllable, and the time and the means to achieve an orderly return to a safe condition are still available.

For most events in the second and third categories or on the failure of scram A to perform as expected, it must be assumed that we no longer have full control of the loop. In such a case, a second shutdown procedure, designated scram B, will be invoked, which consists essentially of cutting off power and control signals to all components and allowing them to move to predetermined fail-safe states. Bundle power and circulator power will be cut off, the test section valve will fail closed to avoid quenching the test section, and the attemperator and bypass flow control valves will fail open to provide a path for the circulator coastdown flow. Heat-exchanger blower power will be cut, and heat-exchanger vanes and dampers will fail closed to prevent overcooling.

1.3.4.11 Data Acquisition System — K. J. Cross

The design review for the CFTL DAS was completed in August 1978. Questions concerning specifics of the DAS design were answered to the satisfaction of the members of the design review team.

Approvals required to initiate procurement of the DAS equipment were obtained, and all major components of the system are ordered or have been delivered, with the exception of one item that is discussed below. Three operator terminals, memory expansion units, and the electrostatic printer/plotter are undergoing acceptance tests.

The remaining major piece of equipment is the analog input subsystem (AIS), which includes multiplexers for 640 analog channels and interface to the PDP-11 computer. The original DAS design was based on the AIS used in a similar existing data system. That AIS is no longer available, and negotiations are currently being made with various manufacturers to supply equipment that will meet the requirements of the CFTL.

1.3.4.12 Evaluation of X-Ray Imaging Equipment — S. P. Baker, J. E. Batey, and K. K. Klindt

An evaluation of x-ray imaging for measuring the bowing of test bundle duct and FRSs and the axial motion of FRSs during transient operation was completed. Both film radiography and real-time image intensifiers were evaluated. The draft of a report covering all evaluation work done to date was prepared and is being reviewed internally.[23]

The report recommends that x-ray imaging be used because it is a useful, practical tool for making the needed structural measurements. For transients that last 10 min or longer and for all steady-state tests, film radiography is recommended as the imaging medium with an expected resolution in FRS movement of 0.125 mm (0.005 in.) or better. For all transients of less than 10 min, image-intensifier systems are recommended. With certain restrictions, all the FRSs in a 91-rod test bundle, except for possibly the center rod, can be imaged with an integration time of less than 8 TV frames (8/30 s) with an expected resolution of better than 0.25 mm.

For this evaluation a simulated 91-rod fuel test bundle, complete with a thermal shield and a 12-mm-thick test vessel, was fabricated. Platinum markers 0.5 mm in diameter were placed on selected rods that could be bowed by calibrated amounts. Table 1.11 lists the results of a film radiography test in which two rods were bowed in various amounts. A radiograph was made of the unbowed configuration and then of each bowed configuration. Microdensitometer tracings were made of the area of bowing in each radiograph. From a datum, differential position measurements of the platinum marker on the bowed rods were made and then corrected for magnification. These results demonstrate the potential of the use of film radiography in this application to give accurate results. Future experiments of this type will be performed next year for both film radiography and an image intensifier.

Table 1.11. Rod bowing

Calibrated rod bowing (mm)	Measured rod bowing (mm)	Difference (%)
0.13	0.13	0
0.25	0.26	+4
0.47	0.45	-4

1.3.5 Loop Schedules and Cost Estimating — H. L. Mitchell

The E-Z PERT schedules and work breakdown structure (WBS) were revised to reflect funding authorization and to show the progress that was made in the design and construction of the CFTL loop. In addition, the schedules and the WBS have been revised for FY 1979.

A new Title I cost estimate, based on nearly complete Title I design, was issued in August 1978.

1.3.6 Loop Procurement Activities — W. R. Huntley

A procurement schedule and status report was established to aid in coordinating (1) procurement, (2) storage of procured material, and (3) equipment retrieval for installation in the CFTL. The procurement report is segmented according to the six major categories of the WBS, that is, electrical power system, heat-removal system, helium system, test vessel, building facilities, and instrumentation and controls systems.

Procurement for the CFTL is in the early stages when long delivery items are of primary interest. Currently, we have requisitioned more than $1 million worth of equipment (Table 1.12), which represents about one-fourth of the total procurement costs for the Stage 1 CFTL.

Table 1.12. CFTL Material That Has Been Ordered for Loop Construction

Electrical
Primary power transformers and switchgear
Cable, 500 ft, 350 MCM
Current transformers, ground detectors, and silicon controlled rectifiers
One zone of test bundle power supply for test and evaluation
Instrumentation and controls
Thermocouple and signal wire
Circulator speed detectors
Data acquisition system
Mechanical
Circulator pressure vessels and stators, 2 each
Tube and header material for HX-1 and HX-2
Air blowers and dampers for HX-1 and HX-2
Primary helium pipe and fittings (2-, 4-, and 6-in., schedule 80)

1.4 TEST BUNDLE DESIGN AND DEVELOPMENT — C. W. Collins and H. C. Young

1.4.1 Test Bundle Design — J. A. Seneker

1.4.1.1 Bundle Concept Design Study

The design study of the traditional or "pressurized" test bundle concept was completed. In the pressurized concept the test bundle tube sheet not only maintains the proper pitch configuration among all the FRSs but is part of the vessel pressure boundary. Only the external surface of the FRS cladding sustains the helium gas pressure inasmuch as the interior of the FRS is connected to atmospheric pressure at its entrant end.

In addition, a substantial effort was devoted during 1978 to a study of an alternative "pressure-equalized" concept for test bundle design. The pressure-equalized concept relieves the test bundle tube sheet from the vessel pressure boundary function of the pressurized concept. Also in the pressure-equalized concept, the helium gas pressure across the FRS cladding is equalized because both sides of the FRS cladding are exposed to a high-pressure environment. During the study the

impact of changing the FRS pitch from 11.2 to 9.8 mm (0.440 to 0.386 in.) was investigated for both the pressurized and the pressure-equalized concepts.

Two versions of the pressurized test bundle concept were considered. In the first the FRSs, upstream of the 9.8-mm (0.386-in.) pitch in the test section and internal to the tube sheet, are splayed to a larger pitch before penetrating the sheet. In the other, the 9.8-mm (0.386-in.) test section pitch for the FRSs is maintained through penetration of the tube sheet, and the splaying of the FRS terminals to a larger pitch takes place outside the tube sheet. The splaying helps to make somewhat easier the attachment of the power leads to the FRS leads.

The internal splayed design (Fig. 1.32) was eliminated because the structure at the upper end of the bundle differs significantly from that of

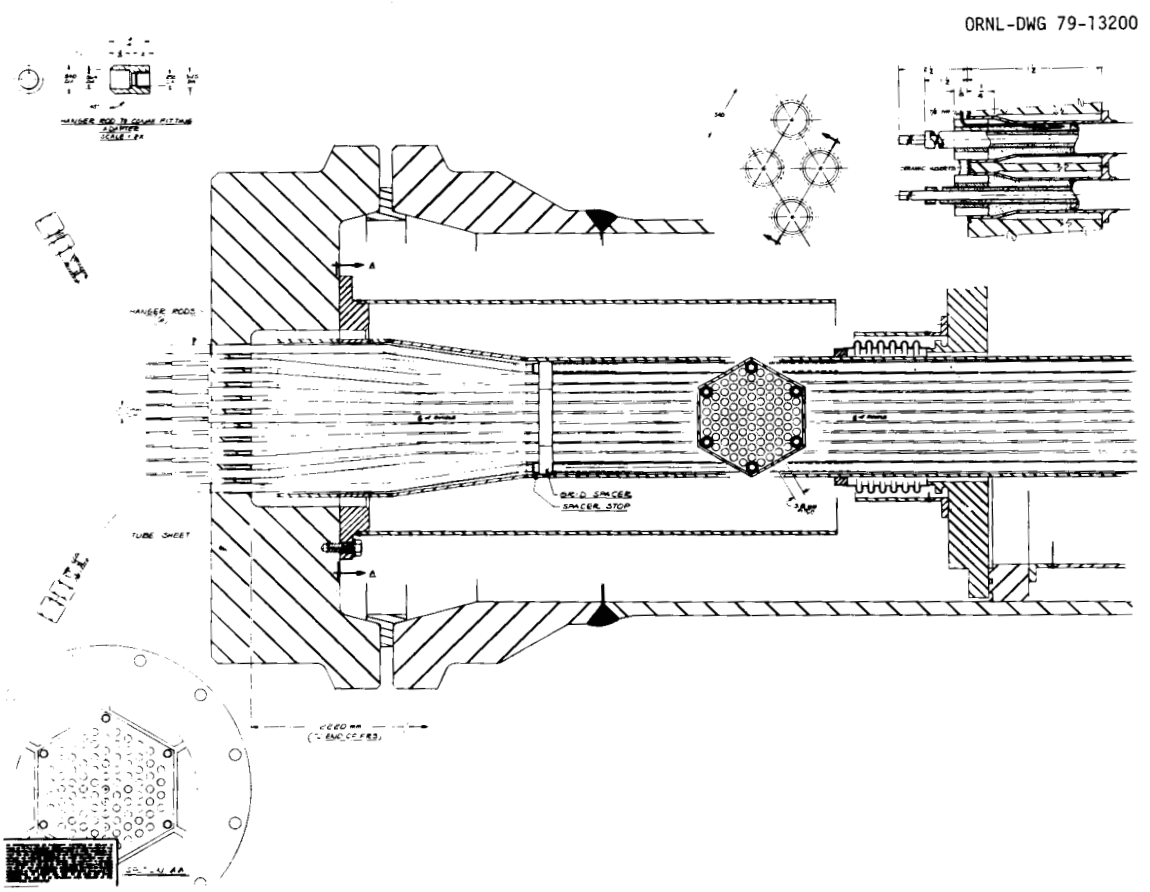

Fig. 1.32. Traditional Core Flow Test Loop Pressurized Bundle Design. The tube sheet and the exterior surface of the fuel rod simulator cladding are pressurized; the fuel rod simulators are splayed inside the test vessel.

the GCFR fuel assembly and because replacement of an FRS after joining the FRSs to the tube sheet is started is impracticable. The external splayed design (Fig. 1.33) is the accepted design to represent the pressurized test bundle concept.

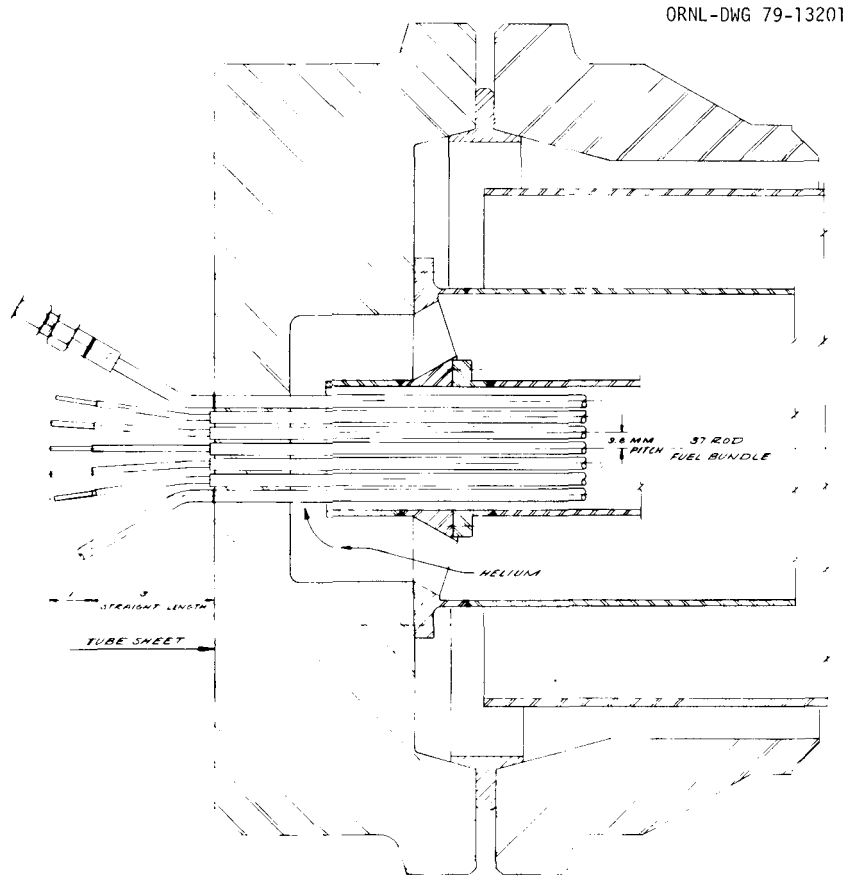

Fig. 1.33. Traditional Core Flow Test Loop Pressurized Bundle Design with the Fuel Rod Simulators Splayed External to the Test Vessel.

Two versions of the pressure-equalized concept were considered in the study. Both versions use a double-chamber test vessel in which the upper chamber above the tube sheet contains gas at controlled high pressure to balance the pressure across the tube sheet and the FRS cladding. The FRS power leads are located in the upper chamber, and each lead wire penetrates through the chamber wall. Nitrogen is the

gas in the upper chamber in the design shown in Fig. 1.34; helium is the gas in the other design (Fig. 1.35). Subsequent testing with a prototypic FRS in helium indicated a voltage-breakdown between the cladding and the annular terminal lead, which causes arcing to occur at voltage levels needed for the operation of CFTL test bundles. However, the level of breakdown voltage with the use of nitrogen was found by test to be sufficiently high that it is prudent to use nitrogen for the pressure-equalized concept.

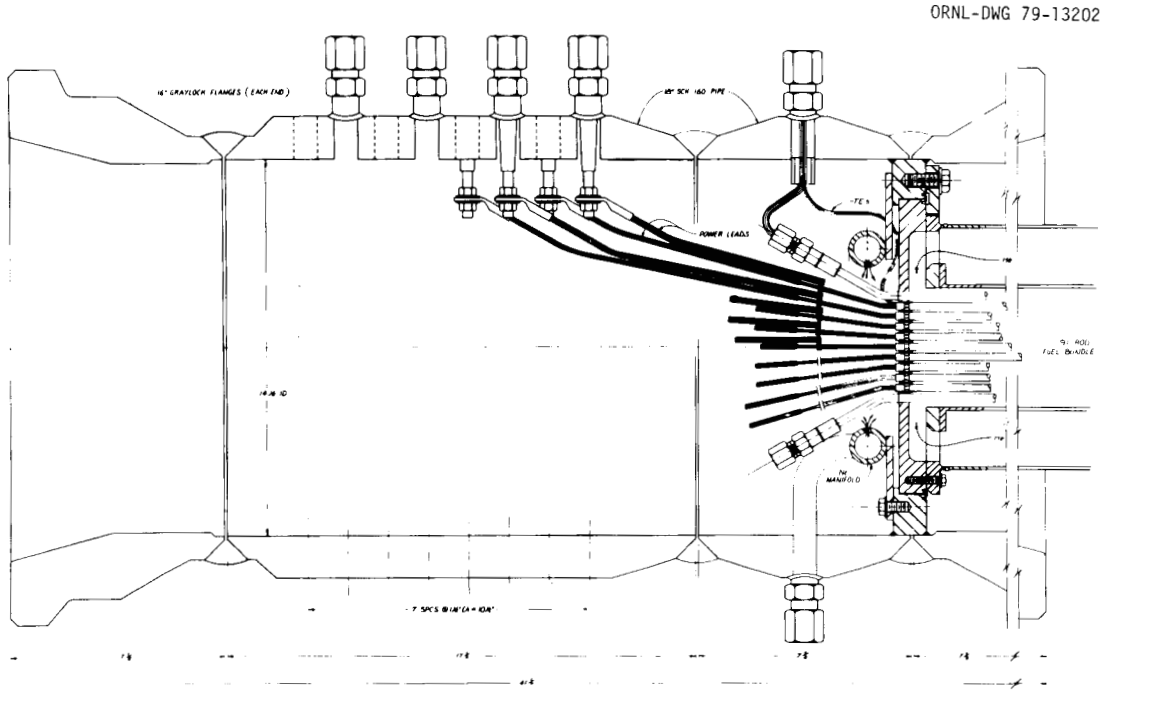

Fig. 1.34. Core Flow Test Loop Pressure-Equalized Bundle Design. Helium is applied to one side of the tube sheet and to the exterior surface of the fuel rod simulators, and nitrogen is applied to the other side of the tube sheet and to the interior surface of the fuel rod simulators.

The design that uses nitrogen gas in the upper chamber (Fig. 1.34) is therefore the most favorable for a CFTL test bundle in the pressure-equalized concept.

Additional details and a discussion of the study are presented elsewhere.[24] After much consideration, we determined that the pressurized

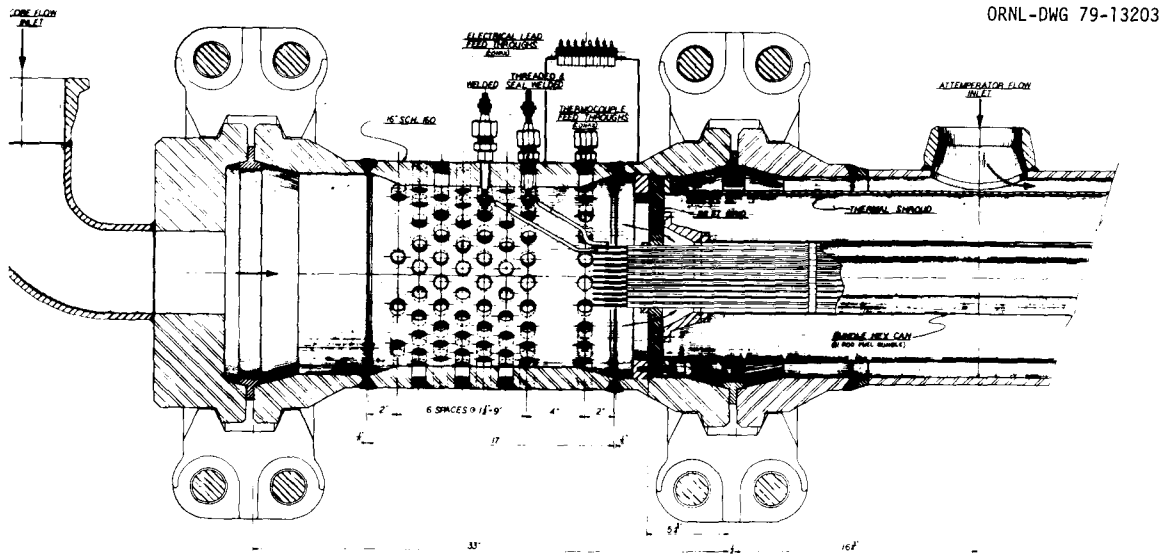

Fig. 1.35. Core Flow Test Loop Pressure-Equalized Bundle Design. Helium is applied to both sides of the tube sheet and the fuel rod simulators.

design shown in Fig. 1.33 would remain the concept for the first fuel test bundle; if the FRS pitch remains at 11.2 mm (0.44 in.), the splaying of FRS terminals above the tube sheet will be eliminated.

1.4.1.2 Thermomechanical Design

Following the design studies, we conducted an extensive thermal and stress analysis of the test bundle tube sheet to determine temperature and stress levels that would exist in the thinned and perforated tube sheet when subjected to design pressure and temperature conditions and heating from FRS power leads. Figure 1.36 shows the model used to perform the thermal analysis by the HEATING 5 code. We conducted a study by changing the radii of the annular rings to simulate change in FRS pitch, by removing the outermost rings to simulate the 61- and 37-rod fuel test bundles, and by changing the heat generated in the rings to simulate change in rod power levels. Results of the thermal analysis as well as the model shown in Fig. 1.37 were used to conduct a finite-element stress analysis by the FEATS code. The center portion

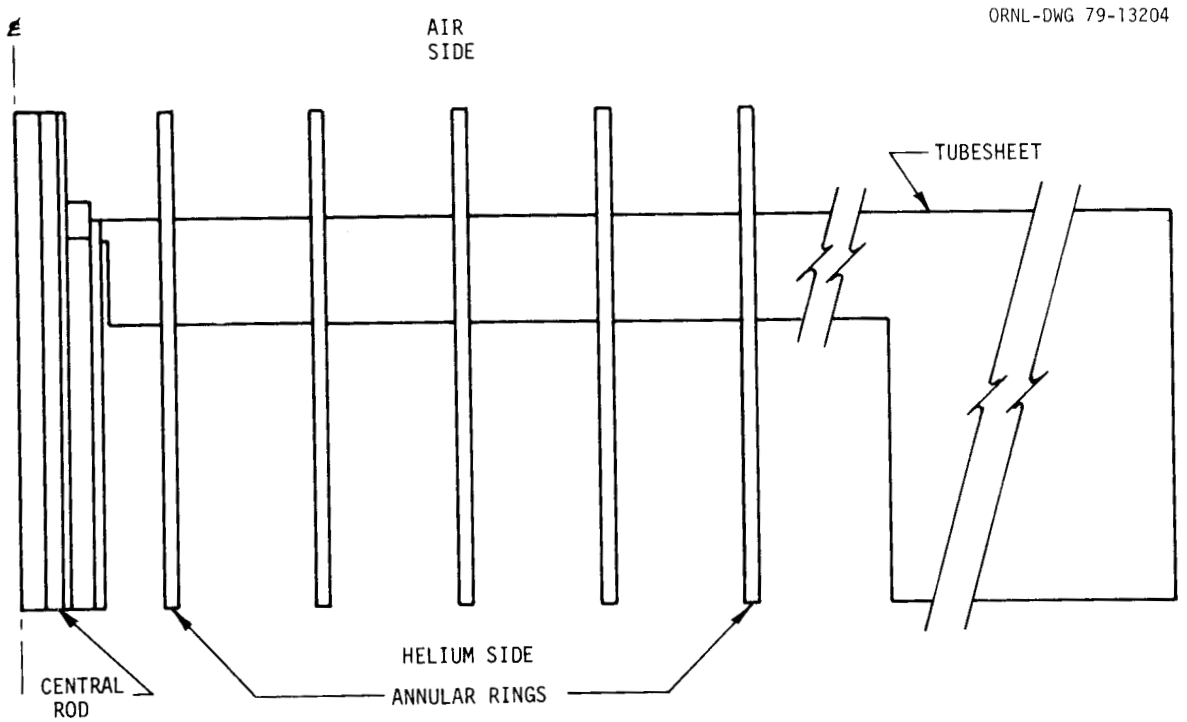

Fig. 1.36. Thermal Analysis Model of the Tube Sheet and the Fuel Rod Simulators for Core Flow Test Loop Test Bundle.

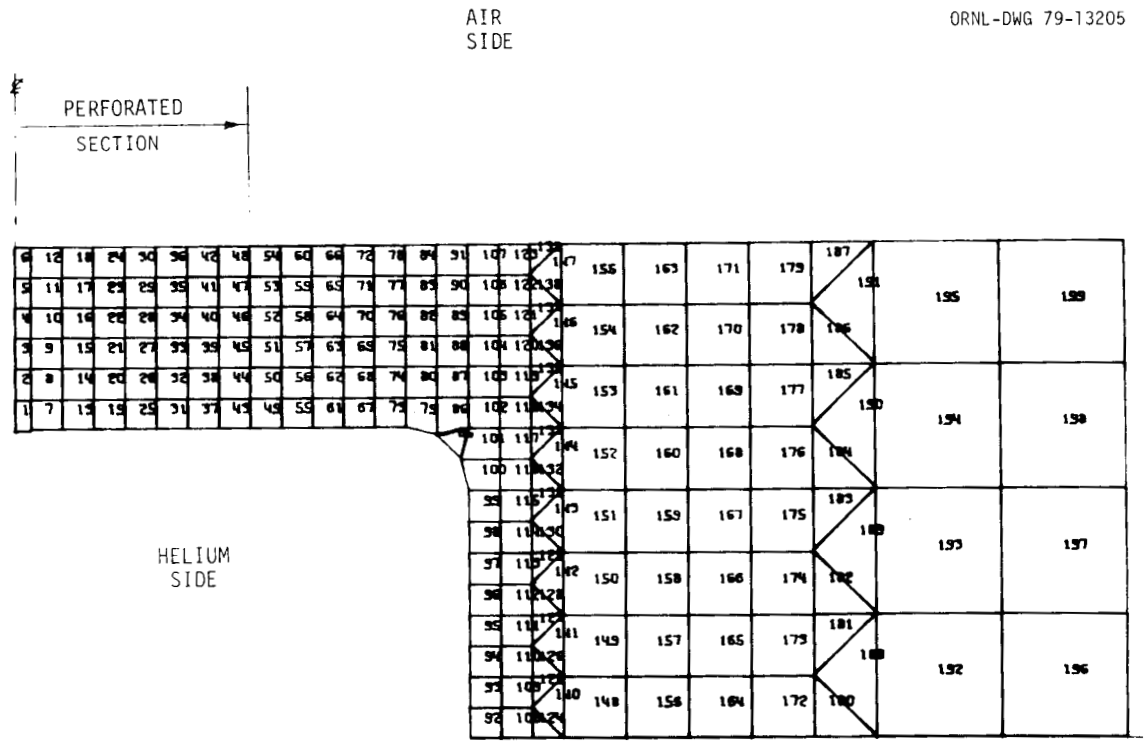

Fig. 1.37. Thermal Stress Analysis Model of the Tube Sheet and the Fuel Rod Simulators for Core Flow Test Loop Test Bundle.

of the tube sheet, which has reduced thickness and is perforated to accommodate the FRSs, is simulated by lowering the material constants for those elements in the perforated region.

Results of these analyses indicate that, for all cases studied, the temperatures in the tube sheet are below design temperatures and that stresses are lower than maxima allowed. It was therefore determined that the reference pressurized bundle design was acceptable for all fuel test bundles. Details of the analyses are presented elsewhere.[25]

In addition to the tube-sheet analyses, several drawings of the test bundle design were completed. Layouts of the fuel, control rod, and blanket bundles as installed in the test vessel were completed, which show clearances and space for inlet plenum flow baffles. We prepared several designs of the seal between the main and attemperator flows and of modifications to the hexagonal duct to accommodate the seal. Concepts were completed of the attachment of the duct to the tube sheet, of the design of the instrument feed-throughs, and of the attachment of hanger rods to the tube sheet. The design layouts of the FRS electrical and thermocouple disconnect panel and the FRS terminal cooling system were prepared. These layouts and concepts are currently being studied from the viewpoint of fabrication and assembly.

1.4.1.3 Instrumentation

Progress was made in determining what instrumentation will be included in the first test bundle. Instruments for other bundles have not yet been agreed on. The first test bundle will contain TCs in the FRSs, on selected grid spacers as practical, and on the hexagonal duct; x-ray imaging markers in the FRSs; pressure taps on the hexagonal duct; microphones; and accelerometers. Strain gages will not be installed in the corner hanger rods of the first test bundle.

Location of the FRS thermocouples was finalized, design and development was completed, and procurement of thermocouples for the first test bundle was initiated. Thermocouple locations on grid spacers

were determined, but techniques for attaching and routing the TCs have not been developed. Location of TCs on the hexagonal duct was also completed.

Locations of pressure taps on the hexagonal duct to measure pressure losses within the bundle have been completed, but methods of attaching ports to the duct have not been finalized. We have determined that no development effort will be expended on microphones and accelerometers and that the instruments that will be installed in the first bundle will be off-the-shelf components. Exact locations and method of attachment of these items have not been finalized.

1.4.2 Development in Support of Test Bundle Design — H. C. Young

The evolutionary approach that was adopted for the CFTL loop in late 1978 was extended to cover the test bundles. The practical effect is that the obtaining of information on FRS thermal ratchetting, the deflection of the tube sheet at design conditions, the cooling of FRS electrical leads and connectors, and the leakage behavior of the Grayloc flange joint at the tube sheet will be deferred until the operation of the first CFTL test bundle.

However, we will continue some bundle development tests to provide input for design decisions and to verify design. These tests include sufficient work on the FRS cladding-to-tube-sheet joint to permit a selection between the electron beam (EB) and the gas tungsten arc (GTA) welding processes and also to determine whether or not joints can be made for an FRS pitch as small as 9.8 mm (0.386 in.). Methods for joining the electrical connectors to the FRS electrical terminals and to the power supply leads must be proved. A method for bending or splaying the electrical connectors and the bundle assembly techniques must be developed. Development of the FRS and limited work on small-diameter TCs and other bundle instrumentation are continuing.

1.4.2.1 Fuel Rod Simulator Cladding-to-Tube-Sheet Joint — H. C. Young and T. B. Conley

Six capsules[26] were pressure cycled from 11.7 to 0.10 MPa (1700 to 50 psig) and temperature cycled from 371 to 93°C (700 to 200°F) for a total of 500 cycles to evaluate test weld joints between the cladding of dummy FRSs and a simulated tube sheet. Each capsule has seven dummy rods on an 11.2-mm (0.440-in.) pitch that are joined to a simulated tube sheet as shown in Fig. 1.38. All capsule weld joint components are made from appropriate austenitic stainless steel materials. The test rig having the six test capsules installed is shown in Fig. 1.39.

In two of these test capsules, the seven weld joints were made with the EB welding process; in the other four, the joints were made with the GTA welding process. The weld joints were leak-tested after each 50 test cycles and after 500 test cycles by use of a helium mass spectrometer leak detector that had a sensitivity of 2×10^{-11} std cm^3/s; no leaks were detected.

A test cycle consisted in heating the test capsule to 371°C (700°F), holding at this temperature for about 1 h, cooling to 93°C (200°F) in about 40 min, and repeating the temperature cycle. Simultaneously, the gas pressure is raised from 0.1 to 11.7 MPa (0 to 1700 psig) at the start of the first test cycle and maintained at this pressure except at the midpoint of each temperature hold period at 371°C (700°F). At this point the gas pressure is momentarily reduced to 0.34 MPa (50 psig) and returned to 11.7 MPa (1700 psig).

It is necessary to store the FRS TC extensions on the FRS terminals as shown in Fig. 1.38 to protect them from heat damage during the welding process. Sections about 355 mm (14 in.) long of each of the four small-diameter FRS TCs were stored satisfactorily. It was necessary to install a quartz sleeve over the TCs during the GTA welding process to avoid burning through the TC sheaths.

Tests were conducted to determine the histogram of the temperature imposed on the TC sheath adjacent to the weld arc during joint welding. With the quartz sleeve in place, the maximum temperature measured was 365°C (690°F), which should not result in decalibration of the TCs.

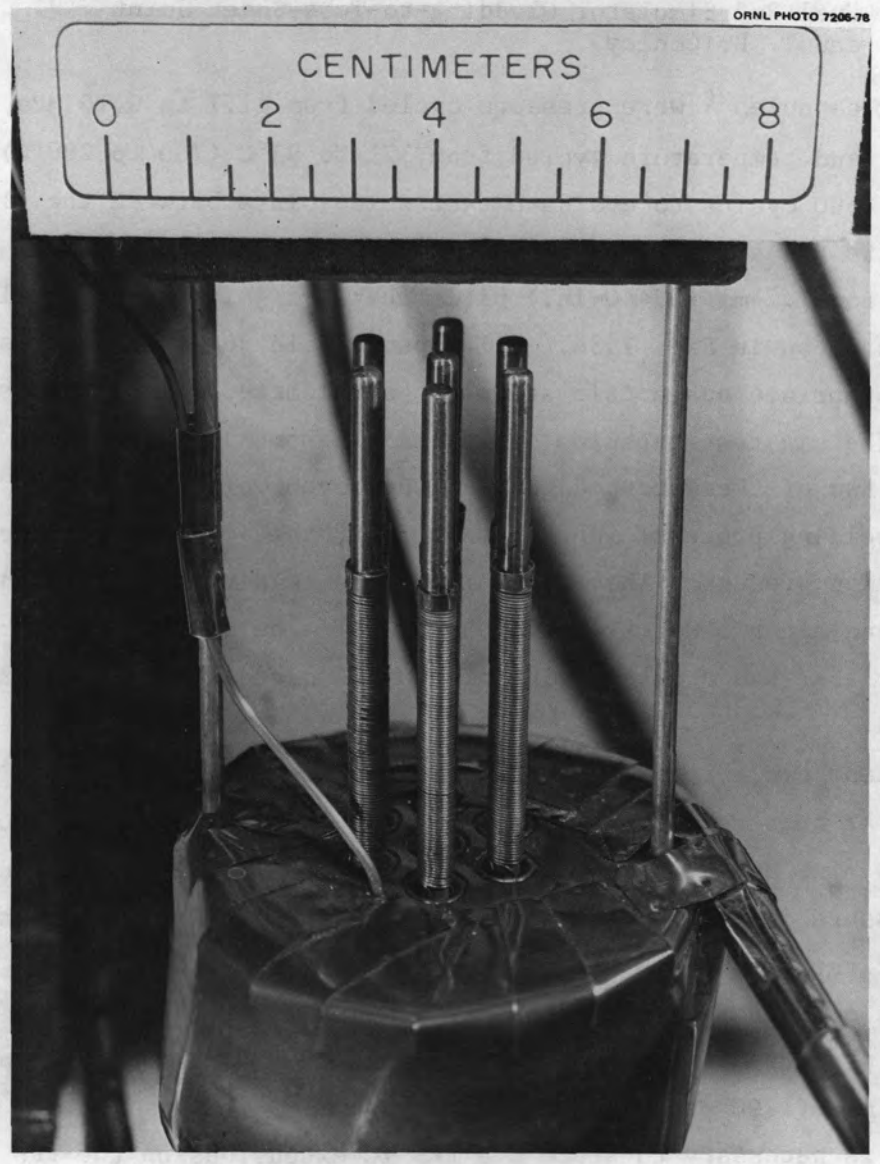

Fig. 1.38. Capsule for Testing Welded Joints Between the Fuel Rod Simulator Cladding and the Tube Sheet of Core Flow Test Loop Test Bundle. Capsule consists of a simulated tube sheet and seven dummy fuel rod simulators, each with four thermocouple extensions wrapped for storage during welding on the power terminals.

Because we believe that the GTA weld process will generate higher local temperature than will the EB process, we did not repeat the test for the EB process.

Another test was conducted to determine if the TC materials, particularly the somewhat brittle Alumel, would survive being wrapped

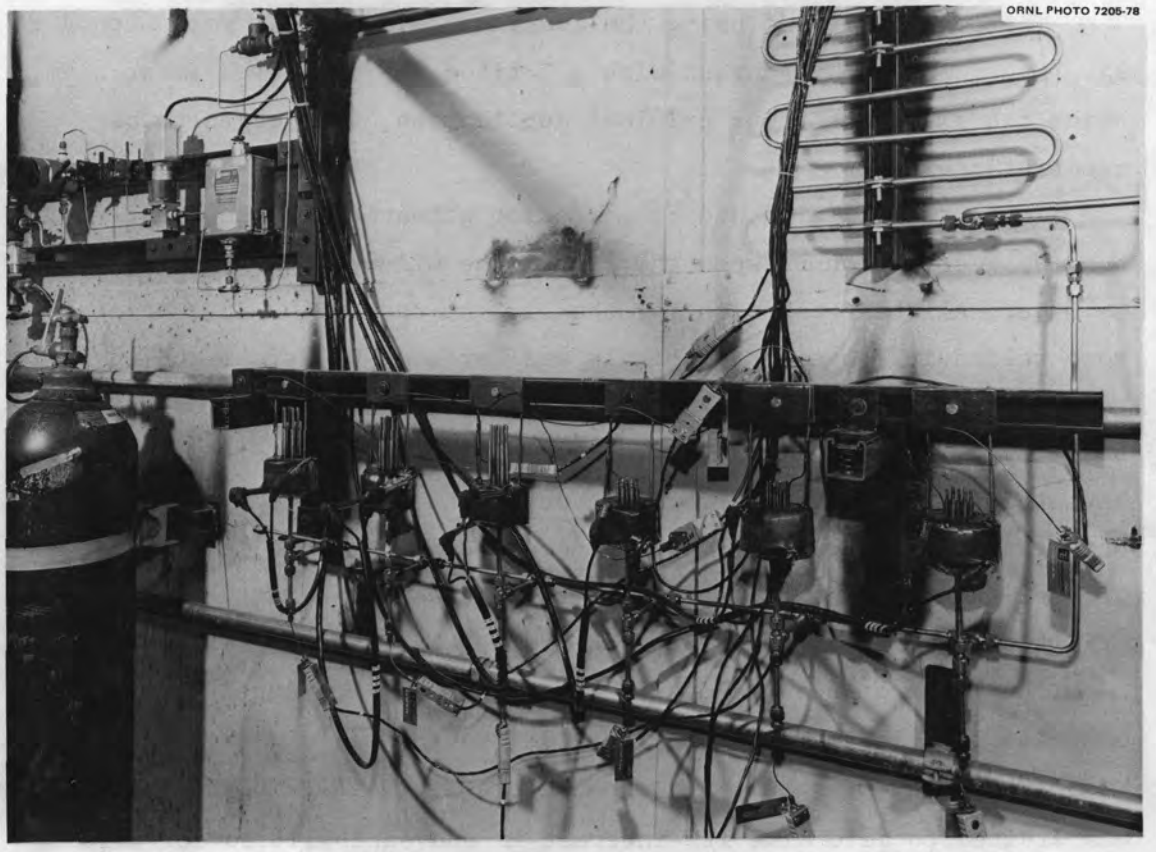

Fig. 1.39. Core Flow Test Loop Bundle Test Stand Setup. Welded joints between cladding and tube sheet are subjected to pressure and temperature cycles. Setup permits cycling six capsules simultaneously.

around the FRS terminal and unwrapped after the joint welds were made. Several lengths of prototypic Inconel-sheathed TC material were wrapped around a metal rod of appropriate diameter and unwrapped for a total of three wrap and unwrap cycles. The wire-to-wire and wire-to-sheath resistance was measured, and the Inconel sheath was inspected with dye penetrant after each wrapping cycle; no evidence of deterioration of the TC material was found.

All capsules tested to date have the reference FRS pitch distance of 11.2 mm (0.440 in.); however, GA has stated that the FRS pitch after the first fuel bundle may have a value in the range of 11.2 to 9.8 mm (0.440 to 0.386 in.). Therefore, four more capsules are being fabricated to compare the EB and GTA welding methods for the 9.8-mm (0.386-in.) spacing.

The possibility of using the continuous-laser-beam weld method to make the joint was discussed with a California firm. The laser beam, being too diffuse for our critical application, was judged to be unsatisfactory.

To meet the design and construction schedule for the first test bundle, a selection between the EB and the GTA welding processes must be made. All test capsules for the 11.2-mm-rod (0.440-in.) spacing were welded in house by the Metals and Ceramics Division, and we expect that it can weld the test capsules for the 9.8-mm-rod spacing by both the EB and GTA methods. However, Metals and Ceramics does not have the facilities to perform production EB welding for a CFTL test bundle configuration, nor does it have the manpower to devote to the production welding of the cladding-to-tube-sheet joints in the actual CFTL test bundles by either the EB or the GTA process.

The Electron Beam Welding Company (EBW) in Los Angeles, which has made the cladding-to-tube-sheet joints for all the Breeder Reactor Program-Thermal Hydraulic Out-of-Reactor Safety (BRP-THORS) test bundles, was visited to determine its interest in and capabilities for welding the CFTL bundles. The CFTL bundle is much longer and heavier than the THORS bundle and exceeds the size and weight limitations of the EBW vacuum chamber and work tables. Costs to modify the EBW vacuum chamber and to pay for the downtime during the modification period were considered prohibitive. The EBW determined that Chemtronics in San Diego has a vacuum chamber that is large enough and heavy-duty work tables that are adequate to handle the CFTL bundle. Chemtronics personnel stated that they would be willing to rent this facility to EBW. Thus, it appears feasible to have EBW personnel, with their substantial experience and know-how, EB weld the CFTL bundles by using the Chemtronics facility.

1.4.2.2 Connecting FRS Terminals to Power-Supply Leads — H. C. Young and T. B. Conley

A necessary task to be accomplished during the installation of a bundle into the CFTL is connecting the FRS terminals to the power-supply system leads. Early in FRS design the two terminals were made of molybdenum and consisted of a 2.15-mm-diam (0.085-in.) solid wire

center terminal concentric with a 4.2-mm (0.165-in.) tubular terminal having a 0.25-mm (0.010-in.) wall thickness. These two terminals were to be connected to the power supply leads, 5.2-mm-diam (0.204-in.) copper wire. A commercially available spring-loaded connector had been tested earlier and failed because of the high heat generation in the connector. In addition, the use of a Nitinol[27] compression ring to clamp a connector to a terminal had been considered but appeared to be feasible for the center terminal only. Calculations indicated that the heat generation in the molybdenum at a rated current of 150 A produced excessively high temperatures in the tube sheet and FRS terminals. Therefore, the terminals will be made of copper, which will reduce the heat generation substantially. Although brazing is considered to be the best method for copper terminals, leads, and connector, it was not actively pursued until late in 1978, when the start of Title II design of the first bundle refocused our efforts on the connector problem.

Two brazing methods are being evaluated, and both methods require the use of a fluxless braze because of the difficulty of removing excess flux in the restricted space available. The more sophisticated method is to use the same precision head that is needed to make the cladding-to-tube-sheet weld by the GTA process for brazing the tubular terminal to its lead and then brazing the center (solid-rod) terminal with a hand-held GTA torch. The second brazing method is to use a hand-held gas torch and Sil-Fos, a fluxless braze material, to make both joints.

A number of individual connectors have been brazed with a gas torch. The braze joints are being checked for resistance, voltage drop, and temperature rise by passing the design current of 150 A through the connector. If the torch-brazed joint proves acceptable, a test bundle mockup that consists of 12 dummy rods mounted in a 60° segment of a dummy tube sheet and that provides all the space constraints encountered in a 37-rod test bundle will be fabricated. After brazing, the joints will be evaluated with a design current test. The gas-torch braze and the GTA methods will be evaluated for both 11.2- and 9.8-mm (0.440- and 0.386-in.) FRS pitches.

For the 9.8-mm (0.386-in.) pitch, it is necessary to bend or splay the FRS terminals to provide space for connectors. Thus, the terminals will extend farther above the tube sheet, which, in turn, will complicate welding the cladding-to-tube-sheet joints.

1.4.2.3 Fuel Rod Simulators for CFTL Test Bundles — R. W. McCulloch

This section delineates the progress made during 1978 toward the development of a reliable, high-temperature, high-heat-flux FRS for use in CFTL test bundles. The cladding of the FRS (Fig. 1.40) is to be of prototypic GCFR fuel rod cladding material and is to have the same dimensions, configuration, and thermal characteristics as the GCFR fuel rod cladding.

ORNL-DWG 78-10905

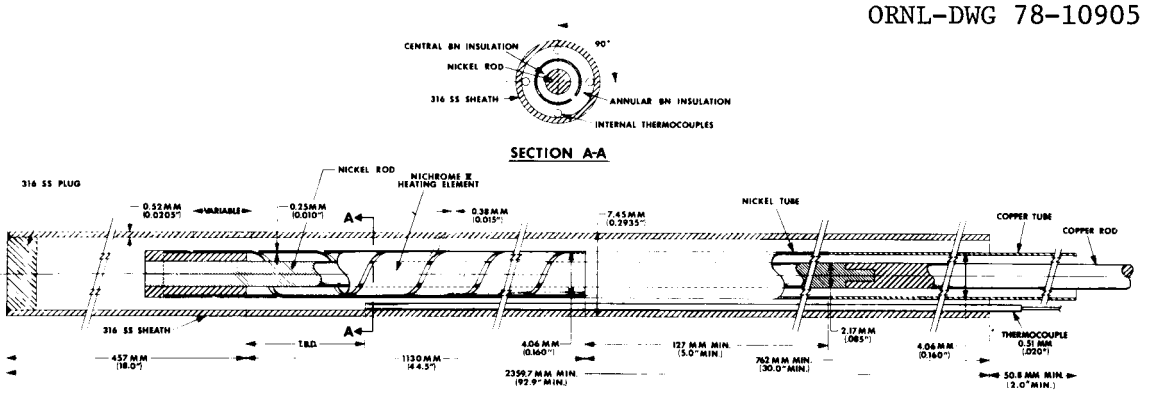

Fig. 1.40. Cross-Section Drawing of Core Flow Test Loop Fuel Rod Simulator.

The reference FRS is reentrant in design; that is, both power terminals enter at a single end. A copper tubular terminal joined to a tubular nickel lead is, in turn, joined to the variable-width Nichrome V heating element, which is designed to provide a cosine heat-flux distribution that has a maximum-to-average heat-flux ratio of 1.21. The center terminal is made of a solid copper rod and is joined to a nickel lead, which, in turn, is joined through an adapter to the heating element to form the electric-current-carrying circuit in the FRS. Cold-pressed BN preforms provide electrical insulation between (1) the cladding and the heating element and its associated tubular lead and

terminal (outer annulus) and (2) the heating element and the center lead and terminal (inner annulus). The BN preforms also provide thermal conduction between the cladding and the heating element. Four small-diameter type K TCs that have 0.5-mm (0.02-in.) Inconel sheaths and ungrounded junctions are installed inside the FRS cladding. The sheaths of the TCs, which are attached at the axial location of the junction to the inside surface of the cladding, run longitudinally along the inside surface and are located equidistantly around the perimeter of an FRS cross section.

The total length of the FRS is 2258 mm (88.9 in.), including a heated length of 1130 mm (44.5 in.).

The FRS will be designed to operate at power levels up to a 45-kW maximum and will provide a heat flux of 1.7 MW/m^2 (540,000 Btu h^{-1} ft^{-2}) at a maximum cladding temperature of 1000°C (1832°F) and a matching maximum heating-element temperature at 45 kW of 1300°C (2372°F). Higher cladding temperatures can be obtained at reduced values of rod power.

The operating conditions place stringent requirements on all materials used in the FRS. The heating element must operate at the maximum temperature without property degradation. The BN must maintain both high thermal conductivity and electrical resistivity at the maximum temperature; in addition, its properties must remain uniform axially and circumferentially to provide accurate simulation of the cosine heat flux. The FRS must also maintain its integrity while enduring thermal transient tests.

The FRS development program staff at ORNL has performed materials, fabrication, inspection, testing, and failure analysis tasks to prepare procedures that are satisfactory for the production of adequate CFTL FRSs.

During 1978 seven FRS prototypes were fabricated, and five were subjected to operational testing. Steady-state tests were run at high power and relatively high temperature (45 kW, 975°C) and at low-power-high-temperature (8 kW, 1200°C) conditions. The capability of the FRS to meet CFTL thermal transient requirements was firmly established, and the effects of thermal cycling on FRS operation were found to be negligible. During this time the reference FRS design was changed from

swaged to nonswaged, the first prototypes with variable-width elements were operated, and evaluation of a proposed design change on heating-element material from Nichrome V to Kanthal A1 alloy was initiated.

We found, however, that the FRS internal TCs were extremely susceptible to early failure from thermal cycling and that their lifetime was drastically shortened at operating temperatures of 1000°C (1832°F) and above. Thermocouple life was found to be increased (1) by maintaining a small (0.025-mm) grain size in the thermoelements and (2) by maintaining TC elongation below 3%, which can be achieved with a nonswaged, but not a swaged, FRS.

The design of the FRS is being optimized by fabricating and testing thermal conductivity cells. The problems of joining terminals to leads internally have been solved, and the first Kanthal variable-width heating elements have been fabricated. Progress has been made on increasing the purity and reducing metallic contamination in BN powder, and the quality and thermal properties of BN preforms have been further improved through development based on results of conductivity cell tests.

In summary, it has been demonstrated for the first time that the GCFR-CFTL FRS can be fabricated and will meet most major CFTL testing requirements. Further property optimization, operational testing, and fabrication of the FRSs for the first test bundle will take place in 1979.

1.4.2.3.1 Integrated Technology Development for Fuel Rod Simulator Fabrication. In response to the continued lack of progress in obtaining FRSs from industrial manufacturers which meet both programmatic operating requirements and schedules and ORNL quality assurance requirements, an integrated FRS technology development program was established. The program now supports the four FRS user programs at ORNL [GCFR-CFTL, the Blowdown Heat Transfer-Thermal-Hydraulic Test Facility (BDHT-THTF), the BRP-THORS, and the Multirod Burst Test (MRBT)]. The purpose of the program is to develop the needed FRS fabrication technology and processes for preparing detailed specifications for industrial manufacturers to use in the fabrication of an FRS that has been shown to meet all expected

program operational requirements. Accomplishment of this program purpose includes developing the fabrication techniques and processes, verifying that the inspections are adequate to control the processes, testing FRSs to verify that operational requirements are met, and fabricating sufficient FRSs to assemble one or more test bundles.

Prior to the establishment of this technology development program, the BN preform development and the FRS fabrication work were initiated under the sponsorship of the BRP-THORS program. Since establishment of the integrated program, FRS fabrication technology has been developed successfully for the MRBT program and is more than 80% complete for the BDHT program. We anticipate completing detailed fabrication procedures and specifications for the FRSs needed in THORS bundle 12 in FY 1979 and for the FRSs needed in the GCFR-CFTL early in FY 1980.

1.4.2.3.2 Swaged Fuel Rod Simulator Development. Table 1.13 summarizes the principal features and test results of the FRS prototypes and conductivity cells that were operated during 1978. The fabrication and operation of the swaged rods are discussed below.

Fuel rod simulator prototype GLR-L-7P contained a constant-width Nichrome V heating element, a nickel tubular terminal, and a nickel central rod and terminal. The stainless steel sheath contained four internal 0.5-mm (0.020-in.) type K Inconel sheath TCs. Fabrication was normal, and final infrared inspection indicated that the transient heat flux profile was close to the ±5% maximum tolerance. Concentricity was excellent (no eccentricity was measurable throughout the heated length), final BN density was about 90% of theoretical and very uniform, and all electrical checks were normal.

However, because the transient heat flux profile was expected to be more uniform than it was, the cause of the variations was investigated further. The investigation revealed variations in cladding thickness of 7 to 10%. When these variations were eliminated by calculation from the infrared scans that were made during core and cladding transient tests, the profile appeared to be markedly improved.

To accommodate a previous change by GA in the cladding thickness from 0.7 to 0.5 mm (0.028 to 0.020 in.), the wall thickness of our existing

Table 1.13. Summary of CFTL Fuel Rod Simulator and Conductivity Test Cell Fabrication

Serial No.	Heating element material	Tubular lead materials	Central rod materials	Instrumentation[a]	Tested	Remarks
GLR-L-7P	Nichrome V	Nickel	Nickel	Four 0.5-mm type K SDI TCs with Inconel 600 sheath; all IJ	Yes	Successfully fabricated; tested at 700-900°C for more than 1000 h; completed more than 1000 transients; ran to failure at 1250°C; TCs showed susceptibility to to transients and high temperature
GNR-L-8P	Nichrome V	Nickel	Nickel	None	No	First nonswaged rod prototype; fabricated for evaluation purposes
GR-L-9P	Nichrome V, variable width	Nickel-copper	Nickel-copper	Four 0.5-mm type K SDI TCs with Inconel sheath, all IJ	No	Nonswaged preforms caused excessive movement of heating element; TCs got crossed; terminal region was shortened to correct problem; postfabrication inspection normal, but length too short to test
GR-L-10P	Nichrome V, variable width	Nickel-copper	Nickel-copper	Four 0.5-mm type K SDI TCs with Inconel sheath; 3 IJ, 1 GJ	Yes	Encountered copper spalling of central rod during fabrication; rod failed prematurely during testing because of spalling; developed nondestructive elongation method of correcting spalling and testing Cu-Ni braze joint
GNR-L-11P	Nichrome V, variable width	Nickel-copper	Nickel-copper	Four 0.5-mm type K SDI TCs with Inconel sheath; all IJ	Yes	First successful nonswaged FRS; tested to destruction in Single-Rod Sodium Loop
GNR-L-12P	Nichrome V, variable width	Nickel-copper	Nickel-copper	Four 0.5-mm type K SDI TCs with Inconel sheath; all IJ	Yes	Repeat of 11P; all satisfactory, tested in Single-Rod Sodium Loop; first FRS to meet all normal CFTL requirements
GNT-L-13S	Nichrome V	Nickel-copper	None-Pt (type B) TC	Four 0.5-mm type K SDI TCs with Inconel sheath; all IJ	Yes	First conductivity cell tested in water-cooled test stand
GNT-L-14S	Nichrome V	Nickel-copper	None-Pt (type B) TC	Four 0.5-mm type K CSG TCs with Inconel sheath; 1 IJ, 3 MGJ	Yes	Tested in water-cooled test stand and in Single-Rod Sodium Loop; showed clearly high nonswaged thermal conductivity and its dependence on power and sheath temperature
GNK-L-15P	Kanthal Al	Nickel-copper	Molybdenum-copper	Four 0.5-mm type K CSG TCs with Inconel sheath; 2IJ, 1 MGJ, 1 BNBF IJ	No	First FRS with Kanthal heating element; Kanthal-tube weld failed during fabrication
GNK-L-16P	Kanthal Al	Nickel-copper	Nickel-copper	Four 0.5-mm type K CSG TCs with Inconel sheath, 1 GJ, 3 MGJ	Yes	Successfully fabricated; test in helium test stand to determine thermal cycling effect on Kanthal FRS tested satisfactorily; TCs survived more than 400 stringent transient cycles
GNT-L-17S	Kanthal Al	Nickel-copper	None-Pt (type B) TC	None	Yes	Tested in water-cooled test stand to obtain additional BN k vs temperature and power data
GNT-L-18S	Kanthal Al	Nickel-copper	None-Pt (type B) TC	None	Yes	Tested in water-cooled test stand to obtain additional BN k vs temperature and power data

[a] IJ = insulated junction, GJ = grounded junction, MGJ = modified grounded junction, BNBF = boron-nitride backfilled, SDI = Sensor Dynamics, Inc., CSG = C. S. Gordon.

cladding had been suitably reduced by centerless grinding. Radiographs of these tubes, made after the wall-thickness variation with GLR-L-7P was discovered, revealed that several tubes had very large variations in wall thickness, whereas others did not. The cladding used on prototype GLR-L-7P had been randomly selected from these tubes.

The GLR-L-7P was then installed in the helium test stand (HTS) to undergo long-term, steady-state testing, to evaluate the fast transient capability of CFTL (FRSs), and to observe the effects of thermal cycling, if any, on ratchetting of the FRS. The FRS was operated in the HTS for more than 1000 h at steady-state conditions and successfully completed about 1100 thermal transient cycles at various power and temperature levels. Tables 1.14 and 1.15 summarize these tests.

Steady-state operation, most of which was at 900°C (1650°F), was completed and showed no degradation of heating element or BN insulation properties. We anticipate that the first test bundle will be operated in the CFTL for a total of about 1000 h and at a maximum expected cladding temperature of 870°C (1600°F) for a fraction of that time. Thus, we feel that this test series demonstrated adequately the capability of the prototypic swaged rod to meet the steady-state operation requirements of the first bundle.

Thermal cycling of GLR-L-7P ranged from low-power, relatively slow transients of 1.5-min duration in the temperature range from 350 to 870°C (660 to 1600°F) to high-power, relatively fast transients of 6 to 15-s ramp times in the temperature range of 350 to 1000°C (660 to 1830°F). Although over one-half of the transients completed were relatively fast, the posttest electrical and infrared scan inspections showed no degradation of the power profile or of other FRS properties.

Length measurements indicated that the rod grew about 3 mm (0.120 in.), or about 0.2%. This growth, which is possibly but not necessarily caused by thermal ratchetting, had no adverse effect on rod properties.

However, the behavior of the four internal TCs indicated some problems. Two of the four failed before the 1000-h steady-state testing was completed, one at 263 h and one 426 h. Both TCs had junctions located 150 mm (6 in.) above the lower end of the heating element.

Table 1.14. Steady-State Operational Tests of GLR-L-7P

(Total steady-state operational hours = 1005)

Temperature [°C (°F)]	Duration (h)	Potential voltage (max)	Power (kW)
700 (1290)	234	141	2.09
800 (1470)	168	160	2.66
850 (1560)	23	177	3.29
900 (1650)	580	188	3.60

Table 1.15. Thermal Cycling Tests of GLR-L-7P

(Total thermal cycles = 1097)

Power	Rise time (s)	Hold time (min)	Fall time (min)	Temperature change (°C)	Number of thermal cycles
3.40	90	3.0	1.5	350–870	202
3.40	90	9.0	1.5	350–870	339
13	12	4.74 (3.4 kW)	1.5	350–870	241
13	15	1.0 (5.6 kW)	1.75	350–1000	105
18	9	1.1 (5.6 kW)	1.75	350–1000	107
27 av (38 max)	6	1.1 (5.6 kW)	1.75	350–1000	103

The two TCs that survived the 1000-h testing exhibited erratic behavior early. One failed at 114 and the other at 170 cycles in the first 202-cycle test series. Both regained continuity when the rod was cooled to room temperature. Posttest evaluation showed that the grains in the Alumel thermoelement had grown enough to span the entire 0.075-mm-diam (0.003-in.) element cross section. Thermal expansion differences in the Alumel and in the stainless steel cladding apparently stressed the elements causing boundary separation of the large grains.

Subsequent investigations revealed that an elongation of about 5% put into TCs during FRS swaging predisposed the TCs to early failure, particularly when operating temperatures were sufficiently high to permit recrystallization of the thermoelements. The absence of the 5% elongation in the nonswaged FRS has turned out to be a major advantage of that design.

After completion of steady-state and transient tests, GLR-L-7P was intentionally operated to destruction to define better the FRS low-power-high-temperature maximum operation point. Table 1.16 summarizes this operation.

Failure occurred after 10 min of operation at 1250°C (2280°F) had been completed and while power was being increased to achieve 1300°C (2370°F) cladding temperature. The 316 stainless steel cladding and Nichrome V heating element melted in a region near the element terminal end. Subsequent analysis indicated that failure occurred in a 2.5-cm-long (1 in.) region at the upper (terminal) end of the heating element. The tantalum coating on the exterior of the rod cladding that is needed to enhance radiative heat transfer had not been properly extended during fabrication to cover the area that suffered the damage. The lowered emissivity in this area compared with the rest of the heated section resulted in the area reaching a temperature that was higher than expected or indicated.

In summary, the tests of prototype GLR-L-7P demonstrated that the swaged FRS is capable of long-time, steady-state operation, of repeated thermal cycling, and of high-temperature-low-power operation. The tests also identified weaknesses in TC lifetime in the temperature range of 800°C (1470°F) and above and TC susceptibility to thermal cycling.

Prototypes GNR-L-8P and GR-L-9P were primarily associated with development of the nonswaged FRS. Although neither FRS was operated, several major fabrication innovations were developed and applied to prototype GR-L-10P. This prototype was successfully fabricated, but problems were encountered with metal spalling from the copper center terminal. The braze connection of the nickel-copper rods left the copper very soft. The action of the preform tamping tools caused copper

Table 1.16. Summary of GLR-L-7P Final Operation

Time (min)	Sheath temperature [°C (°F)]	Power (kW)
18	750 (1380)	2.5
15	950 (1740)	4.4
15	1000 (1830)	4.9
25	1050 (1920)	5.6
5	1100 (2010)	6.4
5	1150 (2100)	6.9
15	1200 (2190)	8.5/6.5[a]
10	1250 (2280)	7.1[a]

[a]Vacuum.

to spall off into the inner annulus during preform filling. The problem was corrected by an elongation of about 1%, which hardened the copper rod sufficiently to prevent further metallic spalling. This simple, but effective, way of eliminating copper spalling was incorporated into the evolving fabrication procedure for subsequent FRSs.

The GR-L-10P prototype was tested in the SRSL; it was gradually brought up to 29.9 kW at a cladding temperature of 715°C (1315°F). Operation at these conditions was sustained for 47.5 h until the crowbar protection system terminated the tests. Radiographic examination revealed that an insulation breakdown had occurred in the terminal region 250 mm (10 in.) above the top of the heating element, the region where copper spalling had occurred during fabrication. Even though it was known that a filling problem had occurred, the radiographic and insulation checks appeared to warrant operational testing. This result emphasizes how critical the fabrication process is to subsequent proper operation of an FRS.

Because of the success of the nonswaged development, GR-L-10P was the last swaged prototype to be fabricated. The information gained from fabrication and operation of 10P was successfully applied to subsequent

nonswaged prototypes. In addition, the elongation test provided a key to the solution of the perplexing problem of obtaining a practical inspection of the rod and tubular braze joints between the copper terminals and nickel leads.

1.4.2.3.3 Fuel Rod Simulator Terminal Development. The development of a suitable high-temperature braze for the rod and tubular joints between the copper terminals and nickel leads has been an ongoing task for the past two years.

From Fig. 1.40, it is apparent that several joints between dissimilar materials must be made. Three joints (copper to nickel for both center rod and tubular terminals and nickel tubular to Nichrome V heating element) must be made; each must be capable of carrying 150 A, must maintain its integrity at 1000°C (1830°F) or higher, and must withstand mechanical stresses induced by fabrication and by thermal cycling during programmatic test operation. The tubular terminals and the heating element have wall thicknesses of 0.25 mm (0.010 in.), which makes their joining operation quite difficult. In addition, the tolerance on the inside and outside diameters of the tubular parts is ±0.025 mm (0.001 in.).

The heating-element-to-ground-plug and ground-plug-to-center-rod joints also have to withstand high temperatures, mechanical stresses, and high current, but these joints are less difficult to braze because of the configuration and the larger total mass of these parts compared with tubular parts.

Repeated problems occurred with nickel-copper braze joints for both rod and tubular forms. Several successful connections were made by use of an Ni-Cu-Au braze alloy having a 1100°C (2000°F) remelt temperature, but occasional failures occurred, and no suitable inspection method was developed.

Poor control of brazing temperatures and inadequate control of the joint surfaces were determined to be the major problems. The induction brazing process was replaced with a vacuum-furnace brazing process, and the machining of the joint surfaces was transferred to a machine shop capable of better control. These changes resulted in our making braze joints that, based on pull tests and micrographic sections, were adequate to meet established criteria.

Attempts at nondestructive testing of completed braze joints (infrared scanning, x-ray, and resistance heating) were unsuccessful. When it became necessary to elongate the copper rod to correct metallic spalling, we decided to use this also as a nondestructive test to detect poor braze joints as well because plastic deformation of the copper induced tensile stresses that were, felicitously and serendipitously for us, high enough to cause poorly made braze joints to fail.

This nondestructive test, along with a visual inspection at 10 times magnification after dressing the brazed joint to proper diameter and after elongation and a radiographic examination of the joint, was incorporated into our procedures. This combination of three nondestructive tests has successfully eliminated poor joints and has thus far eliminated failure of brazed joints in FRSs subsequent to fabrication.

1.4.2.3.4 Nonswaged Fuel Rod Simulator Development. Because the substantial deformation of cladding during swaging made it quite difficult to achieve the required cladding cold work and to maintain the tolerances on diameter, ovality, and straightness that are necessary to perform postswaging roughening of the cladding, the development of a nonswaged rod was initiated.

A nonswaged FRS has several major advantages. The cladding is roughened prior to FRS fabrication, which eliminates the difficulties and risks of roughening a completed swaged FRS. With the nonswaged FRS, the swaging step is eliminated, which results in the following cost-saving and performance advantages:

1. elimination of the handling and shipping of rods to and from the manufactory for roughening of the cladding,
2. cost savings by reduction in the number of FRSs having roughening defects,
3. improved final outside diameter and straightness tolerances,
4. improved instrumentation and dimensional location of the heating elements,
5. receipt of FRS cladding that has cold work identical to that of the GCFR fuel rod cladding,

6. reduction in FRS fabrication costs, and
7. increased thermocouple lifetime.

The last advantage is crucial to long-term transient testing in CFTL test bundles that use type K TCs. As reported above, premature failure of FRS TCs occurred in most tests that used swaged rods. Preliminary information gained during tests with nonswaged FRSs (reported in this section) is much more optimistic.

However, a nonswaged FRS has two disadvantages compared with a swaged one. The nonswaged FRS will probably achieve operation at lower maximum power for the same cladding temperature (assuming the same heating-element material) and will probably show some loss in uniformity of heat-flux profile.

With the advantages and the disadvantages understood, a nonswaged FRS should meet three major criteria:

1. Uniform heat flux profile, as defined by infrared temperature measurement, in a 1-s core transient should be within ±5%.
2. A reasonable thermal conductivity of the outer annular BN must be attained so that the FRS can achieve the power-temperature requirements indicated in the GA CFTL program plan.
3. Most of the internal TCs must be able to withstand the thermal transients imposed upon them without premature failure.

These criteria (which also apply to the swaged FRS) have guided the nonswaged FRS development described.

Prototype GNR-L-8P was the first nonswaged FRS to be fabricated. Several improvements were incorporated into the fabrication technology. The major improvements were the use of high-energy (400 in.-lb/in.^{3}) crushing techniques in filling the inner preforms and the use of annular preforms with an initial density of 1.8 g/cm^3 (0.065 lb/in.^{3}) (80% theoretical).

The resultant preform density (after fill) of the volume between the coil and the nickel rod (inner annulus) was 1.82 g/cm^3 (0.066 lb/in.^{3}) compared with 1.6 to 1.7 g/cm^3 (0.058 to 0.061 in.^{3}) for previous swaged

prototypes after filling and prior to swaging. The higher density of the inner annulus preforms, combined with a preform density of 1.85 g/cm^3 (0.067 lb/in.^{3}) in the volume between the heating element and the cladding (outer annulus), made the concept of a nonswaged FRS feasible for the first time. Because the thermal conductivity of the BN powder is a strong function of density, a minimum density of 80 to 85% of theoretical is necessary to achieve a moderately high heat flux [100 to 200 W/cm^2 (300 to 600 kBtu/h-ft^2)].

The transient infrared scan variation of prototype 8P was a disappointing ±16.7%. This poorer-than-expected result to meet criterion 1, by use of relatively high-density preforms made of grade HCM BN powder, caused us to investigate the usefulness of several other BN powders. Table 1.17 summarizes pertinent properties of these powders.

Table 1.17. Property Evaluation of Several Types of Boron Nitride Preforms

Powder	TS-1325 1/2-1/2 lubrication[a]	TS-1325 1 camphor lubrication[b]	HCM die-body lubrication
Powder particle size, μm	7–20	7–20	50–750
After pressed density, g/cm^3 (%)	1.84 (82)	1.86 (83)	1.94 (87)
After purified density, g/cm^3 (%)	1.58 (70)	1.76 (78)	1.89 (84)
After filled density, g/cm^3 (%)	1.69 (75)	1.85 (82)	1.89 (84)
After filled strength	Strong	Very strong	Weak
Transient infrared scan profile deviation	±5–7.5%	±3–4%	±5–10%

[a] 1/2% dodecane–1/2% dodecanol by weight in boron nitride.

[b] 1% camphor by weight in boron nitride.

The known higher final density of the HCM grade of BN powder led to its initial selection as the major candidate for nonswaged FRSs because it was expected that greater profile uniformity and higher thermal conductivity would accompany higher density. Table 1.17 reveals, however, that this assumption was not valid. Although higher preform density is possible with HCM powder, the much larger particle size reduces strength and impedes the achievement of intimate contact with the inside diameter of the cladding (analogous to the degree of surface contact of gravel versus sand in a glass jar). Better thermal contact with the cladding for preforms made of both TS-1325 powders is indicated by their strength. Relative strength for all three preforms was determined by the difficulty of removing the crushed powder from the annular area. Core transient infrared scan data also indicated enhanced contact of the TS-1325 powders but showed that final density is also a factor. From these data, preforms made of camphor-treated TS-1325 powder were determined to be the best candidates for a nonswaged FRS.

Preforms fabricated of camphor-lubricated grade TS-1325 of BN powder were used in the fabrication of prototype GR-L-9P. Although this prototype was fabricated by using swaged FRS dimensions (larger cladding diameter and annular gap) and was subsequently swaged, a major purpose of its fabrication was to evaluate TS-1325/camphor preforms and newly developed techniques for crushing inner annulus preforms. This was also the first FRS to be fabricated with a variable-width Nichrome V heating element.

During filling the preforms into the outer annulus, the internal TCs became crossed. Attempts to uncross them were unsuccessful, so the terminal region was cut back to within 7.5 cm (3 in.) above the heating element to eliminate the crossed section. Although the shortened length precluded testing the rod in the SRSL, all the other physical, electrical, mechanical, and infrared scan evaluations were acceptable.

Radiographic examination of the rod indicated that the upper 2.5 cm (1 in.) of the variable-width heating element stretched more than was anticipated and thus caused the turns to become distorted and the coil diameter to increase. Although this result has little effect on profile

uniformity, the change in heating-element diameter caused binding of the preform tamping tool, which subsequently led to the crossing of the TCs. The additional movement of the heating-element turns resulted from use of the camphor-treated TS-1325 BN powder. Crushing of the TS-1325 preforms individually in the rod during fabrication caused a 3 to 4% density increase compared with no measurable increase in the previous use of HCM preforms. This density increase was accompanied by greater axial movement of powder and therefore of the heating element. Although the incremental heating-element movement per preform crushed was small ($\sim$0.05 to 0.1 mm per 15 mm preform), it resulted in disturbing the last three or four turns of the heating element and the subsequent binding of the tamping tool.

The infrared scan, although skewed because of coil movement, indicated that local variations were within the ±5% requirement of criterion 1. This result was the first positive indication that the newly developed fabrication techniques and the camphor-treated TS-1325 preforms might yield an acceptable nonswaged FRS.

Nonswaged prototypes GNR-L-11P and 12P were then fabricated by using the information gained on FRSs 8P and 9P. Some binding between the heating element and the tamping tool was encountered on 11P, but the prototype was successfully fabricated. Fuel rod simulator 12P was filled after further modifying the fabrication procedure to allow extension of the internal TCs beyond the exit at the closed end of the FRS. Annular preforms were then filled from each end to the longitudinal center of the heating element; the previous, normal procedure had been to fill all preforms from the terminal end only. The new filling procedure allowed use of tamping energies of 70 kJ/m^2 (400 $in\text{-}lb/in.^2$) during preform crushing and eliminated the binding problem that was encountered previously with TS-1325 preforms.

Nonswaged prototypes 11P and 12P both met all postfabrication inspection requirements, including being within the allowable ±5% tolerance on heat flux profile uniformity as inspected with infrared scan during the core transient, criterion 1. At this point we believed we had the capability to fabricate both swaged and nonswaged FRSs.

However, swaged prototype 10P had met criteria 1 and 2, but not 3, prior to failure, and nonswaged rods were yet to be tested for meeting criteria 2 and 3.

Thus, it was decided that GNR-L-11P would be tested in the SRSL to determine how well it met criterion 2. Because of the lower BN density in a nonswaged compared with a swaged FRS and resultant reduced contact pressure between BN and cladding, we anticipated that the effective thermal conductivity of the BN would be lower, possibly by a factor of 10. Thus, maximum power operation might be limited to about 10 kW at 1000°C (1830°F) sodium stream temperature. Table 1.18 summarizes these tests and indicates that higher-than-anticipated-thermal conductivity was achieved.

Failure occurred as a result of the melting of the Nichrome V heating element [mp, ∿1400°C (2550°F)] at about 250 mm (9.8 in.) from the end of the heating element, nearer to the closed end of the FRS. The location is in the region of the maximum expected temperature that is based on cosine heat generation, the thermal transport differential temperature of the sodium, and uniform BN thermal properties. That melting occurred here is a strong indication that the BN properties were uniform. By using the local heat flux and temperature conditions, we found that the calculated BN thermal conductivity is about one-third of that evidenced for a fully swaged FRS. Based on the calculated BN conductivity, the physical dimensions of the FRS, and a maximum safe heating-element temperature of 1300°C (2370°F), an anticipated operation curve for the nonswaged FRS (Fig. 1.41) was obtained.

Figure 1.42 is a plot (obtained from V. Casal, GFK, Karlsruhe, Germany) of BN thermal conductivity k versus density ρ for a powder-filled FRS. The calculated thermal conductivity for GNR-L-11P is also plotted. Two items of interest are: (1) the Casal data show that k is strongly dependent on ρ for $\rho > 70\%$ and (2) the conductivity for 11P approximately doubles the anticipated value at the 83% density that we achieved with 11P. This higher-than-anticipated conductivity is probably the result of a high degree of radial orientation that was achieved with cold-pressed preforms; the Casal data are for random-to-axial

Table 1.18. Single-Rod Sodium Loop Operational Tests of GNR-L-11P

Power[a] (kW)	Sodium stream temperature [°C (°F)] Inlet	Outlet	Time (h)
20	445 (830)	620 (1150)	5.0
20	550 (1020)	825 (1510)	1.0
24	650 (1200)	1000 (1830)	2.0
28	550 (1020)	1000	1.5
29	550	1000	1.5
31	550	1000	1.3
34	550	1000	0.7[b]

[a]Power data do not include 2% of power dissipated in terminals.

[b]Failure occurred.

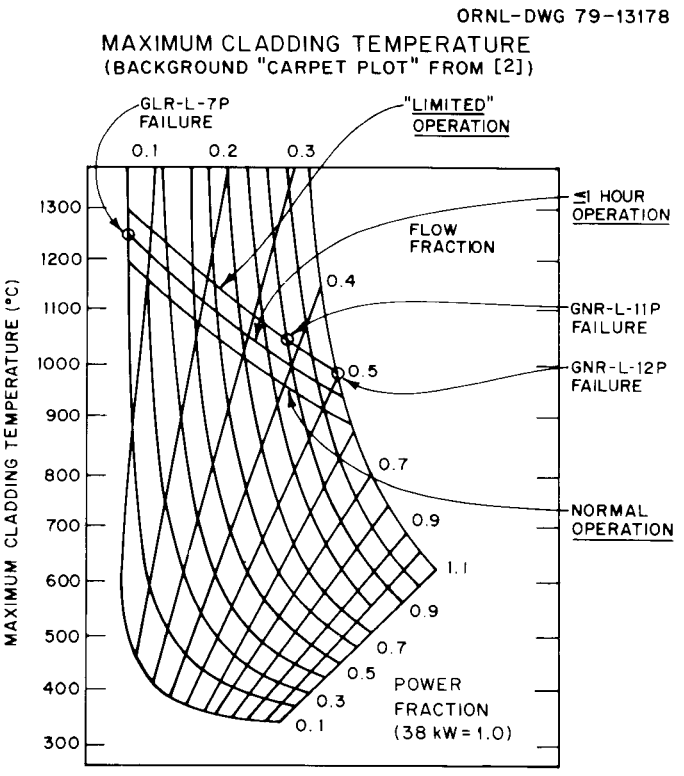

Fig. 1.41. Maximum Expected Operating Capability of Core Flow Test Loop Fuel Rod Simulator.

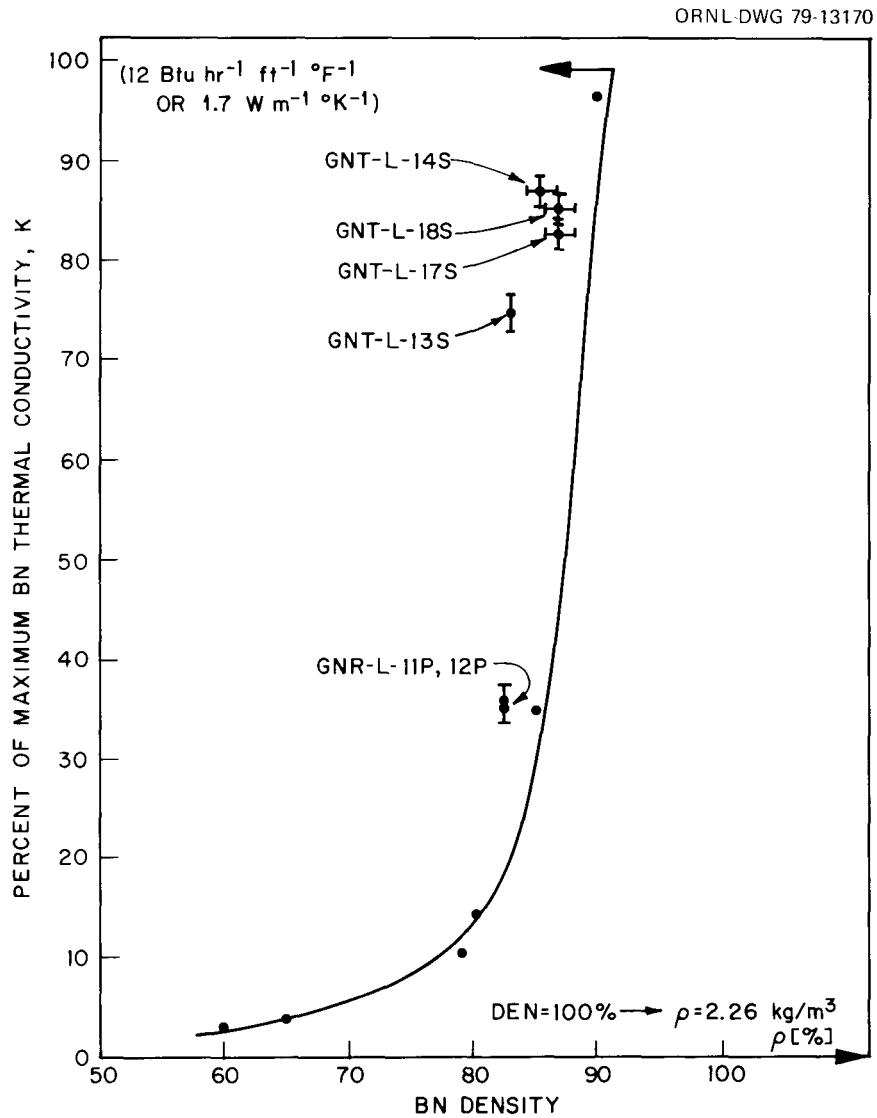

Fig. 1.42. Thermal Conductivity as a Function of Boron Nitride Density for Core Flow Test Loop Fuel Rod Simulators and Thermal Conductivity Cells Versus German Powder-Filled Fuel Rod Simulators. Solid line courtesy V. Casal, GFK, Germany.

favored orientation. The data also appear to indicate that a relatively modest increase of about 5 to 7% in as-filled preform density in an unswaged FRS may yield values of BN thermal conductivity nearly as high as those for a fully swaged FRS.

Based on this information, we initiated plans to fabricate a series of thermal conductivity cells for further investigation of the

thermal conductivity versus the density relationship of BN preforms. Meanwhile, prototype GNR-L-12P was installed in the SRSL for tests. Our intent was to qualify the nonswaged FRS at 110% power (42 kW) and 1000°C (1830°F) and to determine its thermal cycling capability. Table 1.19 summarizes this test operation.

Prototype GNR-L-12P survived more than 700 h of tests, endured more than 2150 thermal transients, and operated at 110% of design power and at 975°C (1785°F) cladding temperature before failure. The initial 693 h were at steady-state test conditions that were similar to those expected in many of the CFTL bundle tests. The rod was then subjected to thermal transients that simulated approximately those anticipated in CFTL tests in number and duration. At the completion of these steady-state and transient tests, both prototype 12P and three of the four internal TCs were still operational. The remaining internal TC broke at the terminal end during installation of the FRS in the test loop. Posttest continuity checks also showed 12P to be operational.

Fuel rod simulator 12P was then intentionally operated at conditions approaching expected failure. Failure occurred within about 25°C of the predicted failure of 950°C at 42 kW. Worth noting is that, in both this test and in that of GNR-L-11P, operation was normal up to the point of melting the Nichrome V heating element. This result indicates that the electrical resistance of the central BN preform is adequate for operation up to about 1400°C (2550°F) without failure. The central annular BN preform had previously been perceived to be one possible weak point in FRS capability to operate at high temperatures.

The radial temperature difference ΔT between the sodium stream and the internal TC indications was higher in a nonswaged than in a swaged FRS. An average ΔT of 115°C that was measured at 30 kW and 760°C (1400°F) sodium outlet temperature in nonswaged prototypes GNR-L-11P and 12P compares with 78°C for swaged prototype GR-L-10P that was measured under the same conditions. The large ΔT for a nonswaged FRS was expected and is attributed to the lower BN thermal conductivity and the lower contact pressure between the heating element and the stainless steel cladding and TCs caused by the elimination of swaging in the fabrication of a nonswaged FRS.

Table 1.19. Summary of Test Results for Nonswaged Rod GLR-L-12 in Single-Rod Sodium Loop

Test No.	Operation method[a]	Power			Maximum cladding temperature (°C)	Transient ΔT [°C (°F)]	Period (min)	Number of cycles (required/ completed)	Total time (h)
		Total kW	(V)	(A)					
1	SS	29.4	261	113.3	760				693
2	Tran.	29.0	260	112.0	760	236 (457)	1.0	0/305	5.10
3	Tran.	30.5	265	116.0	760	56 (133)	1.0	150/184	3.10
4	Tran.	30.5	265	116.1	760	255 (491)	2.0	20/241	8.0
5	Tran.	31.0	266	117.0	760	114 (237)	2.0	1200/1420	47.3
6	Tran.	31.0	266	117.0	760	250 (482)	2.0	0/34	1.0
7	SS	28.8	255	113.0	710				15 min
8	SS	34.6	280	123.5	800				5 min
9	SS	39.4	300	131.5	900				1.0
10	SS	43.4	315	137.8	900				35 min
11	SS	45.0	322	140.0	900				17 min
12	SS	43.3	315	136.0	900				5 min
13	SS	43.3	315	136.0	932				40 min
14	SS	43.3	315	136.0	968				10 min
15	SS	43.3	315	135.8	972				22 min
16	SS	43.3	315	135.8					

[a]SS = steady-state operation; Tran. = transient operation.

The successful fabrication and operation of nonswaged FRSs GNR-L-11P and GNR-L-12P led to the program decision to use the nonswaged FRS as the reference design. We thus gained the advantages pointed out at the beginning of this section. However, some sacrifice in uniformity of heat-flux profile occurs during a power transient, as indicated by infrared scan and by rod reliability. Reliability is lost because the heating element reaches necessarily a higher temperature in the nonswaged FRS at a given operational condition when compared with the swaged FRS. Both sacrifices are the direct consequence of reduction in both the thermal conductivity and the density of BN that can be achieved with a nonswaged FRS.

However, areas in which improvement in both operational capability and reliability of the nonswaged FRS can be obtained are:

1. increasing BN preform density and consequent thermal conductivity,
2. further improvements in fabrication techniques, and
3. the use of Kanthal A1 instead of Nichrome V as the heating-element material.

Items 1 and 2 are being investigated through the fabrication and testing of thermal conductivity cells. Item 3 is the subject of prototype GNK-L-15P and -16P (the K in GNK denotes a Kanthal A1 alloy heating element). The rationale for the use of Kanthal A1 for a heating element is elucidated in the following section on conductivity cell testing.

Prototypes 15P and 16P were fabricated primarily to test the capability of the Kanthal material to withstand the fabrication and the thermal cycling of CFTL FRSs. The postfabrication inspections of prototype 15P revealed that the laser weld joint between the Kanthal heating element and the associated tubular nickel lead had failed. Although previous weld tests with Kanthal had been successfully completed, the new procedure was obviously not successful with prototype 15P.

Prototype 16P, which contains a constant-width heating element made of Kanthal A1 alloy, was fabricated successfully. Extensive prefabrication testing of the nickel-Kanthal laser weld joint proved it to be very durable. The prototype was run in the HTS; Table 1.20 summarizes these tests.

Table 1.20. Summary of Rod GNK-L-16P Operational Tests in the Helium

Test	Power (kW)	Maximum cladding temperature [°C (°F)]	Transient ΔT [°C (°F)]	Period (min)	Number of cycles	Total time (h)
1	2.3	730 (1345)	380 (715)	3.0	81	4.05
2	3.5	870 (1600)	520 (970)	3.0	112	5.60
3	6.0	860 (1580)	520 (970)	3.0	70	3.50
4	6.0	1010 (1850)	675 (1245)	3.0	42	2.10
5	7.5	1065 (1950)	705 (1300)	3.0	160	8.00
6	7.6	1075 (1965)	705 (1300)	3.0	224	11.20
7	1.8	700 (1290)	[a]			11.00
8		1180 (2155)	[b]			1.0+

[a] Steady state.

[b] Slow increase to failure.

The primary intent of the tests was to determine the stability of the laser-welded butt joint between the Kanthal and the adjoining nickel tube under high thermal stress conditions. Thermal transients were conducted in which the rise rate and then the cladding temperature were increased with each test. The second objective was to determine TC lifetime under relatively large and rapid thermal transient conditions, such as in tests 2 through 7.

The Kanthal-nickel tube butt weld operated normally through 689 transients and 46.5 h of operation before failing. Although the weld area will be sectioned and analyzed to obtain more detailed information, its successful operation throughout the severe transients strongly indicates that the weld may be reliable enough to permit the use of Kanthal A1 heating elements in GCFR-CFTL FRSs.

Rod GNK-L-16P contained three modified-grounded-junction TCs and one grounded-junction TC. Table 1.21 lists the cycles to failure of each.

Table 1.21. Rod GNK-L-16P Thermocouple Transient Cycles Before Failure

Thermocouple	Junction type	Cycles to failure
1	MGJ[a]	305
2	MGJ	347
3	MGJ	505
4	GJ[b]	684

[a]Modified-grounded junction.

[b]Grounded junction.

The thermal transients in the 16P tests were more severe than those anticipated in the first CFTL test bundle. The failure of all three modified-gounded-junction TCs before failure of the gounded-junction type is an indication that the modified-grounded junction is less reliable than the grounded junction. The modified-grounded junction is a low-mass junction that is welded directly to the cladding and, hence, should experience the effects of differential thermal expansion more directly than the gounded-junction TC. However, insulated-junction TCs have been shown to be the most reliable, possibly because additional thermal shock resistance is supplied by the insulator material.

Subsequent tests of prototypes will include transients that are more typical of those expected in bundle operation. No TC reliability problems are anticipated with the current reference insulated-junction TC.

1.4.2.3.5 Thermal Conductivity Cell Fabrication and Testing. A series of conductivity cells was fabricated and tested to obtain information about the effective thermal conductivity of the crushed cold-pressed BN preforms in an FRS. Information was needed on the relationship of conductivity to inner and annular BN density, FRS power, cladding temperature, and the fabrication process. A water-cooled test stand (WCTS) was assembled for testing the cells.

The conductivity cell configuration is similar to that of the CFTL FRS (Fig. 1.40) except that it has a heated length of 30.5 cm (1 ft) and that the center terminal (current return) is replaced with a 1.5-mm (1/16-in.) type B (Pt-6% Rh versus Pt-30% Rh) TC. The current return is provided by attaching the far end of the heating element to the cell cladding and grounding the cladding to complete the electrical circuit. Some cells contain the FRS sheathed TCs, and some do not.

Four conductivity cells have been fabricated and tested to date. Table 1.22 summarizes the pertinent conditions for these cells. Calculated density values are accurate to within ±2%.

Table 1.22. Conductivity Cell Conditions

Number	Density (%)		Internal thermocouples[b]	Where tested[c]
	Inner	Annular[a]		
GNT-L-13S	77	84	2 GJ,2 IJ	WCTS
GNT-L-14S	83	87	2 GJ,2 IJ	WCTS/SRSL
GNT-L-17S	84	89	None	WCTS
GNT-L-18S	85	88	None	WCTS

[a] 100% density = 2.25 g/cm^3.

[b] GJ = grounded junction; IJ = insulated junction.

[c] WCTS = water-cooled test stand; SRSL = Single Rod Sodium Loop.

Each test cell was mounted horizonally in the WCTS. Two or three TCs were attached to the outer cladding surface in an intrinsic junction configuration. All junctions were located in the radial plane that contains the junction of the internal, central type B TC and at equidistances around the perimeter.

Figure 1.43 summarizes thermal conductivity k versus power for the WCTS tests of the conductivity cells. The data were repeatable to within ±10%. Pertinent information gleaned from the conductivity cell tests includes:

1. Thermal conductivity k is sensitive to the differential thermal expansion of the heating element and the BN insulation.

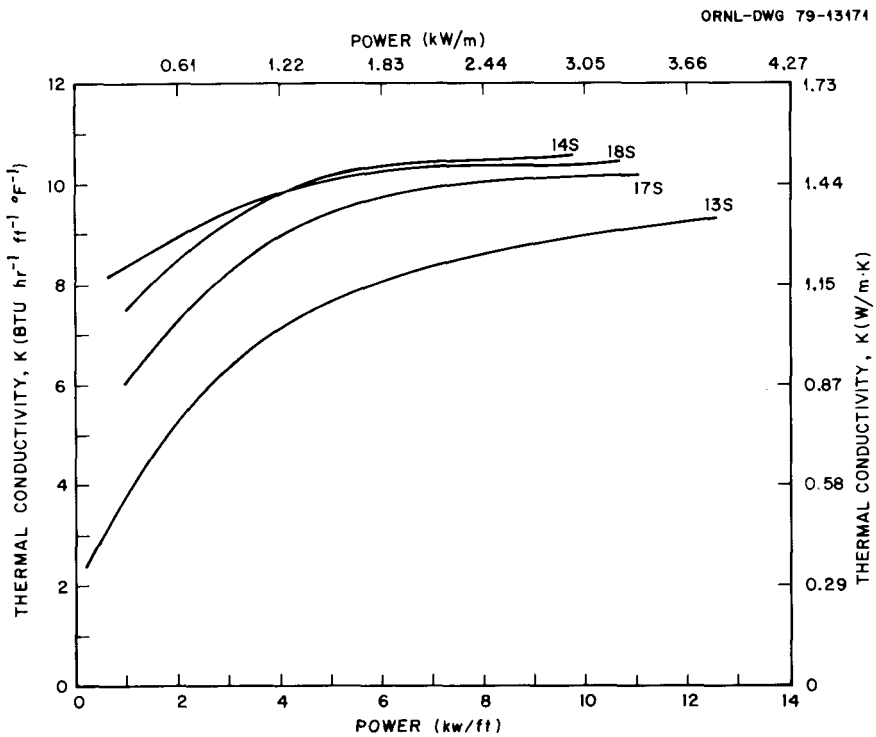

Fig. 1.43. Thermal Conductivity as a Function of Power for Several Conductivity Cells Tested in the Core Flow Test Loop Water-Cooled Test Stand.

2. In the last three cells tested, conductivity reached a maximum value of about 17 W m^{-1} k^{-1} (10 British units), that is, 80 to 85% of that achievable in a highly densified, swaged FRS.

3. Thermal conductivity is sensitive to the density of both the inner and outer annulus preforms. The degree of the dependence and whether the major dependence is on the inner or the outer annulus preforms is not clear.

4. The value of thermal conductivity as a function of density is always higher for the conductivity cells than is the value in the Casal data for a powder-filled FRS (Fig. 1.42).

The cladding was held at an approximately constant temperature in the boiling water in the WCTS. The cell center temperature, measured with the type B TC, varied with heat flux and reached temperatures as much as 250°C (450°F) higher than the heat sink temperature at the high

heat-flux values. The thermal expansion associated with this radial differential temperature tightens up the internal cell components and increases the contact pressure between the heating element BN and the internal surface of the cladding. The leveling off of the thermal conductivity versus power (heat flux) indicates that effective thermal conductivity was achieved.

To investigate further the dependence between thermal conductivity and operating conditions, conductivity cell GNT-L-14S was tested in the SRSL to higher temperatures than achieved in the WCTS. Figure 1.44 summarizes the test results. Although the value of thermal conductivity

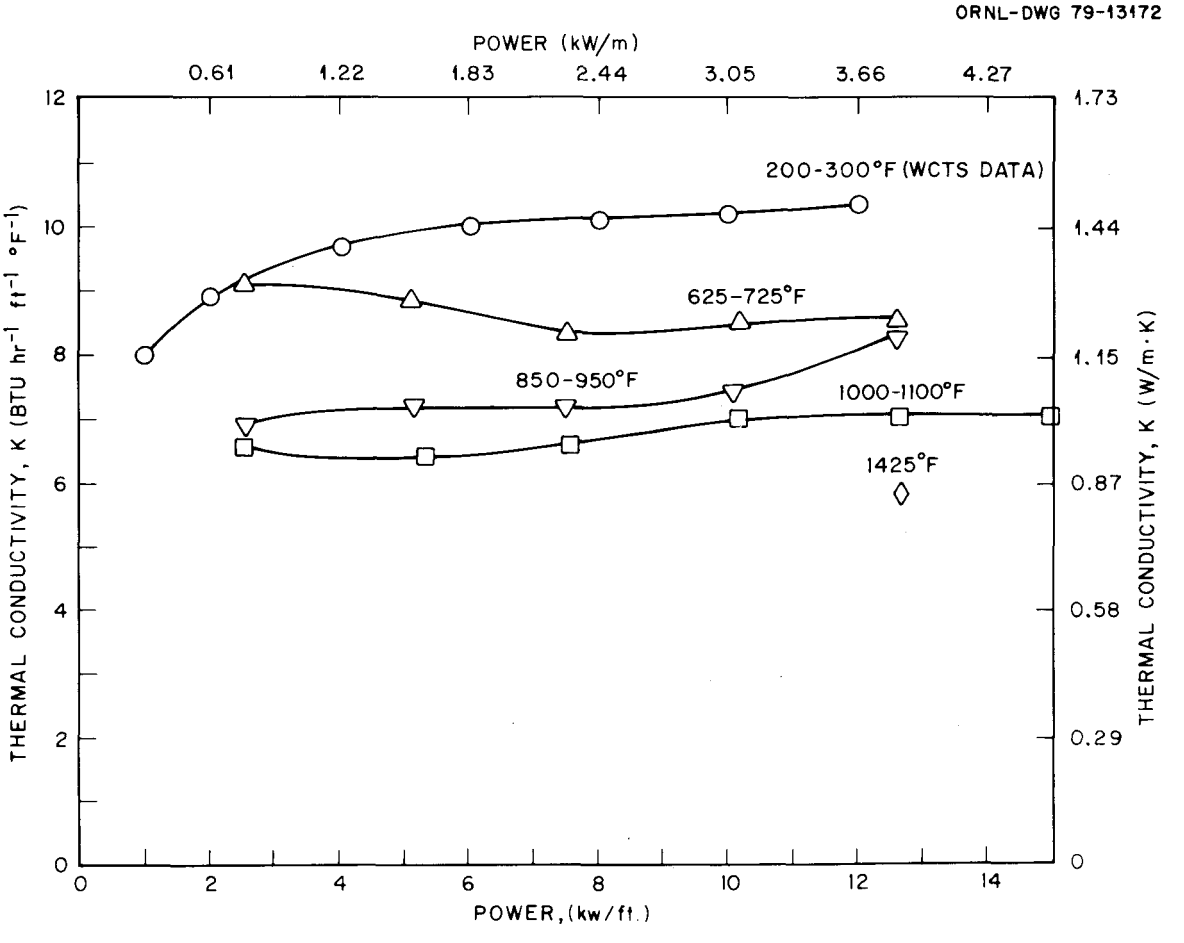

Fig. 1.44. Thermal Conductivity as a Function of Power at Several Different Temperature Levels for Core Flow Test Loop Conductivity Cell GNT-L-14S.

was reasonably constant as a function of power, it decreased with increased cladding temperatures. The thermal expansion of the stainless steel cladding apparently offsets the salubrious effects of the thermal expansion of the FRS internal components and, thus, lowers the effective thermal conductivity.

A modified inner annulus preform that has increased thermal expansivity is being developed in an attempt to maintain good contact pressure between cladding and internals at high temperatures. The preform contains a mixture of 85% magnesium oxide (MgO) and 15% BN powder. The higher thermal expansion of MgO may achieve the desired tightening effect. A sacrifice in inner annulus thermal conductivity may occur with the modified preform, but this property is not as important in the inner annulus as we currently believe the enhanced thermal expansivity to be. A conductivity cell using the modified preforms will be fabricated and tested in the near future to evaluate the modified preform.

Meanwhile, Kanthal A1, a higher-melting-point alloy that is being tested as a heating-element material, may provide higher operational capability of the nonswaged FRS, even with the current unmodified preforms.

1.4.2.3.6 Investigations of Kanthal A1 as a Heating-Element Material. The decision to use a nonswaged reference FRS in the CFTL test bundles involved the redesign of the variable-width heating element because that element elongated about 50 mm (2 in.) during swaging. In addition, redesign of the heating element to increase electrical resistance and consequently to decrease current would decrease gratuitous heat generation in FRS terminals. Kanthal A1 is a widely used commercial heating-element material and has a melting point of 1500°C (2750°F) about 100°C (180°F) higher than Nichrome V (1400°C) (2550°F); it has a temperature-resistance characteristic that is slightly better than Nichrome V. However, Kanthal A1 is difficult to fabricate and weld and has lower high-temperature mechanized strength than Nichrome V.

An attempt was made to adapt the laser welding technique to the joining of the nickel lead to the Kanthal heating element. As indicated above for prototype GNK-L-16P, the laser welding technique was found to be satisfactory for making the nickel-to-Kanthal joint.

Fifteen variable-width heating elements have been fabricated with Kanthal A1 alloy. The first will be used in prototype GNK-L-20P, to be fabricated in the near future. If high power and thermal cycling tests prove to be successful with prototype 20P and in subsequent tests with a few additional prototypes, Kanthal A1 will be the heating-element material for the reference nonswaged FRS.

1.4.2.3.7 Thermocouples for Use in CFTL Fuel Rod Simulators. The small-diameter type K TC in an Inconel sheath of 0.5 mm (20 mil) diameter showed premature failure in swaged prototypes 7P and 10P and better-than-expected reliability and longevity in nonswaged prototypes 11P and 12P. We studied the effects of temperature on grain size and of cold work (i.e., the elongation of the TC during swaging or other processes) on sample TCs from two manufacturers, C. S. Gordon (CSG) and Sensor Dynamics, Inc. (SDI).

Specimens from TCs of both manufacturers were elongated to 1, 2, 3, 5, and 10% strain levels. The specimens were cut into short lengths, and samples of each strain level were sealed in evacuated quartz capsules, 10 samples per capsule, and heated 4 h at temperatures of 650, 760, 870, and 1010°C (1200, 1400, 1600, and 1850°F). Metallographic examination revealed the following:

1. The starting grain size of the SDI thermoelement material was larger than that of the CSG material. The Alumel element had some grains that traversed the entire wire diameter.
2. The SDI grain size, being quite large initially, showed little significant change from cold work or temperature.
3. The CSG material retained its relatively fine grain size (∿1 mil av diam) for all strains at 650 and 760°C (1200 and 1400°F), through 5% strain at 870°C (1600°F), and for 3% strain at 1010°C (1850°F). Some grain growth occurred for 10% strain at 870°C (1600°F) and 5 and 10% strain at 1010°C (1850°F).

These data indicated that poor performance of the SDI TCs was a result of large grain size (single grains traversing the thermoelement

diameter in some cases) in combination with the 4 to 5% elongation encountered when an FRS is swaged. The grain boundaries are weak points and, when subjected to additional strain, cause open-circuit failure of the Alumel element. The additional strain is supplied by thermal expansion difference between the thermoelements and the FRS stainless steel cladding at elevated temperatures and during transient testing.

The best conditions for reliable TC operation, then, are (1) fine grain size in the as-received thermoelement material and (2) low strain levels on TCs during FRS fabrication. The second condition is inherent in the nonswaged FRS. The first condition will be sought in future TC procurement.

A 0.5-mm type K TC that has an insulated junction and a stainless steel sheath and uses BN insulation back-filled in the junction region was developed. The work was done by personnel in the Fuel Rod Simulator Technology Development Program in the ORNL Engineering Technology Division and by personnel of Groth-Mazur Industries, Addison, Illinois. The work was supported by the Pressurized-Water Reactor BDHT program and was funded by the Nuclear Regulatory Commission. The new TC has noise immunity equivalent to that of a similar TC that is insulated completely with MgO. However, it has a time response of 20 to 25 ms, which is 25% faster than that of a grounded-junction TC of similar size and more than twice as fast as that of a similar MgO-insulated-junction TC. The BN back-filled junction also presents less resistance to radial heat flow in the FRS compared with MgO insulation.

1.4.2.4 Breakdown Voltage at the Electric Terminals of a Fuel Rod Simulator — W. R. Huntley and T. B. Conley

Tests were performed to determine the breakdown voltage at the terminal ends of an FRS in helium, nitrogen, and air atmospheres. The tests were performed at 1 to 2 atm pressure and from 20 to 350°C (68 to 660°F) temperature. The area of concern was the 0.64-mm (0.025-in.) gap between the tubular terminal and sheaths of the four internal TCs at the open end of the FRS. The tests were performed to ensure a sufficient safety margin between FRS operating voltage and the breakdown voltage.

The need for the test was first indicated during the bundle concept design study when reducing the FRS pitch from 11.2 to 9.8 mm (0.440 to 0.386 in.) was considered. The closer spacing led to the consideration of a pressure-equalized bundle concept in which the pressure would be nearly balanced across the FRS cladding and the tube sheet. Such a design permits the use of a relatively thin tube sheet because the differential across it would be small compared with the full design pressure of 11.8 MPa (1715 psia) across the tube sheet in the traditional or pressurized concept. In addition, the thin tube sheet reduces the cooling that is needed to remove electrical heat generated in the copper terminals in the vicinity of the tube sheet.

Two series of tests were run. In series I, tests were run in helium and nitrogen at gas pressures up to 2 atm to simulate the pressure-equalized concept during GCFR depressurization accidents. In series II, the tests were run in air at 1 atm pressure to simulate the pressurized concept; a duplicate test was run in helium for comparison with series I.

Initially in series I a screening test was performed with a modified FRS that did not have the four internal TCs and therefore had a larger-than-normal gap [1.1 mm (0.045 in.)]. No arcing occurred in a nitrogen atmosphere at standard conditions up to the maximum available potential of 1000 V dc. Breakdown was observed in helium at 250 V dc. The low breakdown voltage in helium led to the next set of tests in series I.

Helium breakdown voltage tests were conducted by use of an available swaged FRS, GLR-L-7P, that had four internal TCs with a terminal-to-TC gap of about 0.64 mm (0.025 in.). The test facility (shown schematically in Fig. 1.45) allowed the operation of the FRS in vacuum or in helium at pressures to 0.2 MPa (29 psia). An electrical heater and TCs were located on the pressure boundary surrounding the upper end of the FRS to control the temperature near the arc gap.

The helium for all tests came from a single bottle of specially conditioned, high-purity helium that was chosen because it approximated the purity expected in the CFTL helium. Moisture content of the helium could be adjusted and monitored as shown schematically in Fig. 1.45.

Initial voltage breakdown testing was done by use of a low-amperage dc power supply to preclude damage to the terminal end of the FRS during

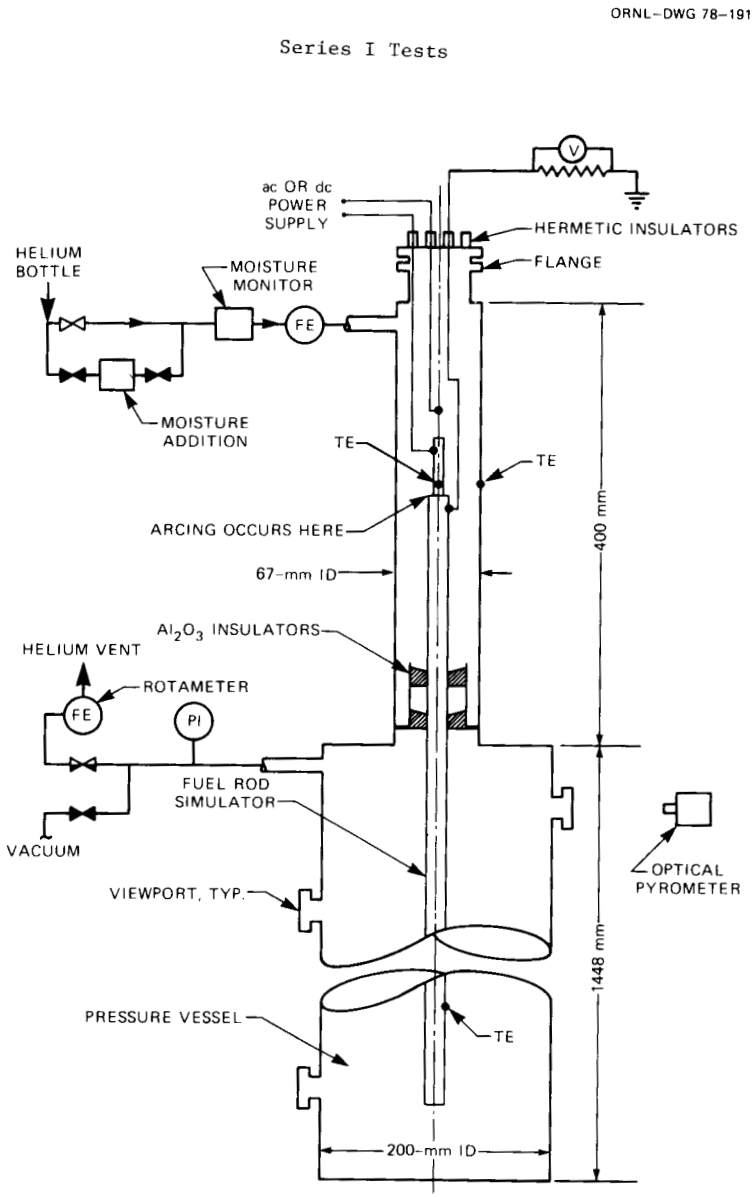

Fig. 1.45. Apparatus for Voltage Breakdown Tests with Core Flow Test Loop Fuel Rod Simulator.

arcing. Final testing was done by using a prototype of the test bundle power supply and a protective "crowbar" circuit to limit damage during arcing.

The series II tests were performed on 305-mm (12-in.) lengths of three available FRSs: GR-L-10P, GNR-L-11P, and GNR-L-12P. The FRS 11P and

12P were nonswaged, and 10P was swaged. The series II tests were performed for the following reasons:

1. to confirm the belief that a CFTL FRS could be operated with a sufficient safety margin in air at atmospheric pressure,
2. to confirm the results of the series I test in helium, and
3. to test nonswaged rods in addition to the swaged rod that had been used in series I.

A difference exists in the gap widths in the swaged and nonswaged FRSs; the swaged FRS gap is about 0.64 mm (0.025 in.), and the nonswaged FRS gap is about 0.58 mm (0.023 in.). The four internal TCs are bent back at the point of their emergence from the FRS (Fig. 1.46) to prevent formation of a sharp edge that could reduce breakdown voltage gratuitously at the point of concern. A TC was mounted near the edge of the cladding to monitor the temperature near the expected point of breakdown. The test section was then placed in an open-ended 25.4-mm-ID (1-in.) quartz sleeve and baked in a tube oven at about 230°C (450°F) from 3 to 4 h to drive the moisture out of the BN before the actual data were taken.

The series I test data for dc breakdown voltage in helium at the terminal end of FRS-7P ranged from 200 to 340 V at 0.2 MPa (29 psia). The first test indicated breakdown at about 320 V, which was relatively constant at test temperatures from 38 to 370°C (100 to 700°F). Additional dc tests showed a lowered breakdown potential of about 220 V. The data show very little temperature dependence, which does not agree with Paschen's law ($V \propto 1/T$) and is not understood. Tests with the prototypic ac bundle power supply were conducted only at elevated temperatures of 382 and 426°C (720 and 800°F). These data show a slightly lower average breakdown voltage of about 170 V.

Posttest examination of the gap for swaged FRS GLR-L-7P showed that one of the four TC sheaths was damaged by repeated arcing to the surface of the tubular terminal. The surface of BN insulation was darkened near this TC, and the inner surface of the FRS cladding was covered with fine particles adjacent to the TC. We speculate that the arcing damage observed may be the reason for the abrupt change in breakdown voltage from about 320 to 220 V during the early testing.

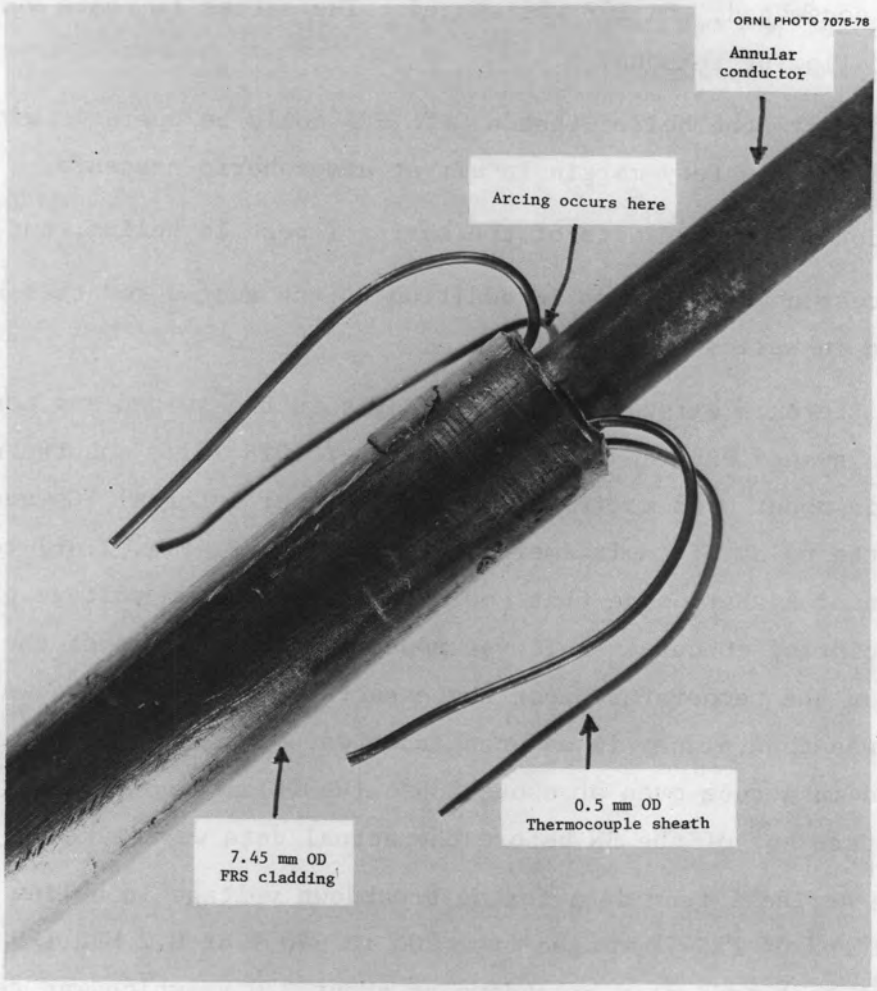

Fig. 1.46. Open End of a Core Flow Test Loop Fuel Rod Simulator Used in the Series II Voltage Breakdown Tests.

During the series I tests, we attempted to observe the effects of moisture content in the helium that flowed over the end of the FRS terminals. No significant effects on breakdown voltage were noted at water contents of 10, 100, 500, or 1000 ppm in the inlet helium.

In the series II tests FRS 11P was operated during shakedown testing to determine the proper experimental technique. Failure was caused by the presence of moisture within the BN insulation. The moisture caused a reduced breakdown voltage without visible arcing. An attempt to produce visible arcing led to the failure. This experience indicates that the CFTL bundle may need to be brought to full power slowly to drive out the moisture trapped in the BN.

Initially, two sets of air tests were done on both FRS 10P and 12P. The scatter of the data was no greater than was anticipated in an experiment subject to so many variables. The swaged FRS 10P achieved a higher breakdown voltage than the nonswaged 12P (Fig. 1.47). Part of this difference may have been caused by the difference in gap widths in the two types of FRSs. At temperatures of about 340°C (650°F), the

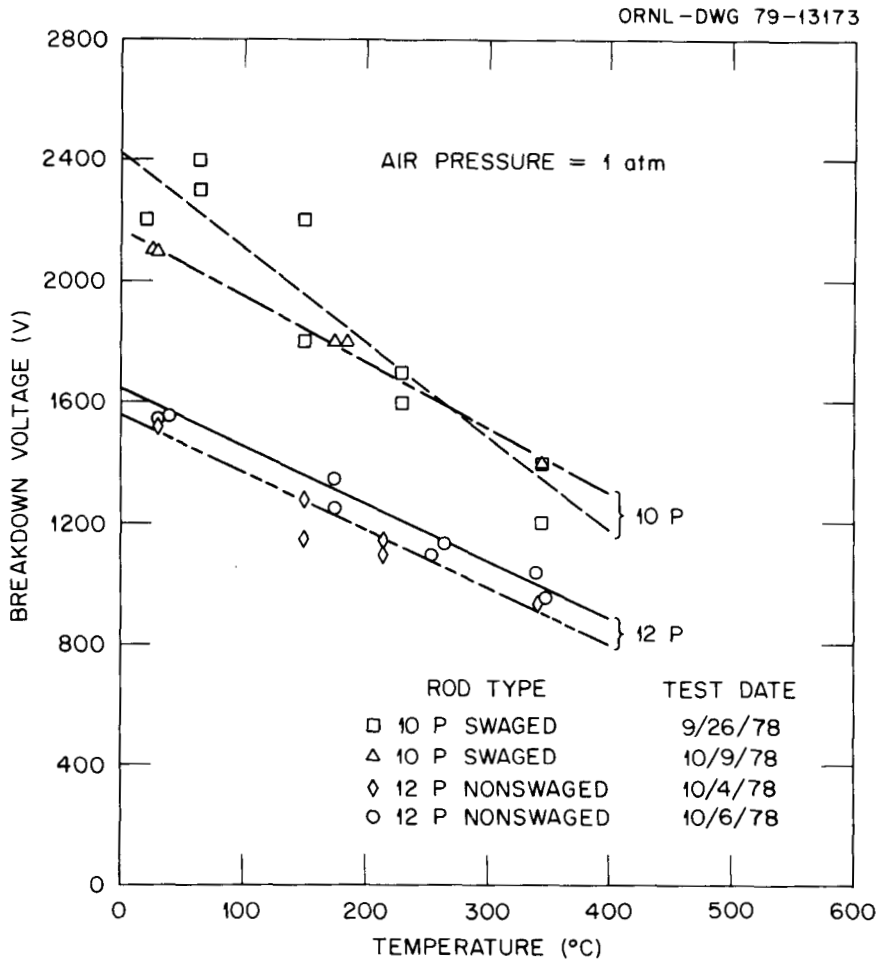

Fig. 1.47. Breakdown Voltage (ac) in Air as a Function of Temperature for the Core Flow Test Loop Fuel Rod Simulators Used in the Series II Tests.

breakdown voltage in air was between 950 and 1000 V ac for the nonswaged FRS 12P. This figure is substantially higher than the maximum expected operating voltage of 350 V ac.

The breakdown voltages in helium ranged from 215 to 280 V ac for swaged FRS 10P and from 200 to 240 V ac for nonswaged FRS 12P. The results of the series I and series II tests are plotted in Fig. 1.48. Although the data for FRS 7P are for dc voltages and the data for FRS 10P and 12P are for ac voltages, general agreement between the two different test series indicates that breakdown voltage across the gap of CFTL FRS is indeed low with helium.

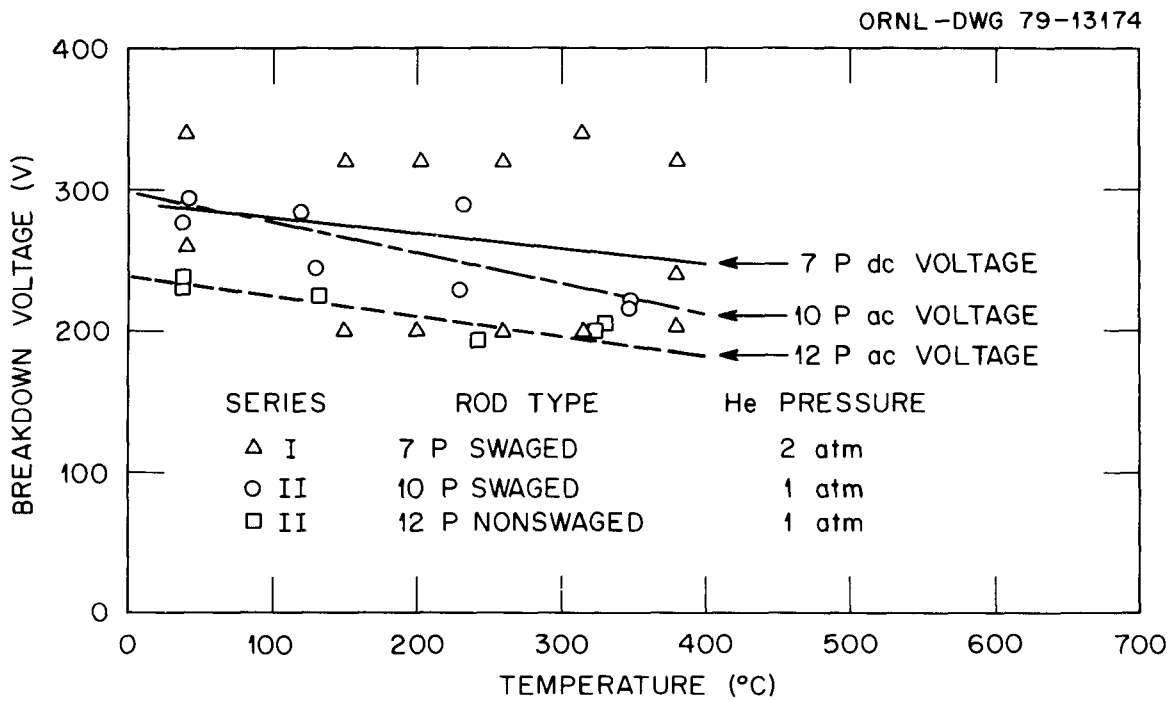

Fig. 1.48. Breakdown Voltage in Helium as a Function of Temperature, Core Flow Test Loop Fuel Rod Simulator.

At the conclusion of series II testing, confirmation tests and visual observations were made with FRS 10P and 12P to determine if any arcing damage had occurred. None was observed.

The main conclusions derived from the results of these tests are:

1. Helium is not recommended for blanketing the electrical terminals of the FRSs because of its lower breakdown voltage as compared with that for air (or nitrogen).

2. The resistance of BN drops markedly with moisture content.

3. The FRSs should be brought to power gradually during bundle startup to drive moisture from the BN and thereby maintain adequate electrical insulation properties.

4. The low breakdown potential of helium was confirmed by the general agreement of data from three test series: the original screening test, test series I, and test series II.

5. The series II data demonstrate that the voltage breakdown of the gap between power terminal and TC sheath in helium at standard temperature and pressure is one-sixth to one-eighth that of air. At 350°C (660°F) and atmosphere pressure, the breakdown voltage is one-fifth to one-sixth that of air.

6. If future design changes require reconsideration of the use of helium in the FRS terminal region, additional testing at high pressure appears justified because (1) the current tests were limited to less than 2 atm of pressure by the test apparatus design and (2) the safety margin for breakdown voltage in helium is small.

1.4.2.5 Permeation of Gases Through Boron Nitride Inside a Fuel Rod Simulator — W. R. Huntley and T. B. Conley

Bundle concept design studies in which an FRS pitch of 9.8 mm (0.386 in.) was investigated directed our interest to a pressure-equalized FRS. The helium coolant in this FRS not only transports heat from the external cladding surface but also can enter into the FRS through the entrant (open) end of the FRS. This concept permits the existence of a nearly pressure-equalized condition across the cladding during steady-state operation. However, the concept raised questions about the differential pressure that would exist across the cladding during simulation of a GCFR depressurization transient. In this transient the gas in the FRS interior would need to diffuse axially through the BN insulation and leave through the open end of the FRS to reduce internal gas pressure to the level of

the depressurized condition of the system helium coolant. Therefore, tests were performed to determine how closely in time the gas pressure inside a CFTL FRS can follow a pressure transient occurring at the open end of the FRS. Individual tests were performed with helium, nitrogen, and argon in a typical FRS. The interior of a test FRS was pressurized to 8.9 MPa (1290 psia) through the open end, and the pressure was then reduced as rapidly as practicable.

Nonswaged FRS GNR-L-11P was tested with helium, nitrogen, and argon, and swaged FRS GLR-L-5P was pressurized with helium and nitrogen. The testing was done at room temperature in the setup shown schematically in Fig. 1.49. The permeation rates were deduced by measuring the elastic

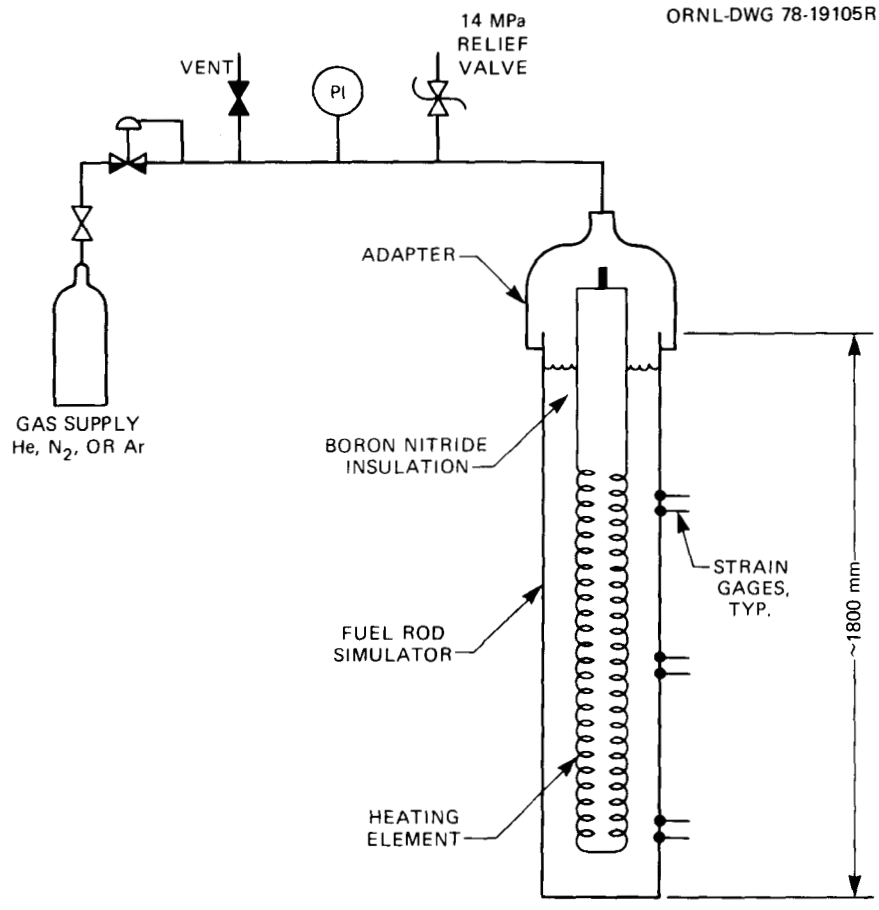

Fig. 1.49. Core Flow Test Loop Fuel Rod Simulator Apparatus for Gas Permeation Tests.

displacement of the FRS cladding with strain gauges mounted on the external cladding surface. Circumferential and axial strains were measured at three different axial locations along the FRS, which corresponded to the two ends and the middle of the heating element inside the FRS. After zeroing the strain gauge readout instrumentation, the interior of the FRS was pressurized through its open end with the test gas to about 8.9 MPa (1290 psia). Strain gauge readings were taken periodically until an equilibrium internal pressure was indicated. The gas pressure at the open of the FRS was then released suddenly, and the decay of the internal pressure was deduced in the same manner as was the pressure increase.

Figure 1.50, which presents the behavior of nonswaged FRS 11P pressurized with nitrogen, is a graph of the strain measurements made at

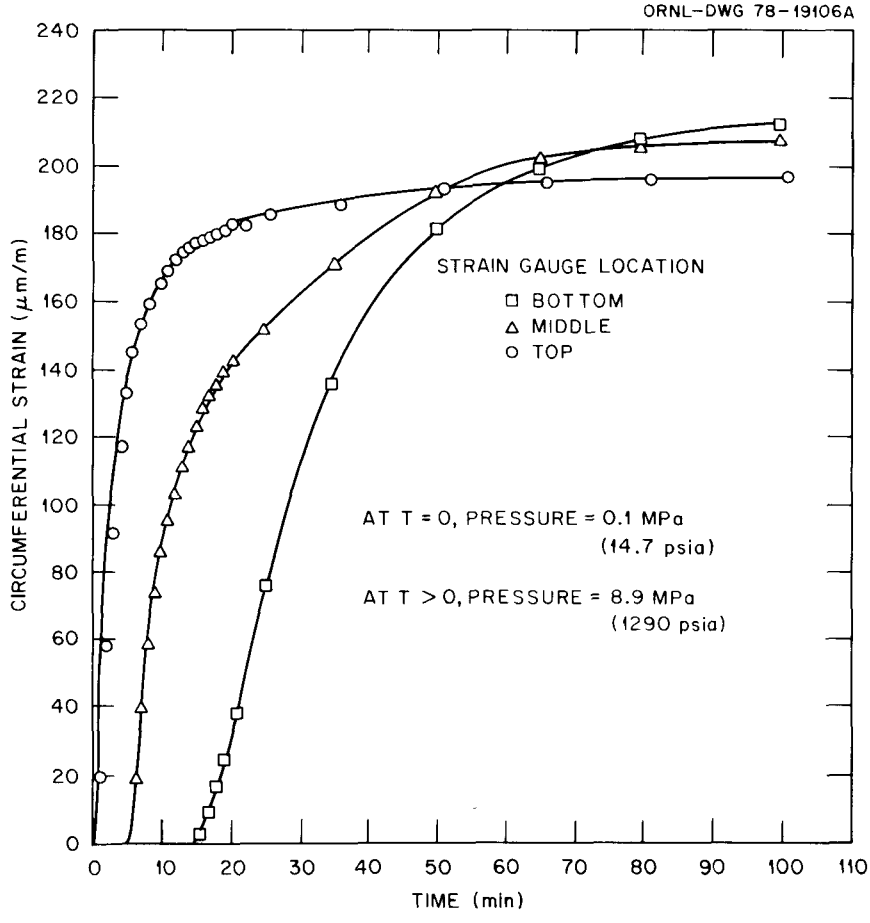

Fig. 1.50. Permeation Rate of Nitrogen at Room Temperature During Pressurization of Nonswaged Core Flow Test Loop Fuel Rod Simulator GNR-L-11P.

the three axial locations. The time required to reach the indicated internal equilibrium pressure is about 100 min. Figure 1.51 shows the behavior of the same FRS during depressurization. The time required to reach a significant reduction in pressure throughout the FRS is substantial. A comparison of the behavior of the rod for each of the three test gases (helium, nitrogen, and argon) is shown in Fig. 1.52. Helium, the lightest gas, diffuses most quickly through the BN, as expected. Again, the time required to reach a significant reduction in pressure throughout the FRS is substantial.

The data in Fig. 1.53 indicate that the permeation rate is vastly different in the swaged compared with the nonswaged FRS. The nonswaged rod reached equilibrium strain gage readings in about 1 h for nitrogen, compared with about 240 h in the swaged rod.

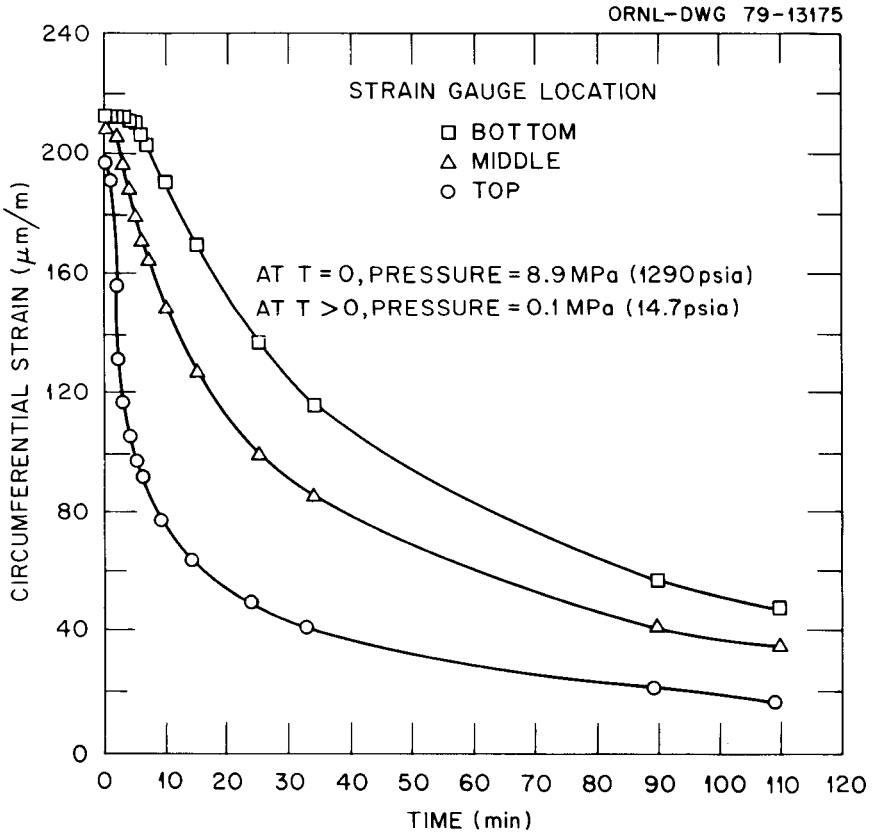

Fig. 1.51. Permeation Rate of Nitrogen at Room Temperature During Depressurization of Nonswaged Core Flow Test Loop Fuel Rod Simulator GNR-L-11P.

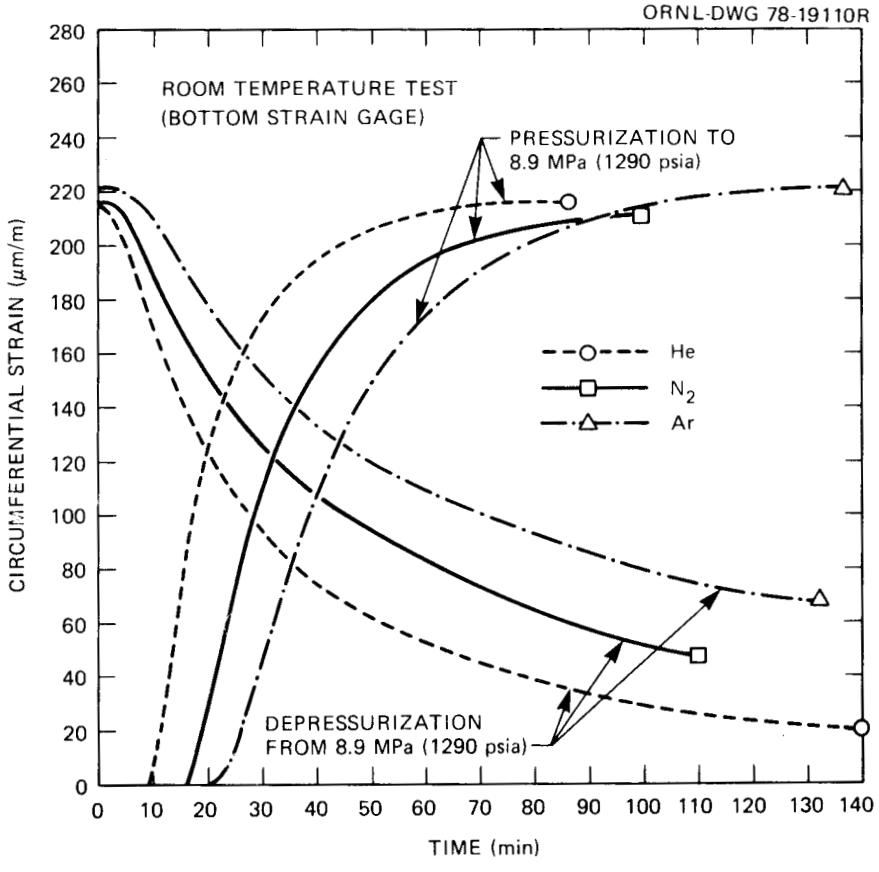

Fig. 1.52. Comparison of Permeation Rates for Helium, Nitrogen, and Argon at Room Temperature During Pressurization and Depressurization of Nonswaged Core Flow Test Loop Fuel Rod Simulator GNR-L-11P.

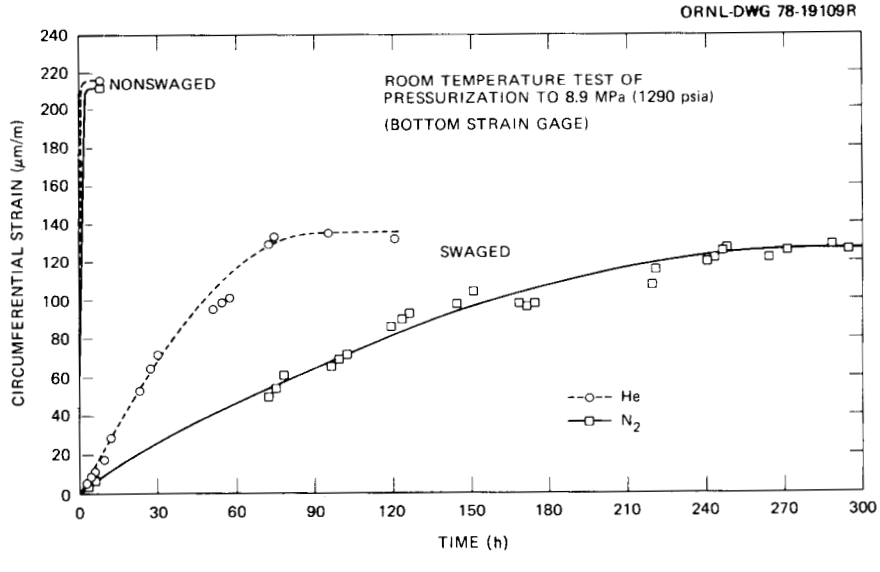

Fig. 1.53. Comparison of Permeation Rates for Helium and Nitrogen at Room Temperature During Pressurization of a Swaged and a Nonswaged Core Flow Test Loop Fuel Rod Simulator.

These tests indicate that the FRS internal pressure could not respond rapidly enough to follow anticipated CFTL depressurization transients from 9 to 0.15 MPa (1300 to 22 psia) in times as short as 1 min. In such tests the trapped gas within the FRS would likely overstress the FRS cladding and could result in permanent damage because the cladding will be at extremely high temperatures after depressurization and have a low yield strength. The rate of diffusion through BN in a high-temperature FRS is expected to be proportional to the square root of the absolute temperature and would be greater than that observed in these room-temperature tests. However, we do not expect this increased diffusion rate to be adequate to relieve the linear increase in trapped gas pressure that would occur in the FRS as its temperature increases rapidly after depressurization. If future design changes require reconsideration of the pressure-equalized concept, it may be necessary to confirm these speculations with high-temperature tests.

1.4.2.6 Small-Diameter Thermocouples for Fuel Rod Simulators — R. L. Anderson

The high-temperature decalibration of small-diameter TCs was compared for type K materials processed in air or in argon. The TCs were covered with 0.5-mm-diam (20-mil) sheaths made of either 304 stainless steel or Inconel 600. The chemical changes involved in the high-temperature decalibration were investigated by the ion microprobe. In addition, the excessive failure rate of the Inconel-sheathed small-diameter TCs after installation in prototypic FRSs was investigated intensively. The Inconel sheath was found not to be a factor in the failures; rather, the failures were caused by a combination of differential thermal expansion between the 316 stainless steel FRS cladding and the thermoelements and the excessively large grain sizes found in some of the thermoelement materials. The latter is apparently a result of the TC manufacturing process.

1.4.2.6.1 Decalibration of Air- and Argon-Processed Type K Thermocouples. The decalibration of 0.5-mm-diam (20-mil) sheathed type K TCs above 900°C (1650°F) has been shown to be strongly dependent on the choice

of sheath materials;[28] TCs sheathed in stainless steel decalibrate more rapidly and more extensively than those sheathed in Inconel 600. Because of their importance in electrical heating elements, the oxidation and corrosion of nickel and nickel-chromium alloys have been intensively investigated. It has been shown in some of these investigations that the presence of water vapor can enhance corrosion,[29] particularly that of nickel-chromium alloys. Hence, argon-processed fabrication should improve the stability of sheathed TCs at high temperatures by eliminating water vapor inside the sheath.

Argon processing of sheathed TC materials includes several additional manufacturing steps that tend to eliminate water contamination: (1) after assembly of the thermoelements and insulators in the sheath, one end of the tube is welded shut; (2) the assembly is baked at high temperature [800 to 900°C (1470 to 1650°F)] and vacuum pumped; (3) the assembly is cooled, backfilled with argon, and the remaining open end is welded shut; and (4) after sealing, the assembly is reduced to the specified size by the normal drawing process without exposing the interior to air or water vapor.

Samples of air- and argon-processed 0.5-mm-diam (20 mil) type K TC materials that have either a 304 stainless steel sheath or an Inconel 600 sheath were purchased from CSG. Test TCs were fabricated from these materials in an inert-atmosphere glove box. The initial calibration of these four samples showed that each TC behaved somewhat differently (Fig. 1.54). The initial differences between TCs with identical sheath

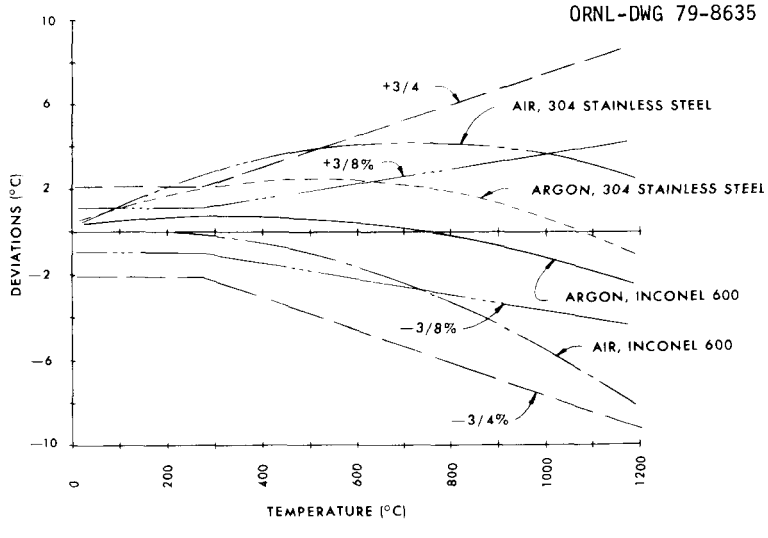

Fig. 1.54. Initial Calibration Runs with Core Flow Test Loop Type K, Small-Diameter Thermocouples.

materials are assumed to reflect the additional steps involved in baking out the argon-processed materials. The initial differences between TCs that received like processing but had different sheath materials are assumed to be caused by changes in thermoelement composition resulting from the annealing steps during manufacture. These differences are summarized in column 3 of Table 1.23.

After reaching 1100°C (2010°F) the TCs were held at this temperature for 50 h and the outputs recorded periodically. These results are shown in Fig. 1.55. After 50 h at 1100°C (2010°F), the net changes listed in column 4 of Table 1.23 were observed.

After the 50-h exposure at 1100°C (2010°F), the TCs were calibrated while cooling; these results are shown in Fig. 1.56. Comparison of the calibration data in Fig. 1.54 with those in Fig. 1.56 shows that very little change occurred in the Inconel-600-sheathed TCs, whereas the calibration of the type 304 stainless-steel-sheathed TCs after the high-temperature exposure is markedly changed from that in Fig. 1.54.

After the test assembly had cooled to about 100°C (200°F), the TCs were shifted out of the furnace by 9 cm (3.5 in.) and recalibrated to 600°C (1110°F). Shifting the TC test assembly out of the furnace placed a portion of the TCs that had been exposed to 1100°C (2010°F) in the interior of the furnace into the sharp temperature gradient at the entrance to the furnace. The results of this test are shown in Fig. 1.57 for two of the four test TCs. Column 5 in Table 1.23 gives the error in indicated temperature at 600°C (1110°F).

These results show that the choice of sheath materials is more critical to the stability of type K TCs than the atmosphere used in the processing. The TC manufactured by argon processing had less initial drift, but after the 50-h high-temperature exposure, the air- and the argon-processed TC materials behaved almost identically. One can surmise that, after a brief exposure to high temperature, the residual oxygen in the air-processed materials is exhausted by chemical reactions in the high-temperature zone with the inside surface of the sheath and the thermoelements, which inhomogeneity scans of these TCs confirm. At 175°C (350°F) the change in the Seebeck coefficient, 5 cm from the measuring junction, was -2.8% for the Inconel-600-sheathed TCs and

Table 1.23. Summary of Decalibration of Small-Diameter Type K Thermocouples

Sheath material	Processing atmosphere	Deviation at 1100°C (initial calibration) (°C)	Change after 50 h at 1100°C (°C)	Change in indicated T at 600°C (shifted 9 cm (°C)	Change in Seebeck coefficient after 50 h at 1100°C (%)
Stainless steel	Argon	-0.2	-10.9	-59	-10
Stainless steel	Air	+3.2	-11.4		
Inconel 600	Argon	-1.4	+0.26	-11.2	-2.8
Inconel 600	Air	-6.5	+1.2		

ORNL-DWG 79-8636

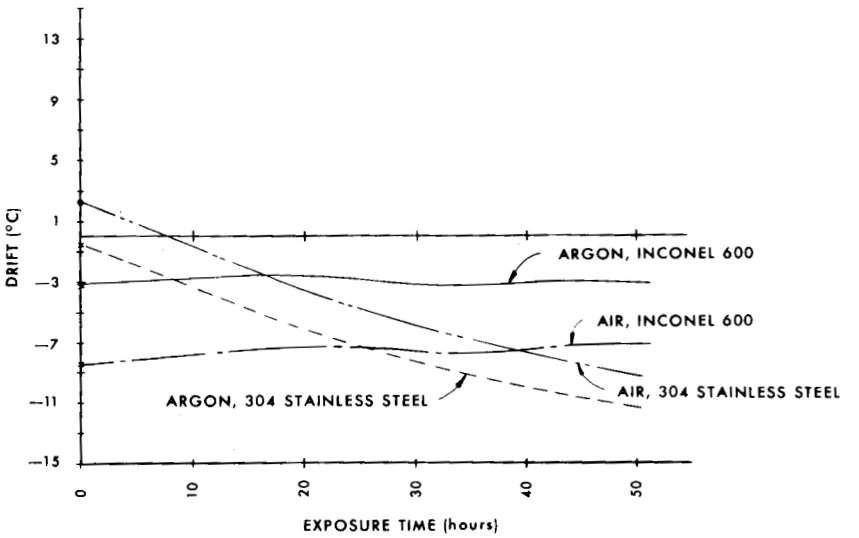

Fig. 1.55. Drift During 50-h Exposure at 1100°C with Core Flow Test Loop Type K, Small-Diameter Thermocouples.

ORNL-DWG 79-8638

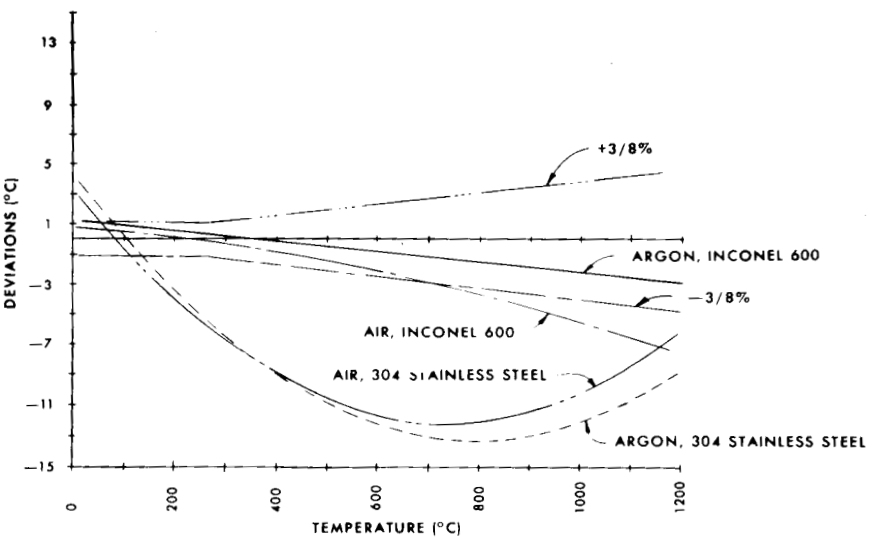

Fig. 1.56. Small-Diameter Core Flow Test Loop Thermocouple Calibration During Cooling after 50 h at 1100°C with Type K Thermocouples.

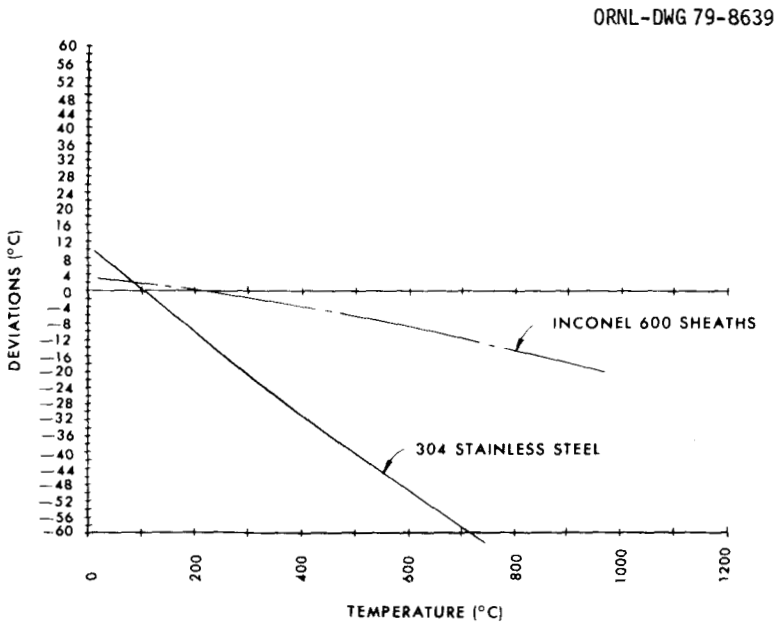

Fig. 1.57. Calibration After Shifting Core Flow Test Loop Type K, Small-Diameter Thermocouple 9 cm out of Furnace.

-10% for the type 304 stainless-steel-sheathed TCs (also shown in column 6 of Table 1.23).

1.4.2.6.2 Ion Microprobe Analysis of Type K Thermocouples. Other decalibration tests on type K TCs with 304 stainless steel and Inconel 600 sheaths have been described previously.[28] Samples were cut from four or five locations along the length of two of the four test TCs exposed at 1100°C (2010°F) for 50 h, mounted, and analyzed with the ion microprobe. Some results of this analysis are given in Table 1.24. In general, the changes observed in compositions were greater for the wires in the stainless steel sheath than for those in the Inconel 600 sheath. This result is in agreement with the changes observed in the thermoelectric properties of these TCs during the high-temperature exposure. In addition, greater changes were found in the composition of the Alumel wires than in the Chromel. Again, this result agrees with the thermoelectric data. Some of these results, along with a description of special techniques developed for these analyses, have been accepted for publication.[30]

Table 1.24. Compositional Changes in Type K Thermoelements in 0.5-mm-diam (20-mil) Sheaths of Type 304 Stainless Steel and Inconel 600 After 50 h at 1100°C (2010°F)

	Al	Si	Cr	Mn	Fe
Type 304 stainless steel					
Alumel wire					
Nominal composition	4.19	3.53	0.0002	3.01	0.031
Change in section					
A	-3.89		0.799	2.75	0.22
B	-3.91		1.189	2.66	0.30
C	-3.88	None	1.319	1.70	0.45
D	-3.49	None	0.51	3.34	0.05
E[a]	+0.44		-0.0002	-0.07	0
Chromel wire					
Nominal composition	0.021	0.92	10.37	0.010	0.35
Change in section					
A	0.003	-0.12	-1.20	3.29	0.09
B	0.004	0.12	0.25	3.47	0.25
C	0.037	0.14	-0.66	3.56	0.07
D	0.046	-0.11	-0.74	3.17	0.06
E[a]	0.011	-0.02	-0.67	0.003	0.09
Inconel 600					
Alumel wire					
Change in section					
A	-2.03	1.04	0.176	-2.16	0.048
B	-2.11	-0.10	0.173	-2.31	0.056
C	-1.87	-1.00	0.095	-1.86	0.047
D[a]	+0.05	-1.42	0.001	-0.30	0.001
Chromel Wire					
Change in section					
A	0.191		0.97	0.42	
B	0.238	None	-0.01	0.377	None
C	0.166	None	0.03	0.130	None
D[a]	0.002		0.25	0.006	

[a]Indicates as-received material, not exposed to high temperatures.

1.4.2.6.3 Disordering Kinetics in Chromel. Although Kollie et al. made extensive measurements of the rate of formation of short-range order in Chromel,[31] the converse (i.e., the rate of disordering) was not investigated. Throughout the operation of the CFTL, portions of some FRS TCs will be exposed alternately to temperatures that increase the formation of short-range order and then to temperatures that reduce the amount of order. Hence, it is important to know the rates at which these changes occur for estimating uncertainties in the temperature measurement, particularly during and immediately after temperature transients.

Seven sheathed TC assemblies were preordered over their length by heating them to 480°C (896°F) for 2 d. Five-cm-long (2 in.) segments of the TCs were then electrically heated for periods of time varying from about 1 min to 1 h. The temperature was controlled by attaching a small TC to the center of the heated section and using the output to control the electric current in the sheath with a current-adjusting electronic controller. Seven of the 5-cm (2-in.) segments of a particular TC assembly were subjected to the same temperature for different periods of time. After this treatment, the TC assembly was scanned for inhomogeneities. A typical trace is shown in Fig. 1.58.

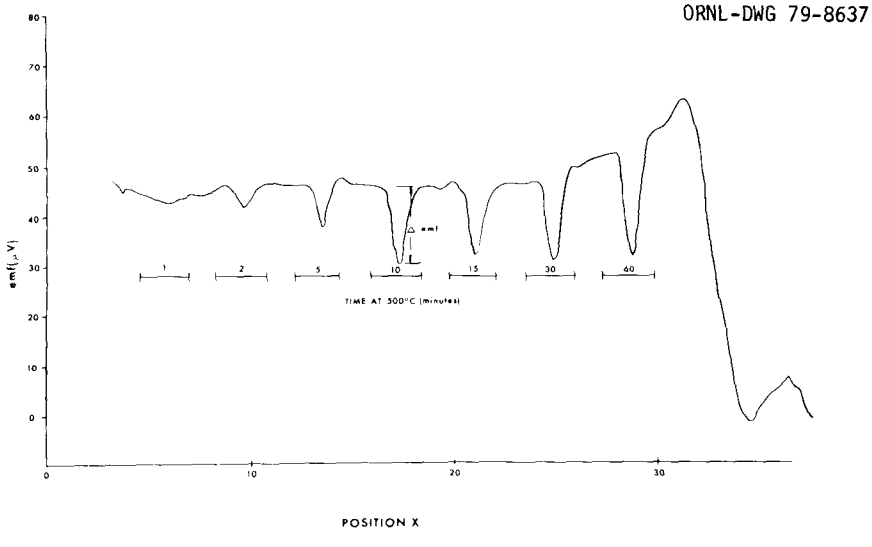

Fig. 1.58. Study of Ordering and Disordering in a Type K, Small-Diameter Core Flow Test Loop Thermocouple. Inhomogeneity trace is of a previously ordered thermocouple in which 5-cm-long segments were subsequently heated along the length shown to 500°C for the times indicated.

The results of these tests showed that the rate of formation of short-range order and the rate of disordering of previously ordered Chromel are essentially the same. The results of Kollie et al.[31] on the rate of formation of short-range order can therefore be used for the rate of disordering.

1.4.2.6.4 Pros and Cons of Intrinsic-, Grounded-, and Insulated-Junction Thermocouples. From the standpoint of analysis of the thermal data from the CFTL, the most desirable TC for the FRSs would be the intrinsic TC. (An intrinsic TC is formed when the metallic body whose temperature is to be measured is made a part of the TC electrical circuit by attaching each TC wire to the body, leaving a slight separation between the wires.) The intrinsic TC has a minimum amount of thermal shunting compared with grounded- or insulated-junction TCs. In addition, the response time of intrinsic TCs is in the range of microseconds.

Disadvantages of the intrinsic TCs include: electrical noise pickup, difficulty of fabrication, and fragility of the small wires. Tests have been reported[32] that compared the noise pickup of intrinsic, grounded-junction, and insulated-junction TCs in a room-temperature test. The noise pickup in the intrinsic TCs was about seven times that of the insulated-junction TCs. The active filters designed to retain the speed of response necessary for the temperature measurements during transients can be saturated by a noise signal that is too high. One condition must be met with an intrinsic TC: the attachment of the TC wires to the body must be in an isothermal plane. R. W. McCulloch has devised a method for attaching intrinsic TCs to the inner diameter of the FRS cladding,[33] which minimizes the handling of the delicate small wires; however, the differential thermal expansion between the TC assembly and the FRS cladding would probably result in the early failure of such TCs. Recent tests on an FRS prototype fabricated with intrinsic TCs confirm this supposition.[34]

The grounded-junction TC tends to have larger thermal shunting errors than the intrinsic but smaller than those with the insulated-junction TC. The noise pickup for the grounded junction in the above-mentioned test was about five times less than that of the intrinsic TC but about twice that of the insulated-junction TCs. The response time of the grounded-junction TC is about 2 or 3 ms, a factor of 2 or 3 faster than the

response time of the insulated-junction TC. This type of TC, however, has had a higher failure rate in thermal cycle tests. Breakage of grounded-junction TCs typically occurs near the junction, where the stress caused by differential thermal expansion between the thermoelements and the sheath is at a maximum.

The insulated-junction TC was chosen as the reference for the CFTL FRS TC because it has better reliability and minimal noise pickup compared with the other two junctions.

1.4.2.6.5 Failure of Fuel Rod Simulator Thermocouples. A high rate of failure of small-diameter TCs in FRS prototypes during thermal cycling tests prompted an investigation into the causes of the failures. Because thermal data are of prime importance to the CFTL program, extensive TC failure is intolerable.

The majority of the TC failures occurred during thermal cycling of the FRS prototypes while the temperature of the FRS was being increased. Upon cooling, the TC circuits often reclosed and the TCs read normally. Several factors were explored to determine the cause of the breakage: (1) differential thermal expansion, (2) grain size, (3) heating rate, and (4) temperature range of cycling.

(1) Differential Thermal Expansion. The differential thermal expansion between the various components in the TCs and the FRS is one contributing factor to the failure of small-diameter TCs. Figure 1.59 presents a comparison of thermal expansion of the 316 stainless steel used as the FRS cladding; the Inconel 600 used as the sheathed material for the small-diameter TCs; and Chromel, Alumel (the thermoelements in type K TCs), and platinum. Thermal expansions of the Inconel 600 and the Alumel and Chromel are very closely matched. An approximate 0.3% difference occurs in the average thermal expansion between the Inconel 600 (and also the Alumel and Chromel) and 316 stainless steel at 1000°C (1830°F).

(2) Breakage Tests. Room-temperature breakage tests were performed on new, unused samples of 0.5-mm-diam (20-mil) TCs from two different manufacturers, SDI and CSG. Six samples, each 25 mm (1 in.) long, were

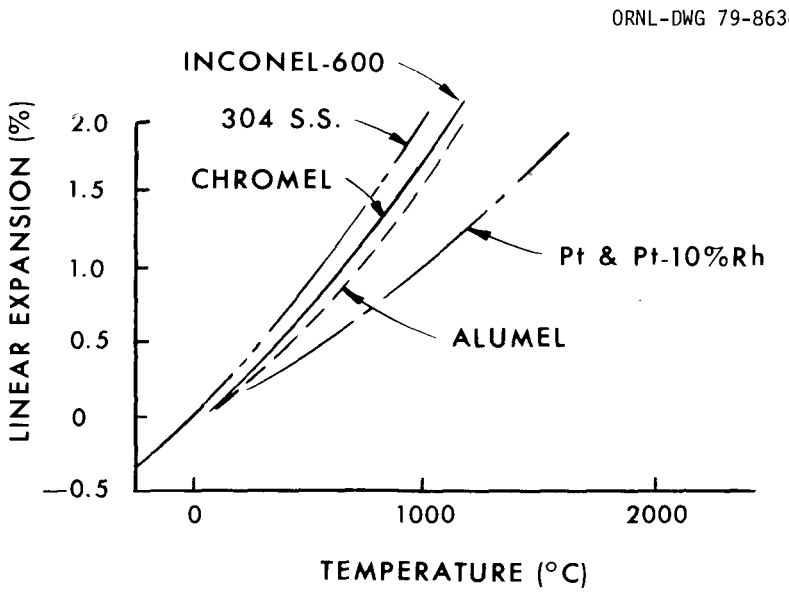

Fig. 1.59. Average Linear Thermal Expansion of Materials Being Considered for Core Flow Test Loop Small-Diameter Thermocouples.

mounted in a device that measured both the force applied to the sample and the sample elongation. Results of the tests are given in Table 1.25. In general, the Inconel-600-sheathed type K TC materials from CSG withstood about a 5% greater elongation before breaking than did the materials from SDI. With Inconel-sheathed material, both the wires and the sheaths broke at the same time. Sample of type K materials sheathed in type 304 stainless steel were also tested. In these samples, the thermoelements broke before the sheath. Four samples of type S (Pt–10% Rh versus Pt) TC material sheathed in stainless steel were tested also. In all these samples, the Pt–10% Rh wire broke. (In all cases the tests were terminated at the first breakage.) Samples taken from portions of both SDI and CSG TCs that had been heated to 1100°C (2010°F) previously during calibration runs were tested, and these samples broke with approximately the same applied load and with nearly identical elongation as the new, unused samples. The data in Table 1.25 indicate that differential thermal expansion among the sheath, insulation, and thermoelement materials in the TCs is not sufficient to explain the TC breakage in the FRS prototypes. Additional testing at more representative physical conditions and restraints was indicated.

Table 1.25. Results of Breakage Tests on Thermocouples from Two Different Manufacturers

Sample	Number of tests	Elongation (%)	Load (lb_f)
Type K in Inconel 600 sheath			
Sensor Dynamics, Inc., 120, unheated	3	16.5	13.2
Sensor Dynamics, Inc., 120, previously heated	1	14.9	10.2
C. S. Gordon, unheated	3	21.8	14.2
C. S. Gordon, previously heated	1	14.6	11.5
Type S in stainless steel			
C. S. Gordon, heated and unheated	4	25.92	16.9
Type K in stainless steel			
C. S. Gordon, unheated	3	31.2	19.0

(3) Thermal Cycling Tests. A test apparatus was designed and constructed to simulate the combined effects of thermal cycling and differential thermal expansion on the failure of FRS TCs without the necessity of fabricating FRSs. Samples were prepared by collapsing 1.5-mm-diam (60-mil) stainless steel tubing over a length of 0.5-mm-diam (20-mil) TC material. The clamping of the collapsed tubing to the outside diameter of the TC sample is intended to simulate the strong mechanical connection that exists between the FRS cladding and TCs, chiefly through the medium of the compacted BN insulation. The ends of the TC materials were stripped to expose the thermoelements. The ends of the collapsed stainless steel tube were clamped in a test stand. The clamps were also the electrical contacts for the current used to heat the tubing. The thermoelements were connected at one end of the sample, and at the other end, the two wires were connected to a circuit to monitor the loop resistance of the sample wires during testing. Changes of the loop resistance were recorded on a strip-chart recorder during the thermal

cycle tests. When a break occurred in one of the thermoelements, the recorder pen went off-scale and tripped a microswitch to shut down the system. Any desired thermal cycle can be programmed into a microprocessor-based programmer. The temperature of the sample was monitored with a small bare-wire TC spot welded to the stainless steel tube at the center of the test specimen, the point of maximum temperature. This TC was also the sensor for the system controller. Table 1.26 gives the results of the thermal cycle tests. As indicated, the rates of temperature changes were either 100 or 20°C/s (180 or 38°F/s). The TC temperature was raised from 350 to 850°C (660 to 1560°F) in 5 s, held at 850°C for 60 s, cooled at 350°C in 5 s, and held there 60 s before repeating the cycle.

Of the SDI Inconel-sheathed TC specimens, only one endured 1200 or more thermal cycles. The CSG Inconel-sheathed TC specimens endured on the average two or three times more thermal cycles than did the SDI TC samples or did not fail. Subsequent tests with additional samples of CSG TC materials were run with temperature cycling from 350 to 750°C (660 to 1380°F) at 15°C/s (25°F/s). These samples endured about 5000 cycles before failure.

Two samples from each of two SDI assemblies were stretched by 5% before thermal cycling. This treatment reduced the number of cycles to failure by a factor of about 2.

The wires from selected samples of the thermally cycled TC materials were subjected to metallographic analysis.

(4) Metallography of Failed Thermocouples. Metallography was performed on wires from failed TCs from both the thermal cycle tests and from TCs extracted from FRS prototype GLR-L-7P. Figures 1.60*a* and 1.60*b* are microphotographs of the Alumel and Chromel wires, respectively, from the FRS. Two features of these photographs are of importance in explaining the failure of the TCs during thermal cycling: (1) the large grain sizes in both wires and (2) the formation of what appears to be voids across the diameter of the wires. Such structures tend to weaken the wires so that they can more easily be pulled apart by differential thermal expansion. Additional samples (footnoted *a* in Table 1.26) were taken (1) from the center section of the thermal cycle test TC materials that had received the maximum temperature exposure,

Table 1.26. Small-Diameter Thermocouple, Thermal Cycling to Failure[a]

Source	Sheath material	Cycles to failure
Sensor Dynamics, Inc.,		
-120	Inconel 600	113
-120	Inconel 600	1756; no break
-120	Inconel 600	166
-129	Inconel 600	509
-129	Inconel 600	662[b]
-129	Inconel 600	264 (after 5% elongation)
-129	Inconel 600	198
-23	Inconel 600	93
-23	Inconel 600	52
-74	Inconel 600	260
-74	Inconel 600	135
-74	Inconel 600	75 (after 5% elongation)
-74	Inconel 600	80
C. S. Gordon		
-2	Inconel 600	1111 (heated to 1100°C for 50 h)[b]
-2	Inconel 600	1023 (from unheated section)[b]
x4652	304 stainless steel	385
HP2001	304 stainless steel	999 (unheated section)
HP2001	304 stainless steel	277 (from heated section; calibrated to 870°C)
HP2001	304 stainless steel	450 (unheated section)[c]
HP2001	304 stainless steel	579 (unheated section)[c]
x32726	Inconel 600	1457; no break[b]
x32726	Inconel 600	786[c]
x32726	Inconel 600	374[a]
x32726	Inconel 600	1305; no break[c],[b]
x32726	Inconel 600	1199; no break[c]
x32726	Inconel 600	1307; no break[c]
x32726	Inconel 600	5498; no break (350 to 750°C in 30 s or ∿15°C/s)
x32726	Inconel 600	4709; no break

[a] In the cycle the TC temperature is raised from 350 to 850°C in 5 s (100°C/s), held at 850°C for 60 s, cooled to 350°C in 5 s, and held there 60 s before repeating.

[b] Samples subjected to metallography.

[c] Same as above cycle, except duration of heating and cooling periods was increased to 30 s (∿20°C/s).

Fig. 1.60*a*. Polished and Etched Section of Alumel Wire Taken from Fuel Rod Simulator GLR-L-7P (200 ×).

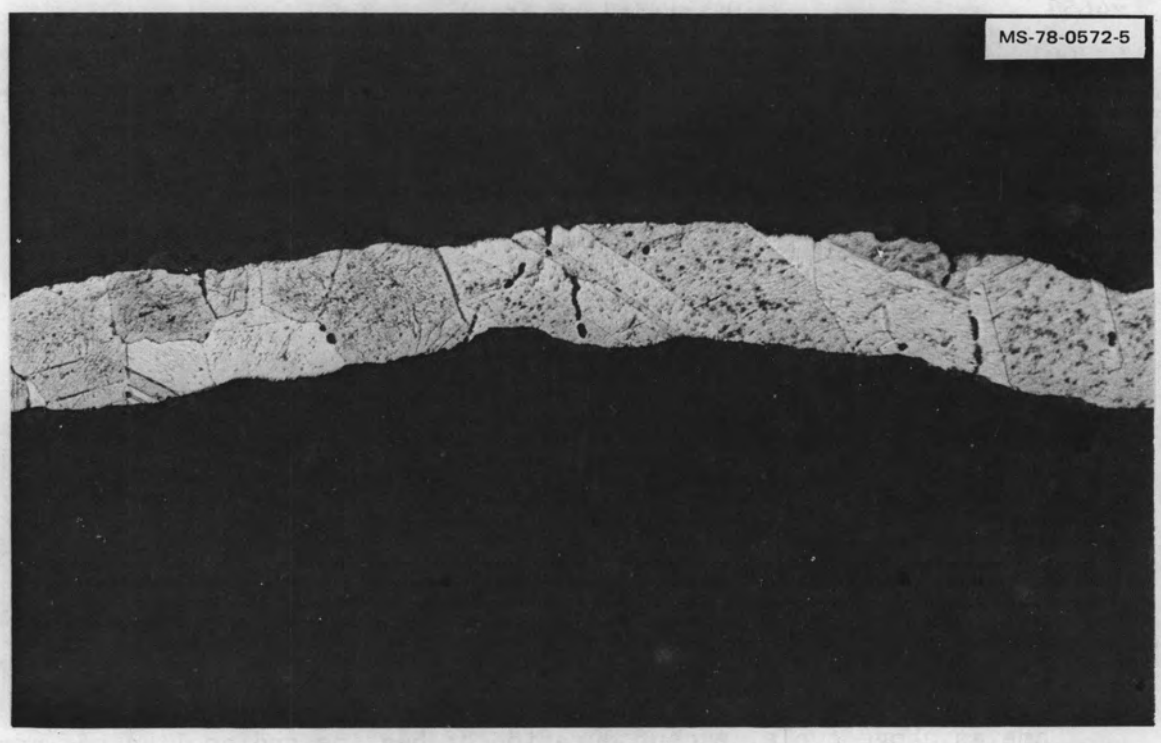

Fig. 1.60*b*. Polished and Etched Section of Chromel Wire Taken from Fuel Rod Simulator GLR-L-7P (200 ×).

(2) from the ends that were under the clamps and remained essentially at room temperature, and (3) from a point about 2 cm (1 in.) from the end in the region of the greatest temperature gradient.

Figures 1.61*a* and 1.61*b* are Chromel and Alumel samples from the center of SDI assembly 129, which failed after 662 cycles. Figures 1.61*c* and 1.61*d* are Chromel and Alumel samples from the ends (unheated portion) of the same test specimen. Little, if any, increase in grain size was caused by the thermal cycling, but the grain size in these samples was comparatively large initally. The Alumel from the center of the test section shows the formation of what appears to be voids. Repolishing a similar sample with diamond abrasive and analysis by electron microprobe showed that these apparent voids were high concentrations of aluminum, segregated out at the grain boundaries. The voids in the photograph were apparently formed by the etching of the polished samples.

In comparison, the Chromel and Alumel wire in Figs. 1.62*a* and 1.62*b*, from a CSG test specimen that did not fail after more than 1450 thermal cycles, exhibited much smaller grain sizes. Evidence of grain boundary segregation similar to that observed in the SDI samples was also found in the Alumel. However, in a CSG specimen having the smaller grain size, no boundaries that extend across the diameter of the wire were found. Figures 1.62*c* and 1.62*d* are samples taken from the unheated portion of the test specimen. The grain size is appreciably smaller than that in the unheated SDI samples.

Figures 1.63*a* and 1.63*b* show samples of Chromel and Alumel taken from a CSG specimen that was held at 1100°C (2010°F) for 50 h before being subjected to the thermal cycle tests. Even after this rather severe heat treatment, the specimen endured 1111 thermal cycles before failure. In both the Chromel and Alumel, evidence exists of grain boundary segregation. In the case of the Chromel, the electron microprobe showed that the material that segregated at the boundaries was mainly chromium. Again, the grain size is smaller in the samples from the unheated (in the thermal cycle tests) section in Fig. 1.63*c* and 1.63*d* than that in comparable samples from the SDI specimens (Fig. 1.61*c* and 1.61*d*), even after 50 h at 1100°C (2010°F).

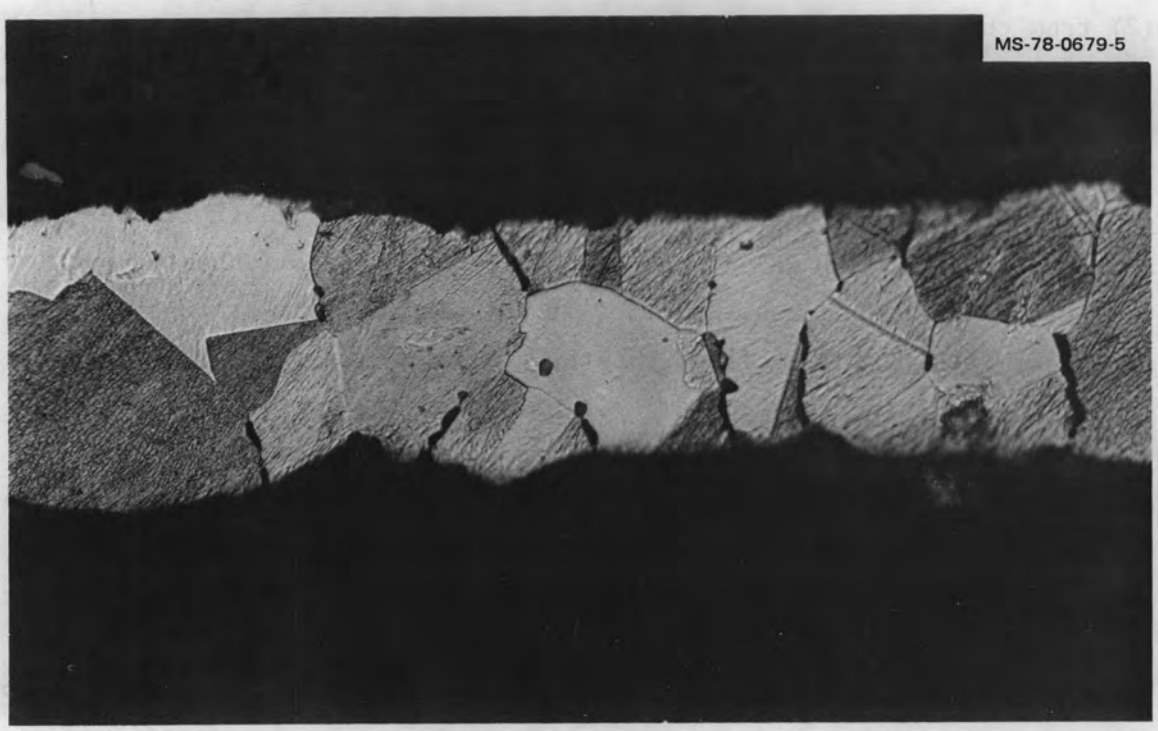

Fig. 1.61*a*. Polished and Etched Section of Alumel Wire from Heated Part of Thermally Cycled Sample from Sensor Dynamics, Inc., Assembly 129 (400 ×).

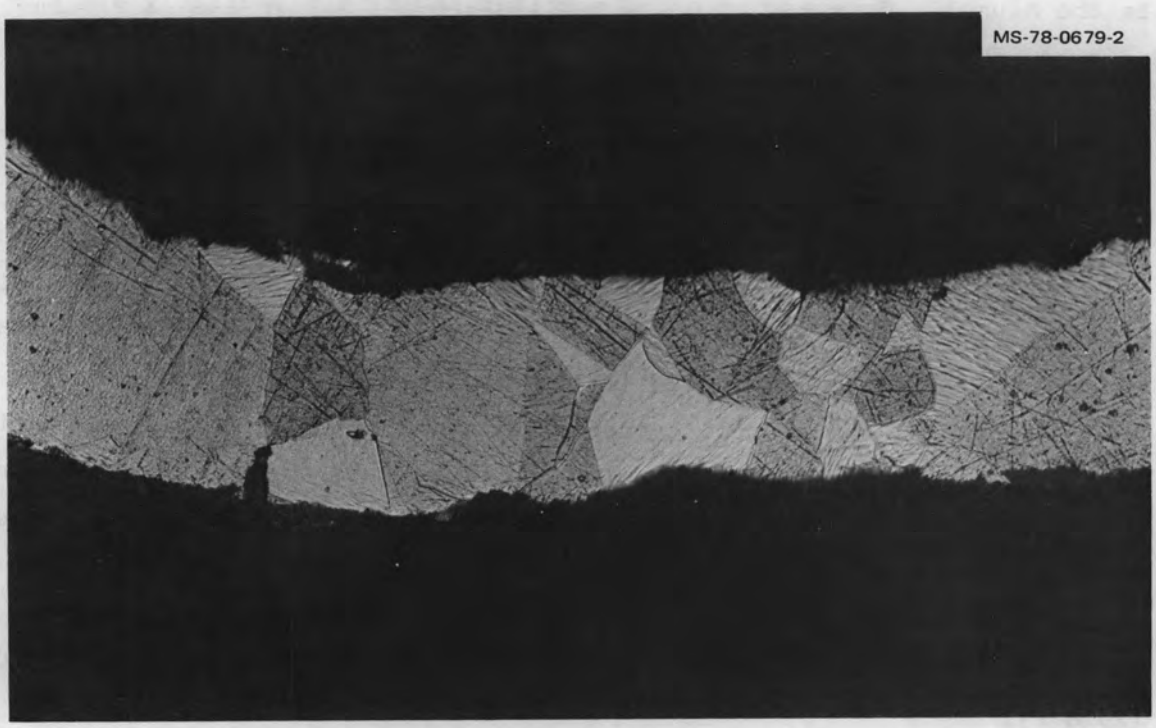

Fig. 1.61*b*. Polished and Etched Section of Chromel Wire from Heated Part of Thermally Cycled Sample from Sensor Dynamics, Inc., Assembly 129 (400 ×).

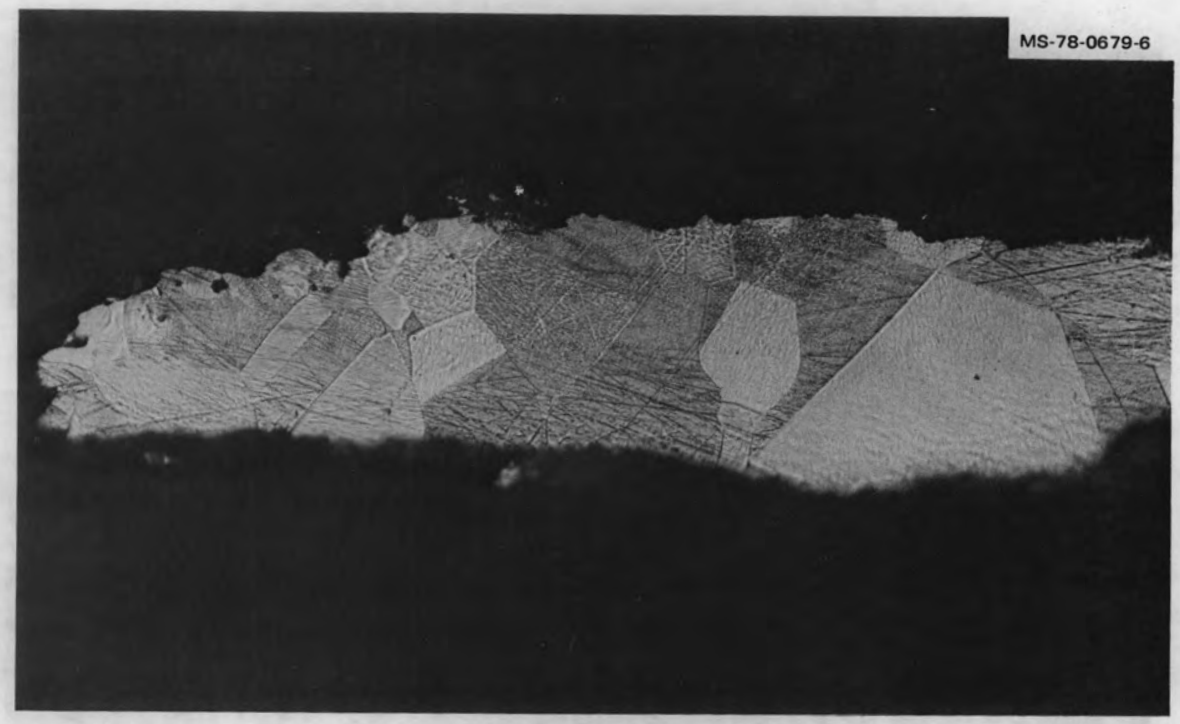

Fig. 1.61*c*. Polished and Etched Section of Alumel Wire from Unheated Part of Thermally Cycled Sample from Sensor Dynamics, Inc., Assembly 129 (400 ×).

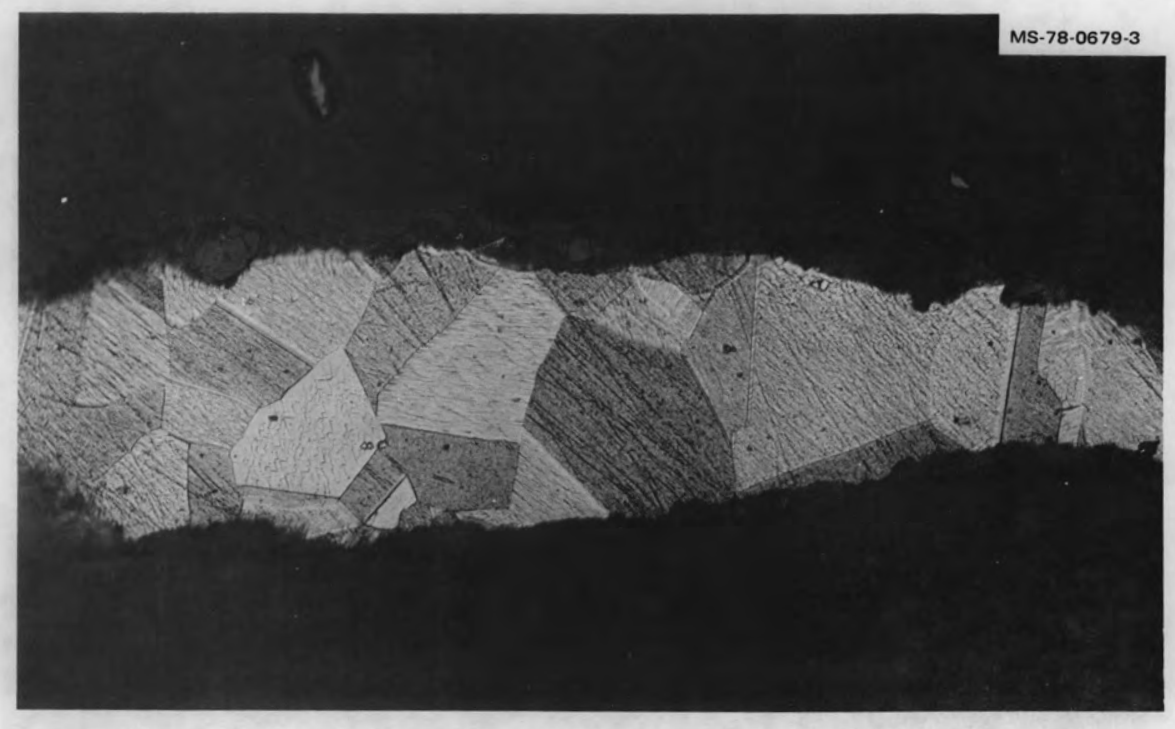

Fig. 1.61*d*. Polished and Etched Section of Chromel Wire from Unheated Part of Thermally Cycled Sample from Sensor Dynamics, Inc., Assembly 129 (400 ×).

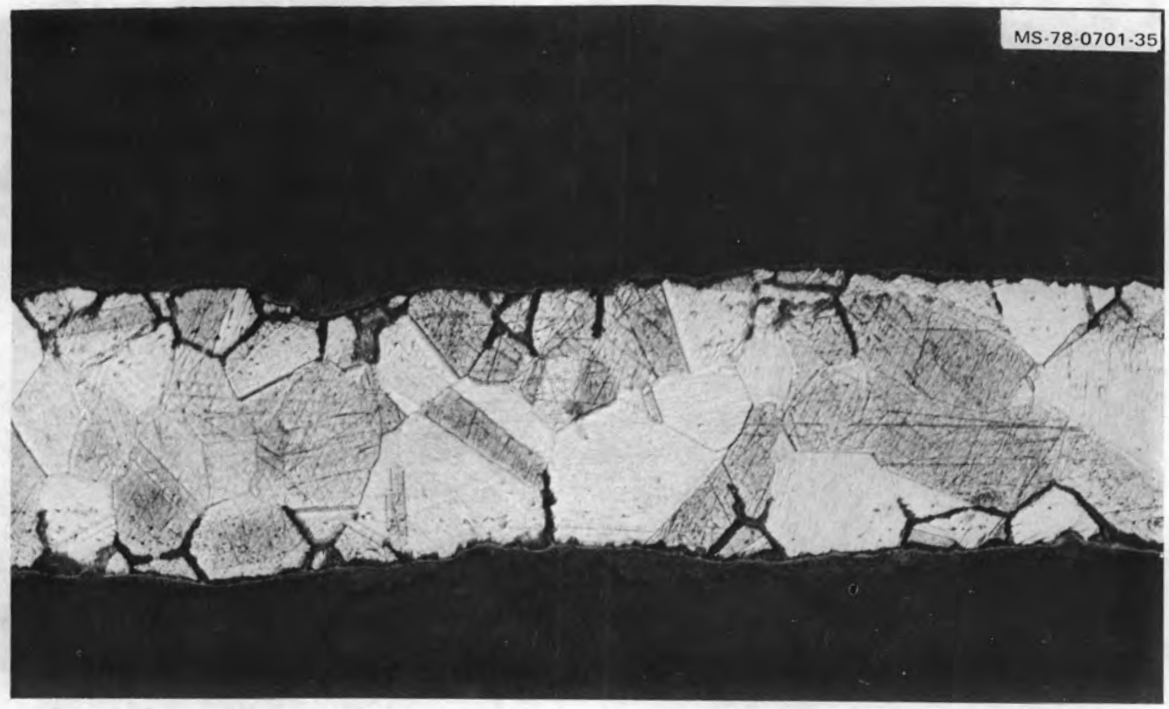

Fig. 1.62*a*. Polished and Etched Section of Alumel Wire from the Heated Part of Thermally Cycled Sample from Bulk Material That Did Not Fail During Thermal Cycling (400 ×).

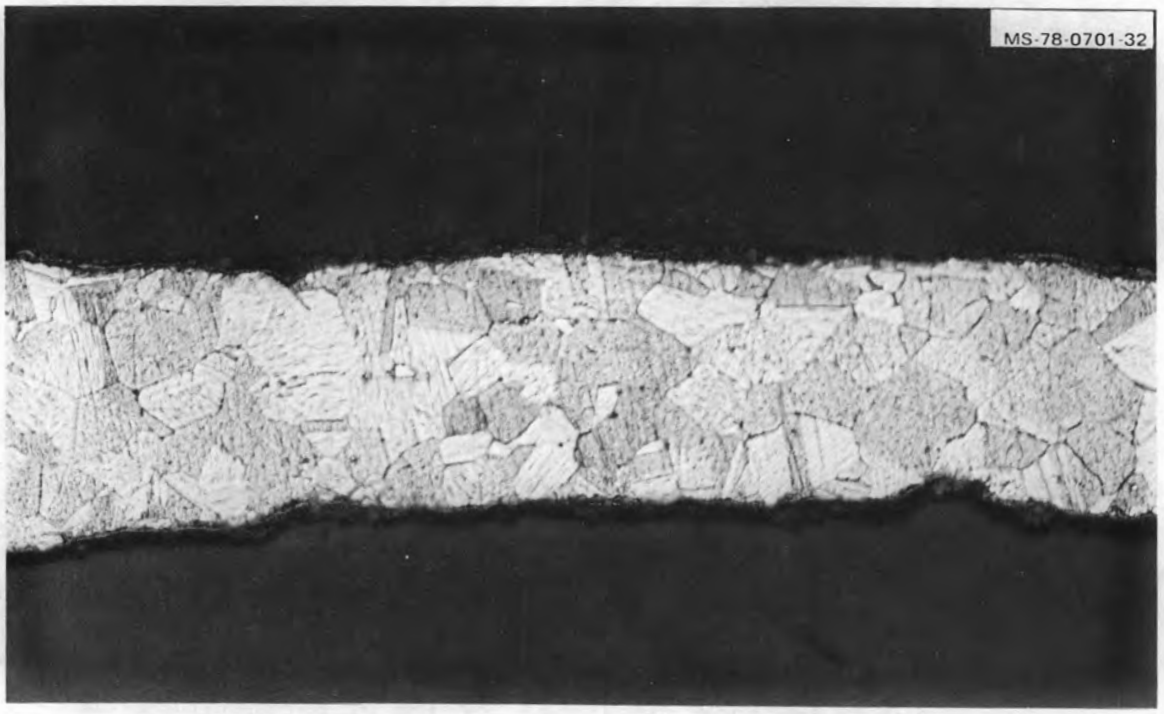

Fig. 1.62*b*. Polished and Etched Section of Chromel Wire from the Heated Part of Thermally Cycled Sample from C. S. Gordon Bulk Material That Did Not Fail During Thermal Cycling (400 ×).

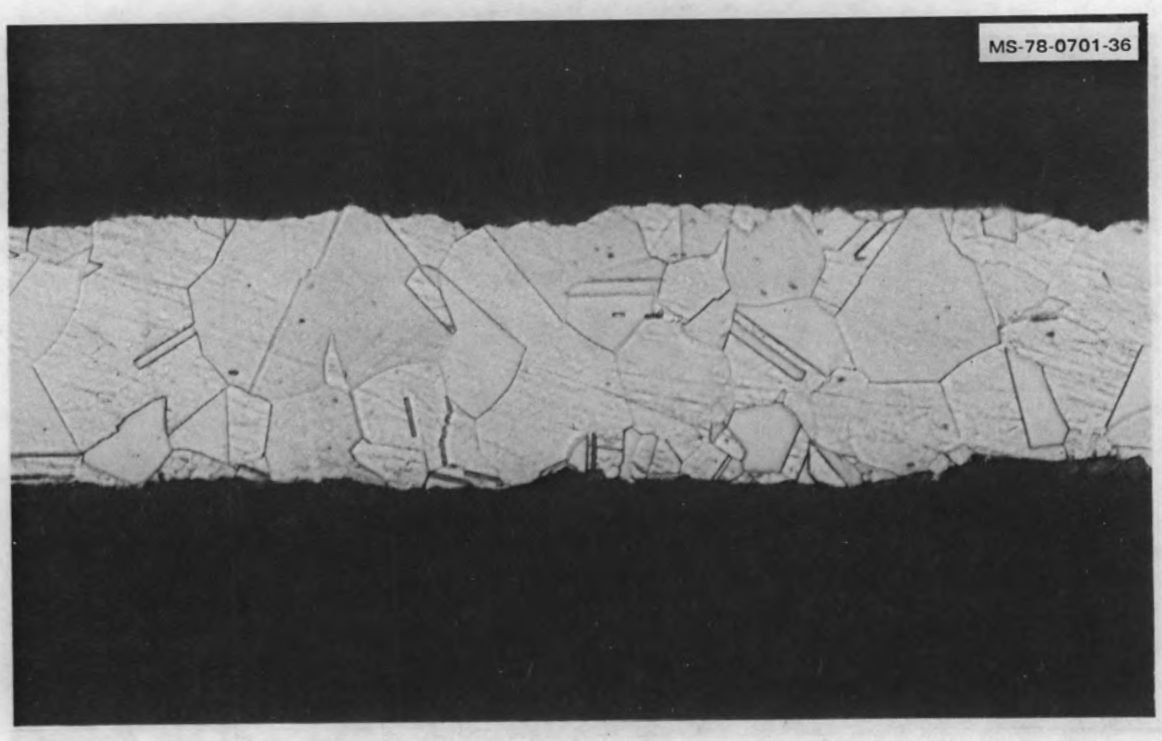

Fig. 1.62*c*. Polished and Etched Section of Alumel Wire from Unheated Part of Thermally Cycled Sample from C. S. Gordon Bulk Material That Did Not Fail During Thermal Cycling (400 ×).

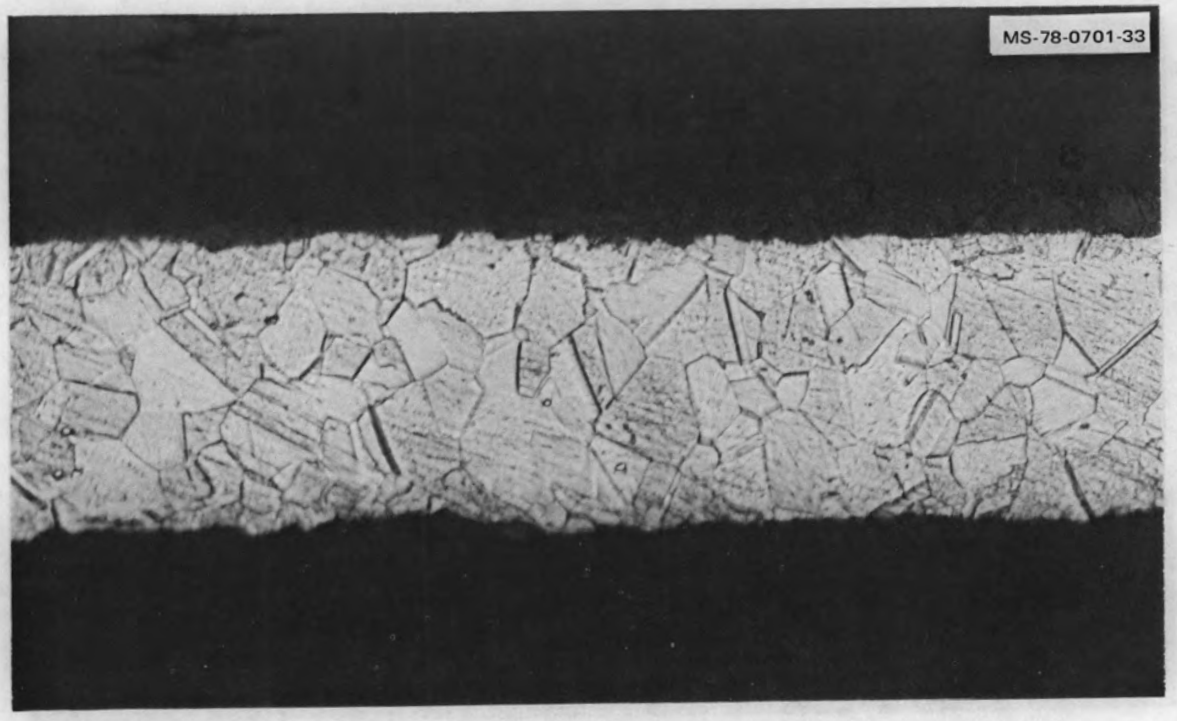

Fig. 1.62*d*. Polished and Etched Section of Chromel Wire from Unheated Part of Thermally Cycled Sample from C. S. Gordon Bulk Material That Did Not Fail During Thermal Cycling (400 ×).

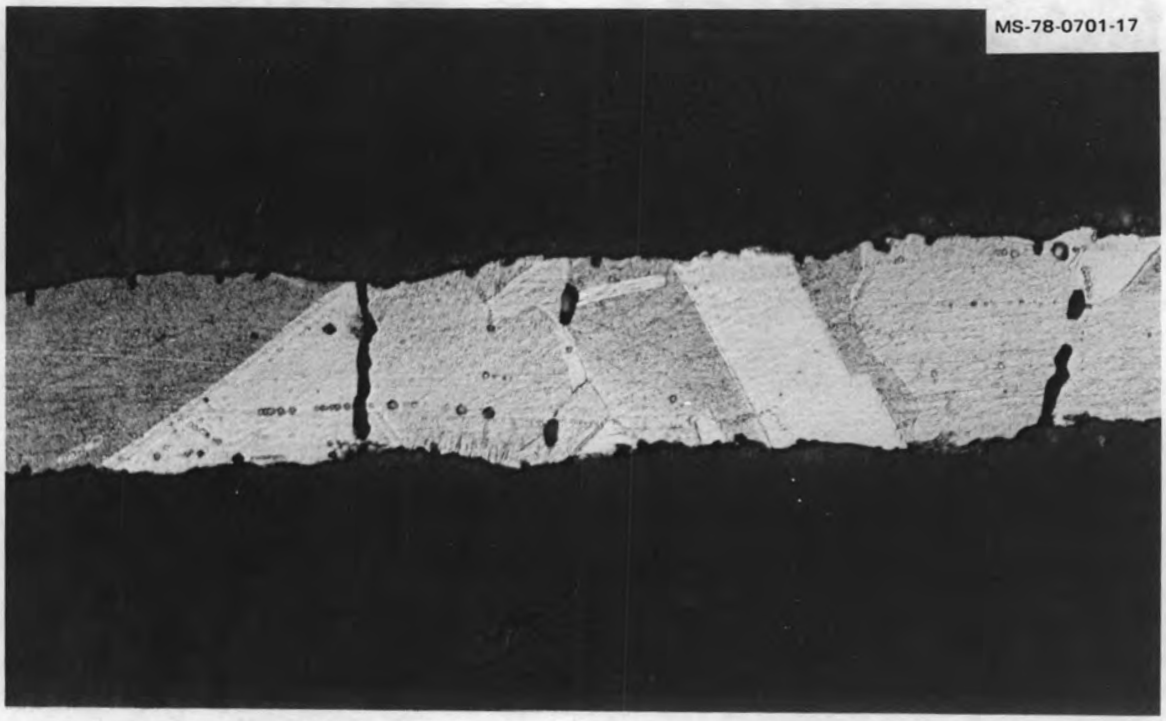

Fig. 1.63*a*. Polished and Etched Section of Alumel Wire from Heated Part of Thermally Cycled Sample from a C. S. Gordon Test Thermocouple That Had Been Exposed to 1100°C for 50 h Before Thermal Cycling (400 ×).

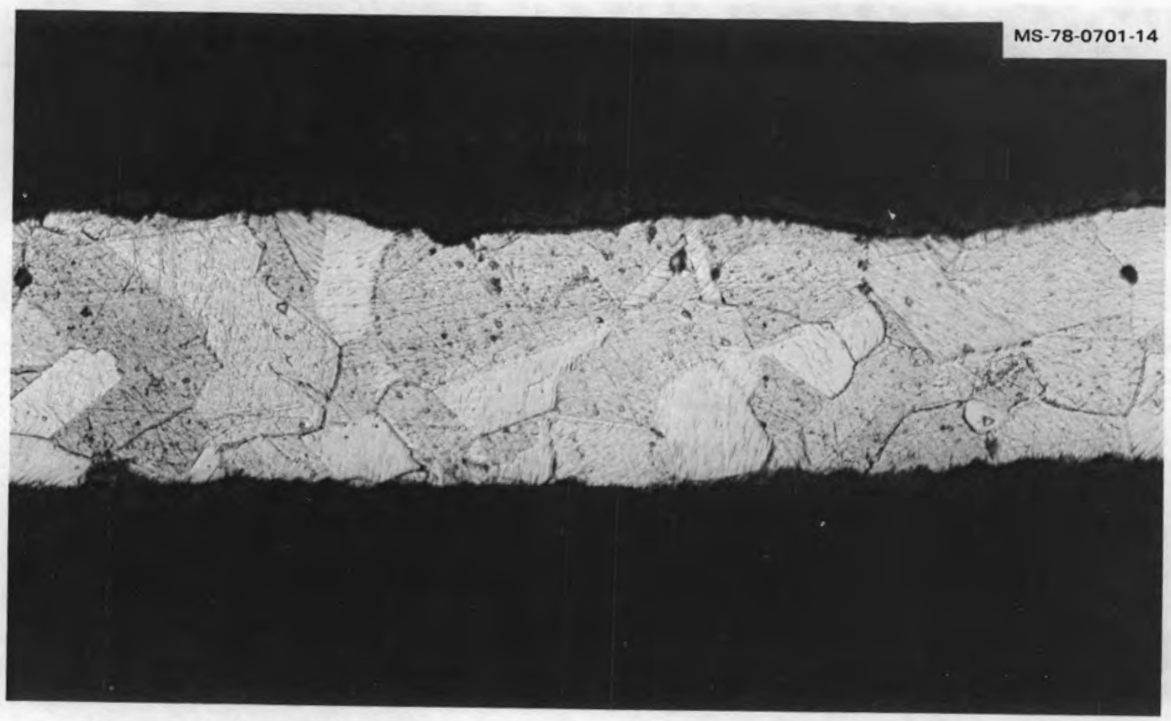

Fig. 1.63*b*. Polished and Etched Section of Chromel Wire from Heated Part of Thermally Cycled Sample from C. S. Gordon Test Thermocouple That Had Been Exposed to 1100°C for 50 h Before Thermal Cycling (400 ×).

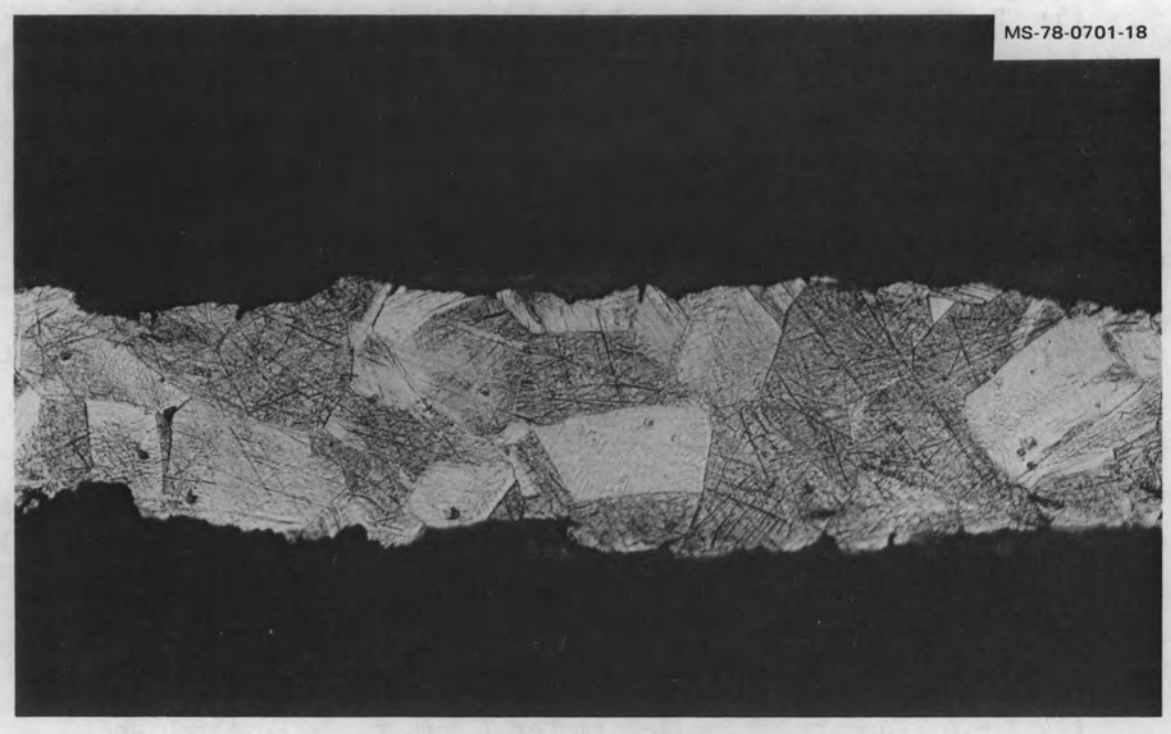

Fig. 1.63*c*. Polished and Etched Section of Alumel Wire from Unheated Part of Thermally Cycled Sample from a C. S. Gordon Test Thermocouple That Had Been Exposed to 1100°C for 50 h Prior to the Thermal Cycling Test (400 ×).

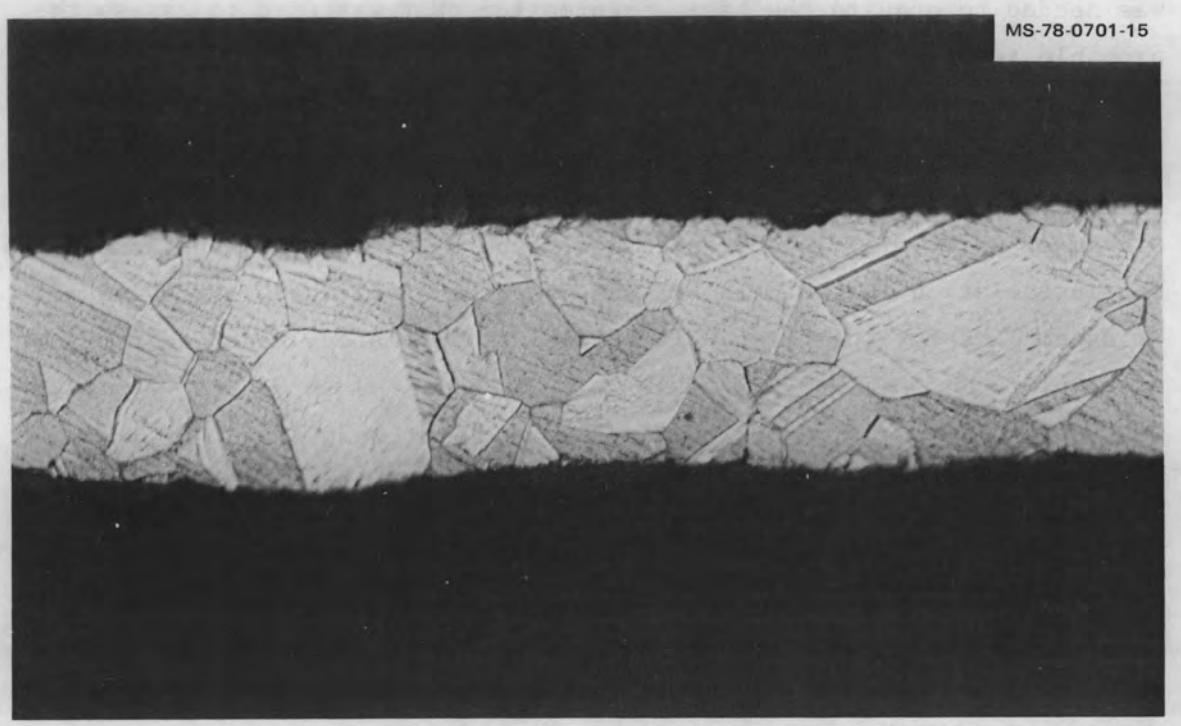

Fig. 1.63*d*. Polished and Etched Section of Chromel Wire from Unheated Part of Thermally Cycled Sample from C. S. Gordon Test Thermocouple That Had Been Exposed to 1100°C for 50 h Prior to the Thermal Cycling Test (400 ×).

(5) Summary of Thermocouple Failure Analysis. The almost 100% failure rate of the small-diameter FRS TCs in static tests and during thermal cycling was found to be caused by a combination of the grain size of the thermoelements and of the differential thermal expansion between the 316 stainless steel FRS cladding and the Inconel 600 TC sheath and the thermoelements (the Inconel 600 sheath and the thermoelements can be considered as a unit because their thermal expansions are very nearly identical). As shown in the microphotographs, the Alumel is more susceptible to excessive grain growth.

The SDI TCs exhibited a wider variation of loop resistance (100%) and thermoelectric properties in initial testing than is usually found even in 0.5-mm-diam (20-mil) TCs. Thermocouples made from CSG Inconel-600-sheathed type K bulk materials that were subsequently installed into the nonswaged FRS prototype have exhibited good reliability during testing.

1.4.2.6.6 Summary of Small-Diameter Thermocouple Research and Error Analysis. A description of the research and development activities conducted over the past three years on small-diameter sheathed TCs has been prepared for publication.[35] A substantial amount of this research was needed to acquire the basic information that was used to assess the probable temperature measurement errors of CFTL.

1.4.2.6.7 Specifications for Small-Diameter Inconel-600-Sheathed Type K Thermocouples for CFTL. A new specification for the purchase of 0.5-mm-diam (20-mil) Inconel-sheathed, type K TC materials and assemblies for installation in the CFTL FRS was prepared and issued. Purchase of TC assemblies for the first CFTL bundle was initiated, based on this document.

1.4.2.7 Structurally Related Measurements — S. P. Baker and H. J. Metz

An extensive search of the offerings of manufacturers of high-temperature accelerometers and microphones was made. Several manufacturers of high-temperature accelerometers and one of high-temperature microphones were found who can meet or nearly meet the measurement and environmental requirements of the CFTL. The accelerometer manufacturers are West Coast

Research, Kaman, Endevco, and Vibro-Meter; the microphone manufacturer is Kaman. The optimum transducer for each application will be chosen next year, and specifications for purchase will be written.

1.4.3 Test Bundle Procurement — H. C. Young

Figure 1.64 presents a summary schedule of the major components that must be procured for the first test bundle. Title II design of the bundle started in October 1978, and the bundle is to be assembled and completely ready for installation in the CFTL by September 1981.

With the formal decision in October 1978 to change from the swaged to the nonswaged FRS, the plans for procurement of the rod cladding were revised. Previously ORNL was to provide the cladding and, after completing fabrication and swaging, was to send the FRS to GA for surface roughening.

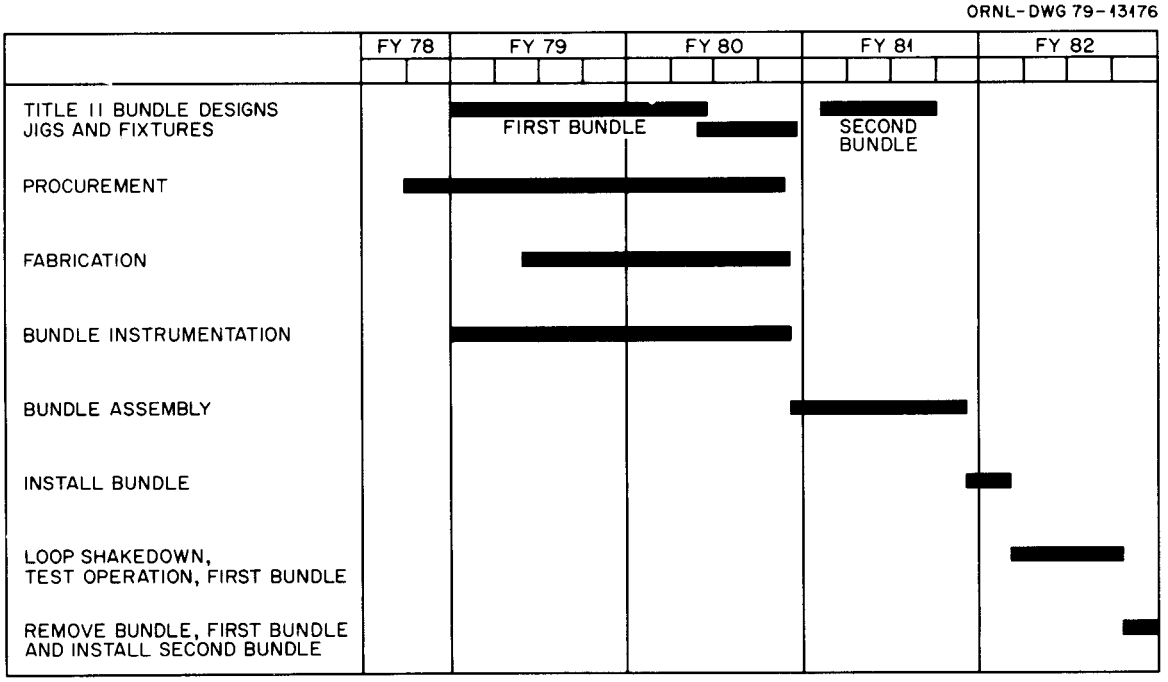

Fig. 1.64. Schedule for Design, Construction, Assembly, and Operation of the First and Second Core Flow Test Loop Bundles.

As part of the 1978 decision, GA was requested to provide and roughen 75 claddings, each 2420 mm long, for the first bundle FRSs. The cladding is to be to the material specifications, rod dimensions, cold-worked condition, and quality assurance requirements that GA is specifying for the GCFR rods. The requested delivery date is August 1, 1979. General Atomic Company considered procurement to RDT standards; however, ORNL recommended that procurement of the cladding be to ASME Materials Standard SA 213 and that additional tests and inspections meet the requirements of Section III, Class 1, of the ASME Code.

All FRS internal parts are expected to be delivered in 1979. All materials for the FRS power terminals, namely, the solid 2.15-mm-diam (0.085-in.) copper and nickel center rods and the 4.2-mm-diam (0.165-in.) by 2.5-mm-wall (0.010-in.) copper and nickel tubing, will be ordered and delivered during 1979. Materials for making either Kanthal or Nichrome V heating elements are on hand. Winding of the variable-width heating element will be initiated in 1979. Delivery of BN preforms is expected in 1979.

The location of the FRS internal TCs was agreed upon between ORNL and GA. The TCs will be fitted with wire extensions of the same diameter as the TC from the junction to the bottom of the FRS to provide a uniform crushing process for the BN preforms. In some TCs the otherwise Inconel extension will include a short length of platinum of the same diameter as the TC inserted at a specified elevation to act as a marker for the x-ray imaging process for measuring FRS movement.

The ORNL Instrumentation and Controls Division prepared and the CFTL project reviewed and approved Specification I.S. 523-0 for the procurement of 0.5-mm-diam (0.020-in.) FRS internal TCs that utilize MgO insulation and ungrounded junctions. Based on poor delivery experience on similar orders for small-diameter TCs, we will order TC assemblies plus spare TC bulk material length from more than one manufacturer. Delivery of the TCs is expected in September 1979. Initial work with a TC in which the immediate region about the junction is backfilled with BN rather than with MgO indicates a much improved response time. If this work proves fruitful, TCs backfilled with BN will be installed in the CFTL FRSs as soon as practicable.

The hexagonal duct, grid spacers, and hanger rod assemblies are to be provided by GA. Upon delivery of the items by June 1980, ORNL will make any necessary modification to install instrumentation and to seal the hexagonal duct against bypassing the test bundle with helium coolant and at the same time to permit unrestrained duct bowing during skewed power and transient operations. Thermocouples are also to be installed on some grid spacers if practicable.

The tube sheet for the first test bundle will be machined from a blank for a Grayloc flange. The Grayloc flange, clamp ring, and seal ring will be ordered in time to provide for weld-overlaying the tube-sheet surface with austenitic 308 stainless steel and for drilling penetration holes for the FRSs. The weld overlay is to prevent crack formation during the subsequent welding of the FRS cladding-to-tube-sheet joints.

Bundle instrumentation must be designed, bid and awarded, and delivered to accomplish installation in the first bundle by the end of FY 1980.

1.5 REFERENCES

1. H. C. Hopkins, Jr., *Program Plan for GCFR Core Flow Test Loop (CFTL)*, Rev. 1, GA GCFR 780515029, General Atomic Company, (May 15, 1978) (revision pending).

2. General Atomic Company, *Scope of Total CFTL Test Specifications*, GA GCFR 780104226 (Jan. 4, 1978).

3. Oak Ridge National Laboratory, *GCFR Annu. Prog. Rep. Dec. 31, 1977*, ORNL-5426 (August 1978).

4. A. G. Grindell and W. R. Huntley, *System Design Description for the GCFR Core Flow Test Loop*, ORNL/GCR-77/26, Rev. 1 (June 5, 1978).

5. W. R. Huntley, *CFTL Quality Assurance Program Plan*, Q-11590-ET-001-S-0, Oak Ridge National Laboratory (Oct. 31, 1978).

6. Ref. 3, pp. 97–99.

7. C. L. Wheeler et al., *COBRA-IV-I: An Interim Version of COBRA for Thermal-Hydraulic Analysis of Rod Bundle Nuclear Fuel Elements and Cores*, BNWL-1962, Pacific Northwest Laboratories (March 1976).

8. H. C. Hopkins, Jr., *TSPEC — A Computer Program to Predict Approximate Model Performance in the Core Flow Test Loop*, GA-A14057, General Atomic Company (November 1976).

9. A. Martelli, *SAGAPO — A Computer Code for the Thermo-Fluiddynamic Analysis of Gas-Cooled Fuel Element Bundles*, KFK-2483 (EUR 5510e), Gesellschaft fur Kernforschung M.B.H., Karlsruhe, F.R.G. (August 1977).

10. Mario Dalle Donne, *Heat Transfer from Rough Surfaces*, KFK-2937, Kernforschungszentrum Karlsruhe, F.R.G.; translated from German and distributed as EURFNR-1428 Dept. of Energy Technical Information Center (February 1978).

11. Ref. 3, pp. 98–99.

12. D. S. Rowe, *COBRA IIIC: A Digital Computer Program for Steady-State and Transient Thermal-Hydraulic Analysis of Rod Bundle Nuclear Fuel Elements*, BNWL-1695, Pacific Northwest Laboratories (March 1973).

13. Ref. 3, pp. 98–99.

14. Klaus-Jurgen Bath, *ADINA: A Finite Element Program for Automatic Dynamic Incremental Nonlinear Analysis*, Report 82448-1, Massachusetts Institute of Technology, Cambridge, Mass. (May 1977).

15. Mechanicap Properties Data Center, *Aerospace Structural Metals Handbook*, vol. 2, Sect. Code 1307, AFML-TR-68-115, Traverse City, Mich., 1978, p. 15.

16. Union Carbide Corporation, *UCAR Boron Nitride Certified Grade HBC Hot-Pressed Shapes*, Tech. Bull. 442-217, New York (August 1977).

17. Ref. 3, pp. 47–53.

18. S. P. Baker et al., *CFTL Flowmeter Engineering Feasibility Assessment*, CFTL 78-99 (June 16, 1978).

19. General Atomic Company, *Test Specification for GCFR-CFTL Rod Simulator Blanket Assembly*, Document 903576 (Mar. 28, 1978).

20. General Atomic Company, *CFTL Test Specifications — Tentative Revisions to Requirements for Test Conditions*, Document 780831226 (Aug. 31, 1978).

21. Ref. 3, pp. 20–24.

22. Ref. 3, p. 28.

23. S. P. Baker, *X-Ray Imaging — A tool for Making Structural Measurements on CFTL Test Bundles, A Feasibility Evaluation*, ORNL report, to be published.

24. J. A. Seneker, *Design Study of Various CFTL Test Bundle Concepts to Accommodate Change in FRS Pitch and to Equalize Pressure Across the FRS*, CFTL 78-111 (June 30, 1978).

25. J. A. Seneker, *Thermal and Stress Analysis of CFTL Test Bundle Tube Sheet*, CFTL 78-181 (Aug. 30, 1978).

26. Ref. 3, p. 9.

27. Ref. 3, p. 10.

28. Ref. 3, pp. 56–72.

29. C. E. Lowell and D. L. Deadmore, *Formation and Breakdown of a Protective Layer of Chromium Sesquioxide on F-605 Alloy at 1100°C*, NASA TN D-7255, National Aeronautics and Space Admin., Washington, D.C. (1973).

30. W. H. Cristie et al., "Microprobe Analysis of Decalibrated Chromel versus Alumel Thermocouples: A Quantitative SIMS Analysis Using Indexed Sensitivity Factors and Oxygen Flooding," to be published in *Applications of Surface Science*.

31. T. G. Kollie et al., "Temperature Measurement Errors with Type K (Chromel vs Alumel) Thermocouples Due to Short-Range Ordering in Chromel," *Rev. Sci. Inst.* 46: 1446 (1975).

32. Oak Ridge National Laboratory, *GCFR Program Prog. Rep. July 1, 1975–Dec. 31, 1976*, ORNL-5294 (1977), pp. 27–31.

33. R. W. McCulloch, ORNL Engineering Technology Division, private communication, Nov. 15, 1978.

34. *GCFR-CFTL Prog. Rep. December 1978 and January 1979*, ORNL/GCR/F-79/1, p. 9.

35. R. L. Anderson and T. G. Kollie, *Accuracy of Small Diameter Sheathed Thermocouples for the Core Flow Test Loop*, ORNL-5401, to be published.

2. GCFR SHIELDING AND PHYSICS STUDIES

D. E. Bartine

2.1 INTRODUCTION — D. E. Bartine

Activities carried out in the GCFR Shielding and Physics Program during 1978 include completion of the grid-plate shield experiment and associated analyses; preanalysis of the radial blanket and shield experiment; design support analysis for the upper and lower axial shield areas; investigation of heterogeneous GCFR core configurations for alternate fuel cycles, including the use of time-dependent fuel cycle sensitivity methods; and analysis of the critical experiments performed at the Swiss Federal Institute for Reactor Development (EIR), Würenlingen, Switzerland, using thorium oxide pins in a GCFR-type core and axial blanket.

The grid-plate shield experiment investigated the effectiveness of the grid-plate shield design and attempted to establish the validity of the methods used for shielding calculations. Before the experiment, a factor-of-2 uncertainty was assumed in the application of calculations of the grid-plate shield effectiveness. Comparison of calculations with experiment indicated agreement within 50% at the grid plate in all cases and within the 10% experimental uncertainty in many cases. As part of this experiment, pin-pitch and duct-spacing variations were employed to measure the effect of these parameters on axial leakage. The results indicated a significant increase (up to 60%) due to employing 91-pin subassemblies instead of 127-pin subassemblies but showed little change due to varying the duct spacing from 12.7 to 3.18 mm. The radial blanket and shield experiment includes generic thorium oxide radial blanket configurations to give measurements of deep-penetration neutron spectra and gamma-ray production in thorium blankets. Major shield-design-support calculations were performed with a special modification of the DOT-IV code to permit very large calculations, indicating that shielding problems still exist for the lower portion of the outer radial shield. Investigations of GCFR heterogeneous core configurations indicated a small fissile inventory penalty for insertion of radial and inner thorium oxide blanket assemblies (compared with UO_2 blankets) and

achieved a high ^{233}U production rate, which would be very desirable for an "inside" fast reactor in a symbiotic system with "outside" thermal advanced converters.

2.2 GRID-PLATE SHIELD-DESIGN CONFIRMATION EXPERIMENT — F. J. Muckenthaler, C. O. Slater, S. N. Cramer, and D. T. Ingersoll

2.2.1 Experimental Results

Measurements for the grid-plate shield-design study, completed during April 1978, were divided into four parts: (1) measurements of the TSR-II reactor neutron flux distribution inside the void where the fuel pins were to be placed, (2) measurement of the neutron leakage spectrum from the fuel pins onto the grid-plate shield, (3) measurement of the neutron flux distribution incident upon the grid plate, and (4) determination of the neutron source term incident upon the upper axial region (i.e., emerging from the prototypic grid plate).

The variables in the program plan were the number of fuel pins in each of the seven subassemblies that served as a mockup of the GCFR core and the spacing between these subassemblies. Priorities were established so that the measurements would be made in their order of importance.[1]

We began the experimental program in October 1977 and during the remainder of the year completed the measurements for priority 1A (127 fuel pins per subassembly with 12.7-mm spacing between subassemblies). The remaining four priorities (1B, 1C, 2, and 3) were completed during 1978. For priority 1B the number of fuel pins per subassembly remained at 127, but the spacing between subassemblies was changed to 6.35 mm. In priority 1C the subassemblies contained only 91 fuel pins each, and the spacing between subassemblies reverted to 12.7 mm. In priority 2 the fuel pin and grid-plate shield mockups were the same as in priority 1C except for removal of seven fuel pins from the center of the central subassembly. Priority 3 also contained 127 fuel pins per subassembly with the spacing between subassemblies reduced to 3.2 mm.

The measurements consisted of (1) neutron spectral determinations behind several of the configurations using the NE-213 scintillator and hydrogen-filled proton recoil counters and (2) radial and axial traverses at selected distances behind and along the axis of the mockups using the cadmium-covered and 5-in. Bonner balls and the Hornyak button. The experiment and the resulting measurements are described elsewhere.[2]

2.2.2 Analysis of Results

We completed the analysis of selected configurations of the experiment and began drafting the final report. The various configurations are described elsewhere.[2] The configurations analyzed were (1) the basic empty cavity case; (2) all fuel pin arrangements (five in all) except the one with the control rod mockup; (3) two configurations with subassemblies spaced 12.7 mm apart, which contained the grid-plate shields and either 91 or 127 fuel pins per subassembly in the core; (4) the 127-fuel-pin subassembly, 12.7-mm subassembly spacing case with the solid steel plates behind it; and (5) the latter case with the prototypic grid plate. Thus, a total of nine configurations were analyzed. The calculations were done with the DOT IV[3] discrete-ordinates computer code and the MORSE[4] Monte Carlo code.

Several detectors were used in the measurements. The various Bonner balls, whose response functions are reasonably well known, were used to make integral measurements within and behind the configurations. The 2-in. cadmium-covered and 5-in. Bonner balls were used most often, whereas the 2-in.-bare, 3-in., 6-in., 8-in., 10-in., and 12-in. balls were used only at selected locations, mainly as indicators of the neutron spectrum. The NE-213 and hydrogen counter spectrometers were used to measure the fast-neutron spectrum behind both the fuel pins and the grid plate for the 127-fuel-pin subassembly with a 12.7-mm subassembly spacing. We believe that the unfolded spectrum from these spectrometers is quite accurate. The response function is unity, so there is no uncertainty in the response function used in the calculation. The other detector used was the Hornyak button, which has a diameter of either 6.35 mm or 12.7 mm and a thickness of about 1.6 mm. Because the

Hornyak-button count rate was correlated with a dose rate by normalization to a dosimeter reading at a key position, we took the response function to be a first-collision tissue dose-response function. The energy cutoff for the response function was determined by the voltage at which the gamma-ray discriminator was set in the dosimeter and by Hornyak-button measurements.

In the empty cavity case, configuration II.A, we measured with the 2-in. cadmium-covered and 5-in. Bonner balls as well as with the Hornyak button in an axial traverse down the center of the cavity and a radial traverse 0.30 m behind the configuration. Figure 2.1 shows a relative comparison of the calculations with the measurements. The DOT-calculated curve shapes agree well with the measured shapes, but the magnitudes are higher by 45, 30, and 55% for the Hornyak button and the 2-in. cadmium-covered and 5-in. Bonner balls, respectively. Better agreement was hoped for in this configuration because it would be a part of all other configurations. The Monte Carlo (MORSE) results follow the DOT results except for the first point, which lies near the measurement. The MORSE code used a boundary source generated by DOT about 40 mm from the inner edge of the 0.3-m-thick concrete shadow shield.

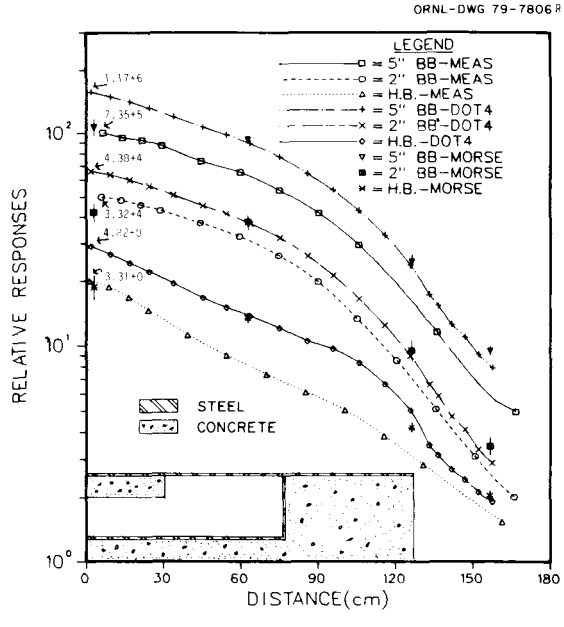

Fig. 2.1. Relative Measured and Calculated Responses for Axial Traverses down the Center of the Empty Cavity of GCFR Grid-Plate Shield Experiment Configuration II.A.

The next step up from the empty cavity case is a configuration loaded with fuel pin subassemblies. The results of the DOT calculations of four of the five core arrangements are compared in Tables 2.1 and 2.2, which show calculated and measured centerline results, respectively, for the Hornyak button and the 2-in. cadmium-covered and 5-in. Bonner balls, both 0.30 and 3.0 m behind the configurations, which are described in the tables. Close behind the configurations the calculated Bonner-ball count rates show excellent agreement with the measurements. At greater distance, though, there is substantial overprediction. Since the Hornyak-button results overpredict close-in, we agreed that the response function was probably in error. The Hornyak-button results show about the same relative overprediction (compared with 0.30 m) at 3.0 m as do the Bonner-ball results. When treated as fixed-source calculations with the fission source from DOT, the MORSE calculations gave statistical mean values that agreed well with the measurements at 0.30 m behind configuration II.B

Table 2.1. Comparison of DOT-Calculated and Measured Responses on Axis 0.30 m Behind the Fuel Pins

Detector	Configuration[a]			
	II.B	III.A	IV.A	VI.A
2-in. cadmium-covered Bonner ball				
Calculated	8.30E+1	8.48E+1	1.17E+2	8.43E+1
Measured	8.80E+1	8.63E+1	1.43E+2	8.69E+1
C/E	0.94	0.98	0.82	0.97
5-in. Bonner ball				
Calculated	8.53E+3	8.38E+3	1.18E+4	8.15E+3
Measured	8.53E+3	7.95E+3	1.25E+4	7.88E+3
C/E	1.0	1.05	0.94	1.03
Hornyak button				
Calculated	4.18E-2	4.10E-2	6.39E-2	3.97E-2
Measured	2.99E-2	2.55E-2	4.75E-2	2.34E-2
C/E	1.40	1.61	1.35	1.70

[a]Configuration II.B — 127 fuel pins per subassembly, 12.7-mm subassembly spacing; configuration III.A — 127 fuel pins per subassembly, 6.35-mm subassembly spacing; configuration IV.A — 91 fuel pins per subassembly, 12.7-mm subassembly spacing; and configuration VI.A — 127 fuel pins per subassembly, 3.18-mm subassembly spacing.

Table 2.2. Comparison of DOT-DISKTRAN-Calculated and Measured Responses on Axis 3.0 m Behind the Fuel Pins

Detector	Configuration[a]			
	II.B	III.A	IV.A	VI.A
2-in. cadmium-covered Bonner ball				
Calculated	6.32	6.39	8.87	6.45
Measured	4.32	3.28	7.28	3.61
C/E	1.46	1.95	1.22	1.79
5-in. Bonner ball				
Calculated	4.65E+2	4.96E+2	6.68E+2	4.91E+2
Measured	3.48E+2	3.6E+2	5.30E+2	3.03E+2
C/E	1.34	1.57	1.26	1.62
Hornyak button				
Calculated	2.87E-3	3.13E-3	4.71E-3	3.09E-3
Measured	1.68E-3	1.43E-3	2.75E-3	1.35E-3
C/E	1.71	2.19	1.71	2.29

[a]Configuration II.B — 127 fuel pins per subassembly, 12.7-mm subassembly spacing; configuration III.A — 127 fuel pins per subassembly, 6.35-mm subassembly spacing; configuration IV.A — 91 fuel pins per subassembly, 12.7-mm subassembly spacing; and configuration VI.A — 127 fuel pins per subassembly, 3.18-mm subassembly spacing.

(127 fuel pins per subassembly, 12.7-mm subassembly spacing) and were in slightly better agreement than DOT-DISKTRAN* at 3.0 m. Also, on the centerline, 1.38 m behind configuration II.B, fast-neutron spectrum and 3-in., 6-in., and 10-in. Bonner ball measurements were made. The DOT-DISKTRAN calculations are compared with the measurements in Table 2.3. The calculated results agree quite well with the measured results. The agreement of the calculated integral neutron fluxes with the measured ones reinforced our belief that the Hornyak-button response function was in error. Good spectral agreement is shown in Fig. 2.2.

*DISKTRAN is a specially written code that uses the angular fluxes from the DOT scalar flux-and-moments data set to calculate responses at detectors within a void. The angular flux in a localized quadrature is computed at the detector position and is summed with weights to give the total flux. Variation of angular flux over the DOT quadrature is allowed to be constant, linear, or exponential in both the azimuthal and polar directions. Constant and linear variations with radius are options.

Table 2.3. Comparison of DOT-DISKTRAN-Calculated and Measured Detector Responses on the Centerline 1.38 m Behind the Fuel Pins of GCFR Grid-Plate Shield Experiment Configuration II.B[a]

Response type	Response		
	Measured (E)	Calculated (C)	C/E
Count rate, counts/min W			
3-in. Bonner ball	280	356	1.17
6-in. Bonner ball	1270	1470	1.16
10-in. Bonner ball	600	647	1.08
Neutron flux, cm^{-2} min^{-1} W^{-1}			
E > 0.9 MeV	219	233	1.06
E > 0.12 MeV	656	656	1.00

[a]Configuration II.B — 127 fuel pins per subassembly, 12.7-mm subassembly spacing.

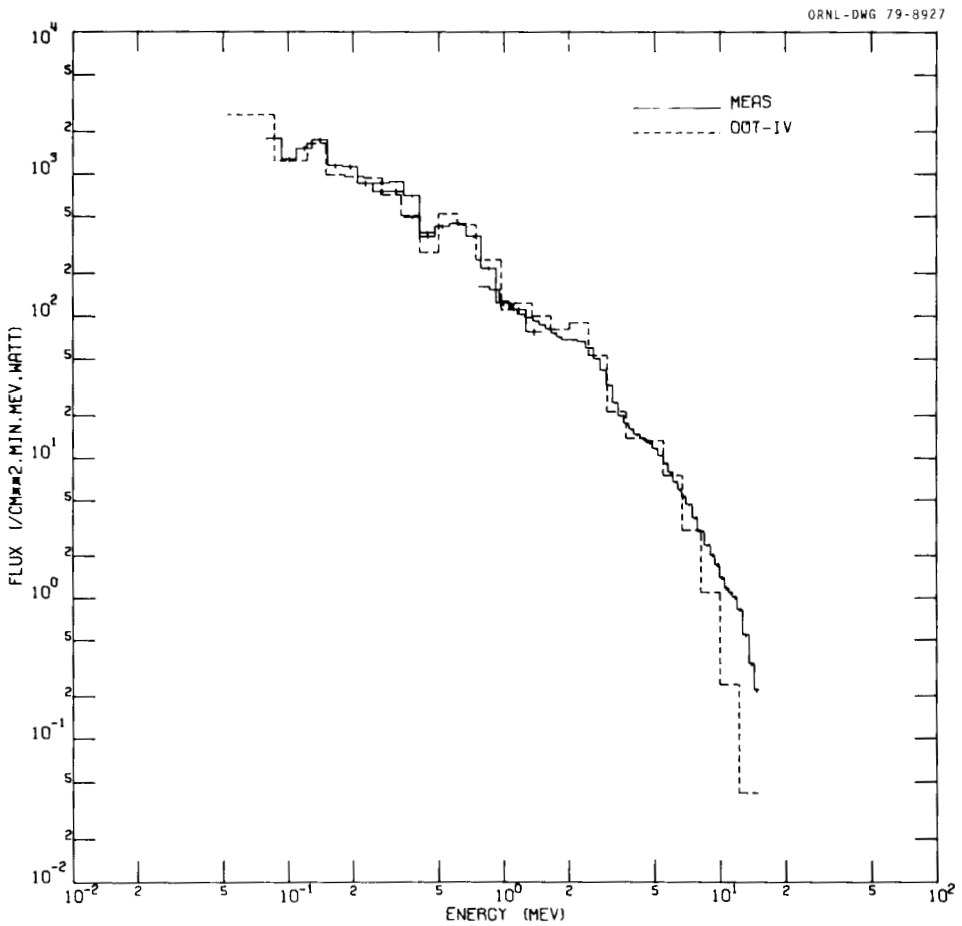

Fig. 2.2. Comparison of DOT-Calculated and Measured Neutron Spectra 1.38 m Behind the Fuel Pins of GCFR Grid-Plate Shield Experiment Configuration II.B.

We studied two cases after the addition of the grid-plate shield module behind the fuel pin or core module. In configuration II.D the shield module followed the core configuration II.B, which had 127 fuel pins per subassembly and a 12.7-mm subassembly spacing. Likewise, in configuration IV.B the shield module followed the core configuration IV.A, which had 91 fuel pins per subassembly and a 12.7-mm subassembly spacing. Axial traverses down the center shield subassembly of configuration II.D and close behind the shields in both cases were made with the Hornyak button and the 2-in. cadmium-covered Bonner ball. The DOT and MORSE results agreed well with the measured results in the axial traverse, with the Hornyak-button results being off by a normalization factor. Radial-traverse results were also relatively good, although the 2D modeling forced the calculated hole in the outer shield to be narrower than the measured hole. Hence, the calculations showed narrower and higher peaks than were seen in the measurements. The results for the 2-in. cadmium-covered Bonner-ball radial traverse behind configuration II.D in Fig. 2.3 are noteworthy. Tables 2.4 and 2.5 show comparisons of calculated with measured centerline detector responses behind

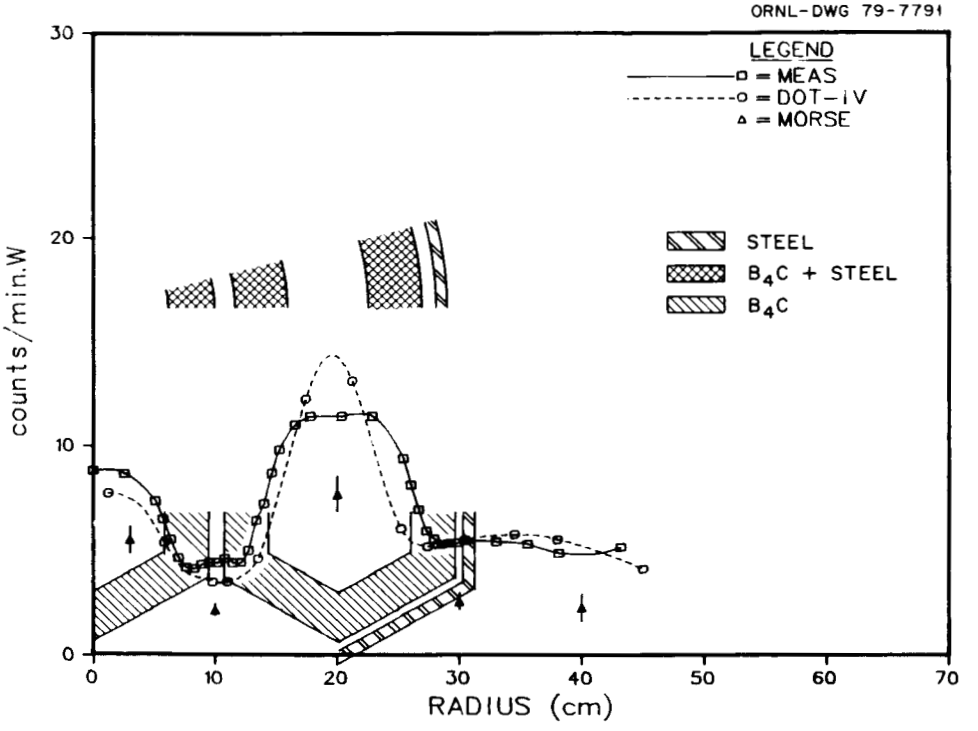

Fig. 2.3. Comparison of Calculated and Measured 2-in. Cadmium-Covered Bonner-Ball Count Rate for a Radial Traverse 31.8 mm Behind GCFR Grid-Plate Shield Experiment Configuration II.D.

Table 2.4. Comparison of DOT-DOT- and DOT-DISKTRAN-Calculated Detector Responses with Measured Values on the Centerline Behind GCFR Grid-Plate Shield Experiment Configuration II.D[a]

Response type	Distance from shield (m)	Value		
		Calculated	Measured	*C/E*
Hornyak button, ergs/ghW	0.30[b]	5.94E-3	2.91E-3	2.04
	3.0	1.25E-3	5.94E-4	2.10
2-in. Cd-covered Bonner ball, counts/min W	0.30[b]	5.20	4.92	1.06
	3.0	1.66	1.22	1.36
5-in. Bonner ball, counts/min W	0.30[b]	1120	976	1.15
	3.0	187	118	1.58

[a]Configuration II.D — 127 fuel pins per subassembly in core, 12.7-mm fuel and shield subassembly spacing.

[b]DOT-DOT calculations, i.e., DOT calculation in configuration followed by DOT calculation in void behind configuration.

Table 2.5. Comparison of DOT-DOT- and DOT-DISKTRAN-Calculated Detector Responses with Measured Values on the Centerline Behind GCFR Grid-Plate Shield Experiment Configuration IV.B[a]

Response type	Distance from shield (m)	Value		
		Calculated	Measured	*C/E*
Hornyak button, ergs/ghW	0.30[b]	1.08E-2	5.40E-4	2.00
	3.0	1.99E-3	9.58E-4	2.08
2-in. Cd-covered Bonner ball, counts/min W	0.30[b]	9.37	9.91	0.95
	3.0	2.70	2.14	1.26
5-in. Bonner ball, counts/min W	0.30[b]	1730	1520	1.14
	3.0	265	177	1.50

[a]Configuration IV.B — 91 fuel pins per subassembly in core, 12.7-mm fuel and shield subassembly spacing.

[b]DOT-DOT calculations, i.e., DOT calculation in configuration followed by DOT calculation in void behind configuration.

configurations II.D and IV.B, respectively. The close-in results were obtained by a DOT-DOT combination (i.e., a DOT calculation through the configuration followed by one in the void behind the configuration), whereas the distant results were obtained from a DOT-DISKTRAN combination. Again, the Bonner-ball results close-in (0.30 m) agree well with the measurements, and those at 3.0 m show slightly larger discrepancies than were seen behind the fuel pins.

Configurations II.D and IV.B permitted us to determine how well the calculations predicted the peak fast-neutron exposure to the grid plate by use of the results from the Hornyak-button measurements to detect the large variation in the fast-neutron exposure rate across the subassembly gap. Because the calculated Hornyak-button results were not properly normalized, results at the center of the traverse were normalized such that the C/E at the center was the same as that for the 5-in. Bonner ball at 0.30 m. We then compared the normalized, calculated and the measured peak values and found that the calculated-to-measured peak fast-neutron exposure ratios were 0.98 and 1.00 for configurations II.D and IV.B, respectively. Thus, although the calculations did not show the well-defined peaks of the measurements (Fig. 2.4), the peak fast-neutron

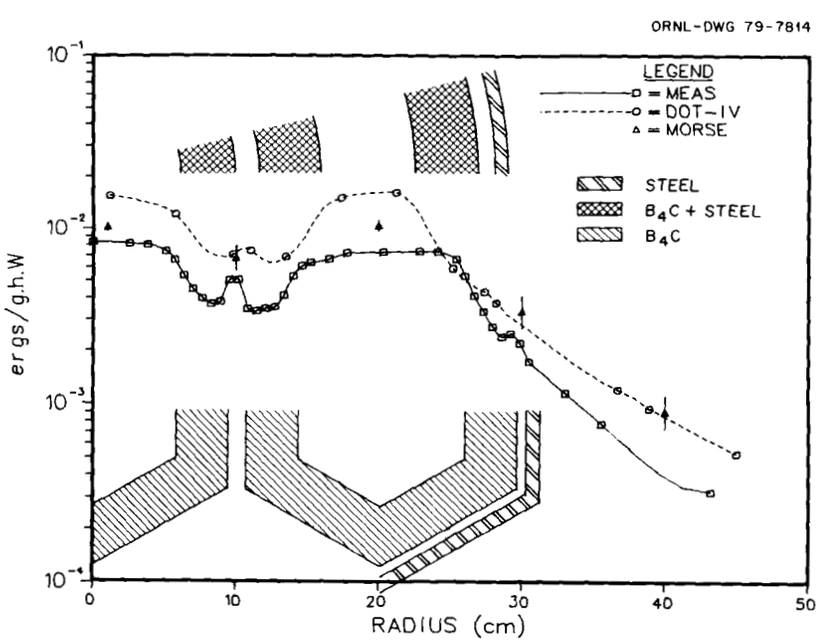

Fig. 2.4. Comparison of Calculated and Measured Hornyak-Button Response for a Radial Traverse 22.2 mm Behind GCFR Grid-Plate Shield Experiment Configuration II.D.

exposure would appear to be calculated to well within the uncertainty of the measurements (≤10%).

Finally, we took measurements behind the prototypic grid plate (configuration II.F) by use of spectrometers, Hornyak button, and several Bonner balls. Table 2.6 compares several detector responses calculated on the centerline with the measured ones. Even close-in, up to a 54% overprediction occurs with DOT (with a second DOT calculation for the close-in points and a DISKTRAN calculation for the distant points). At 3.0 m the overprediction is a factor of 2. The MORSE code slightly underpredicts the fast-neutron flux 0.34 m behind the grid plate and agrees much better than does DOT.

We conclude that (1) in the range of interassembly gap sizes considered, the gap size has little effect on neutron streaming (≤5%); (2) the void fraction within a subassembly has a large effect on neutron leakage (about 50% between 44.5%- and 60.2%-void fraction); (3) the peak fast-neutron exposure to the grid plate can probably be calculated well with our methods; (4) up through the botton of the grid plate, the DOT calculations agree well with the measurements, and design calculations would be expected to be accurate up to that point; and (5) the neutron source into the GCFR upper axial regions is likely to be conservative as a result of the large calculation-to-measurement ratios behind the grid plate in the experiment. More detailed analyses will be reported later.

2.3 RADIAL BLANKET AND SHIELD EXPERIMENT — D. T. Ingersoll and F. J. Muckenthaler

2.3.1 Preanalysis

We designed an integral experiment to verify radiation transport methods and nuclear data used for the design of the radial shield for the proposed 300-MW(e) GCFR.[5] The scope of the experiment was chosen to include a thorium oxide radial blanket mockup and several radial shield configurations. The blanket measurements are needed to reduce the large uncertainties that exist in the cross-section data required for calculating neutron transmission through a thorium blanket, thereby reducing

Table 2.6. Comparison of Calculated and Measured Detector Responses on the Centerline Behind the Grid Plate of the GCFR Grid-Plate Shield Experiment Configuration II.F[a]

Response type	Distance from grid plate (m)	Measured (E)	Calculated (C)			
			DOT	C/E	MORSE	C/E
3-in. Bonner-ball count rate, counts/min W	0.34	42.6	59.0	1.4		
E > 0.9 MeV neutron flux, n/cm^2 min W	0.34	26.61	40.99	1.54	23.62 ± 3.42	0.89 ± 0.13
E > 0.12 MeV neutron flux, n/cm^2 min W	0.34	99.22	146.4	1.48	72.0 ± 4.38	0.73 ± 0.04
Bonner-ball count rates, counts/min W	3.0					
2-in.		0.493	1.08	2.1		
3-in.		12.3	25.6	2.1		
5-in.		55.1	116	2.1		
6-in.		62.1	127	2.0		
8-in.		50.8	101	2.0		
10-in.		29.6	62.6	2.1		
12-in.		16.8	36.4	2.2		

[a]Configuration II.F — 127 fuel pins per subassembly in core, 12.7-mm fuel and shield subassembly spacing, plus prototypic grid plate.

the uncertainties in the calculated source terms for the radial shield. Similarly, the shield measurements are needed to reduce the uncertainties in the calculated radiation damage to the Prestressed Concrete Reactor Vessel (PCRV). Measurements are also needed to bound the uncertainties in calculated gamma-ray heating rates in the blanket and shield.

The preanalysis of the experimental configurations began with a one-dimensional (1D) calculation of the current GCFR shield design from the core centerline to the PCRV at the vertical level of the core midplane. The specific shield design has been designated as Conceptual Shielding Configuration I (CSC.1).[6] The 1D calculation, which used a distributed fission source calculated at General Atomic Company (GA), provided the flux spectra within the GCFR. These spectra guided the selection of spectrum modifiers in the experiment design, specifically at the core-blanket interface and the blanket-shield interface.

2.3.1.1 Preanalysis of Blanket Configurations

Because the neutron energy spectrum emerging from the Tower Shielding Facility (TSF) is not typical of a GCFR, a spectrum modifier is required to yield a source with the proper spectral characteristics. We performed several 1D transport calculations for various trial compositions of the spectrum modifier to be used for the blanket configurations. A modifier consisting of 100 mm carbon steel and 90 mm aluminum, followed by 25 mm Boral yielded the best source leakage spectrum when compared with the core leakage calculated for the CSC.1 design. Figure 2.5 compares the leakage spectrum from the spectrum modifier, the CSC.1 core, and the TSF. Although the low-energy portion of the modified spectrum could be improved with additional Boral, the relatively low importance of low-energy neutrons did not warrant the additional expenditure and the consequential loss of source strength.

Our original intent was to include in the blanket phase of the experiment a duplicate set of measurements on UO_2 blanket mockups and ThO_2 mockups. However, readily available amounts of UO_2 were insufficient, which left primarily three alternatives: (1) UO_3 available at Savannah River Plant (SRP) could be fabricated into suitable slabs, (2) previously fabricated CRBR-type UO_2 slabs available at the TSF could be used, or

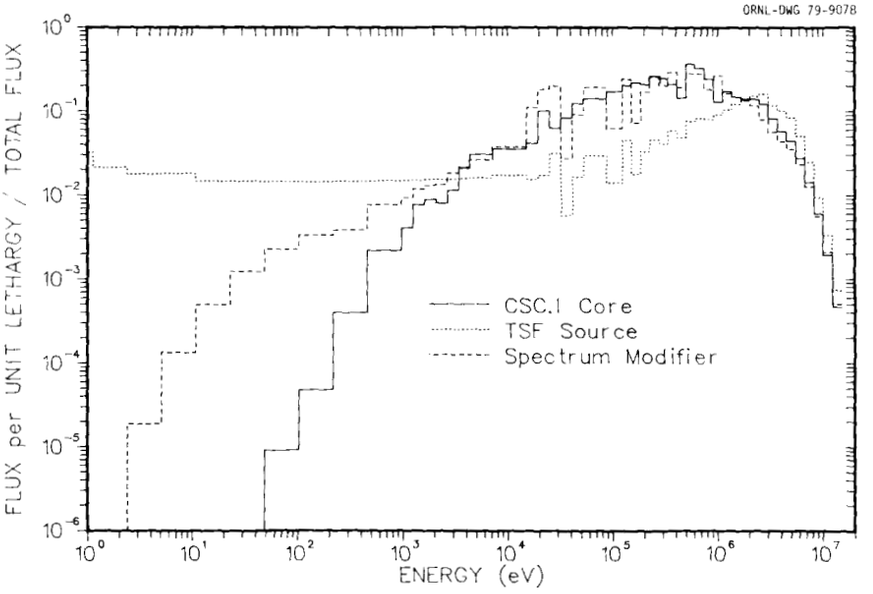

Fig. 2.5. Calculated Neutron Leakage Spectra from GCFR Core, TSF Reactor Beam.

(3) the UO_2 blanket measurements could be discarded. The CRBR-type blankets contain sodium and aluminum, whereas the SRP UO_3 contains significant amounts of water and nitrates. By use of calculations, we concluded that neither the CRBR-type UO_2 nor the SRP UO_3 was satisfactory for the "benchmark-type" comparison with ThO_2 that was intended. We therefore decided to reduce the UO_2 measurements to only two configurations by use of the CRBR-type assemblies.

We used sensitivity analysis to determine an acceptable arrangement for the gamma-ray heating measurements within the thorium blanket mockup. We determined that when a thermoluminescence detector (TLD) is sandwiched between two 0.13-m-thick ThO_2 slabs encased in 9.5-mm type 304 stainless steel, about 20% of its response resulted from gamma-ray production in the stainless steel immediately adjacent to the detector. The remaining 80% of the TLD response resulted primarily from $Th(n,\gamma)$ reactions inside the blankets. Although this signal-to-noise ratio appeared high enough to provide the desired data regarding thorium gamma-ray production, the stainless steel background was further reduced by redesigning one of the three blanket slabs as two 66-mm slabs encased in 4.8-mm type 304 stainless steel. This feature retained the proper atomic

ratio of ThO_2 to stainless steel while allowing less steel to border the TLD. It also permitted us to make neutron transmission measurements in finer increments of thickness.

The TLD sensitivity analysis also indicated that the TLD measurements were sensitive to the material both behind and in front of the detector. With the TLD located on the beam centerline between blanket rows 2 and 3, row 3 contributed to the response only slightly less than row 2. Also, ThO_2 farther than 0.25 m from the TLD location contributed nothing toward the response. We incorporated all these considerations into the experiment specifications (Sect. 2.3.2).

2.3.1.2 Preanalysis for Shield Configurations

Preanalysis of the shield configurations began in 1978 with a 1D calculation from the TSF source through the spectrum modifier and ThO_2 blanket mockup to provide the angular boundary source needed for the shield calculations. Although a full three rows of blanket provided the most prototypic source spectrum for the shield, fewer rows were desirable for source strength. In particular, each blanket row added an attenuation factor of 3 to 4. We determined that two blanket rows ($\sim$0.3 m total thickness) represented the best compromise of spectral shape and source strength.

Portions of the GCFR radial shield design use a boronated graphite mixture containing 25 wt % boron and having a bulk density of 1.6 g/cm^3. We initially believed that a 25 wt % boron mixture of graphite and boron carbide (B_4C) powder could be vibration-packed to the desired density of 1.6 g/cm^3; therefore, the type 304 stainless steel cans to contain the mixture were designed and fabricated with the thickness dimensions specified in the CSC.1 design. However, on attempting to fill the containers, the vendor of the boronated graphite mixture could achieve only a bulk density of 1.1 g/cm^3.

To determine the effect of several corrective alternatives, we performed 1D calculations through the shield configuration by using different density and different boron content graphite mixtures. Because the resulting analysis indicated only changes in the magnitude of the

neutron flux transmitted through the mixture rather than a change in spectrum, we decided to proceed with the original mixture. At the same time, the expertise used at ORNL during the packing of B_4C for the grid-plate shield experiment was offered to the vendor in an attempt to increase the density attained.

Additional preanalysis of the shield configurations will be performed before the initiation of the experiment, which is scheduled for February 1979.

2.3.2 Experimental Configuration and Measurement Specifications

Fabrication of the experimental configurations began in 1978. The design of the experiment is similar to previous shield experiments performed at the TSF for the LMFBR program.[7,8] The configurations will consist of 1.5- by 1.5-m slabs of blanket and shield material placed perpendicular to the TSR-II[9] neutron beam centerline. The slabs will be built up in succession, and measurements will be performed behind each configuration. Figure 2.6 shows the experimental arrangement for

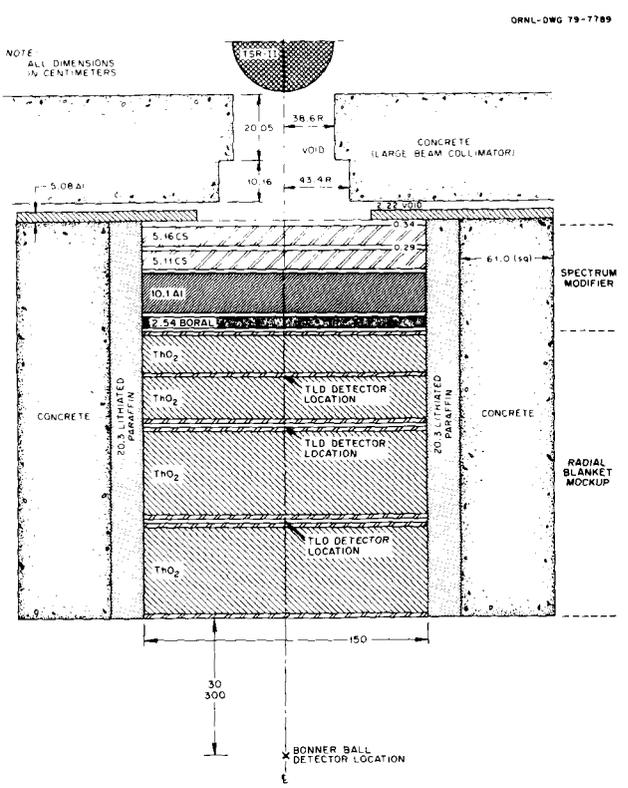

Fig. 2.6. Experimental Configuration of GCFR Radial Blanket Mockup.

the ThO_2 blanket mockup. The concrete that surrounds the configuration provides a biological shield for TSF personnel, while the lithiated paraffin minimizes the contribution of neutrons that reflect from the concrete back into the test assembly.

Detectors will include Bonner balls for integral neutron flux measurements, NE-213 and hydrogen counters for fast-neutron spectra measurements, NE-213 for gamma-ray spectra measurements, and TLDs for gamma-ray heating measurements. All measurements except the TLD data will be made with the detectors located behind the slab configurations.

The ThO_2 blanket mockups consist of four type 304 stainless steel cans filled with ThO_2 powder, which is packed to a density of 7.0 g/cm^3. The ThO_2 powder and loading are provided by National Lead of Ohio. Two of the blanket cans are 0.15 m thick and represent full blanket rows, whereas the other two cans are 76 mm thick and represent half-rows. The shield configurations consist of type 304 stainless steel slabs, solid graphite slabs, and cans filled with a mixture of graphite and B_4C powder. The graphite and boronated graphite mixture is supplied by Carborundum Company. The geometry and material specifications for the primary blanket and shield configuration are given in Table 2.7. Alternative blanket and shield configurations will also be assembled by rearranging the basic configuration and by using additional materials available at the TSF.

All configurations to be investigated are summarized in Table 2.8, which also assigns relative priorities. Configurations 18 through 29 in Table 2.8 constitute an investigation of shield heterogeneity effects and deep penetration into concrete. Although these items are not likely to be completed, they do represent important concerns and may be investigated later.

2.4 SHIELDING ANALYSIS IN SUPPORT OF GCFR DESIGN — C. O. Slater and D. T. Ingersoll

2.4.1 Upper Axial Shield

Much of the analysis of the GCFR upper axial shield was done in 1977 and has been reported.[10]

Table 2.7. Geometry and Materials Specifications for Blanket and Shield Phases of Tower Shielding Facility Experiment[a]

Region	Material	Assembly thickness (m)	
		GCFR	Experiment
Radial blanket 1	Thorium oxide	153[b]	152
Radial blanket 2	Thorium oxide	153	152
Radial blanket 3	Thorium oxide	153	152
Helium		219.4	
Inner shield 1	Stainless steel	9.5	9.5
	Boronated graphite	127.8	127
	Stainless steel	12.7	12.7
Helium gap		51	
Inner shield 2	Stainless steel	150	152
Helium gap		51	
Outer shield	Stainless steel	51	52
	Boronated graphite	51	51
	Stainless steel		7.9
	Graphite	226	229
	Stainless steel		7.9
	Boronated graphite	51	51
	Stainless steel	51	52

[a]Corresponds to Conceptual Shielding Configuration I.

[b]Average "radial penetration thickness," which is 0.75 × (diameter across corners).

Further analysis of the upper axial shield included (1) the analysis of neutron flow paths around the shield to the junction of the inlet duct with the PCRV liner, (2) the effect of quadrature on radiation streaming through the gap between the shield and the PCRV liner, and (3) the effect of the new "Shielding Core Model A"[11] on radiation levels in the upper axial regions. The flowpaths were analyzed by using channel theory. Concern was mainly with those points near the top of the gap between the upper axial shield and the PCRV liner. Hence, we selected an adjoint source position just slightly above the junction of the inlet duct with the PCRV liner. The $E > 0.1$ MeV neutron flux was one of the

Table 2.8. Configurations and Measurements for GCFR Radial Blanket and Shield Experiment

No.	Configuration	Priority	Description[a]	Measurements[b]
1	I.A	1A	Spectrum modifier	BB, S
2	I.B	1A	1/2 Th blanket row	BB
3	I.C	1A	1 Th blanket row	BB
4	I.D	1A	2 Th blanket rows	BB, S, TLD
5	I.E	1A	3 Th blanket rows	BB, S, TLD
6	I.F	1A	3 Th blanket rows + reflector	TLD
7	II.A	1A	3 U blanket rows	BB, S, TLD
8	II.B	1A	3 U blanket rows + inner radial shields	BB, S
9	III.A	1B	Inner radial shield row 1	BB, S
10	III.B	1B	Inner radial shield rows 1 and 2	BB, S
11	IV.A	1C	Inner + 1/3 outer radial shield	BB
12	IV.B	1C	Inner + 2/3 outer radial shield	BB
13	IV.C	1C	Inner + outer radial shield	BB, S
14	IV.D	1C	Radial shield + PCRV	BB, TLD
15	V.A	1D	Graphite + SS inner shield	BB, TLD
16	V.B	1D	SS + SS inner shield	BB, TLD
17	V.C	1D	SS + (C + B_4C) + SS shield	BB, TLD
18	VI.A	2	Graphite with 51-mm 304 SS	HB
19	VI.A	2	Graphite with 25-mm 304 SS	HB
20	VI.A	2	Graphite with 6.4-mm gap	HB
21	VI.A	2	Graphite with 13-mm gap	HB
22	VI.B	2	304 SS with no gap	HB
23	VI.B	2	304 SS with 6.4-mm gap	HB
24	VI.B	2	304 SS with 13-mm gap	HB
25	VI.B	2	304 SS with 25-mm gap	HB
26	VII.A	3	CS + 0.15 m concrete	BB, S
27	VII.B	3	CS + 0.30 m concrete	BB, S
28	VII.C	3	CS + 0.61 m concrete	BB, S
29	VII.D	3	CS + 0.91 m concrete	BB, S

[a] Inner and outer shields refer to Conceptual Shielding Configuration I design, SS = stainless steel, and CS = carbon steel.

[b] BB = Bonner ball, S = spectrometer, TLD = thermoluminescent detector, and HB = Hornyak button.

responses selected; its contributon flux plot is shown in Fig. 2.7, and the upper axial geometry is shown in Fig. 2.8. The source plane is at the top of the grid plate. Figure 2.7 also shows that the major neutron flow path is up the center of the cavity and over the top of the shield. However, the path between the upper axial shield and the PCRV liner (location of deep depression in center of figure) seems to be significant.

We determined the effect of quadrature on the flux levels by rerunning the foward problem with S_{12} (96 angles) instead of S_6 (30 angles). Significant increases (32% for E > 1.0 MeV and 14% for E > 0.1 MeV) occurred at point 4 (Fig. 2.8) near the top of the gap. However, radiation levels peaked at the top of the plenum. For example, at point 5 of Fig. 2.8 the E > 1.0 MeV flux increased by 60% and the E > 0.1 MeV flux increased by 43%. Thus, the higher-order quadrature increases the streaming in the gap between the shield and the liner and should show a bigger contributon flux than that shown in Fig. 2.7.

The final study of the effect of Shielding Core Model A[11] on the radiation levels used the adjoint calculations mentioned above and the

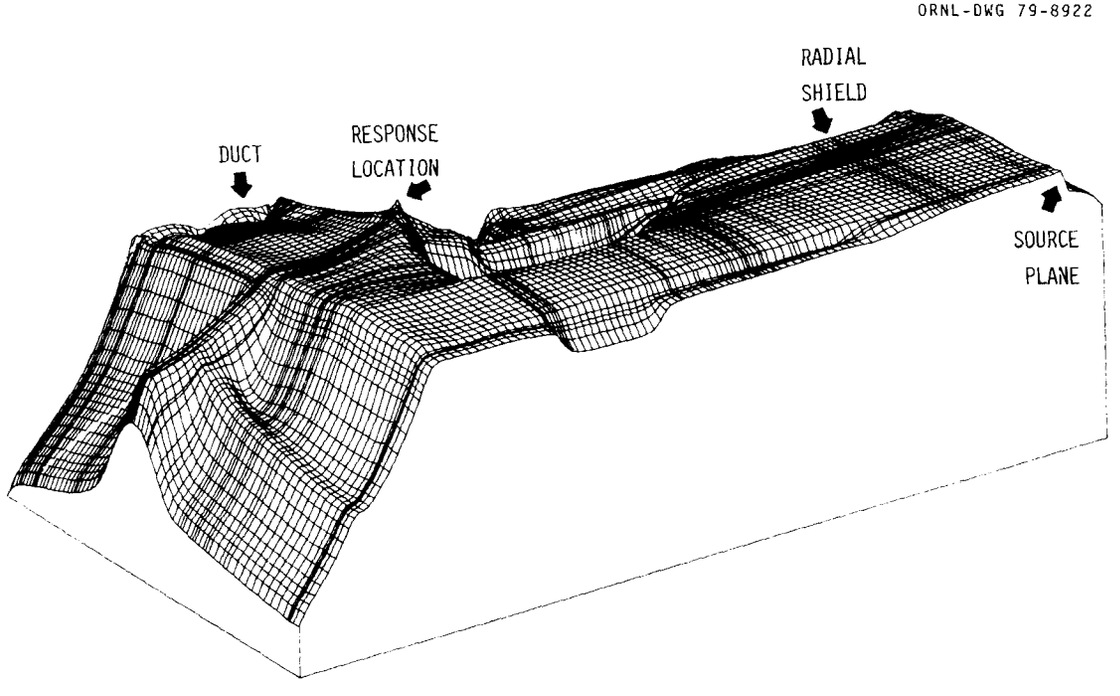

Fig. 2.7. Contributon Flux for E > 0.1 MeV Neutron Flux Above the GCFR Inlet Duct/PCRV Liner Bottom Junction.

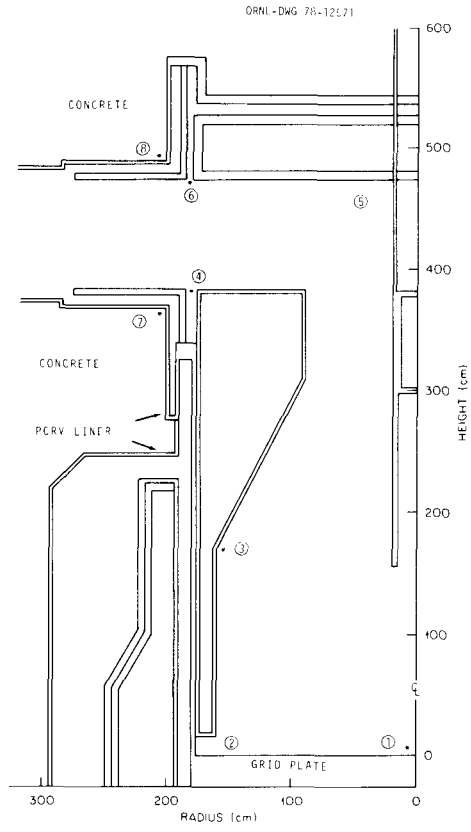

Fig. 2.8. Model of the GCFR Upper Axial Regions with Closed Outlet Duct. Conical surfaces are represented by stepped cylinders (conserving volume) in the two-dimensional model.

boundary angular flux from a flux-and-moments output file based on a *k*-calculation of the model. The downward adjoint angular flux at the top of the grid plate was coupled with the upward angular flux from a forward boundary source. The boundary source was obtained by using the radial distribution from the *k*-calculation along with results from a cell calculation to normalize the distribution to that for an end-of-cycle core. Comparison of the results obtained from coupling the adjoint to the old source (for a partially depleted model) with results obtained with the new source representing a fully depleted core indicated that the 47°C nil-ductility temperature shift in the PCRV liner would nearly double. Similar increases can be expected for the other responses.

Because a major design change was expected in the upper axial region, detailed recalculations of the region with the new source were omitted.

2.4.2 Revised Radial and Lower Axial Shield Design

We performed design support analysis for the revised radial and lower axial shields. The new reference design, which is designated CSC.1, was provided by GA[6] and is shown in Fig. 2.9. New features of the design include a third row of fresh blanket assemblies, two rows of removable inner radial shield assemblies that extend into the lower plenum region, and a depleted uranium postaccident fuel-containment system. The design also includes a laminated outer radial shield and a tapered wraparound shield.

The CSC.1 design was modeled below the core midplane in order to calculate the adequacy of the shield design to satisfy the design criteria. The large low-density coolant plenum and the streaming path between the outer shield and the PCRV liner make the lower axial shield calculation inappropriate for bootstrapping techniques, so that the entire geometry was modeled. The resulting 2D cylindrical model of the design is shown in Fig. 2.10. The geometry appears inverted because the transport code prefers that the axes of symmetry be located on the left and bottom boundaries.

The large physical dimensions of the problem required using over 11,000 mesh cells to model reasonably the configuration. We found it desirable to use the GCFR cross-section library containing 51 neutron energy groups and 25 gamma-ray groups and a minimum angular quadrature of S_6 (30 symmetrically directed angles). These factors combined to make the calculation an enormous problem that required state-of-the-art methods. We used the latest version of the DOT-IV discrete ordinates code,[3] which was not only desirable but probably required because of the magnitude of the problem. The computation consumed several hours of computer time on the ORGDP IBM 360/195 and was executed as a series of restarts. The restarts were required because of machine and code failures and because the calculation initially failed to converge. To accommodate the problem, several fixes and/or improvements were implemented in the DOT-IV code. The flux convergence was improved most by the use of coarse mesh rebalance methods.

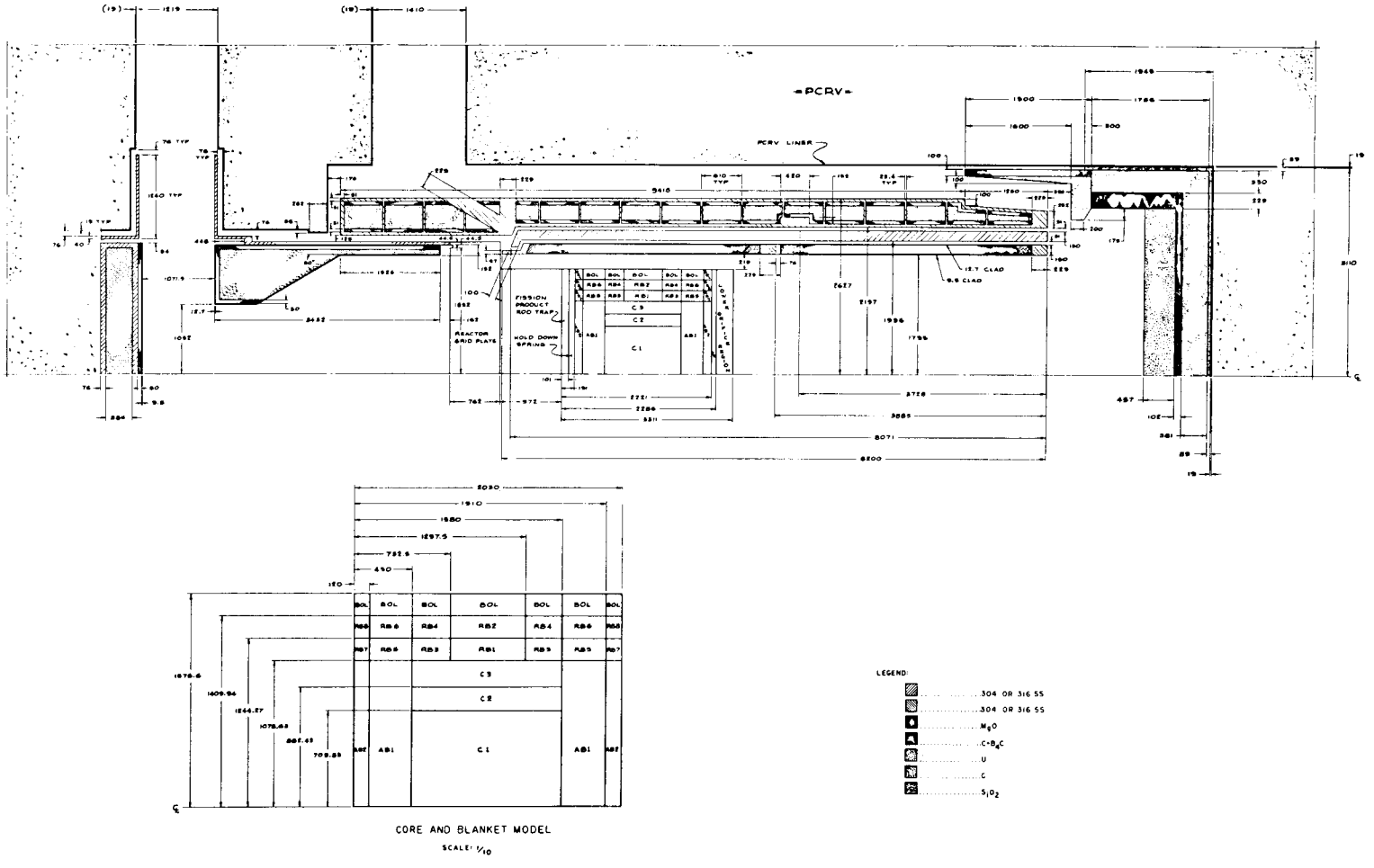

Fig. 2.9. Schematic of General Atomic Company's Conceptual Shielding Configuration I.

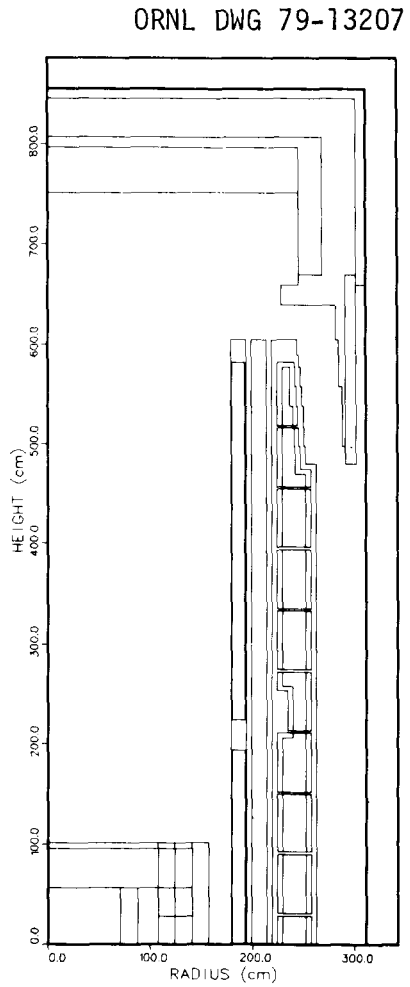

Fig. 2.10. Two-Dimensional Cylindrical Model of CSC.1 Design for the Lower Axial Region. The axial centerline is at the left boundary, and the core midplane is at the bottom boundary.

The calculation did not succeed in converging all energy groups until the final weeks of 1978; therefore, only preliminary calculations are described here. Figure 2.11 shows an isoflux plot of the 24-full-power-years neutron fluence for the entire lower axial region. The figure shows that the 10^{21} total fluence limit for permanent components is not satisfied at the bottom end of the outer radial shield. Also, significant streaming is observed in the duct between the outer shield and the PCRV liner. Although the results of the calculation will be studied in detail before the shield designs are modified and recalculated, major redesign in the wraparound shield region is likely to be required.

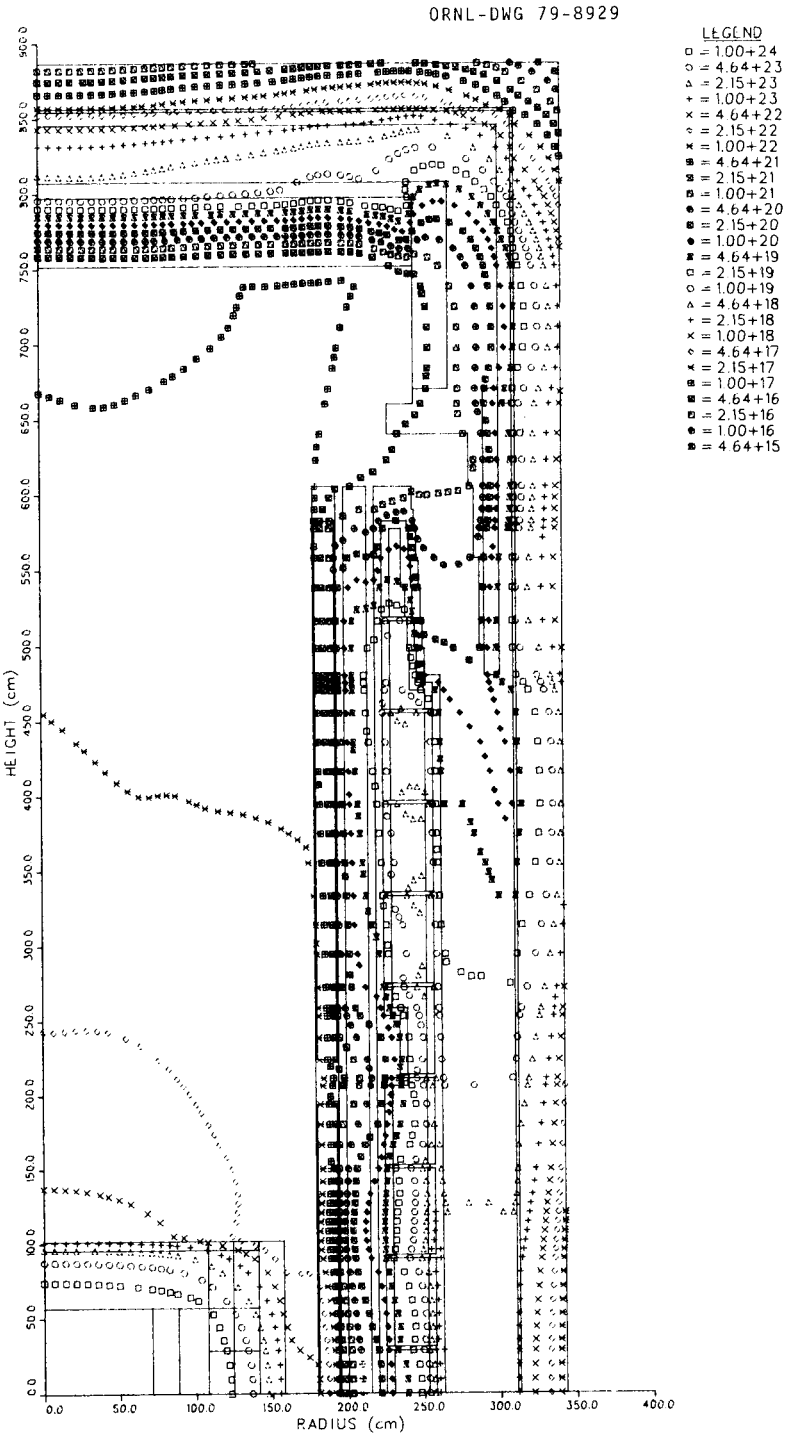

Fig. 2.11. Isoflux contours for the CSC.1 Calculation. The values indicate a 24-full-power-years fluence in units of cm^{-2}.

2.5 GCFR REACTOR PHYSICS ANALYSIS — T. J. Burns, J. R. White, M. L. Williams, and D. T. Ingersoll

2.5.1 Analysis of Alternate Fuel Cycles

2.5.1.1 Heterogeneous GCFR Core Concepts

Recent changes in the U.S. nuclear energy policy have led to a greatly expanded study of proliferation-resistant nuclear fuel cycles. We have performed several preliminary investigations[12-14] to assess the feasibility of these alternate fuel cycle concepts for LMFBRs. Our intent here is to summarize the results of a similar evaluation of alternate fuel cycles for GCFRs. The study included both the homogeneous concept and an advanced heterogeneous design. However, because alternate fuel cycles for homogeneous GCFRs have been reported elsewhere,[15] the emphasis here is on the heterogeneous model.

The reference reactor used for this preliminary evaluation was based on an early GA 1200-MW(e) homogeneous design.[16] We constructed a heterogeneous design with 60° symmetry from the same fuel and blanket assemblies as used in the reference case. After some iteration, the final core design had four fissile rings, each separated by a row of fertile blanket assemblies. As in the reference design, a three-row radial blanket encompassed the core regions. Criticality adjustments were possible with 24 control rods and 6 safety rods placed symmetrically throughout the core. The principal neutronic analysis tool used in this evaluation was the CITATION[17] computer code. Nine-group cross sections generated from ENDF/B-IV data were used throughout the study.

Early in the study we tried to verify that the *R-Z* concentric annuli reactor model used in the depletion calculations described below was a realistic simplification of the 3D fast reactor. The position and relative worth of the control rods in the 2D model were of particular interest. Table 2.9 contrasts the results of 2D and 3D static beginning-of-life (BOL) calculations for a 1200-MW(e) GCFR with (Pu, U)O_2 fuel assemblies and ThO_2 radial and internal blankets. This comparison reveals that the simplified *R-Z* calculational model produces accurate results with a significant reduction in cost and effort. Also the radial power distributions for the two reactor models are in good agreement.

Table 2.9. Comparison of 2D and 3D Calculational Models for a Pu-UO_2/ThO_2 Heterogeneous GCFR

Beginning-of-life parameters	No control in core		Control rods fully inserted	
	2D model	3D model	2D model	3D model
k_{eff}	1.0100	1.0100	0.9646	0.9653
Max. power density, W/cm^3	419.0	421.6	428.5	440.6
Max. linear heat rate, kW/m	38.7	39.0	39.7	40.7
Fissile enrichment	0.283	0.286	0.283	0.286
Total breeding ratio	1.527	1.521	1.545	1.541
^{233}U component	1.122	1.121	1.138	1.137
Fissile Pu component	0.405	0.400	0.407	0.404

We employed a three-step calculational procedure for the fuel burnup calculations. An initial depletion calculation determined the reload enrichment necessary to achieve an effective multiplication factor of unity at the end of the equilibrium cycle (i.e., the cycle for which the discharge isotopics are identical with the preceding cycle). A fuel-management scheme in which one-third of each fissile region, one-half of each fertile row, and one-sixth of the radial blanket assemblies were replaced annually was used, and a capacity factor of 0.75 was assumed. Additional computations determined the minimum first-cycle fissile loading that is consistent with criticality requirements over the initial cycles. Finally, using the initial core and reload specifications determined in the above two steps, we did a final burnup calculation in which the control material was adjusted to maintain a just-critical configuration at each depletion time-step.

The primary alternate fuel cycle scenario analyzed by using the above procedure was the energy center/dispersed reactor concept, in which proliferation-resistant denatured reactors are coupled to ^{233}U-production reactors operating in secure energy centers. Various

alternative fissile-fertile combinations were analyzed as proposed fuel for reactors both inside and outside the energy center.

Table 2.10 presents the equilibrium cycle results for these various alternate-fuel-cycle heterogeneous GCFRs. The penalties incurred by substituting the alternate fuels into the reference reactor are apparent. More important, however, is that the minimum denaturing (cases 4 and 5) for the current model was about 29% $^{233}U/U$. This high ^{233}U concentration in the fresh fuel essentially eliminates this heterogeneous GCFR concept as a proliferation-resistant denatured-fuel-cycle option. On the other hand, the large breeding ratio and ^{233}U production capability of cases 1–3 make the plutonium-fueled heterogeneous GCFR an attractive energy center reactor.

2.5.1.2 Fuel Cycle Sensitivity

During the past several years static perturbation-theory methods have been increasingly used for reactor analysis in lieu of more detailed and costly direct computations. Recently, perturbation methods that incorporate time dependence have also received attention, and the applicability of these methods to fuel burnup analysis has been demonstrated. In addition to time and cost advantages, these approaches permit a better understanding of the mechanisms responsible for the observed behavior of a given response. These benefits will be especially useful for parameter-type scoping calculations such as those being performed in current alternate GCFR fuel cycle studies. Our objective here is to demonstrate that a time-dependent perturbation method can be applied easily and accurately to realistic depletion problems.

A general theoretical framework for burnup sensitivity theory has been developed and is compatible with the conventional "quasi-static" method for solving depletion problems. Three adjoint equations (flux shape, flux normalization, and nuclide density) are required to account fully for variations in the neutron and nuclide fields that arise from variations in initial conditions and nuclear data. The final value problem comprising these adjoint equations defines a sensitivity function that relates changes in some specified integral response function to variations in the material concentrations initially loaded in the reactor.

Table 2.10. Equilibrium Cycle Results for Alternate Fuel Cycle 1200-MW(e) Heterogeneous GCFRs

Case	Description				Breeding ratio	Initial fissile loading	Mass balance (kg/year)					CFDT[a] (years)
	Driver	Axial blanket	Inner and radial blanket	^{233}U in U (%)			Charge	Discharge		Net gain		
								^{233}U	Pu	^{233}U	Pu	
1	$(Pu, U)O_2$	UO_2	UO_2		1.530	5163	1721		2139		418	11.4
2	$(Pu, U)O_2$	UO_2	ThO_2		1.456	5647	1882	797	1450	797	-433	14.3
3	$(Pu, Th)O_2$	ThO_2	ThO_2		1.371	6110	2037	1025	1309	1025	-728	19.0
4	$(^{233}U, U)O_2$	UO_2	ThO_2	29.2	1.246	5510	1837	1816	244	-21	244	22.8
5	$(^{233}U, U)O_2$	ThO_2	ThO_2	29.2	1.241	5510	1837	1889	165	52	165	23.5
6	$(^{233}U, U, Th)O_2$	ThO_2	ThO_2	40.0	1.218	5665	1889	1984	104	95	104	26.3
7	$(^{233}U, Th)O_2$	ThO_2	ThO_2	100.0	1.168	6017	2006	2162		156		35.6

[a]Compound fissile doubling time, assuming no reprocessing losses.

Once this importance function has been calculated, the effect of an initial perturbation can be estimated by an evaluation of a simple integral expression.

We have developed a time-dependent sensitivity module based on this theory and have integrated it into the VENTURE-BURNER modular code system. The new depletion perturbation theory (DEPTH) module solves for the nuclide adjoint vector and the normalization adjoint, $N^*(\bar{r},t)$ and $P^*(t)$, respectively. It then calculates the generalized adjoint source necessary for the flux adjoint calculation. Using this source, the VENTURE module solves for the generalized adjoint shape function $\Gamma^*(\bar{r},E)$ and evaluates several integrals that involve both the forward and adjoint shape functions. Calculational control is then returned to DEPTH, where the sensitivity function is determined from the previously computed adjoint functions. This procedure is repeated for each depletion time step, backward through time, until the initial time (in the forward sense) is reached. The importance function now relates a change in some integral response to a variation in initial nuclide concentrations.

We used a simplified test problem to examine the adequacy of both the sensitivity module and the coupled neutron-nuclide perturbation concept in general. Although 2D and 3D modeling is possible, we chose a 1D spherical reactor model with three core regions and two blanket zones to test the capability. Nine-group cross sections generated by use of a fast reactor spectrum were employed for all calculations. Test responses included k_{eff} and various nuclide inventories after reactor operation. We investigated the effects of several perturbations, including fissile, fertile, and structural material variations (i.e., design changes).

Some typical perturbation results are compared with direct calculations in Table 2.11 for the case of a 20% denatured (i.e., ^{233}U-^{238}U-^{232}Th) FBR after 91 d of reactor operation. The last two columns indicate that accurate results can be obtained by use of this perturbation approach. Further investigation showed that the differences from the direct calculations can be attributed to nonlinear effects not included in the perturbation formulation. In all cases, if the amount of perturbation is reduced to only a few percent, the direct and perturbation results become identical.

Table 2.11. Comparison of Coupled Neutron-Nuclide Perturbation Theory Results with Direct Calculations

Specified response (T_f = 91 d)	Case[a]	Change in response (%)				
		Perturbation results				Direct calculation
		N^* effect	P^* effect	Γ^* effect	Total	
k_{eff}	1	-0.9094	0.0040	-0.0093	-0.9137	-0.9017
	2	4.2584	0.3015	-0.0164	4.5436	4.4312
	3	1.8353	0.1644	0.0461	2.0458	2.0380
	4	-0.0654		-0.0127	-0.0781	-0.0853
^{232}U inventory	1	2.1705	-0.1189	0.0534	2.1050	2.0985
	2	7.3401	-8.8703	2.5673	1.0370	1.2806
	3	4.0213	-4.8351	1.5027	0.6890	0.8531
	4			-2.8108	-2.8108	-2.7300
^{233}U inventory	1	0.1834	0.0029	-0.0058	0.1805	0.1801
	2	5.8030	0.2162	-0.0465	5.9726	6.0735
	3	4.1991	0.1178	0.0929	4.4099	4.4145
	4			-0.0698	-0.0698	-0.0687
^{239}Pu inventory	1		-0.0154	-0.0306	-0.0460	-0.0468
	2		-1.0646	-0.2058	-1.2704	-1.2716
	3		-0.6253	-0.1330	-0.7583	-0.7425
	4			0.1294	0.1294	0.1291

[a]Case 1 — 10% increase in initial ^{232}Th concentration in all core zones, case 2 — 10% increase in initial ^{233}U concentration in all core zones, case 3 — 10% increase in initial ^{233}U concentration in core zone 3, and case 4 — 10% increase in initial stainless-steel concentration in all core zones.

Table 2.11 also gives the relative contributions of the three adjoint functions. The N^* effect is the same result that would be obtained from uncoupled perturbation theory.[18-20] It is the P^* and Γ^* effects that differentiate the coupled from the uncoupled perturbation formulation. However, the Γ^* effect is negligible for many of the cases tabulated. This is important since most of the overall computational effort was expended in its calculation. This imbalance becomes more pronounced as the size of the problem increases. Therefore, an option to bypass the $\Gamma^*(r,E)$ calculation has been built into the DEPTH module. The consequence of this option is a fast and inexpensive but slightly less general perturbation theory result. However, the maximum cost of a full adjoint calculation is roughly the same as that for the reference forward depletion calculation.

The depletion perturbation theory capability summarized above represents an attractive alternative computational method for burnup analysis. Because space- and time-dependent sensitivity coefficients are by-products of this approach, a more detailed understanding of various neutronic processes is possible. Time-dependent perturbation theory may also lead to improvements in core optimization techniques because the effect of initial design changes on responses such as end-of-cycle k_{eff}, fissile inventory, net fissile gain, and breeding ratio can be determined easily.

2.5.2 Analysis of Swiss Critical Experiments for Prototypic GCFR Core Configurations Containing Thorium

Under the GCFR umbrella agreement, a cooperative program between the United States and Switzerland was initiated. The program included pre- and postanalyses of a series of Swiss critical experiments to validate neutron physics data for thorium-bearing GCFR lattices. During 1978 the experiments included several configurations that used PuO_2-UO_2 and ThO_2 pins in prototypic GCFR core and axial blanket mockups.

The PROTEUS critical facility located at the EIR laboratory is a hybrid reactor consisting of a central GCFR-type pin lattice driven critical by annular thermal drivers. A diagram of the reactor is given in Fig. 2.12, which shows the central test zone with a movable central

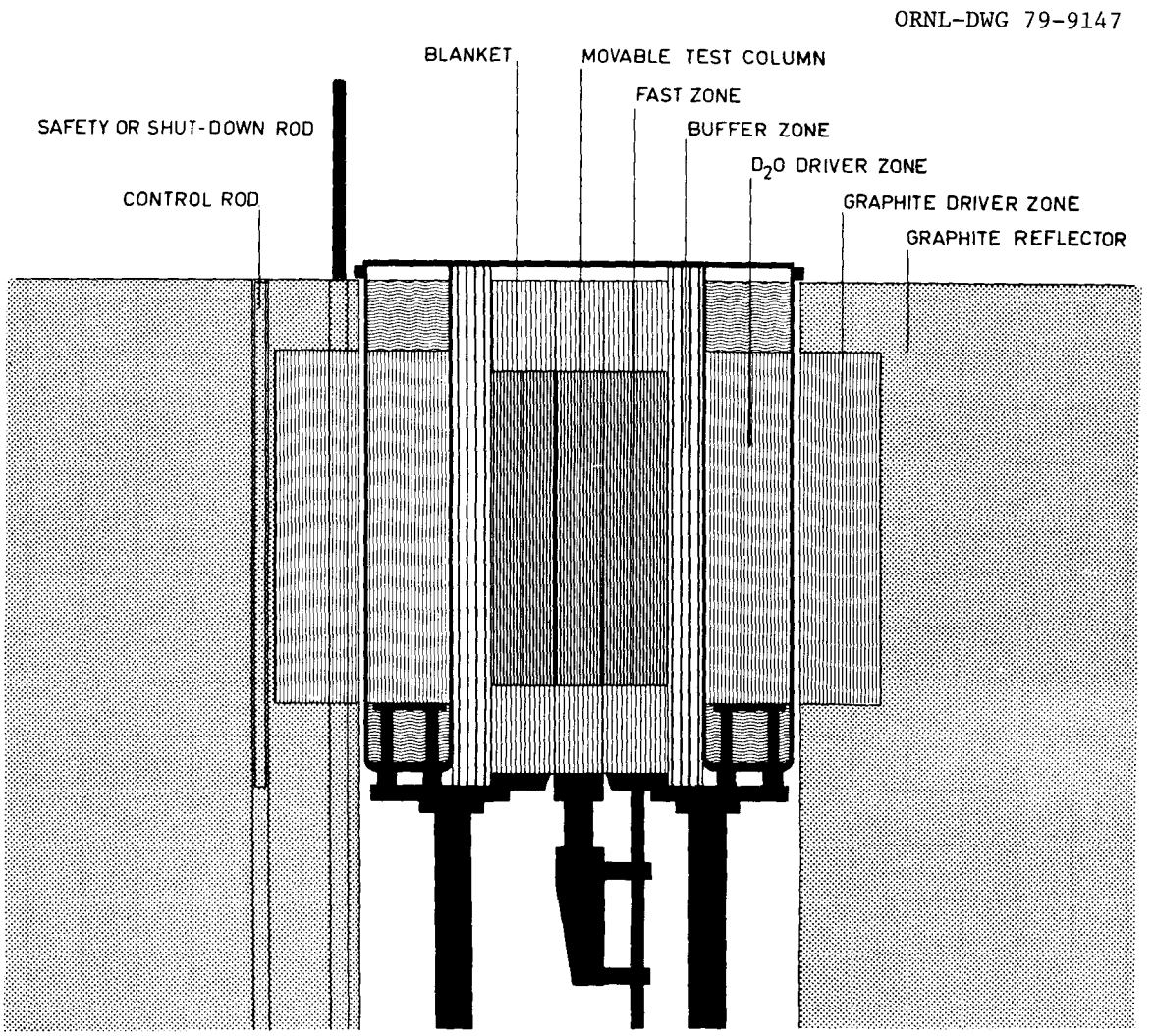

Fig. 2.12. Vertical Cut of Swiss PROTEUS Facility for GCFR Critical Experiments.

column and an axial blanket region. Reaction rate and neutron spectrum measurements are made at the center of the test zone core and axial blanket regions. The measurements are compared with calculated detector responses to test the accuracy of the nuclear data, multigroup processing, and analytical methods.

Our contribution to the program consisted of pre- and postanalyses of EIR experiments. The preanalysis was to determine (1) the sensitivities of proposed measurements to thorium cross-section data and (2) the feasibility of gamma-ray heating measurements and spectral measurements in the axial blanket. The postanalysis was to test ENDF/B-IV nuclear

data and multigroup cross-section sets used in the United States and to verify analytical methods used by EIR.

Two-dimensional models of the PROTEUS configurations with corresponding atom densities were provided by EIR. Ten-group P_0 macroscopic cross sections containing four upscatter groups were also provided to ensure a direct comparison of EIR and ORNL methods. Using identical cross sections and geometric model, EIR and ORNL calculations of k_{eff} for the reference configuration yielded values of 1.0 and 0.996, respectively, which verifies the similarity of methods. The reference lattice, consisting of an all-PuO_2-UO_2 test zone, was then modified to represent the first thorium-bearing configuration, which replaced one-third of the PuO_2-UO_2 pins with ThO_2 pins uniformly over the test zone. This mixed lattice yielded a k_{eff} of 0.972. A "brute-force" sensitivity analysis was performed for the mixed-lattice configuration by performing calculations with a 5% increase in the nuclide densities of ^{232}Th, ^{239}Pu, and ^{238}U. Ratios of the important reaction rates were computed at the center of the test zone for each case, and the sensitivity of each ratio was calculated as the percentage change in the ratio normalized to a percentage change in nuclide density. Table 2.12 summarizes the results of the sensitivity calculations for the mixed lattice. The sensitivity coefficients include only the indirect effects resulting from nuclide density perturbations in the test lattice and do not include the direct

Table 2.12. Sensitivity of Reaction-Rate Ratios to Changes in Mixed-Lattice Nuclide Densities[a]

Ratio	^{232}Th	^{239}Pu	^{238}U
$U_8(\sigma_f)/P_9(\sigma_f)$	-0.088	0.47	-0.22
$T_2(\sigma_f)/U_8(\sigma_f)$	Small	Small	Small
$T_2(\sigma_f)/T_2(\sigma_a)$	-0.048	-0.66	-0.19
$T_2(\sigma_a)/P_9(\sigma_f)$	-0.049	-0.19	-0.035
$T_2(\sigma_f)/P_9(\sigma_f)$	-0.084	0.47	-0.22

[a]Sensitivity of ratio R to nuclide N is given as $(SR/R)/(SN/N)$.

perturbation of the thorium, plutonium, and uranium reaction cross sections used in computing the reaction-rate ratios.

As indicated in Table 2.12, most reaction-rate ratios were relatively insensitive to thorium in the mixed lattice. A further calculation, which deleted all the thorium from the test zone, resulted in only a 5 to 6% change in most ratios. We concluded that the measured reaction rates would be very weakly sensitive to the presence of thorium in the test zone but that there should be an observable difference when compared with the reference lattice.

In addition to the ten-group cross sections based on FGLS* data, the ORNL GCFR cross-section set with 51 neutron and 25 gamma-ray groups was used to calculate reaction-rate ratios in the mixed-lattice configuration. Because of the lack of upscatter in the 51- and 25-group cross sections, the 5-group calculation was accomplished by use of a distributed source computed from a 51-group fission spectrum and a spatial fission source distribution calculated with the EIR 10-group cross sections. The five-group calculations provided additional spectral information, and expecially gamma-ray data.

Two major concerns requiring preanalysis were (1) the sensitivity of gamma-ray measurements in the core and blanket to the presence of thorium and (2) the sensitivity of spectrum measurements in the axial blanket to the presence of the detector and instrumentation ports. Table 2.13 summarizes the results of a series of calculations that determined the gamma-ray dose to be indeed sensitive to the presence of thorium; however, the total dose was completely dominated by the neutron contribution. Therefore, the desired TLD measurements were not feasible.

In our study of the feasibility of spectrum measurements in the relatively small axial blanket, we determined that the spectrum at the center of the axial blanket was insensitive to the presence of a 50-mm gap, which extended from the top to the center of the blanket. Table 2.14 gives the results for two of the configurations: the PuO_2-UO_2 lattice with a UO_2 blanket and the ThO_2 central column lattice with a ThO_2 blanket. Noting that all spectra in this table have been normalized to

*Designation of an European cross-section library.

Table 2.13. Results of DOT Runs for Thorium Gamma Dose in Proteus

	Position			
	Core center	Bottom of blanket	Center blanket	Top of blanket
Case 1: UO_2 blanket				
Gamma-ray dose, no Th γ	3.94E-8	1.05E-8	5.65E-9	1.81E-9
Gamma-ray dose, including Th γ	4.50E-8	1.12E-8	5.76E-9	1.83E-9
Ratio	1.14	1.07	1.02	1.01
Case 2: ThO_2 blanket				
Gamma-ray dose, no Th γ	3.943E-8	5.889E-9	1.048E-9	4.050E-10
Gamma-ray dose, including Th γ	4.500E-8	1.299E-8	6.058E-9	2.57E-9
Ratio	1.14	2.21	5.78	6.36
Total dose, no Th γ	7.464E-6	2.626E-6	1.359E-6	6.316E-7
Total dose, including Th γ	7.470E-6	2.633E-6	1.364E-6	6.337E-7
Ratio	1.00	1.00	1.00	1.00

Table 2.14. Spectrum Plots[a] at Reactor Centerline, Middle of Blanket

Group	UO_2-PuO_2 Case[b]		ThO_2 Case[c]	
	Reference case	50-mm gap	Reference case	50-mm gap
1	5.9803E-2	6.5523E-2	3.4159E-2	3.6883E-2
2	2.3050E-1	2.3840E-1	2.0968E-1	2.1354E-1
3	3.5915E-1	3.5637E-1	3.5005E-1	3.4899E-1
4	2.2365E-1	2.1693E-1	2.4304E-1	2.3886E-1
5	1.0596E-1	1.0165E-1	1.3917E-1	1.3706E-1
6	1.7898E-2	1.7215E-2	1.5126E-2	1.5676E-2
7	9.8606E-4	1.0110E-3	1.4062E-4	1.8820E-4
8	1.6208E-3	1.6937E-3	4.7017E-3	4.8351E-3
9	1.2059E-3	1.1808E-3	3.8794E-3	3.9018E-3
10	3.0147E-6	3.1473E-5	6.1569E-5	6.5829E-5

[a] Normalized to 1.0; *not* per unit lethargy.

[b] Configuration = fast test lattice UO_2 blanket, blanket thickness ≈0.17 m.

[c] Configuration = central thorium column lattice, ThO_2 blanket; blanket thickness = 335 mm.

Table 2.15. Comparison of Experimental and Calculated Reaction-Rate Ratios in the Center of PROTEUS

Reaction-rate ratio	*C/E*–Mixed lattice			*C/E*–Central column lattice		
	ORNL (ENDF)	EIR (ENDF)	EIR (FGLS)[a]	ORNL (FGLS)[a]	EIR (FGLS)[a]	EIR (ENDF)
$T_2(\sigma_c)/P_9(\sigma_f)$	1.02	1.00	1.04	1.22	1.06	0.99
$T_2(\sigma_f)/P_9(\sigma_f)$	0.86	0.88	0.89	0.92	0.90	0.87
$U_8(\sigma_c)/P_9(\sigma_f)$	0.99	1.05	0.98	0.81	1.01	1.04
$U_8(\sigma_f)/P_9(\sigma_f)$	0.93	0.96	1.05	1.10	1.04	0.98

[a]FGLS = designation of an European cross-section library.

unity, the only difference between the no-gap and the with-gap cases is a slight flattening of the with-gap spectra. For both the UO_2 and the ThO_2 blankets, the largest group difference was only 7%.

Table 2.15 compares the reaction-rate ratios calculated by ORNL and EIR. It presents calculated-to-experimental values for the important reactions in the mixed lattice and the central thorium column lattice. The mixed-lattice configuration shows generally good agreement between ORNL and EIR calculations that used different data. However, the ORNL calculation for the central column configuration shows significant differences from the EIR results. Our calculations used only the ten-group cross sections supplied by EIR for the mixed-lattice case so that the self-shielding of the heavy nuclides was inappropriate and considerable manipulation of the macroscopic cross sections was required to produce the correct nuclide atom densities. As a result, our *C/E* values for the central thorium column lattice are not reliable. This problem, however, did emphasize the need for ORNL to generate or obtain a full set of microscopic cross sections capable of analyzing the PROTEUS experiments independent of EIR. Overall, the calculations made with ENDF/B-IV cross sections that collapsed with appropriate self-shielding indicated satisfactory agreement for the $Th(n,\gamma)$ capture reaction rates but underpredicted the thorium fission and $(n,2n')$ reaction rates significantly.

2.6 REFERENCES

1. Oak Ridge National Laboratory, *Gas-Cooled Fast Reactor Program Ann. Prog. Rep. Dec. 31, 1977*, ORNL-5426 (August 1978).
2. F. J. Muckenthaler, J. L. Hull, and J. J. Manning, *The GCFR Grid Plate Shield Design Confirmation Experiment*, ORNL/TM-6580 (January 1979).
3. W. A. Rhoades et al., *The DOT-IV Two-Dimensional Discrete Ordinates Transport Code with Space-Dependent Mesh and Quadrature*, ORNL/TM-6529 (January 1979).
4. M. B. Emmett, *The MORSE Monte Carlo Radiation Transport Code System*, ORNL-4972 (February 1975).
5. General Atomic Company, *300-MW(e) Gas-Cooled Fast Breeder Reactor Demonstration Plant*, GA-A13045, San Diego, Calif. (1974).
6. Letter to Uri Gat from J. H. Broido, General Atomic Company, San Diego, Calif., "Conceptual Shielding Configuration 1," June 27, 1978.
7. R. E. Maerker, *Analysis of TSF Experiments on Radiation Heating in a Stainless Steel–Sodium CRBR Radial Shield Mockup Using a 32-Inch Diameter Collimated Beam Source*, ORNL/TM-5992 (1977).
8. R. E. Maerker and F. J. Muckenthaler, *Measurements and Analysis of the CRBR Inconel–Stainless Steel Radial Shield Experiment*, ORNL/TM-5346 (1978).
9. R. E. Maerker and F. J. Muckenthaler, *Absolute Neutron Spectrum Emerging Through the Large Beam Collimator from the TSR-II Reactor at the Tower Shielding Facility*, ORNL/TM-5183 (1976).
10. Ref. 1, pp. 135-41.
11. Letter with enclosures to D. E. Bartine from C. J. Hamilton, General Atomic Company, San Diego, Calif., End of Equilibrium Cycle Shielding Core Model A, Mar. 11, 1978.
12. T. J. Burns and D. E. Bartine, "Feasibility of Denatured LMFBRs," *Trans. Am. Nucl. Soc.* 26: 285 (1977).

13. T. J. Burns et al., "Denatured Fast Reactor Symbiosis," *Trans. Am. Nucl. Soc.* 27: 454 (1977).

14. T. J. Burns and J. R. White, *Preliminary Evaluations of Alternative LMFBR Fuel Cycle Options*, ORNL-5389 (October 1978).

15. C. J. Hamilton, *A Preliminary Study of Alternate Fuel Cycles for the Gas-Cooled Fast Breeder Reactor*, GA-A14536, General Atomic Company, San Diego, Calif. (1977).

16. Letter to D. E. Bartine from R. J. Cerbone, General Atomic Company (760422032), San Diego, Calif., April 1976.

17. T. B. Fowler, D. R. Vondy, and G. W. Cunningham, *Nuclear Reactor Core Analysis Code: CITATION*, ORNL/TM-2496, Rev. 2 (July 1971).

18. A. Gandini, "Time-dependent Generalized Perturbation Theory for Burnup Analysis," CNEN RT/FI(75)4, CNEN, Rome (1975).

19. J. M. Kallfelz, G. B. Buena, G. Palmiotli, and M. Salvatores, "Burnup Calculations with Time-dependent Generalized Perturbation Theory," *Nucl. Sci. Eng.* 62(2): 304 (1977).

20. M. Williams and C. Weisbin, *Sensitivity and Uncertainty Analysis for Functionals of the Time-dependent Nuclide Density Field*, ORNL-5393 (1978).

3. GCFR PRESSURE VESSEL AND CLOSURE STUDIES

J. P. Callahan, J. R. Dougan,
and G. C. Robinson

3.1 INTRODUCTION

The Prestressed Concrete Reactor Vessel (PCRV), which forms the primary pressure boundary for the GCFR, is designed according to established gas-cooled reactor analysis and procedures. In extending existing technology to the design of the 300-MW(e) GCFR demonstration plant, we are conducting a series of tests to verify satisfactory performance, which involve the PCRV and the closures for both the core and the steam-generator cavities. Three basic types of models are being tested: (1) relatively small models of the closure plugs; (2) larger and more detailed models of the plugs, seal, and hold-down system; and (3) a single model of the entire PCRV.

Development of the models involves a close working relationship with the General Atomic Company (GA), which is responsible for the prototype design. We must therefore schedule these design verification and support activities so that they integrate into the overall GCFR development schedule.

Our studies to date have involved the closures for both the steam-generator and reactor core cavities. Two 1/15-scale models of the steam-generator cavity closure plugs have been tested and final reports published.[1,2] An analytical parametric study was conducted to provide information required by the designer for determining the required depth for the initial small-scale (approximately 1/21-scale) model of the reactor core cavity closure plug. Construction was also completed of a facility for use in conducting tests of the larger-scale closure models and the PCRV model.

3.2 STEAM-GENERATOR CAVITY CLOSURE MODELS

Final reports on the test of the 1/15-scale model of the prototype closure[1] and on the second half-depth model of the same closure[2] were published in 1978. Abstracts of the two reports follow.

As a major participant in the Gas-Cooled Fast Reactor (GCFR) Development Program, the Oak Ridge National Laboratory has been assigned the tasks of planning and conducting structural response tests of the 300-MW(e) demonstration GCFR prestressed concrete reactor vessel closures. These studies are being conducted in close cooperation with General Atomic Company, which has the major design and development responsibility in the overall effort.

This report discusses the design, testing, analysis, and evaluation of the first test of this series (i.e., the 1/15-scale model of the steam-generator cavity closure. The primary objective of this test was to demonstrate the design performance and ultimate load capacity of the closure. Although it had been desired also to obtain information on crack development and propagation and mode of failure of the composite structure, these objectives were not obtained because pressurization was stopped at 75.84 MPa (11,000 psig) prior to obtaining ultimate load. The decision to cease pressurization at this point was influenced by the fact that the load attained was nearly 7.5 times the design load [10.08 MPa (1462 psig)] and that the instrumentation revealed that inelastic action was in progress, and by the desire to prevent the test fixture hold-down mechanism from incurring damage that would preclude its usage on future tests. (Prior hydrostatic testing of the fixture had caused slight thread yielding, thus requiring minor modifications to the design of the fixture.)

Several pretest analyses were made to evaluate the effect of various design details and material parameters. These analyses were culminated by a nonlinear analysis using the finite-element code ADINA, which includes material constitutive models for representing the nonlinear stress-strain response of both steel and concrete components. A comparison of the strains and deformations indicated generally good to fair agreement between the analytical and experimental results; however, in some few instances agreement was rather poor. These poor comparisons are attributed to boundary conditions that were difficult to model and to inadequate constitutive equations for the concrete. Analytical results predicted that failure was imminent at the 75.84-MPa loading.[1]

Oak Ridge National Laboratory is conducting structural response tests of the prestressed concrete reactor vessel (PCRV) closures for the 300-MW(e) GCFR demonstration power plant. This report describes the second in a series of tests of small-scale closure plug models. The model represents a redesign of the steam-generator cavity closure plug to a thickness of one-half that of the original model. The primary objective was to demonstrate structural performance and ultimate load capacity of the closure plug. Secondary objectives include obtaining data on crack development and propagation and mode of failure of the composite structure.

After ten pressurization cycles from zero load to the maximum cavity pressure (MCP) of 10.08 MPa (1462 psig), the model was pressurized in steps until failure occurred. No visual indications of distress were evident prior to failure, although the strains on

metal components exceeded 1.2% and strains recorded by the embedded concrete gages were approximately 1%. Failure occurred by abrupt punching shear at approximately 99.3 MPa (14,000 psig), thereby expelling the central section with considerable force. The failure surface was that of a truncated cone.

Comparisons of strains and deformations calculated using the finite-element code ADINA with experimental values indicated fair agreement. The differences between calculated and measured values are attributed to difficulties in representing the boundary conditions analytically and to the use, in ADINA, of inadequate constitutive equations to represent the nonlinear response of concrete under complex states of stress.

The results of this test demonstrate the inherent strength of the closure plug and also show that calculations made using a finite-element code in conjunction with state-of-the-art concrete constitutive equations provide conservative, but inaccurate, predictions of the failure process. On the basis of these results, we recommend that the design of the steam-generator cavity closure be further refined in order to reduce the excessive factor of safety to a more reasonable value, using thickness as the main variable. We further recommend continued development of more accurate concrete constitutive models to be used in subsequent analyses of the remaining closure models as well as in the PCRV model.[2]

3.3 REACTOR CORE CAVITY CLOSURE MODEL

We undertook an analytical parametric study to aid in the selection of an adequate thickness for the initial reactor core cavity closure plug model. The study was performed both to provide estimates of the failure pressure and to define working stress conditions as functions of the plug thickness.

3.3.1 Description of Closure

Figure 3.1 depicts the geometry of the plug, which is a composite concrete and steel structure (some details have been omitted for clarity). A relatively thin steel liner encloses the side and bottom surfaces of the concrete, and a ring forging is attached to the top of the sidewall liner. The function of the forging is to transmit the pressure loading incurred by the plug during operation to the adjacent axial prestressing tendons. The transfer of load from the closure to the tendons is performed by a series of two-force members called "toggles", which are inclined at an

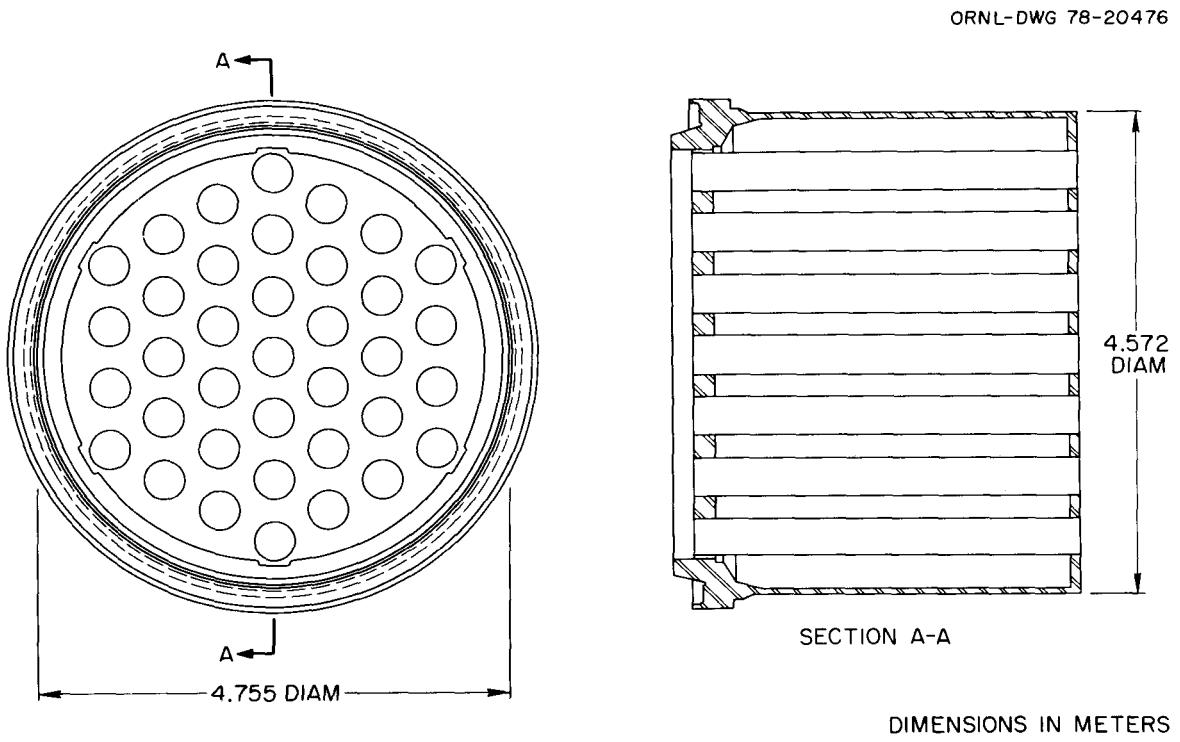

Fig. 3.1. Plan and Vertical Sections of the Prototype Reactor Core Cavity Closure Plug.

angle of 25° from the vertical and are spaced circumferentially along the upper edge of the plug. The toggles exert a radial compression to the ring forging, which, when added to the lateral pressure of the coolant, induces a circumferential prestress effect to the plug that remains proportional to the pressure loading induced by the reactor coolant.

The 37 steel-liner penetrations that perforate the plug in a hexagonal array will experience the same pressure as the bottom and sides of the plug. The design maximum cavity pressure is 10.08 MPa (1462 psig).

3.3.2 Parametric Study

We performed all analyses by use of the finite-element code ADINA,[3,4] which contains material models to represent the nonlinear stress-strain response of both the concrete and steel components. Previous analyses[1,2] indicated that the concrete constitutive model in ADINA is too stiff under triaxial compressive loadings to sustain a hydrostatic state of stress after compressive failure occurs. In an effort to overcome these

discrepancies, a concrete constitutive model utilizing endochronic theory[5] was used in the analyses. The endochronic concrete model is not as stiff as the ADINA concrete model under triaxial compression loadings and includes a strain-softening effect after the peak stress has been reached, which provides a more accurate representation of the concrete behavior.

3.3.2.1 Finite-Element Model

A two-dimensional (2D) axisymmetric analytical model was chosen for the analyses. The hexagonal array of penetrations was converted to an axisymmetric array by defining the average distance from the center of the plug to the penetrations along a specific row in the hexagonal array as being the radius of the circle on which the same penetration will lie in the axisymmetric array.

Presence of the penetrations in the concrete induces a softening effect on the stiffness of the concrete, which has been dealt with in other investigations[6-8] of similar structures by reducing the stiffness of the affected regions in proportion to the amount of material removed by the penetrations in each ring or torus of penetrations. The actual reduction of stiffness in previous investigations was accomplished by reducing the modulus of elasticity of the affected regions. However, such use of a reduced modulus of elasticity results in the computation of fictitious stresses that must be adjusted to compensate for the original assumptions. Because the nonlinear material models used in ADINA require the correct stresses for the formation of the material matrix, the stiffness reduction could not be accomplished by reducing the modulus of elasticity; consequently, another method was developed.

The stiffness-reduction method used in the analyses accomplished the required stiffness reduction by integrating the stresses in an element over a reduced element volume. Normally ADINA calculates equivalent nodal forces by integrating the stresses in an element over the element volume v by using the relationship

$$\{\vec{F}_\sigma\} = \int_v [B]^T \{\vec{\sigma}\} dV \ , \qquad (1)$$

where $\{\vec{F}_\sigma\}$ is the vector of nodal loads equivalent to the stresses in the element, $[B]$ is the matrix of strain-displacement relationships, and $\{\vec{\sigma}\}$ is the vector of element stresses.

To account for the reduced load-carrying capacity of an element caused by penetrations, the program was modified to calculate the equivalent nodal forces by integrating the stresses in the element over a reduced element volume βV,

$$\{\vec{F}_\sigma\} = \int_v [B]^T \{\vec{\sigma}\}\, \beta dV \ , \qquad (2)$$

where β is the stiffness-reduction factor as defined previously.

Integrating over the reduced element volume has the same effect in the linear range as does reducing the modulus of elasticity with the bonus of calculating the true stresses; that is, no stress modification is required for the stresses output by the program. In the nonlinear range the correct stress-strain relationship is followed because the modulus of elasticity has not been modified.

The element mesh layout is shown in Fig. 3.2. Axisymmetric solid finite elements were used to represent tall aspects of the plug with the exceptions of the steel liners in the penetrations and the toggle restraint system, which were modeled as two-force truss elements. Although the modeling of the steel liners as truss elements was recognized as being inconsistent with the prototype, we felt that the technique would work effectively in the nonlinear range while producing a conservative estimate of the failure pressure. The resulting analytical representation consisted of 154 nodes, 25 elastic-plastic steel elements, 3 reduced-stiffness elastic-plastic steel elements, 41 concrete elements, 25 reduced-stiffness concrete elements, and 59 truss elements.

3.3.2.2 Analyses

The primary parameter investigated in the analyses was the plug thickness. The plug thicknesses investigated were 0.91, 1.14, 1.52, 2.29, 3.43, and 4.57 m (35.8, 44.9, 59.8, 90.2, 135.0, and 179.9 in.), which correspond to a span-to-depth ratio of 0.2, 0.25, 0.333, 0.5, 0.75, and

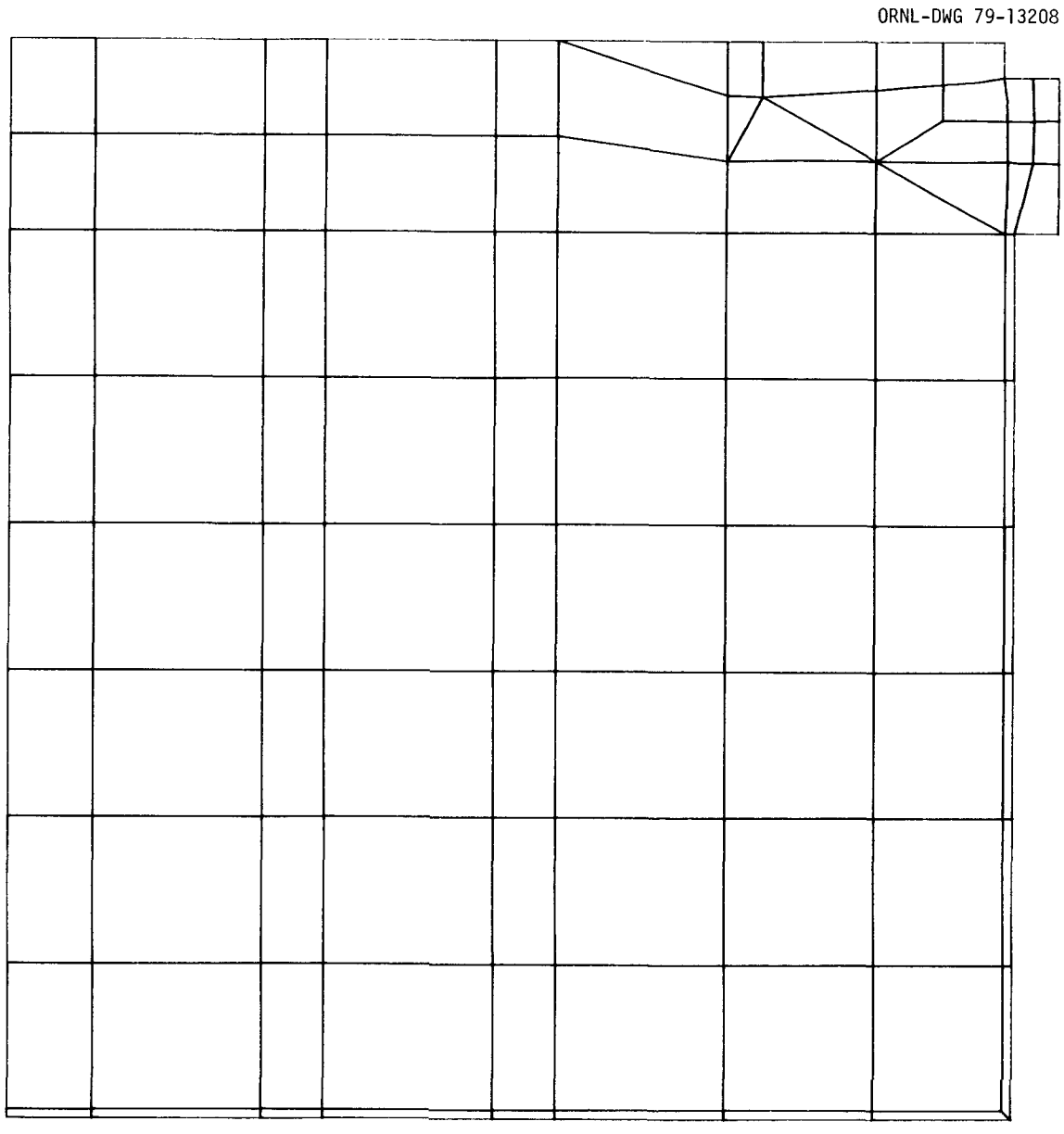

Fig. 3.2. Finite-Element Model Used for Nonlinear Analysis of the Reactor Core Cavity Closure Plug.

1, respectively. We believed that these plug thicknesses would effectively define any trend associated with the effect of plug thickness on failure pressure.

We examined two other parameters during the ultimate-pressure study. Perhaps the most significant of these was the type of restraint system to be used to hold the plug against the pressure. Although the reactor

cavity closure described previously uses a series of toggles spaced circumferentially around the plug and inclined at a specific angle, details of this design had not been finalized. An alternative design that would provide only vertical restraint, rather than the combined vertical and radial restraint provided by the inclined toggles, was also under consideration. Therefore, analyses were conducted on the plug to determine the effects of both types of restraint systems on the ultimate pressure of the plug as a function of plug thickness.

Another factor that was examined during the ultimate-pressure study concerned an analytical technique rather than a particular aspect of the plug design. An analytical technique is used to determine the magnitude of the stiffness-reduction factors by calculating the ratio of the amounts of concrete displaced by the penetrations in a given ring to the amount of concrete that would have been present in the ring if the penetrations were ignored. Two particular methods for calculating the ratio were examined: one using an area concept and the other using a length concept. In the area concept the amount of concrete is defined by the area within the torus containing the penetrations. In the length concept, the amount of concrete is defined by the circumference of the circle that passes through the center of the penetrations. Although we felt that the area concept would be more representative of the actual softening effect of the penetrations on the plug stiffness, we also conducted analyses by use of the length concept to determine the sensitivity of the analysis to the stiffness-reduction factors.

Before examining working stress conditions, two finite-element analyses were performed on the reactor core cavity closure plug in an effort to determine the effect of the pressurized steel penetrations so that the effect could be included in the 2D axisymmetric finite-element analyses. The first analysis was performed by use of 2D plane stress elements with the steel penetrations included as indicated by the mesh layout shown in Fig. 3.3. The second analysis was also performed by use of 2D plane stress elements but used the stiffness-reduction technique in the penetration regions. The mesh layout is shown in Fig. 3.4. Significant differences in the stresses as computed by the two analyses were determined and included in the 2D axisymmetric solutions.

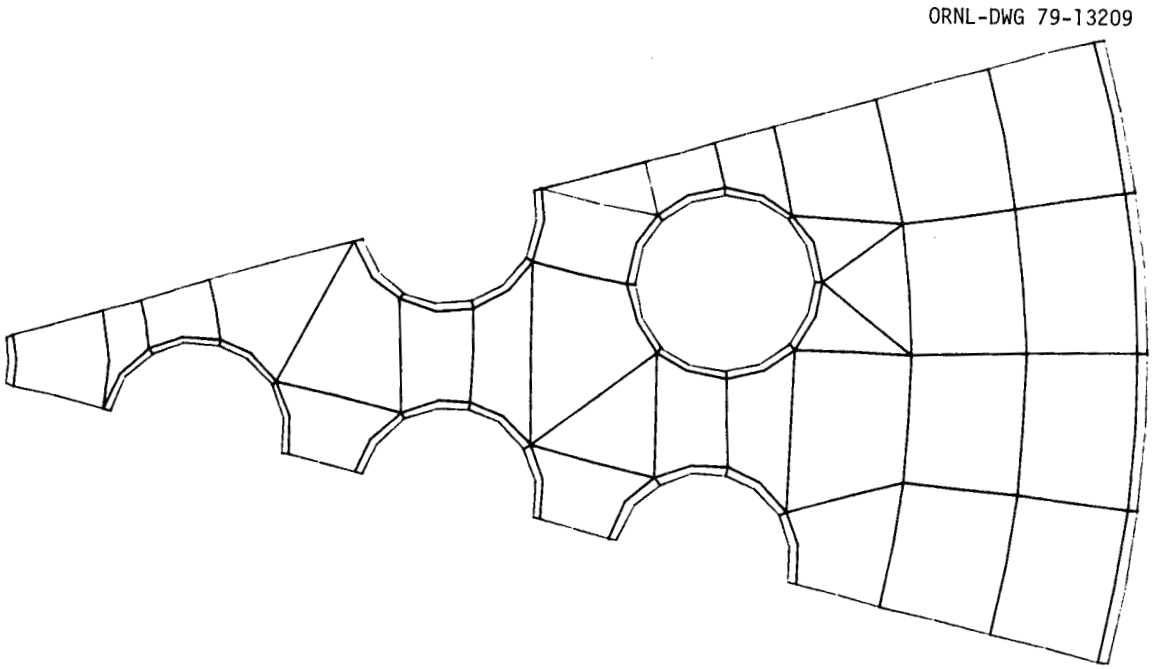

Fig. 3.3. Finite-Element Model of the Reactor Core Cavity Closure Plug Including Steel Penetrations.

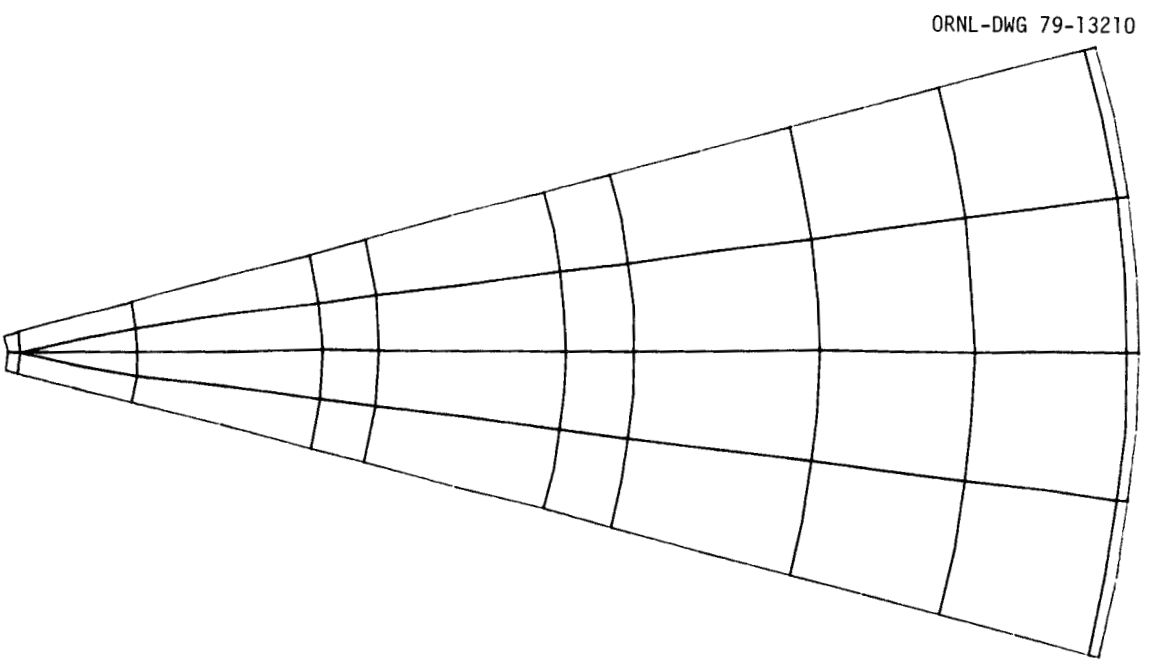

Fig. 3.4. Finite-Element Model of the Reactor Core Cavity Closure Plug Replacing Steel Penetrations with Areas of Reduced Stiffness.

In order to identify working stress conditions, point and average stresses were calculated by using the solutions of the 2D axisymmetric analysis. Point stresses were taken as an average value of integration points over the element being considered by using a weighting technique to account for the variations in element geometry. Stresses were calculated and checked in accordance with the stipulations of GA. Point stresses were checked over the entire cross section as illustrated by the mesh layout shown in Fig. 3.2. Average axial stresses were checked in the concrete elements adjacent to the bottom liner, and average radial stresses were checked in the smeared area that represents the outer ring of penetrations. Average circumferential stresses were checked in the ligament between the central penetration and the first ring of penetrations and also between the outer ring of penetrations and the steel liner, with the higher of the two averages being considered as the controlling value.

3.3.2.3 Results

The effect of plug thickness on ultimate pressure is illustrated in Fig. 3.5. As expected, the analyses incorporating the ADINA concrete model predicted failure pressures that are, for the most part, considerably less than those predicted by analyses performed by use of the endochronic concrete model. By recognizing that analyses using the ADINA concrete model typically underestimate the failure pressure for structures similar to the closure plug and that the endochronic concrete model represents an improved concrete model, we concluded that the failure pressures predicted by using the endochronic concrete model are more representative of the actual failure pressures than those predicted by using the ADINA concrete model. However, only actual testing of the plugs to failure will determine the validity of the calculated failure pressures.

Figures 3.6 and 3.7 show the effects of a vertical restraint system compared with a toggle restraint system on ultimate pressure as determined by the ADINA and the endochronic concrete models, respectively. The radial compressive force induced by the inclined toggles plus the confining pressure experienced by the concrete increased the ultimate capacity of the plug. The one exception is the 1.52-m-thick (59.8-in.) plug analyzed

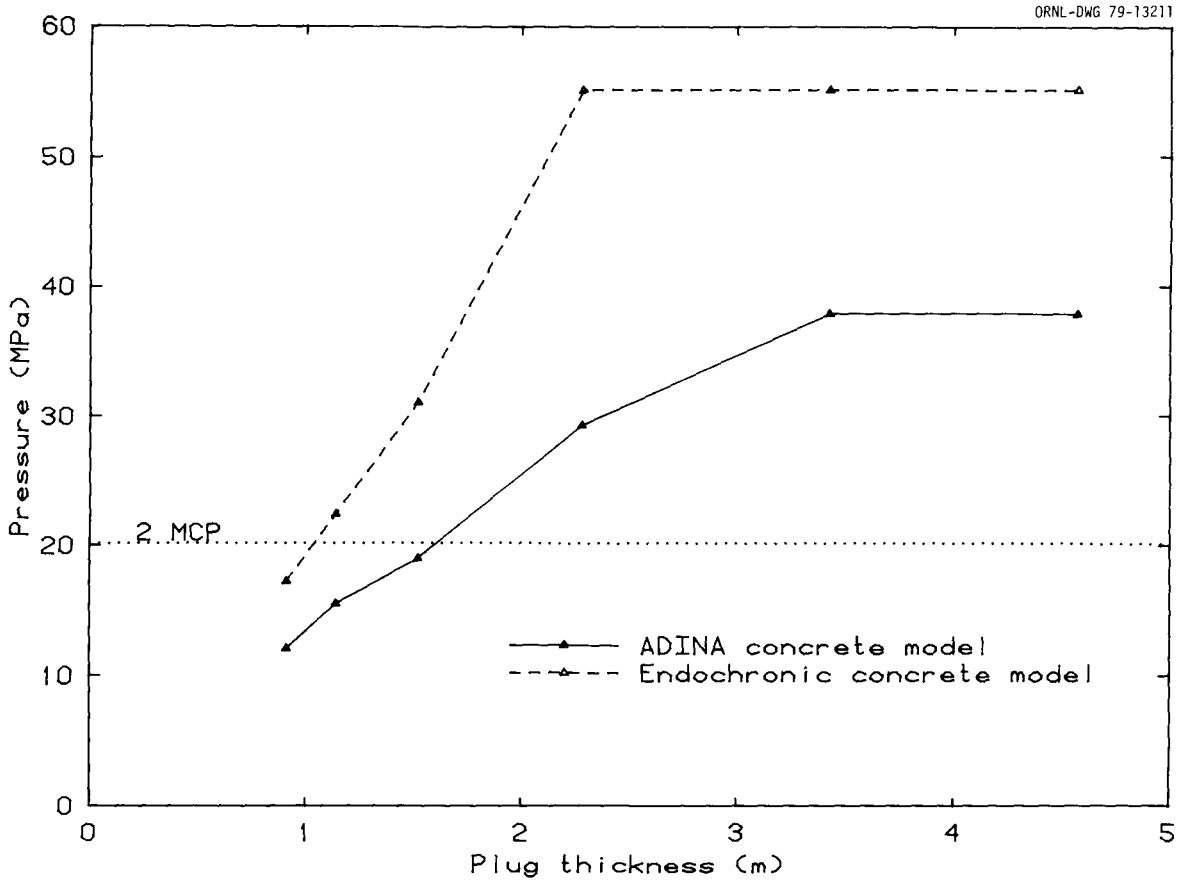

Fig. 3.5. Effect of Plug Thickness on Ultimate Pressure as Predicted by Use of the ADINA and the Endochronic Concrete Models.

with the ADINA concrete model, which probably results from the inability of ADINA to model accurately the past failure behavior of the concrete.

Figures 3.8 and 3.9 show the effect of the area and length concepts on ultimate pressure as calculated by using the ADINA and endochronic concrete models, respectively. Apparently the ADINA concrete model is quite sensitive to the type of stiffness-reduction method employed in the analyses, whereas the endochronic concrete model appears to be relatively insensitive to the method. The analyses that used the length concept were expected to yield lower failure pressures than those that used the area concept because use of the area concept produced a plug with greater stiffness than did use of the length concept.

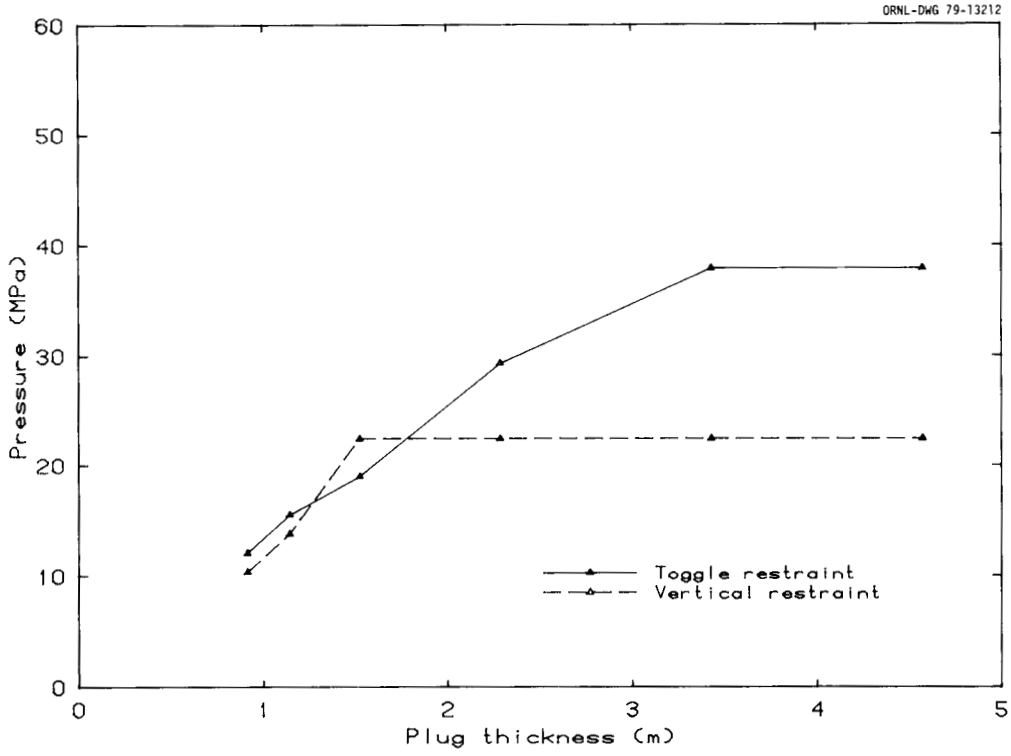

Fig. 3.6. Effect of the Vertical Restraining System Versus the Toggle Restraining System on Ultimate Pressure as Predicted by Use of the ADINA Concrete Model.

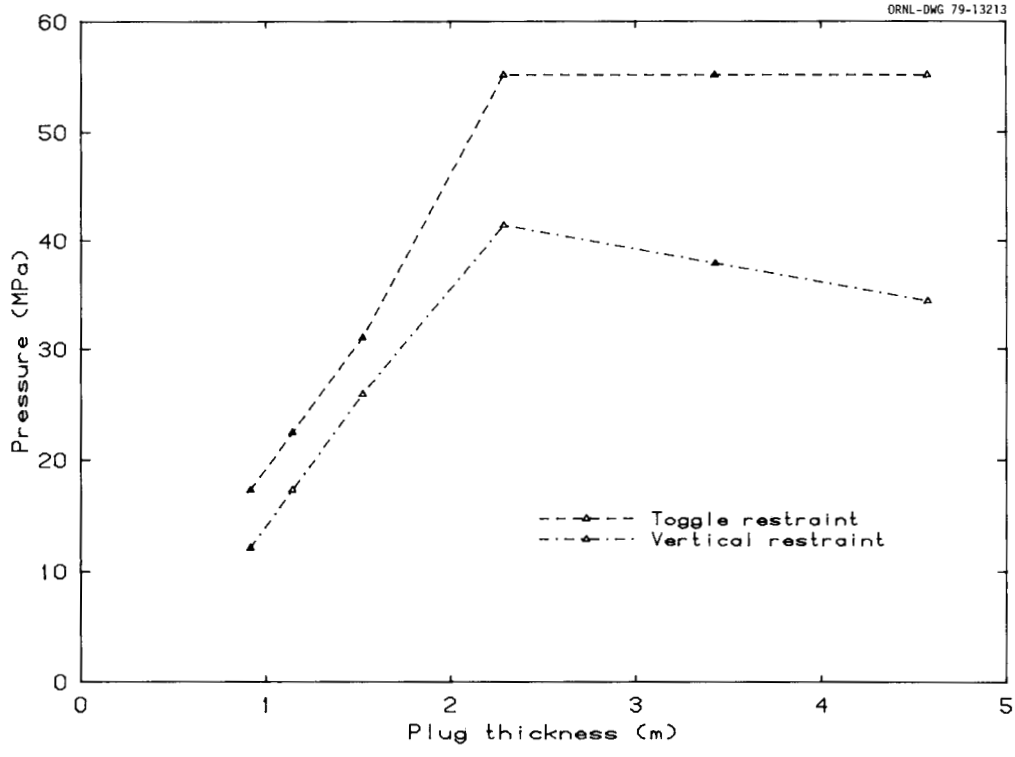

Fig. 3.7. Effect of the Vertical Restraining System Versus the Toggle Restraining System on Ultimate Pressure as Predicted by Use of the Endochronic Concrete Model.

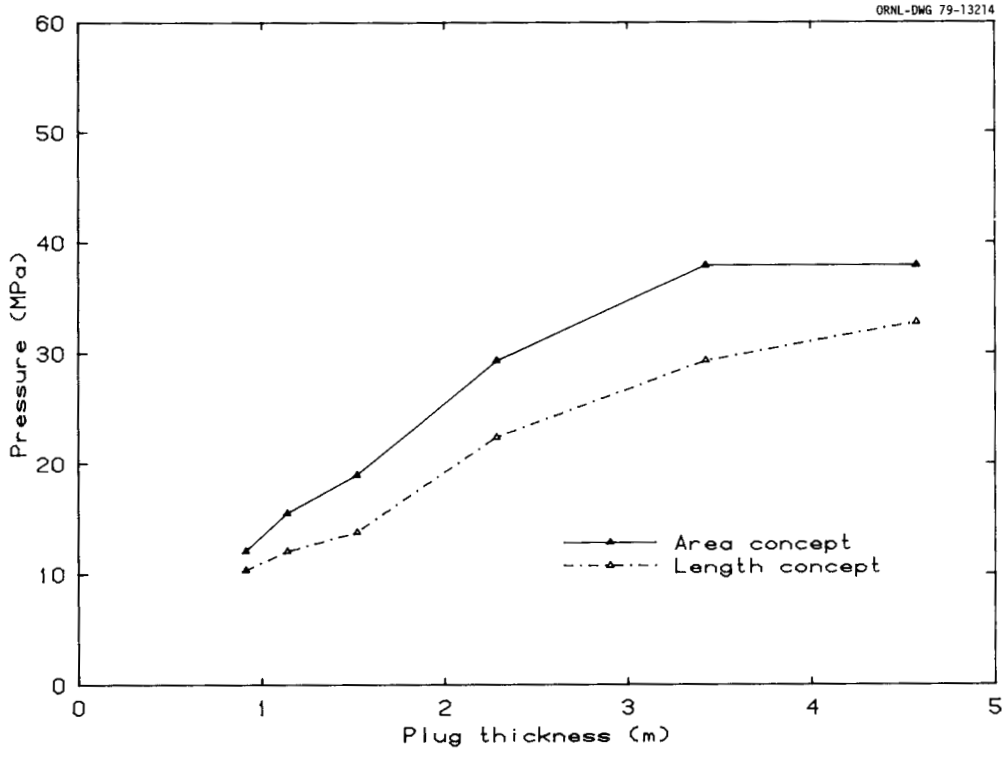

Fig. 3.8. Effect of the Length Concept Versus the Area Concept on Ultimate Pressure as Predicted by Use of the ADINA Concrete Model.

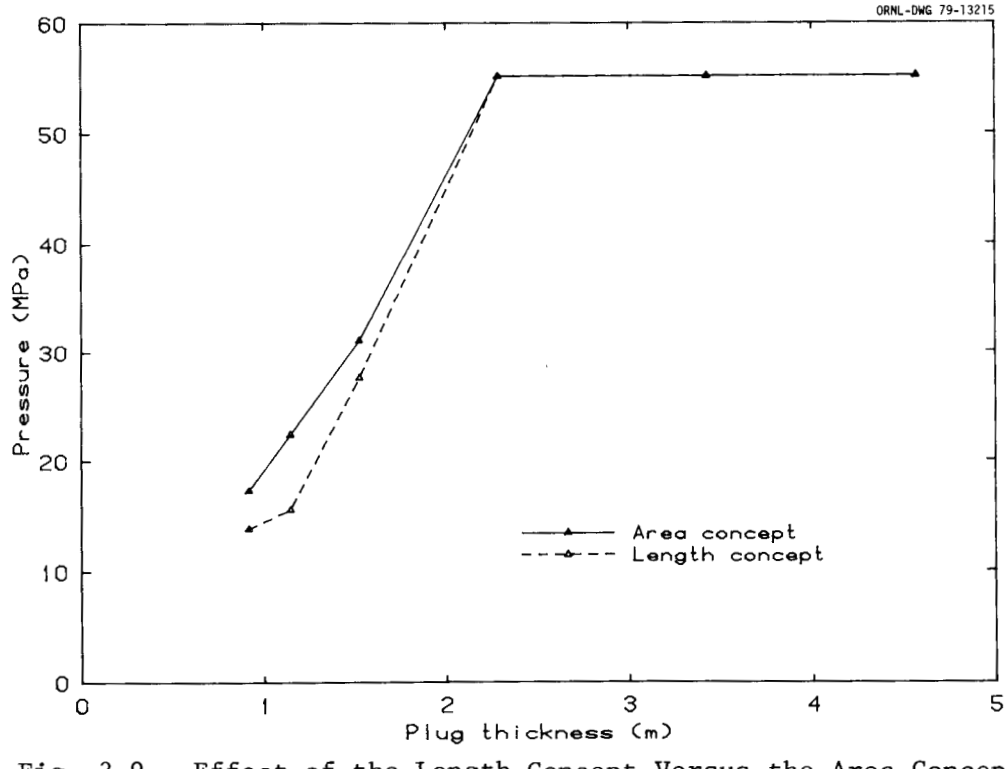

Fig. 3.9. Effect of the Length Concept Versus the Area Concept on Ultimate Pressure as Predicted by Use of the Endochronic Concrete Model.

Figure 3.10 is a plot of plug thickness versus pressure that the plug may experience before exceeding the allowable working stress limits. Each curve represents a particular type of stress and indicates the pressure at which the stress will exceed the allowable working stress limit for a particular plug thickness.

The critical point stress for the 0.91-, 1.14-, and 1.52-m-thick (35.8-, 44.9-, and 59.8-in.) plugs is the circumferential stress adjacent to the central penetration on the bottom surface. The critical point stress for the 2.29-, 3.43-, and 4.57-m (90.2-, 135.0-, and 179.9-in.) thicknesses is in the concrete immediately beneath the forging and inclined at an angle roughly equal to the inclination of the toggle hold-down members.

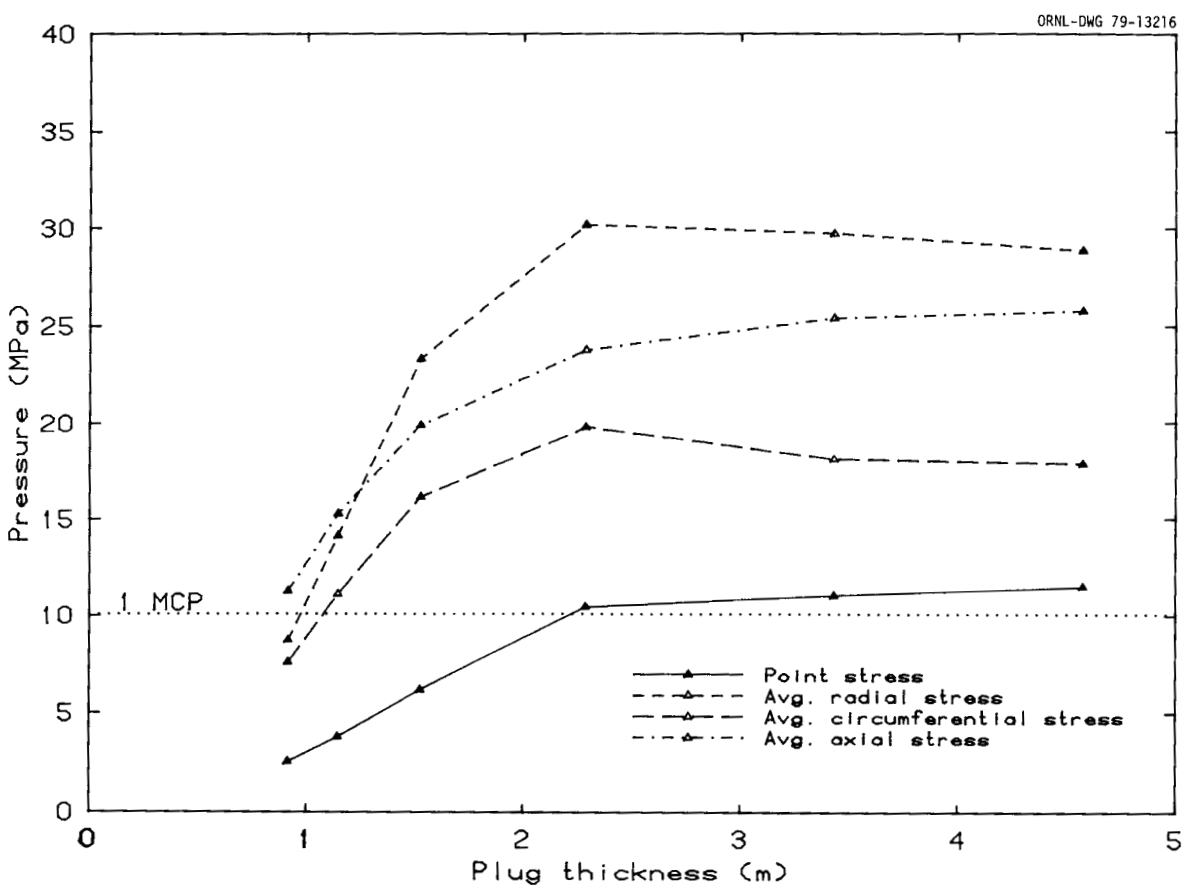

Fig. 3.10. Effect of Plug Thickness on Allowable Pressure Before Exceeding Working Stress Limitations.

3.3.2.4 Conclusions and Recommendations

As a prelude to our conclusions or recommendations, we discuss the methods used to calculate the working stresses and the values against which they were checked. As pointed out previously, the stresses were calculated according to the stipulations of GA and were checked against the allowable stress limits provided by GA. All analyses of working stress conditions were conducted according to the *ASME Boiler and Pressure Vessel Code*, Section III, Division 2, Article CB-3000.[8] In particular, Table CB-3421-1, under the normal/upset stress category, was used to establish the allowable stress limits used in the analyses. A brief discussion of two particular stipulations follows.

Point stresses could be interpreted as the stresses calculated by the finite-element method at the individual integration points. However, point stresses were calculated as the average value of the integration points within a specific element. Because of the stress variation between integration points within an element, this method yields point stress values that are lower than would be obtained by considering individual integration points.

The second stipulation concerns the use of Table CB-3421-1 to define the allowable stress limits for average stresses. The analyses were conducted with pressure loadings only; no attempt was made to include temperature effects or the effect of creep of the concrete. It would follow, therefore, that the allowable stress limits for average stresses would be defined from Table CB-3421-1 by using the primary stress condition. However, the allowable stress limits for average stresses were determined from the table by using the condition of primary plus secondary stress. The allowable stress limit is increased by using the latter category.

We concluded from the results of the analyses that several of the plugs are adequate, based on the ultimate capacity requirement, but that only the 2.29-, 3.43-, and 4.57-m-thick (90.2-, 135.0-, and 179.9-in.) plugs satisfy the working stress requirements. Inasmuch as it is desirable from an economic standpoint to make the plug as thin as possible, the 2.29-m-thick (90.2-in.) closure plug was recommended for the initial structural model test of the reactor core cavity closure plug.

3.4 PCRV MODEL TEST FACILITY

Installation of the PCRV model test facility in Building K-702 at the Oak Ridge Gaseous Diffusion Plant was completed by the cost-plus-fixed-fee contractor. This facility will permit the testing of models up to about 3 m (10 ft) in diameter and 6 m (20 ft) tall. Two parallel connected intensifiers, each capable of delivering test fluids to the models either in this cell or in the adjacent Heavy-Section Steel Technology (HSST) Program test cell, can provide test pressures up to 207 MPa (30,000 psig). Figure 3.11, an elevation view of the exterior of the PCRV test cell, shows the pressurization fluid storage and transfer system, intensifier, pipe and instrument chase bulkhead, and personnel entry plug. Figure 3.12 shows the interior of the cell as viewed from above with the shielding plugs removed, including the pipe and instrument chase bulkhead, opening for personnel access plug, and catch pan for collection of leaking test fluid. This facility will accommodate both the large-scale closure models and the 1/10-scale PCRV models.

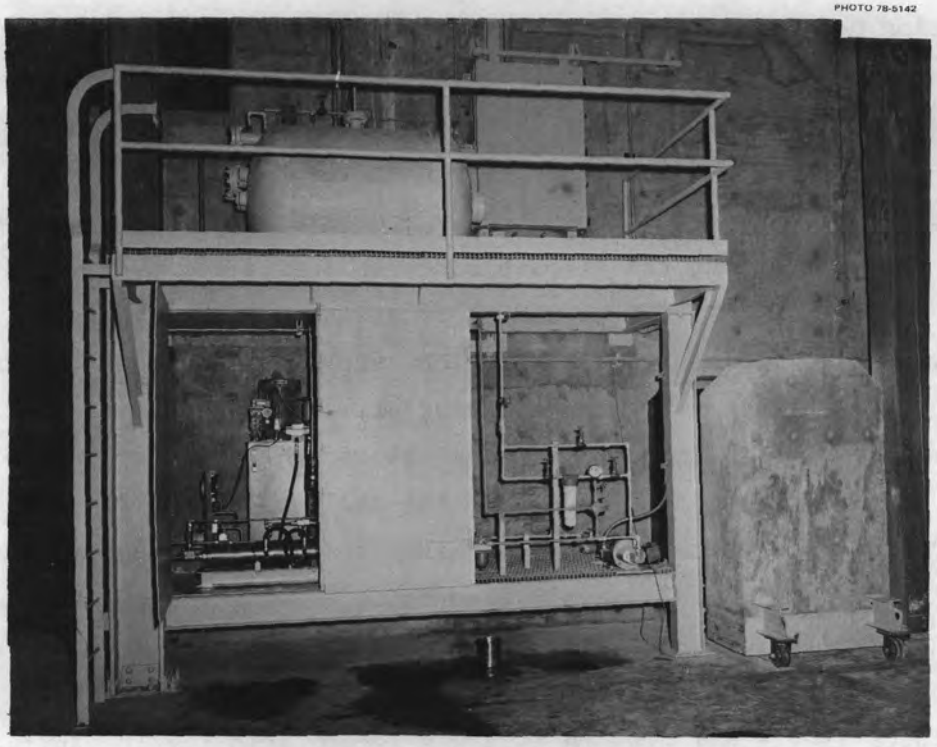

Fig. 3.11. Elevation View of the Exterior of the Prestressed Concrete Reactor Vessel Model Test Cell.

Fig. 3.12. Interior of Prestressed Concrete Reactor Vessel Model Test Cell as Viewed from the Top Opening.

3.5 REFERENCES

1. W. G. Dodge, G. C. Robinson, and J. P. Callahan, *GCFR 1/15-Scale PCRV Steam Generator Cavity Closure Model Test*, ORNL/TM-6005 (April 1978).

2. G. C. Robinson, W. G. Dodge, and J. P. Callahan, *GCFR 1/15-Scale PCRV Steam Generator Cavity Closure Half-Thickness Model Test*, ORNL/TM-6461 (December 1978).

3. K. J. Bathe, *ADINA, Finite Element Program for Automatic Dynamic Incremental Nonlinear Analysis*, Massachusetts Institute of Technology Rep. 82448-1, Cambridge (September 1975, rev. May 1976).

4. K. J. Bathe, *Static and Dynamic Geometric and Material Nonlinear Analysis Using ADINA*, Massachusetts Institute of Technology Rep. 82448-2, Cambridge (May 1976).

5. Z. P. Bazant, P. D. Bhat, and C. L. Shieh, *Endochronic Theory for Inelastic and Failure Analysis of Concrete Structures*, Northwestern University Structural Engineering Rep. 1976-12/259 (ORNL/Sub-4403-1) (December 1976).

6. J. D. Reins et al., *Shear Strength of End Slabs of Prestressed Concrete Nuclear Reactor Vessels*, University of Illinois Rep. UILU-ENG-76-2022 (ORNL/Sub-4164-1) (July 1976).

7. B. I. Karlsson and M. A. Sozen, *Shear Strength of End Slabs With and Without Penetrations in Prestressed Concrete Reactor Vessels*, University of Illinois Rep. UILU-ENG-71-2019 (July 1971).

8. American Society of Mechanical Engineers, "Code for Concrete Reactor Vessels and Containments," Section III, Division 2, *ASME Boiler and Pressure Vessel Code* (January 1975).

GAS-COOLED REACTOR PROGRAMS

JANUARY 1, 1979

PAUL R. KASTEN, DIRECTOR — CMO
JUNE L. ZACHARY, SECRETARY — CMO

AFCEP FUEL CYCLE CHARACTERIZATION AND ECONOMIC STUDIES

P. R. KASTEN,* MANAGER	CMO
A. R. OLSEN,* TASK LEADER	MC
W. L. CARTER*	CT
R. R. JUDKINS*	MC
R. H. RAINEY•	ORAU
W. E. UNGER,* TASK LEADER	CT

DIVISION MANAGERS AND COORDINATORS

J. P. CALLAHAN*	ET
D. A. COSTANZO*	AC
F. J. HOMAN*	MC
R. E. MacPHERSON*	ET
A. P. MALINAUSKAS	CT

HTGR BASE TECHNOLOGY PROGRAM

F. J. HOMAN,* MANAGER — MC
DARLENE KECK,* SECRETARY — MC

PCRV DEVELOPMENT

J. P. CALLAHAN*	ET
D. A. CANONICO*	MC
W. G. DODGE*	ET
D. N. FANNING	ET
R. K. NANSTAD*	MC
D. J. NAUS*	ET
J. E. SMITH*	ET
C. C. HURTT*	ET

HTGR STRUCTURAL MATERIALS STUDIES

J. R. DiSTEFANO*	MC
J. C. GRIESS*	MC
H. INOUYE*	MC
J. F. KING*	MC
H. E. McCOY*	MC
J. P. STRIZAK*	MC
G. W. WEBER*	MC
T. WEERASOORIYA*	MC
E. BOLLING*	MC
L. K. EGNER	MC
J. C. FELTNER*	MC
W. C. HAWKINS*	MC
V. T. HOUCHIN*	PE
E. J. LAWRENCE*	MC
B. McNABB*	MC
E. B. PATTON*	MC

HTGR CHEMISTRY PROGRAM

R. P. WICHNER	CT
R. B. BRIGGS•	
F. F. DYER*	AC
W. P. EATHERLY*	MC
L. L. FAIRCHILD*	CT
J. D. KINTIGH*	AC
M. F. OSBORNE*	CT
S. K. WHATLEY	CT

ANALYTICAL CHEMISTRY STUDIES

D. A. COSTANZO*	AC
J. D. KINTIGH*	AC
F. L. LAYTON*	AC
W. F. ROGERS*	AC

SPECIAL ASSIGNMENT

H. CORDS**	MC
M. J. KANIA*	MC
P. L. RITTENHOUSE*	MC

CHARACTERIZATION AND STANDARDIZATION OF GRAPHITE

W. P. EATHERLY*	MC
J. A. CONLIN*	ET
C. R. KENNEDY*	MC
R. L. SENN*	ET
F. P. JEFFERS*	MC

PEBBLE-BED REACTOR DESIGN STUDY

D. E. BARTINE*	EP
T. J. BURNS*	EP
J. P. RENIER	CS
D. R. VONDY	EP
B. A. WORLEY	EP

FUELED GRAPHITE DEVELOPMENT

F. J. HOMAN* — MC

FABRICATION AND CHARACTERIZATION

W. J. LACKEY*	MC
V. J. TENNERY*	MC
C. S. MORGAN*	MC
J. M. ROBBINS*	MC
D. P. STINTON*	MC
B. R. CHILCOAT*	MC
W. H. ELLIOTT, JR.*	MC
C. HAMBY, JR.*	MC

IRRADIATION TESTING

J. A. CONLIN*	ET
E. L. LONG, JR.*	MC
R. L. SHEPARD*	IC
K. R. THOMS*	ET
C. A. WALLACE*	ET

NUCLEAR ANALYSIS

W. E. THOMAS* — ET

POSTIRRADIATION EXAMINATION AND EVALUATION

F. J. HOMAN*	MC
E. L. LONG, JR.*	MC
J. M. ROBBINS*	MC
T. N. TIEGS*	MC
T. J. HENSON*	MC
E. L. RYAN*	MC
L. G. SHRADER*	MC

IRRADIATION FUEL CHEMISTRY

T. B. LINDEMER	CT
R. L. PEARSON	CT

PRESSURE VESSELS AND CLOSURES

J. P. CALLAHAN,* MANAGER	ET
W. G. DODGE*	ET
D. N. FANNING	ET
G. C. ROBINSON*	ET

SHIELDING AND REACTOR PHYSICS STUDIES

D. E. BARTINE,* MANAGER	EP
D. T. INGERSOLL, TASK LEADER	EP
T. J. BURNS*	EP
N. S. CRAMER*	EP
M. B. EMMETT*	EP
F. J. MUCKENTHALER*	EP
C. O. SLATER	EP
J. R. WHITE*	EP
L. R. WILLIAMS*	EP

GAS-COOLED FAST REACTOR PROGRAM

URI GAT,* PROGRAM MANAGER — ET
PEGGY McNUTT,* SECRETARY — ET

CORE FLOW TEST LOOP PROJECT

URI GAT,* MANAGER	ET
A. G. GRINDELL,* DEPUTY MANAGER*	ET

CFTL LOOP DESIGN DEVELOPMENT SUPPORT

A. G. GRINDELL,* TASK LEADER — ET

I & C SUPPORT

S. P. BAKER,* TASK LEADER	IC
J. E. BATEY*	QAI
D. W. McDONALD*	IC

CIRCULATOR DEVELOPMENT

H. C. YOUNG,* TASK LEADER	ET
T. B. CONLEY*	ET

ELECTRICAL ENGINEERING

T. L. HUDSON,* TASK LEADER — E

CFTL BUNDLE DESIGN AND CONSTRUCTION

H. C. YOUNG,* BUNDLE ENGINEER — ET

BUNDLE DESIGN

C. W. COLLINS,* PRINCIPAL DESIGN ENGINEER	E
J. A. SENEKER*	E

FUEL ROD SIMULATOR DEVELOPMENT

R. W. McCULLOCH,* TASK LEADER — ET

DESIGN DEVELOPMENT FOR BUNDLE

H. C. YOUNG,* BUNDLE ENGINEER	ET
T. B. CONLEY*	ET

I & C DEVELOPMENT FOR BUNDLE DESIGN

S. P. BAKER,* TASK LEADER	IC
R. L. ANDERSON*	IC

BUNDLE PROCUREMENT

H. C. YOUNG,* BUNDLE ENGINEER	ET
T. B. CONLEY*	ET

CFTL ANALYSIS

J. P. SANDERS, TASK LEADER	ET
J. C. CONKLIN*	ET
W. G. DODGE*	ET

CFTL LOOP DESIGN

W. R. HUNTLEY,* LEAD ENGINEER	ET
C. W. COLLINS, PRINCIPAL DESIGN ENGINEER	E

MECHANICAL DESIGN

W. R. CLARK*	E
W. A. HARTMAN	E
J. A. SENEKER*	E

ELECTRICAL DESIGN

R. B. BIGGS, LEAD ENGINEER	E
C. F. HOLLOWAY	E
T. L. HUDSON*	E
M. D. TRUNDLE	E

I & C DESIGN

P. G. HERNDON, PRINCIPAL ENGINEER*	IC
S. J. BALL,* DYNAMIC ANALYSIS AND CONTROLS	IC
K. J. CROSS,* DATA ACQUISITION	IC
A. D. McNUTT	E
C. I. ROSE	E
D. W. McDONALD*	IC

PROJECT ENGINEERING

H. L. MITCHELL, TASK LEADER	E
K. D. COOK,* ESTIMATING	E
F. K. BOOTH,* RUST INTERFACE	E
P. A. TABOR,* SCHEDULING	E

CFTL PROCUREMENT

W. R. HUNTLEY,* LOOP ENGINEER	ET
T. B. CONLEY*	ET
E. M. LEES*	ET
J. R. McGUFFEY	QAI
H. C. YOUNG,* CIRCULATORS	ET

CFTL CONSTRUCTION

W. R. HUNTLEY,* LOOP ENGINEER	ET
T. B. CONLEY*	ET
P. P. HAYDON, CPAF COORDINATOR	ET
D. B. AuBUCHON*	QAI

CFTL QUALITY ASSURANCE

C. A. MILLS,* CFTL QAC — ET

HTGR SAFETY STUDIES FOR NRC/RSR

S. J. BALL,* MANAGER	IC
RENEE WRIGHT,* SECRETARY	IC
J. C. CLEVELAND*	ET
J. C. CONKLIN*	ET
H. GHEZELAYAGH***	ET
J. P. SANDERS*	ET

•CONSULTANT
*PART TIME DUAL CAPACITY
**ASSIGNEE FROM KFA, JULICH
***ASSIGNEE FROM IRAN
†ASSIGNED TO KFA, JULICH

AC ANALYTICAL CHEMISTRY DIVISION
CMO CENTRAL MANAGEMENT OFFICES
CS COMPUTER SCIENCES
CT CHEMICAL TECHNOLOGY DIVISION
EP ENGINEERING PHYSICS DIVISION
ET ENGINEERING TECHNOLOGY DIVISION
IC INSTRUMENTATION AND CONTROLS DIVISION
MC METALS AND CERAMICS DIVISION
QAI QUALITY ASSURANCE AND INSPECTION

ORNL-5560
Dist. Category UC-77

INTERNAL DISTRIBUTION

1-2. Central Research Library
3. Document Reference Section
4-6. Laboratory Records Department
7. Laboratory Records (RC)
8. Patent Office
9-11. Technical Publications Department
12. L. S. Abbott
13. R. K. Adams
14. R. L. Anderson
15. S. P. Baker
16. S. J. Ball
17-18. D. E. Bartine
19. M. Bender
20. R. B. Biggs
21. I. H. Brogden
22. E. H. Bryant
23. T. J. Burns
24-25. J. P. Callahan
26. K. W. Childs
27. W. R. Clark
28. C. W. Collins
29. J. C. Conklin
30. T. B. Conley
31. J. A. Conlin
32. J. H. Coobs
33. S. N. Cramer
34. K. J. Cross
35. J. R. DiStefano
36. W. G. Dodge
37. J. R. Dougan
38. M. B. Emmett
39. D. N. Fanning
40. M. J. Feldman
41. G. F. Flanagan
42. M. H. Fontana
43-54. Uri Gat
55-57. A. G. Grindell
58. W. A. Hartman
59. P. G. Herndon
60. R. F. Hibbs
61. H. N. Hill
62. M. R. Hill
63. R. M. Hill
64. S. A. Hodge
65. C. F. Holloway
66. F. J. Homan
67. T. L. Hudson
68. W. R. Huntley
69. D. T. Ingersoll
70-77. P. R. Kasten
78. K. K. Klindt
79. A. L. Lotts
80. R. E. MacPherson
81. F. C. Maienschein
82. C. D. Martin
83. R. W. McCulloch
84. D. W. McDonald
85. S. A. Meacham
86. C. A. Mills
87. H. L. Mitchell
88. R. L. Moore
89. F. J. Muckenthaler
90. F. H. Neill
91. D. J. Naus
92. J. V. Pace
93. H. Postma
94. J. M. Robbins
95. M. J. Roberts
96. G. C. Robinson
97. J. P. Sanders
98. J. A. Seneker
99. C. O. Slater
100. J. E. Smith
101. R. S. Stone
102. R. D. Stulting
103. P. A. Tabor
104. H. E. Trammell
105. D. B. Trauger
106. M. D. Trundle
107. J. R. Weir
108. J. R. White
109. G. D. Whitman
110. L. R. Williams
111. L. W. Wilson
112. H. C. Young

EXTERNAL DISTRIBUTION

113-118. DOE Division of Nuclear Power Development, Washington, DC 20545, Director; G. A. Newby, GCFR Branch; L. M. Welshans

119. DOE Office Program Management, Research and Space Programs, P.O. Box 81325, San Diego, CA 92138, J. B. Radcliffe

120. DOE San Francisco Operations Office, 1333 Broadway, Wells Fargo Building, Oakland, CA 94162, Manager

121-123. DOE Oak Ridge Operations Office, P.O. Box E, Oak Ridge, TN 37830, Assistant Manager, Energy Research and Development; Director, Nuclear Research and Development Division

124-125. Helium Breeder Associates, 438 Camino del Rio S., Suite B-101, San Diego, CA 92108, General Manager; W. C. Guyker, HBA-GCFR

126-300. DOE Technical Information Center, P.O. Box 62, Oak Ridge, TN 37830; for distribution as shown in TID-4500 Distribution Category UC-77 (Gas-Cooled Reactor Technology)

☆U.S. GOVERNMENT PRINTING OFFICE: 1979-640-079-165